LUND UNIVERSITY

Luminescence Spectroscopy For Biomedical Applications

Mousavi, Monirehalsadat

2019

Citation for published version (APA):
Mousavi, M. (2019). *Luminescence Spectroscopy For Biomedical Applications*. Department of Physics, Lund University.

Total number of authors:
1

LUND UNIVERSITY

PO Box 117
221 00 Lund
+46 46-222 00 00

Luminescence Spectroscopy For Biomedical Applications

Monirehalsadat Mousavi

Lund
University

Academic dissertation which, by due permission of the Faculty of Engineering at Lund University, will be publicly defended on Friday, November 22, 2019, 9:15 AM in the Rydberg hall, at the Department of Physics, Professorsgatan 1, Lund, for the degree of Doctor of Philosophy in Engineering.

Faculty opponent: Prof. Dr. Artur Bednarkiewicz
Polish Academy of Sciences, Poland

DOKUMENTDATABLAD enl SIS 61 41 21

Organization
LUND UNIVERSITY

Atomic Physics
Department of Physics
P.O. Box 118
SE-112 00 Lund
Sweden

Document name
DOCTORAL DISSERTATION

Date of disputation
22nd November 2019

Sponsoring organization

Author(s)
Monirehalsadat Mousavi

Title and subtitle
Luminescence Spectroscopy For Biomedical Applications

This work presents optical methods utilizing visible light for characterization of biological tissue during diagnostics and treatment processes. The main aim has been to improve the therapeutic outcome of treatment modalities in *in vivo* studies. An optical probe instrument based on fluorescence/reflectance spectroscopy was developed for noninvasive monitoring of photosensitizer concentration in the course of a photodynamic therapy (PDT) procedure. Furthermore, upconverting nanoparticles were exploited as probes for fluorescent imaging with direct applications in preclinical research. Photodynamic therapy (PDT) is a minimally invasive treatment modality that uses light, a photosensitizing drug and oxygen to ablate malignant tumours and other diseased tissues. PDT has been investigated for treating malignancies in numerous organs and has become a promising modality for some types of malignancies including some skin tumours and prostate cancers. PDT is, however, a highly complex treatment modality with many parameters influencing the treatment outcome. Improvements in dosimetry for PDT are ongoing, with the goal to better correlate the clinical outcome to what is planned prior to the treatment of PDT. Accurate dosimetry and treatment planning require knowledge of tissue optical properties and an accurate model for the light propagation in the tissue. In the present work, we present a technique, to combine fluorescence and reflectance spectroscopy to yield improvements in the accuracy of the treatment planning. These improvements are further facilitated by multivariate analysis of the recorded data. Extracting the intrinsic fluorescence as well as optical properties of the tissue is demonstrated. This technique does not require *a priori* knowledge of the optical properties of the sample. The application of luminescence spectroscopy as an effective tool that allows detailed observations of tissues to be made via labelling with exogenous probes, is growing remarkably in popularity. Lanthanide doped upconverting nanoparticles (UCNPs) have recently been developed as light-triggered luminescent probes in various biomedical applications. UCNPs have the ability to convert near-infrared (NIR) radiation with low photon energy into visible radiations with higher energy per photon via a non-linear optical process. In this work, the non-linear dependency on the excitation intensity was compensated to improve the accuracy of measurements of the quantum efficiencies of UCNPs. Recently, UCNPs have evolved as an alternative fluorescent label to traditional fluorophores for imaging both *in vitro* and *in vivo*. Their great potential stems from their properties which include high penetration depth into the tissue, low background signal and photostability. The aim of this work was also to optimize the excitation wavelength to achieve significant signal gain in deep tissues.

Key words
biomedical optics, fluorescence, photodynamic therapy, optical properties, dosimetry, *in vivo measurement*, Upconverting nanoparticles, Quantum yield

Classification system and/or index terms (if any)

Supplementary bibliographical information

Language
English

ISSN and key title
ISSN 0281-2762, Lund Reports on Atomic Physics

ISBN
978-91-7895-332-5(print)
978-91-7895-333-2 (pdf)

Recipient's notes

Number of pages
217

Price

Security classification

I, the undersigned, being the copyright owner of the abstract of the above-mentioned dissertation, hereby grant to all reference sources the permission to publish and disseminate the abstract of the above-mentioned dissertation.

Signature ______________________ Date 14 October 2019

LUMINESCENCE SPECTROSCOPY FOR BIOMEDICAL APPLICATIONS

Monirehalsadat Mousavi

Doctoral Thesis
2019

LUND
UNIVERSITY

The image on the cover of the thesis is taken at Alp Flix, a plateau located in Alps mountain in Switzerland. My daughter, Elin, was trying to convince a butterfly to land on her palm. Now, thanks to Photoshop, she holds a big colourful particle when light is scattered and specularly reflected perhaps by sun.

LUMINESCENE SPECTROSCOPY FOR BIOMEDICAL APPLICATIONS

Division of Atomic Physics
Department of Physics
Faculty of Engineering
Lund University

Lund Reports on Atomic Physics, LRAP-561 (2019)
ISBN (print): 978-91-7895-332-5
ISBN (pdf): 978-91-7895-333-2
ISSN: 0281-2762

Printed in Sweden by Media-Tryck, Lund 2019

To my beloved family

Abstract

This work presents optical methods utilizing visible light for characterization of biological tissue during diagnostics and treatment processes. The main aim has been to improve the therapeutic outcome of treatment modalities in *in vivo* studies. An optical probe instrument based on fluorescence/reflectance spectroscopy was developed for noninvasive monitoring of photosensitizer concentration in the course of a photodynamic therapy (PDT) procedure. Furthermore, upconverting nanoparticles were exploited as probes for fluorescent imaging with direct applications in preclinical research.

Photodynamic therapy (PDT) is a minimally invasive treatment modality that uses light, a photosensitizing drug, and oxygen to ablate malignant tumours and other diseased tissues. PDT has been investigated for treating malignancies in numerous organs and has become a promising modality for some types of malignancies, including some skin tumours and prostate cancers. PDT is, however, a highly complex treatment modality with many parameters influencing the treatment outcome. Improvements in dosimetry for PDT are ongoing, with the goal to better correlate the clinical outcome to what is planned prior to the treatment of PDT. Accurate dosimetry and treatment planning require knowledge of tissue optical properties and an accurate model for the light propagation in the tissue. In the present work, we present a technique to combine fluorescence and reflectance spectroscopy to yield improvements in the accuracy of the treatment planning. These improvements are further facilitated by multivariate analysis of the recorded data. Extracting the intrinsic fluorescence as well as optical properties of the tissue is demonstrated. This technique does not require *a priori* knowledge of the optical properties of the sample.

The application of luminescence spectroscopy as an effective tool that allows detailed observations of tissues to be made via labelling with exogenous probes, is growing remarkably in popularity. Lanthanide doped upconverting nanoparticles (UCNPs) have recently been developed as light-triggered luminescent probes in various biomedical applications. UCNPs have the ability to convert near-infrared (NIR) radiation with low photon energy into visible radiations with higher energy per photon via a non-linear optical process. In this work, the non-linear dependence on the excitation intensity was compensated to improve the accuracy of measurements of the quantum efficiencies of UCNPs.

Recently, UCNPs have evolved as an alternative fluorescent label to traditional fluorophores for imaging both *in vitro* and *in vivo*. Their great potential stems from their properties which include high penetration depth into the tissue, low background signal and photostability. The aim of this work was also to optimize the excitation wavelength to achieve significant signal gain in deep tissues.

POPULAR SCIENCE

Cancer is the second most common cause of death worldwide. The successful treatment of cancer is typically only possible when it is detected in its early stage. The conventional diagnostic techniques, such as excisional biopsy, are invasive and can sometimes not be used repeatedly. In this context, optical spectroscopy has emerged as a potential diagnostic tool that helps determine valuable structural and functional information that can be used non-invasively to detect and identify diseased tissues.

This thesis deals with development and evaluation of optical methods to delineate and treat cancerous tumours inside the body with the help of light. A lesion such as a tumour has a molecular composition different to the surrounding normal tissue. The interaction between light and tissue, such as absorption, re-emission and photochemical reactions could be used to differentiate the lesion from the surrounding healthy tissue. In this way, non-invasive or minimally invasive tumour diagnostics can be performed *in vivo* and in real-time.

Among the various optical modalities, fluorescence-based techniques have been of particular interest in various biomedical applications in the past decades. The method is particularly suited in quantifying various substances that are present in human tissue naturally, such as melanin, or are externally introduced as luminescent biomarkers. The introduction of contrast agents is often necessary to enhance the visualization of the lesions. They can also be used as indication of the treatment outcome since the fluorescent light that they emit can be measured and reflect the photochemical states.

Photodynamic therapy is a treatment method that combines light, oxygen, and a light sensitive drug called photosensitizer (PS) to produce reactive oxygen species, which cause oxidative damage to targeted cells and tissues. Unlike radiotherapy, light in itself is completely harmless and this allows a patient to be re-treated several times with minimal side effects. In the present work a key issue has been to define dosimetry for the photodynamic treatment to predict the outcome. Efforts have focused on quantifying the concentration of the photo sensitizing drug in normal and malignant tissues using fluorescent and reflectance spectroscopy techniques. One part of the work presented in this thesis is devoted to using a fluorescence/reflectance system to extract the intrinsic fluorescence from tissues *in vivo* during photodynamic therapy.

Upconverting nanoparticles (UCNPs), a group of photoluminescent contrast agents developed within the last decades, have excellent spectroscopic and physiochemical properties that enables their use in connection with optical techniques. These nanomaterials possess possibilities for low imaging background due to ability to efficient up-convert near-infrared radiation into shorter wavelength. On the other hand, biological detection based on UCNP probes is limited by the low luminescence quantum efficiency of UCNPs, specially at the low excitation fluence rate that is typical in deep biological tissues. One part of this research explores a novel composition of UCNPs that provides an increased signal at larger depth in tissue compared to conventional UCNPs. The major goal of the research on UCNPs is to develop a robust system for measuring the quantum yield of UCNPs in a reproducible way while considering parameters that effect the quantum yield evaluation.

Upconverting nanoparticles attract interest because of their potential in numerous pre-clinical biomedical applications. The use of UCNPs provides promising features such as simpler, faster and more sensitive read out which are beneficial in clinical trials and pre-clinical studies. However, successful translation of the use of UCNPs from laboratories to pre-clinical research and clinical care requires further investigations involving the exploitation of deeper penetration in biological tissue and higher quantum yield.

LIST OF PUBLICATIONS

This thesis is based on the following publications, which are referred to by their Roman numerals:

I **Development of a novel combined fluorescence and reflectance spectroscopy system for guiding high-grade glioma resections: confirmation of capability in lab experiments**
M. Mousavi, H. Xie, Zh. Xie, M. Brydegaard,
J. Axelsson, S. Andersson-Engels.
SPIE Proceeding **9032**, (2013).

II **Design and validation of a fiber optic point probe instrument for therapy guidance and monitoring**
H. Xie, Zh. Xie, M. Mousavi, M. Brydegaard,
J. Axelsson, S. Andersson-Engels.
Journal of Biomedical Optics **19(7),071408**, (2014).

III **Increasing depth penetration in biological tissue imaging using 808-nm excited $Nd^{3+}Yb^{3+}Er^{3+}$-doped upconverting nanoparticles**
H. Söderlund, M. Mousavi, H. Liu, S. Andersson-Engels.
Journal of Biomedical Optics **20(8),086008**, (2015).

IV **Beam-profile-compensated quantum yield measurements of upconverting nanoparticles**
M. Mousavi, B. Thomasson, M. Li, M. Kraft,
Ch. Wurth, U. Resch-Genger, S. Andersson-Engels.
Royal Society of Chemistry **19,22016**, (2017).

V **Real-time photodynamic therapy dosimetry using multi-excitation, multi-emission wavelengths: towards accurate prediction of treatment outcome**
M. Mousavi, L. Moriyama, C. Grecco, M. Nogueira, K. Svanberg, C. Kurachi, S. Andersson-Engels.
(September 2019) *Submitted to Journal of Biomedical Optics.*

VI **Potential biomedical use of diode-laser-induced luminescence from upconverting nanoparticles**
M. Mousavi, S. Andersson-Engels.
(2018) *Handbook of Semiconductor Lasers and Diode-based Light Sources in Biophotonics, Institution of Engineering and Technology.*

VII **Multi-variable compensated quantum yield measurements of upconverting nanoparticles with high dynamic range: A systematic approach**
S. Konugolu, J. Matias, G. Dumlupinar, L. Niemitz, M. Mousavi, K. Komobilus, S. Andersson-Engels.
(2019) *Manuscript in preparation.*

Other publication by the author not included in this thesis:

Novel combined fluorescence/reflectance spectroscopy system for guiding brain tumor resections: hardware considerations

Zh. Xie, H. Xie, M. Mousavi, M. Brydegaard, J. Axelsson, S. Andersson-Engels.

SPIE Proceeding **9032**, C03040 (2013).

ABBREVIATIONS

ALA	aminolevulinic acid
APD	avalanche photodiode
CCD	charge-coupled device
CV	cross validation
DOT	diffuse optical tomography
EU	European Union
FAD	flavin adenine dinucleotide
FD	fluorescence diagnostics
FWHM	full-width at half-maximum
Hb	deoxy-hemoglobin
HbO	oxy-hemoglobin
HpD	hematoporphyrin derivative
IC	internal conversion
ISC	intersystem crossing
LED	light-emitting diode
LOOCV	leave-one-out cross validation
LS-SVM	least squares support vector machines
MC	Monte Carlo
MVA	multivariate analysis
NADH	reduced nicotinamide adenine dinucleotide
NIR	near-infrared
OR	operating room
PCA	principal component analysis
PDT	photodynamic therapy
PLS	partial least-squares
PpIX	protoporphyrin IX
PS	photosensitizer
QD	quantum dot

QOP	quadratic optimization problem
RE	rare earth
ROI	region of interest
ROS	reactive oxygen species
RTE	radiative transport equation
SVM	support vector machines
UCNP	upconverting nanoparticles
UV	ultraviolet
WHO	World Health Organization

CONTENTS

Papers

Chapter 1

INTRODUCTION

Biomedical optic technologies, with well-established knowledge of the light and tissue interaction, are developing and growing rapidly. When light encounters different tissue types, the light collected after interacting with tissue carries useful information about tissue structure that reflects underlying function and composition. The principle is based on different interaction of light with atoms, molecules, and subcellular structures with varying refractive index. There exist many optical methods that use this knowledge to extract valuable information for medical diagnosis processes and treatment strategies [1–6]. Among the optical methods, spectroscopic techniques including absorption, reflectance and fluorescence have become commonly used modalities to study human tissues.

The term 'Spectroscopy' was first used scientifically by Isaac Newton to describe the dispersion of white light through a prism into the rainbow of colors. Later, it was extended to cover all frequencies of electromagnetic radiation, from long-wavelength radio waves, to short gamma rays as depicted in Figure 1.1. Optical spectroscopy (OS) exploits the richness of the visible and near-infrared spectra to provide a set of techniques for a variety of applications in industrial and medical fields. A great advantage with optical spectroscopy is that it is non-invasive and can produced data in real time. Fluorescence spectroscopy and imaging are the current techniques of major interest, with fast and rapid diagnosis abilities. A specific focus of fluorescence spectroscopic and imaging applications has been towards early detection and diagnosis of cancer with high sensitivity and specificity.

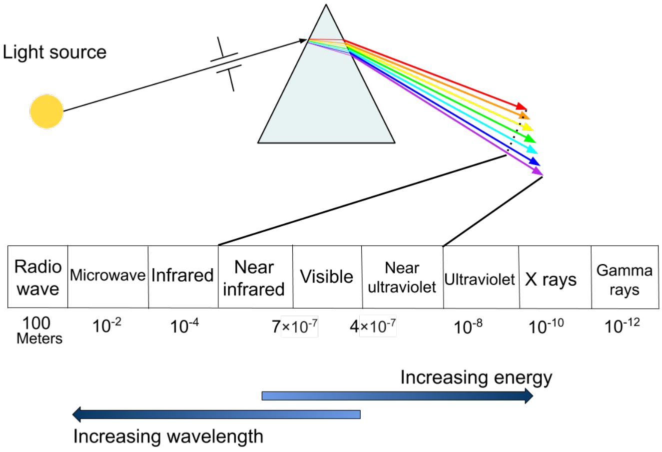

Figure 1.1. *The electromagnetic spectrum.*

The work presented in this thesis exploits optical spectroscopy techniques for the purpose of improvement in medical diagnostics and treatment. More specifically, diffuse reflectance and fluorescence spectroscopy are investigated for quantitative measurement of biological tissue characteristics. A new generation of luminescent agents, named Upconverting Nanoparticles (UCNPs), will also be discussed.

This chapter will provide a brief introduction to the state of the art in optical diagnostic imaging and therapy. In addition, this chapter contains the aims and outline of this thesis.

1.1 Diagnostic imaging and therapy

Tumour growth is initiated by an inappropriate genetic mutation leading to abnormal proliferation of few cells. At an early stage of tumour development, the mutated cells are typically benign and remain confined within the normal boundaries of a tissue. However, further genetic changes allow the tumour to grow and invade the adjacent tissues creating the mass that is now called malignant. It would be of great benefit to patients if one could improve the possibilities for early diagnostics of tissue disorders and further to avoid spreading malignant cells in connection to the treatment planning and prognostic assessments. The survival rate for cancers is highly dependent on the time of detection but varies greatly also with tumour type and severety of the genetic modification. While, for instance, early detection for prostate cancer is associated with 100% 5-year survival as compared to a relatable reference population [7], the corresponding survival rate is approximately 50% for lung cancers, and the most devastating case is pancreatic cancer with an overall 5 year survival rate of about 6% [8].

The development of diagnostics imaging has, during the last 50 years, been towards better visualization *in vivo* and of improved histopathological sample analysis [9]. Medical imaging offers a non-invasive glimpse inside the human body without the need for surgery or tissue sampling. Medical imaging modalities are categorized into radiological imaging and optical imaging. Current radiological imaging modalities include X-ray, computed tomography (CT), ultrasound (US), and magnetic resonance imaging (MRI) as the primary tools to reveal internal structure for deep tissue imaging. Most radiologics exams are only capable of identifying the gross anatomical structure before tumours reach about 1 centimeter or greater in size. For early detection of cancer, it is beneficial to image the tumour physiology and molecular functioning rather than the tumour morphology. Molecular imaging is a relatively new discipline that is capable of visualising variations in molecular concentrations in tissue or cells. Most molecular imaging procedures are carried out using positron emission tomography (PET) and single-photon emission computed tomography (SPECT) imaging devices [10]. Recently, multi-modality imaging, that combines imaging technologies, has become a trend. Typically, an anatomical image is complemented with a functional image modality, for instance, PET-CT and PET-MRI. Such multimodality approaches provide morpho-functional information to overcome the limitations of each individual technique [11]. Various optical imaging (OI) modalities are emerging as promising new additions to medical imaging, performed based on light-tissue interactions [12–15]. Optical techniques use non-ionizing radiation such as visible, ultraviolet, and near-infrared light to interrogate cellular and molecular function in living tissue. This technology offers the potential to differentiate among soft tissues due to their different absorption or scattering properties at various wavelengths. The removal of tissue is not required and the method is both minimally invasive and less time consuming. Table 1.1 presents a comparison of a few different imaging modalities.

Table 1.1. *Comparison between different imaging modalities. * High sensitivity for bone lesion only. ** High in ballistic imaging close to surface and low in diffuse optical tomography for deep tissues.*

Characteristics	**X-ray**	**US**	**MRI**	**CT**	**PET**	**OI**
Spatial resolution	Excellent	Good	Good	Excellent	Poor	Mixed**
Soft-tissue contrast	Poor	Good	Good	Intermediate	Excellent	Excellent
Sensitivity	Excellent*	Good	Good	Good	Excellent	Excellent
Penetration depth	Excellent	Good	Excellent	Excellent	Excellent	Good
Data acquisition	Fast	Fast	Slow	Intermediate	Slow	Fast
Cost	Intermediate	Low	High	Intermediate	High	Low

1.2 Optical diagnosis and therapy

Optical imaging modalities provide highly versatile platforms for pharmaceutical and biotechnological industries as well as medical diagnostics and therapeutics. Optical imaging is extremely sensitive, thereby promising to improve the accuracy of disease detection at early stage and predict treatment response. Recent advances in a wide range of optical imaging technologies such as diffuse optical imaging and near-infrared (NIR) fluorescence imaging further improve the qualitative and quantitative accuracy that are typically limited by the spatial resolution of different light techniques in tissue. Despite the many merits of optical techniques, limited penetration depth caused by absorption and high scattering is a major challenge in biomedical optics and therapy. To overcome this hurdle, specific contrast agents are being developed to optimize contrast in recorded images at NIR wavelengths, for which tissue attenuates light minimally. The exogenous chromophores known as fluorescence probes are administred into tissue to target a specific type of molecule and act as a marker. The sample containing the fluorescence probe is excited by light and the emission spectrum is used to infer information about the sample. The fluorescence probe provides a robust and highly sensitve approach for surgical guidance and non-surgical cancer treatment, e.g., photodynamic therapy (PDT). Photodynamic therapy is a therapeutic procedure that uses a light-sensitive drug, called a photosensitizer, and light at a particular wavelength matching the excitation peak of the photosensitizer used, to treat malignant tumours and other conditions, including acne and skin growths. PDT is today approved for numerous indications [16–19]. Amongst a number of novel fluorescence probes, upconverting nanoparticles (UCNPs), are emerging as promising contrast agents with numerous unique properties. There is a brief introduction to the UCNPs in the following section, and information is available in Chapter 6.

1.3 Upconverting nanoparticles

Luminescence imaging is the visualization of fluorescence probes labelling molecular processes or structures. Lanthanide-doped upconverting nanoparticles are a new class of nanomaterials capable for improving contrast and spatial resolution in luminescence imaging of biotissues. The term upconversion refers to a nonlinear optical process, where the energy of the photons emitted are higher than for those absorbed. In comparison to common luminescence probes, such as quantum dots and organic dyes, they have unique optical properties. This upconversion mechanism offers high signal-to-background ratios and thereby high detection sensitivity due to the absence of tissue autofluorescence. Excitation with NIR light enables deep penetration into the tissue and less photodamage to biological samples. These advantages make them well-suited for bioimaging applications.

1.4 Aim and outline of the thesis

The general aims of the research presented here have been to solve well-defined existing medical challenges with novel methods, and thereby develop paths to improve healthcare for patients. More specifically, two main aims are stated below, along with the references to the papers describing the research in more details:

- to develop and improve the instruments and techniques to retrieve the optical properties of biological tissue *in vivo* from fluorescence and reflectance measurements.
- to improve the use of UCNPs in deep tissue imaging.

Detailed descriptions of the efforts towards these goals are given in the scientific publications appended at the end of the thesis. The general outline and structure of the thesis are as follows.

Chapter 2 describes the interactions of light with tissue as it propagates through biological media. The optical properties of tissue, i.e. its scattering, absorption, and fluorescence are discussed.

Chapter 3 describes the theoretical aspects of light propagation in turbid media such as human tissue. The radiative transport equation (RTE) is introduced and widely used aspects of tissue optics, such as known solutions to transport theory, are discussed.

Chapter 4 presents several aspects related to photodynamic therapy. Important factors in treatment outcome are presented and challenges in forming a dosimetry model to predict outcomes are reviewed. In Paper **V** an instrument incorporating an optical probe fiber to be utilized during photodynamic therapy to evaluate the treatment progression is presented.

Chapter 5 gives an overview of diffuse reflectance spectroscopy and fluorescence diagnostics and imaging. It presents the approaches used to quantify optical properties of the tissue, and fluorescence signals *in vivo* in biomedical applications. Paper **I** looks into the validation of a hand-hold optical fiber probe and Paper **II** reports the first clinical measurement on skin tumours.

Chapter 6 introduces the fundamental principle of upconverting nanoparticles. An overview of UCNPs in different applications is given and an accurate measurements of quantum efficiencies of UCNPs are discussed (Papers **IV** and **VII**). Different methods to increase the efficiency of UCNPs are introduced in this chapter. As one approach, shifting the excitation wavelength to penetrate deeper in biological tissue is reported in Paper **III**. Finally, in Paper **VI** a review of the potential use of UCNPs for biomedical imaging is given.

Chapter 7 concludes the thesis by discussing areas of future study and summarising the manuscript contributions.

CHAPTER 2

LIGHT TISSUE INTERACTIONS

A good understanding of how light propagates in tissue is the basis for the success of a great variety of applications in biomedical optics, and so the fundamental interactions of light with the constituents of tissue must be understood. The light tissue interactions involve different processes caused mainly by tissue scattering, and absorption. Commonly encountered light tissue interactions are depicted in Figure 2.1.

This chapter outlines the mechanisms that are most relevant to this work for a basic understanding of the light tissue interaction. After defining the optical properties of tissue in this chapter, Chapter 3 describes the mathematical

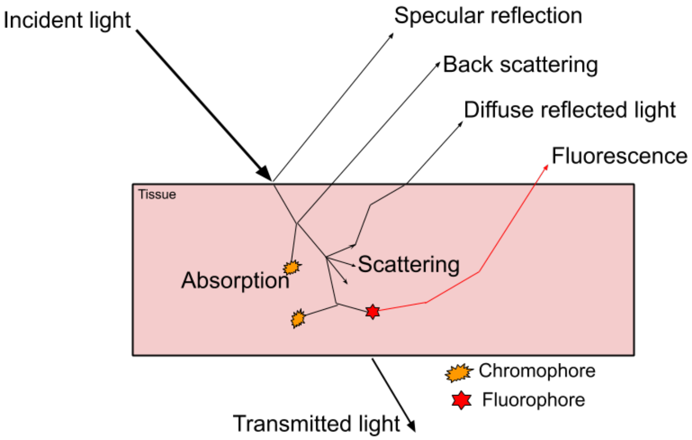

Figure 2.1. *Basic effects of light-tissue interactions.*

basis of light transport in tissue.

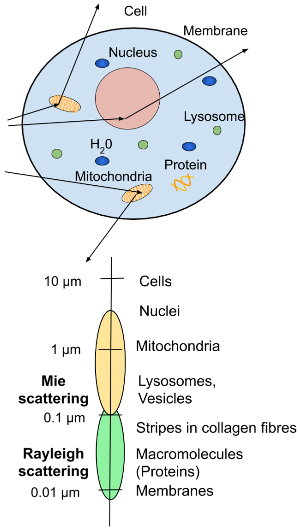

Figure 2.2. *Major organelles and inclusions of the cell.*

Specular reflection from the surface is directed at an angle equal to the incident angle and is generally relatively uninteresting because it contains little information about the underlying tissue. The fraction of the refracted light which emerges from the tissue after single or multiple scattering events is called backscattering. When light penetrates further in the tissue, it undergoes multiple scattering and absorption events by the tissue scatterers and chromophores, respectively. If photons are absorbed by fluorophores, fluorescence can be emitted and can propagate to and beyond the tissue surface. Therefore, light propagation within a tissue depends on the scattering and absorption properties of its components such as cell organelles and their molecules. Although there are numerous types of cells in the human body, they are classified into four categories by forming a particular tissue based on their composition of constituents: Epithelial tissue, connective tissue, muscle tissue, and nervous tissue. For instance, human brain tissue is built by billions of nervous cells whereas connective tissues hold collagen and elastin proteins. Human skin is a multi-layered and inhomogeneous organ in the category of epithelial tissues.
In this chapter, light interaction with tissue will be introduced according to the different phenomena as shown in Figure 2.1.

2.1 Scattering

Biological tissues consist of structures on many different length-scales and compositions. Each such structure carries a specific refractive index [20]. The consequence of these spatial distributions of different refractive indices is that tissues strongly deviate light from its original direction (Figure 2.2). This significant factor in light-tissue interaction is known as scattering. There are two different types of scattering processes: elastic scattering and inelastic scattering. In elastic scattering, the redirected photon retains its energy. Rayleigh and Mie scattering are elastic scattering processes. In the case of inelastic scattering, such as Raman scattering, the energy of the photon is changed as well as its direction. Scattering in biological tissue is mostly elastic without alteration in photon energy. However, Raman spectroscopy is an essential clinical tool for real-time diagnostics of disease and *in situ* evaluation of living tissue [21–23].

Even though the shapes of all scattering materials in biological tissue are not spherical, scattering characteristics of tissue can be analysed by assuming a mixture of spherical particles in various sizes. When scattering occurs by particles much smaller in size than the wavelength of the incident radiation (d $\ll \lambda$), the Rayleigh theory is applicable. For this theory, the scattering cross section is proportional to λ^{-4} and is equally strong in the forward and reverse directions. If scattering is caused by particles of a size similar to the wavelength of the incident light (d $\geq \lambda$), the term Mie scattering is used. Mie scattering tends to be stronger in the forward direction and has a weaker dependence on wavelength (Figure 2.3).

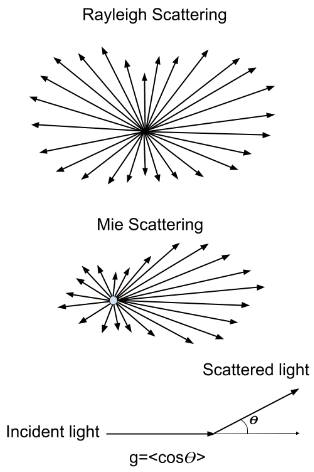

Figure 2.3. *The difference between Mie and Rayleigh scattering.*

The scattering property of tissue can be expressed by the scattering coefficient, μ_s [cm^{-1}], denoting the probability of scattering per unit distance travelled by the light. The reciprocal of the scattering coefficient, $1/\mu_s$ [cm] is the distance light travels before the next scattering event occurs. Forward scattering is predominant in biological tissue. This characteristic is described by the angular distribution function, i.e., the scattering phase function ($p(cos(\theta))$. Here, P indicates the probability function. The Henyey-Greenstein phase function is often used in tissue optics to describe the angular distribution of the scattered light by tissue (Figure 2.4).

$$p(cos\theta) = \frac{1}{4\pi}\frac{1-g^2}{(1+g^2-2gcos\theta)^{3/2}}. \tag{2.1}$$

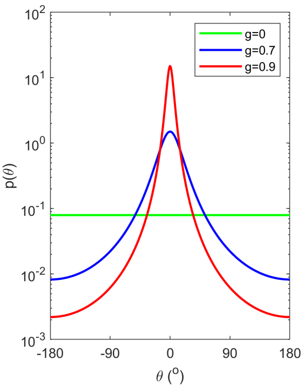

Figure 2.4. *Henyey-Greenstein scattering phase function for g=0, g=0.7, and g=0.9.*

Here g is the anisotropy factor, g=<cos(θ)> [dimensionless], which gives the angular distribution of light intensity scattered by a single particle at a given wavelength. The value of g varies in the range from -1 to 1. For Rayleigh scattering that is symmetric in the back and forward directions (isotropic), g=0 while for Mie scattering (non-isotropic) in biological tissue g>0.8. Taking into account the g value, the reduced scattering coefficient is frequently used in highly scattering biological tissues when there are sufficient scattering events before an absorption event occurs (Figure 2.5). This coefficient is defined as

$$\mu_s^{'} = \mu_s(1-g). \tag{2.2}$$

In highly scattering media, the directionality is lost and the average photon propagation distance becomes dependent on $\mu_s(1-g)$ rather than on the specific value of μ_s and g. Scattering of tissue is typically a combination of Rayleigh and Mie scattering depending on the structure of tissue as shown

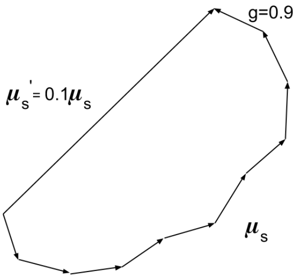

Figure 2.5. *Representation of 10 smaller steps of mean free path equivalent to one big step with a reduced mean free path.*

in Figure 2.2. The general approach is often to describe the spectrally dependent reduced scattering coefficient as follows [24]:

$$\mu_s^{'} = a(\frac{\lambda}{\lambda_0})^{-b}, \tag{2.3}$$

where a and b are related to the tissue structure and λ_0 is a reference wavelength of choice. In Mie theory, a is the scattering amplitude at wavelength λ_0 reflecting the scatter density and b is related to the particles size. Alternatively, $\mu_s^{'}$ can be written as a sum of the separate contributions by Mie and Rayleigh scattering [24]. Figure 2.6 shows that the reduced scattering, $\mu_s^{'}$, versus wavelength λ depends on Rayleigh and Mie scatterers.

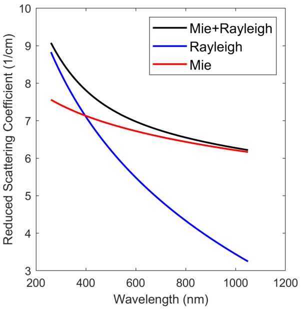

Figure 2.6. *Wavelength dependency of Mie and Rayleigh scattering.*

$$\mu_s^{'} = a'[f_{Ray}(\frac{\lambda}{500nm})^{-4} + (1 - f_{Ray}(\frac{\lambda}{500nm})^{-b_{Mie}}], \tag{2.4}$$

which is a combination of Mie and Rayleigh scattering. In this expression, the wavelength is normalized to a reference wavelength of 500 nm. The factor a' is the value $\mu_s^{'}(\lambda =$ 500nm), which scales the wavelength-dependent term. f_{Ray} indicates the fraction of Rayleigh scattering, where 1 - f_{Ray} corresponds to the fraction of Mie scattering, and b_{Mie} is the scattering power of Mie scattering related to the particle size [25].

2.2 Absorption

Absorption is a process by which one photon excites an atom, ion or molecule from a lower energy level to a higher energy level. These higher states are unstable and during de-excitation the energy is generally converted to heat or fluorescence. An absorbing medium thus consists of atoms and molecules that absorb light at specific wavelengths. According to quantum mechanics, atoms and molecules have discrete energy levels. The lowest energy level an atom or molecule can have is called the ground state. In a semi-classical picture, when light with a certain frequency propagates in a medium, it can be absorbed by atoms or molecules causing them to be excited to a higher energy level. In this case, it will be said that the frequency of the light is in resonance with a transition of the atom or molecule. Hence, absorption is dependent on the frequency (wavelength) of the electromagnetic radiation. This fact provides opportunities for many types of biomedical applications. To describe the absorption probability when light is propagating within a tissue, the absorption coefficient μ_a [cm^{-1}] is introduced. This parameter gives the probability per unit path length that a photon is absorbed in a particular material. The absorption coefficient is described by Equation 2.5 and is proportional to the product of the concentration C$_i$ [M] of molecule i, and its extinction coefficient ε_i [M^{-1} cm^{-1}].

$$\mu_a(\lambda) = \sum_i C_i \varepsilon_i(\lambda). \tag{2.5}$$

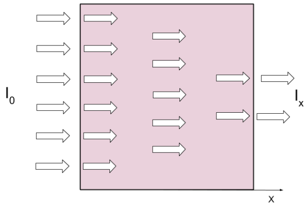

Figure 2.7. *Beer's law describes the diminution in intensity of a beam when it traves through a medium that contains absorber.*

Values of the absorption coefficients for typical tissue lie in the range 10^{-2} to 10^4 cm^{-1} mostly dependent on light wavelength. Haemoglobin and water are the most commonly found absorber in biological tissue. Haemoglobin is an iron-containing protein in the red blood cells that carries oxygen to the entire body. Haemoglobin molecules are present at a high concentration in blood vessels and can appear either as oxygenated haemoglobin (HbO$_2$) or deoxygenated haemoglobin (Hb). The absorption spectra of haemoglobin depends on the amount of oxygen bound to the haemoglobin molecules. This difference in absorption spectra can be used as a valuable tool in assessment of tissue oxygenation. The total absorption coefficient of blood can be approximated as $\varepsilon_{Hb}(\lambda)C_{Hb} + \varepsilon_{HbO_2}(\lambda)C_{HbO_2}$. Haemoglobin strongly absorbs light in the UV and visible spectral range and presents low absorption in the near-infrared spectra range, depicted in Figure 2.8. Water constitutes roughly 70% of the human body and absorbs mainly in the NIR wavelength region. In addition to haemoglobin and water, tissue has a wide variety of other chromophores including absorbers and endogenous fluorophores. In the UV and visible regions, other important absorbing substances include melanins and lipids. Melanin is the primary pigment that effectively absorbs the light to protect the skin from harmful UV rays from the sun. Lipids, which optically are mainly known to cause scattering, are also absorbers.

To model the behaviour of absorption as light propagates through a non-scattering medium, the exponential Beer-Lambert law can be used.

$$I_x = I_0 e^{(-\mu_a x)}, \tag{2.6}$$

where I is the intensity of light after the propagation distance x through the medium. The absorption-induced intensity decreases as the beam travels through a material

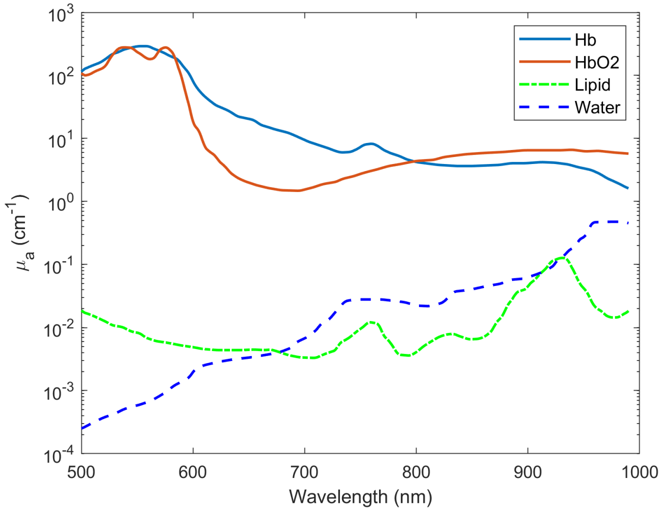

Figure 2.8. *Absorption spectra of the most common chromophores in biological tissue.*

(Figure 2.7). The inverse of the absorption coefficient is called the penetration depth.

$$L_a = 1/\mu_a. \tag{2.7}$$

The penetration depth is defined as the depth at which the intensity of the radiation in the tissue has decresed to 1/e of its initial value. Knowledge of the penetration depth is essential if the Beer-Lambert law is applied in highly scattering media [26].

2.3 Fluorescence

The process of fluorescence involves the emission of a photon from an electronically excited state of a molecule or atom, following absorption of an incident photon. The amount of the light absorbed by the molecules as well as the emitted fluorescence light both depend on the structure of the molecules and the wavelength of the light. A molecules that is able to emit fluorescence light is called a fluorophore. A *Jablonski diagram* illustrating the processes involved between absorption and emission of light is shown in Figure 2.9. It depicts the electronic potentials S_0 and S_1 corresponding to the ground and excited electronic state. Following an absorption, depending on the fluorophore, the molecule may undergo vibrational relaxation (non-radiative), where the molecules fall down to the lowest electronic excited state energy level. This process in on the picoseconds time scale and energy lost is dissipated as heat. A fluorescent emission occurs typically from the lowest vibrational sub-level of the first excited singlet state to the ground state by releasing its energy in the form of light. This fluorescent photon generated has lower energy than an individual excitation photon due to the energy loss in the internal relaxation process. The phenomenon of fluorescence displays several general characteristics for a particular biological situation. One is that the vibrational relaxation is responsible for the emitted photon having lower energy than the incident photon causing a red-shifted emission of the fluorescence relative to the excitation wavelength. Second, emission wavelengths are relatively independent of the excitation wavelength. In general, radiative relaxations which are on a very short time scale, i.e., dipole allowed transitions, are known as fluorescence. A slower time scale of the re-emission is associated with spin conversion and transition from excited state S_1 to the first excited triplet state T_1 (Intersystem crossing). Emission from T_1 yields phosphorescence and lasts much longer, typically with lifetimes spanning from milliseconds to seconds. Luminescence is a more general term to describe relaxation process when light is produced. It includes fluorescence and phosphorescence, and also encompasses bioluminescence and upconverted emission.

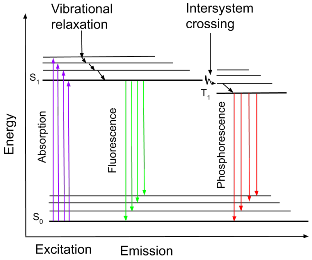

Figure 2.9. *Jablonski diagram indicationg the luminescence process.*

A common parameter to characterize the efficiency of photon emission is the luminescence quantum yield (QY), ϕ,. Luminescence quantum yield represents the fraction of the incoming, exciting photons which results in emitted photons from an optically excited fluorophore [27].

$$\phi = \frac{\#photons - emitted}{\#photons - absorbed} \tag{2.8}$$

The quantum yield is often effected by the micro-environment in which the fluorophore is present. For example, a reduction in temperature generally suppresses non-radiative processes and thus increases the quantum yield. pH and presence of quenchers are also factors that effect luminescence quantum yield and may also induce spectral shifts in the measured fluorescence spectra [28]. The characterization of the QY for fluorescence materials is of paramount importance both for material developments and practical applications. In this thesis, a robust technique to measure the QY of UCNPs is described; see Papers **IV** and **VII**.

2.3.1 Fluorophores

Two broad classes of fluorophores exist - endogenous fluorophores which exist naturally in biological tissue, and exogenous fluorophores, which are introduced into living organisms using biotechniques to enhance image contrast in various fluorescence imaging procedures.

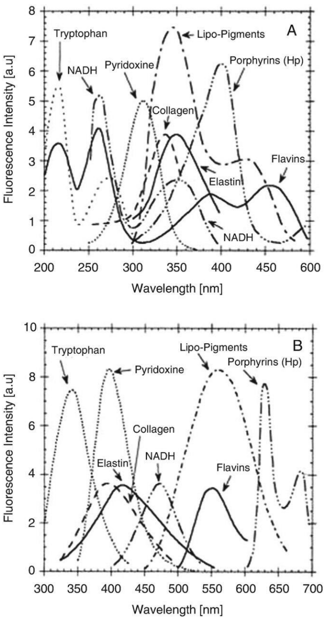

Figure 2.10. *Excitation (A) and emission spectra (B) of the main endogenous fluorophores. The figure is taken from [31] with permission.*

Endogenous fluorophores encompass mainly a variety of aromatic amino acids (Tryptophan, Tyrosine, and Phenylalanine), structural proteins (Collagen, Elastin), Enzymes and coenzymes (FAD and NADH), and different kinds of porphyrins and vitamins. For most endogenous fluorophores, the excitation maxima range between 250 to 450 nm (UV/visible spectral range). The fluorescence from endogenous fluorophores is called *autofluorescence* with emission maxima laying between 300 to 700 nm. The fluorescence spectra of the main endogenous fluorophore are summarised in Figure 2.10. A difficulty with autofluorescnce spectroscopy is to spectrally decompose the measured spectra into its different fluorophore constituents. However, through measurement of autofluorescence signals, it would be possible to identify tissue transformation processes around the onset of carcinogenesis. For example, the fluorescence signal of NADH and FAD are differentiated within tumours relative to healthy tissue due to changes in metabolic states [29, 30]. High tissue absorption in the UV typically only allows surface examination using autofluorescence spectroscopy.

Exogenous fluorophores are non-native biomolecules that can be employed as labels for a variety of tissues, physiological functions and disease conditions. Advantages in the use of exogenous fluorescence for studying biological systems are to label the molecules of interest exogenously by fluorescent molecules with desirable excitation wavelength and high quantum yield. An astounding number of probes are available now, for example, small fluorescent dyes, semiconductor nanoparticles, and a new generation of nanoparticles, the upconversion nanoparticles. Such particles will be introduced in details in Chapter 6.

Photosensitizers (PS) are light triggered fluorescent components that can catalyse chemical reactions within tissue following absorption. They have been broadly used in a wide variety of tissue sites for cancer diagnosis based on fluorescence measurement [32, 33]. The accumulation tendency of PSs in malignant cells makes them attractive to be used in therapeutic applications such as photodynamic therapy. PSs can be endogenous in living cells or they can be introduced as exogenous sources. Porphyrin is one the most widely studied endogenous PS, present in all living cells in small amounts as a precursor to heme. In recent years, the use of 5-aminolevulinic (ALA), a precursor of protoporphyrin IX (PpIX) provides a promising solution in photodynamic therapy of gliomas [34, 35], some cases of skin tumours [36, 37], bladder cancers [38–40] and prostate cancers [41, 42] allowing their complete eradication/ablation. Another well-known photosensitizer, used in this thesis, is Chlorin E6. The extinction and fluorescence emission spectra of these two PSs are shown in Figure 2.11 and 2.12. Their photochemical properties are also shown in Table 4.1 in Chapter 4 where photodynamic therapy is summarized.

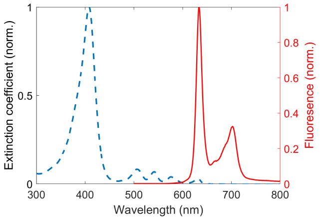

Figure 2.11. *The Extinction (blue) and fluorescence (red) emission spectra of the AlA PpIX. Data are taken from [43].*

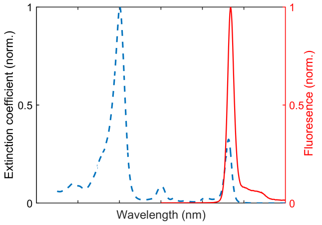

Figure 2.12. *The Extinction (blue) and fluorescence (red) emission spectra of the Chlorin E6. Data are taken from [43].*

CHAPTER 3

LIGHT PROPOGATION IN TISSUE

The simulation of light propagation through biological structures is a prerequisite for quantitative imaging and dosimetry. Two commonly used mathematical descriptions of the light transport in turbid media are the analytical and transport theories. The full analytical theory is based on Maxwell's equations yielding the wave equations under certain conditions. Due to the complex nature of biological tissue, this model is in most cases proven to be impractical to describe multiple-scattering problems. The radiative transfer equation (RTE), in which light is treated as a stream of energetic particles, is yet another well known method for modelling light propagation in a scattering medium. This model neglects the wave nature of light, and is not well suited to describe propagation when that aspect is important. This chapter summarizes different approaches for solving the RTE, as well as the diffusion theory of photon migration through highly scattering media. Before that, the most important physical quantities used to described photon migration in tissue with radiative transport theory are defined.

Photon distribution function $N(r, \hat{s}, t)$ $[m^{-3} sr^{-1}]$ depicts the number of photons per unit volume at position $\bar{r}$ propagating in the $\hat{s}$ direction at time t.

Radiance $L(r, \hat{s}, t)[\mathrm{Wm}^{-2} sr^{-1}]$, describes the power propagation in direction $\hat{s}$ at position $\bar{r}$ and time t per unit area. Radiance is defined as photon distribution function times the photon energy and speed.

$$L(r, \hat{s}, t) = N(r, \hat{s}, t) h v c. \tag{3.1}$$

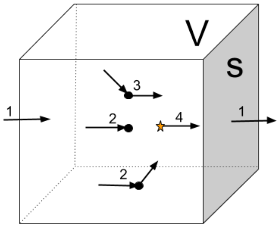

Figure 3.1. *Events relevant for the radiative transport equation: 1: Divergence 2: Extinction 3: Scattering gain 4: Source.*

Here h denotes Plank's constant, v and c frequency and speed of light, respectively.

Fluence rate $\phi(r,t)$ [Wm^{-2}] is the integral of the radiance over all solid angles and thereby disregarding the propagation direction of the photons,

$$\phi(r,t) = hvc \int_{4\pi} N(r,\hat{s},t)d\hat{s} = hvc.\rho(r,t), \tag{3.2}$$

where $\rho(r,t)$ is the *photon density* $[m^{-3}]$ stating the number of photons per unit volume at a given position r and time t.

Photon flux $J(r,t)$[Wm^{-2}] is vector quantity of fluence rate defining the net power flow rate per unit area,

$$J(r,t) = \int_{4\pi} \hat{s}.L(r,\hat{s},t)d\hat{s}. \tag{3.3}$$

3.1 Radiative transport equation

In general, the RTE is an energy balance equation for the radiance L in infinitesimal volumes of the tissue. As photons traverse in tissue volume V with boundary S, the loss or gain in the energy radiance per unit time construct the RTE by considering photon conversation in any direction s. The change in energy radiance is zero and the contribution of the losses and gains can be equated as follow for an arbitrary volume:

$$\frac{1}{c}\frac{\partial L(s)}{\partial t} = \hat{s}.-\nabla.L(s)-(\mu_a+\mu_s)L(s)+\mu_s \int_{4\pi} L(s')\rho(\hat{s},\hat{s'})d\hat{s'}+q(s) \tag{3.4}$$

Here $c[ms^{-1}]$ is the speed of light in the medium, and $\rho(\hat{s},\hat{s'})$, is the scattering phase function describing the probability of a photon being scattered from the direction $\hat{s'}$ into $\hat{s}$. The left-hand side of Equation (3.4) is the change in radiation over time which may be caused by following events on the right-hand side.

$\hat{s}.\nabla.L(s)$ (Divergence) photon transfer across the boundary.

$(\mu_a + \mu_s)L(s)$ (Extinction) photons lost from scattering from direction $\hat{s}$ to other directions and absorption.

$\mu_s \int_{4\pi} L(s')\rho(\hat{s},\hat{s'})d\hat{s'}$ (Scattering) photons scattered into the direction $\hat{s}$ from all other directions.

$q(s)$(Source) [Wm^{-3}] photon energy generated per second within the volume by sources. Considering a small volume V in a domain, the processes leading to lost and gain photons are depicted in Figure 3.1.

Different approaches have been developed to solve the RTE in various physical situations. In most cases, the RTE is solved using numerical techniques where complex geometries and/or heterogeneous optical property distributions need to be considered, or is simplified based on certain approximations so that analytical solution of the RTE can be found for simple geometries. Numerical approaches to analyse the RTE, such as finite element methods [44] or Monte Carlo simulations [45] are extensively employed in various diffusive media to obtain an accurate description of light propogation within the tissue. However, significant computational time and memory size are required to simulate light propagation in highly scattering media. To reduce computation time, the Diffusion approximation (DA) is frequently used instead of the RTE to describe light propagation. It can be solved analytically in specific geometries and numerically in more complete cases.

3.2 Monte Carlo simulation

A gold standard to solve the radiative transport equation is Monte Carlo (MC) simulation. Interaction of photons with a medium is simulated based on its optical properties and light trajectories are predicted by persistent random walk in which the light has to obey the laws governed by the radiative transport equation. A widely used computer program to carry out simulation for light propagation in multi layered tissue is MCML, which is coded by Wang *et al.* [45] For the work in this thesis, CUDAMCML [46] has primarily been employed in an inverse model to retrieve optical properties of the probed tissue by relating simulations to reflectance values of a database generated by using forward MC simulations. The accuracy of MC simulations depends on the number of photon packages launched in the simulation. A larger number of photon packages yield longer computational time, which is the main limitation of MC methods. CUDAMCML enhances the computation performance by using the graphical processing unit (GPU) of the computer to speed up the light propagation modelling.

3.3 Diffusion approximation

When a medium is highly scattering, the directions of the photons are randomized after a few scattering events. Under these conditions, the energy radiance is nearly isotropic and the RTE can be simplified to the differential equation of diffusion theory. To study the radiance in the diffusion limit, a low-order approximation to the RTE can be expressed by translating a serial expansion of the radiance in the RTE into the two first terms, an isotropic and gradient term:

$$L(r,\hat{s},t) \approx \frac{1}{4\pi}\phi(r,t) + \frac{3}{4\pi}J(r,t).\hat{s}, \tag{3.5}$$

$$q(r,\hat{s},t) = q(r,t) + q_1(r,\hat{s},t).\hat{s}, \tag{3.6}$$

being a combination of the fluence rate and the photon flux vector. Subsituation of Equation(3.5) into the RTE (Equation (3.4)), and integration over all solid angles, yields the following scalar differential equation

$$\frac{\partial\phi(r,t))}{c\partial t} + \mu_a\phi(r,t) + \nabla.J(r,t) = q(r,t). \tag{3.7}$$

Substituting Equation (3.5) into the RTE, multiplying both sides by s, and integrating over all solid angles, yields the second differential equation

$$\frac{\partial J(r,t))}{c\partial t} + (\mu_a + \mu_{s'})J(r,t) + \frac{1}{3}\nabla\phi(r,t) = 0. \tag{3.8}$$

The source is here assumed to emit light isotropically (q_1=0 and the temporal change in the flux is assumed to be negligible. With these two assumption, Equation (3.8) reduces to Fick's law

$$J(r,t) = -\frac{1}{3(\mu_a + \mu_{s'})}\nabla\phi(r,t) = -D\nabla\phi(r,t), \tag{3.9}$$

with $D = \frac{1}{3(\mu_a+\mu_{s'})} \approx \frac{1}{3\mu_{s'}}$ denoting the diffusion coefficient and $\mu_{s'} = (1-g)\mu_s$, the reduced scattering coefficient.

Inserting Equation (3.9) into Equation (3.7), yields the time-resolved diffusion equation (DE)

$$\frac{\partial\phi(r,t)}{c\partial t} + \mu_a\phi(r,t) - \nabla D\nabla\phi(r,t)) = q(r,t). \tag{3.10}$$

Truncations and assumptions were made to retrieve the DE, which will constrain its applicability. The truncation to the first-order approximation of the expansion of the RTE is valid only if $\mu_{s'} \gg \mu_a$. This requirement is fairly true for most tissues studied in the red and near-infrared spectral region. Furthermore, the assumptions that sources are isotropic, mean that the diffusion approximation is not valid close to a non-isotropic source. Isotropy is clearly not always the case, however, in a highly scattering media this requirement is fulfilled after a propagation distance of $1/\mu_{s'}$. The second assumption that the temporal change of the flux is negligible is acceptable in the time-dependent migration provided that the angular frequency $\omega \ll c\mu_{s'}$. For steady-state problems, $\omega = 0$.

3.3.1 Solutions to the diffusion equation

Analytical solutions to the DE exist for a variety of geometries, source functions and boundary conditions. For the diffuse equation dealing with the fluence rate, the boundary condition should describe the fact that light approaching a boundary of the medium is partly reflected at the boundary due to the commonly existing refractive index mismatch at the tissue-air interface. In addition, the boundary condition is responsible for assuring that light leaving the medium never returns. This means that the photon flux from the air to the tissue has to be zero. Furthermore, the source term must be specified to solve the DE. Since the DE is valid for isotropic point sources only, any type of directional light source can be approximated as a point source positioned at a depth $1/\mu_{s'}$from the source surface. Another alternative to represent a light source incident to a boundary of a complex geometry is to modify the boundary condition. Below the solutions for geometries with homogeneous optical properties, e.g. an infinite and a semi-infinite medium are presented.

An infinite homogeneous medium is the simplest case: Assuming an infinite homogeneous medium with absorption coefficient μ_a, isotropic scattering $\mu_{s'}$, and diffusion coefficient $D = 1/3(\mu_{s'})$, the time-independent DE reduces to

$$[-\nabla^2 + \frac{\mu_a}{D}]\phi(r) = \frac{p_0}{D}\delta(r), \tag{3.11}$$

where p_0 [Wm^{-3}] is power per unit volume of a point source positioned at r. Assuming a light power P_0 as a point source,

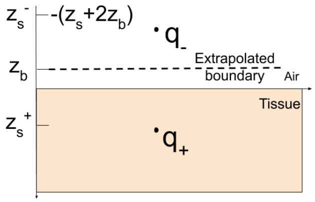

Figure 3.2. *Configuration of extrapolated boundary in semi-infinite homogenous medium.*

then one can solve the DE (Equation (3.11)), using the Green's function approach.

$$\phi(r) = P_0 G(r) = \frac{P_0}{4\pi D r} exp(-\mu_{eff} r), \tag{3.12}$$

where μ_{eff} $[cm^{-1}]$ is called the effective attenuation coefficient and is defined as

$$\mu_{eff} = \sqrt{\frac{\mu_a}{D}}. \tag{3.13}$$

The time-resolved DE for fluence rate following a point illumination in a medium with scattering and absorption is given by

$$\phi(r,t) = \frac{cP_0}{(4\pi Dct)^{\frac{3}{2}}} exp(\frac{-r^2}{4\pi Dct} - \mu_a ct), \tag{3.14}$$

where ct is the accumulated path length of individual photons at time t.

The infinite homogeneous medium or slab geometry is a frequently encountered geometry for which an analytical solution can be obtained through the use of mirrored sources. In this case, a boundary condition, so called extrapolated boundary, needs to be introduced to modify the equation to account for the reflection at the boundary. Figure 3.2 illustrates the case for a semi-infinite medium illuminated from the top with a parallel beam. The light in the beam will have lost its directionality after the depth $\mu_{s'}$. Therefore, considering a light source q_+ positioned inside the scattering medium at a depth $z_s^+ = 1/\mu_{s'}$, a negative mirror image of the first source, q_- is placed above the surface at $z_s^- = -(z_s + 2z_b)$. To account for a refractive index mismatch between the turbid medium and the surrounding an extrapolated boundary is located at distance z_b outside the scattering medium where the fluence rate is set equal to zero $\phi(\rho, z = -z_b) = 0$. The Green's function for the time-independent DE can thereby be written as a sum of two point sources.

$$G(r) = \frac{1}{4\pi D}[\frac{1}{r_+} exp(-\mu_{eff} r_+) - \frac{1}{r_-} exp(-\mu_{eff} r_-)], \tag{3.15}$$

where $r_{+,-} = \sqrt{r^2 + (z - z_s^{+,-})}$.

Note, that by having the sources in these positions, the fluence rate is zero at the extrapolated boundary, as the sources are placed equidistant from those boundaries. In the case of two boundaries, also known as infinite slab geometry, the extrapolated boundary conditions must be fulfilled at both interfaces. In a similar fashion, the analytical solution can be found using an infinite series of positive and negative image sources. In a complex geometry, numerical modelling can be done using the finite element method (FEM), which discretizes the volume into a large number of elements.

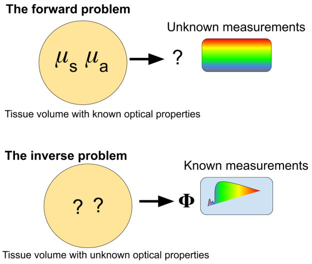

Figure 3.3. *A schematic picture describing the forward problem and inverse problem.*

3.4 The inverse problem

Generally, in the forward problem, models are used to predict light propagation within a medium and the resulting unknown measurements give the spatial distribution of tissue optical properties within the entire model. The inverse problem describes situations where measurements are used to determine the spatial distribution of the optical properties (Figure 3.3). Within the scope of this thesis, the model-based inverse problem is used to extracts the attributes of the tissue optical properties from diffuse reflectance spectra.

CHAPTER 4

PHOTODYNAMIC THERAPY

Photodynamic therapy (PDT) is a treatment modality that relies on the combination of a photosensitizer, light, and molecular oxygen for treatment of various cancers, including lung [47–49], skin [50, 51], cervical [52, 53], prostate [54, 55], and bladder malignancies [56–58]. The therapy involves the administration of an exogenous photosensitive agent (PS), followed by subsequent irradiation of light at the proper dose and wavelength to locally excite the PS in the target tissue. Light irradiation leads among other things to the photochemical conversion of molecular oxygen ($^3O_2$) into singlet oxygen ($^1O_2$) and other reactive oxygen species or radicals which cause therapeutic effects to biologically important structures in the target tissue. The aim in this chapter is not to fully summarize PDT in the clinical arena, but instead a brief introduction to PDT mechanism is provided in order to motivate and highlight the importance of dosimetry in clinically applied PDT.

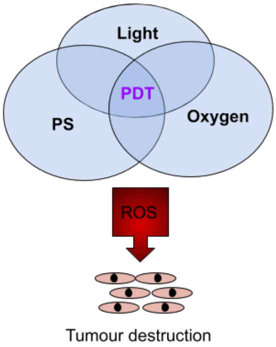

Figure 4.1. *Schematic of PDT.*

4.1 PDT mechanism

Photodynamic therapy requires irradiation of the tumour site with light as well as more or less selective uptake of the PS by the tumour to induce cellular and tissue effects in an oxygen-dependent manner. The drug can be administered to the patient systemically or locally. Different PSs, formulations and application schemes target different tissues. Initially, the PS is in the singlet ground state. Upon excitation by the treatment light of an appropriate wavelength, the PS is promoted to its first excited state (short-lived, nanoseconds). From this excited state, PS relaxes back to the ground state non-radiatively or by fluorescence emission. This intrinsic fluorescence property of PSs is of interest for treatment monitoring and dosimetry and allows *in vivo* fluorescence imaging in living animals or patients. Another alternative for the relaxation from this excited state is intersystem crossing to the excited triplet state. This state exhibits much longer lifetime (milliseconds) than the excited state. The PS excited triplet state can undergo two kinds of reactions catalyzing a treatment response of the targeted tissue (Figure 4.2):

Type I reactions. The PS in the excited triplet state can react directly with a substrate in the tissue, such as a cell membrane or molecules, and transfer a proton or electron to form radicals (often reactive radical oxygen species(ROS)). These radicals are very reactive/destructive and interact with the target tissue.

Type II reactions. The dominant reactions for most sensitizers used in PDT are treatment mediated by the type II reactions. The excited triplet state can transfer its energy directly to ground state molecular oxygen ($^3O_2$) to form highly reactive and cytotoxic singlet oxygen ($^1O_2$).

Both types of reactions coexist and can occur simultaneously and are critically dependant on the concentration of the substrate and presence of oxygen. Tumour destruction by both types of photoreactions can be divided in three independent mechanisms involving direct tumour cell kill, vascular damage and initiation of an immune response against tumour cells. The complex interplay between the PDT pathways above is still not well understood, but each has a specific importance in the therapeutic response to PDT.

4.2 Factors that affect PDT efficacy

Efficiency of PDT depends on the number of factors such as choice of PS, concentration of PS, the anatomical localization, rate of light exposure and light doses, time between administration of the drug and irradiation with light (drug light interval (DLI)), and amount of oxygen in the treated tissue. These parameters are outlined below.

Photosensitizer distribution and concentration in target cells is highly dependent on the chemical structure of a PS and its preferred localization in the tissue. The most effective PSs are hydrophobic and tend to rapidly diffuse into tumour cells

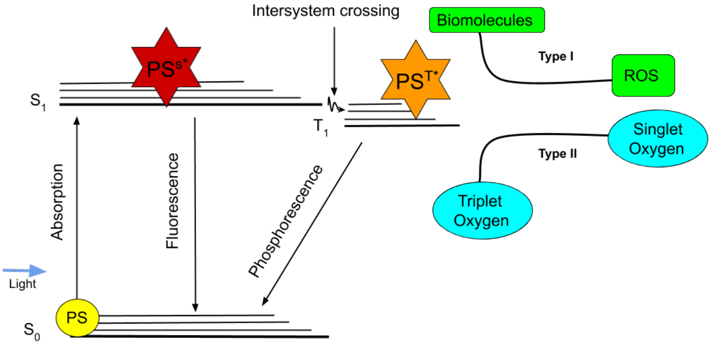

Figure 4.2. *Photochemical reactions in PDT.*

and localize in intra-cellular components such as mitochondria which induce direct tumour damage [59, 60]. More polar compounds tend to stay in blood vessels, rendering vascular destruction. With time, the PS accumulates in tumour tissue and is less likely to be found in the circulatory system [61]. Maximum selectivity of PS accumulation to tumours tissue is always desirable, minimizing the degree of damage to the surrounding normal tissue. Approaches to increase the selectivity of tumour targeting are outlined by Jori [59]. Most of the PSs used in cancer therapy are generally classified as porphyrins and non-porphyrins. Porphyrins were identified over 150 years ago and are the most extensively studied PSs [62]. A purified preparation of Hematoporphyrin became known as Photofrin and was the first clinically approved photosensitizer. Acknowledged disadvantages of Photofrin including skin photosensitivity, low selectivity for tumour tissue, and low molar absorption coefficient, have stimulated research leading to the development of new generation PSs. Effective PSs can be synthesized with absorption bands between 650 and 800 nm to increase the light penetration into the tissue. A PS should have no dark toxicity but be strongly photocytotoxic. It should also have rapid clearance from tissue, thus minimizing a long duration of systemic photon-toxicity. High triplet-state yield and a long triplet-state lifetime are desired to allow for effective production of singlet oxygen and ROS [60, 63].

While numerous PSs have been developed, few have been approved for pre-clinical and clinical PDT applications. Table

Table 4.1. *Some PSs used in pre-clinical and clinical applications. λ - wavelength of the absorption peaks for PDT, and DLI – Drug-light interval.*

PS	**Applications**	**Localization**	**λ (nm)**	**DLI**
Photofrin® [64, 65]	Bladder, bronchus, cervix, lung, head and neck	Golgi apparatus, plasma membrane	630	24–48 h
ALA-PpIX® [66]	Actinic keratoses, Basal cell carcinoma	Mitochondria	635	15 min–4h
Foscan® [67, 68]	Head and neck	Endoplasmic reticulum, mitochondria	652	48-110h
Chlorine E6® [69–71]	Actinic keratoses, Bowen, Basal cell carcinoma	Lysosomes, endosomes	405, 660	4–6 h
TOOKAD® [72]	Acne, prostate cancer	Vascular target	762	10 min–4h

4.1 presents some of the most used photosensitizers along with their photophysical, chemical and pharmacological properties.

Light dose for superficial lesions, given in J/cm^2 is described by

$$F = \frac{P \cdot t}{A} = I_L \cdot t, \tag{4.1}$$

where P[W] is the optical power and t[s] is the exposure time, $A[cm^2]$ is the illuminated area and I_L[W/cm^2] is the delivered intensity of the light. PDT light delivery has an important role to support successful treatment resulting in excellent therapeutic effects [73]. The effect of light dose is clearly reflected in the fact that a low dose leads to activation of apoptosis whereas a high dose results in direct necrosis [74]. The light propagation for a specific treatment session depend on both the geometry and the optical properties of the tissue. It is possible to use diffusion theory or Monte Carlo simulation to predict how light travels into the tissue, thereby adjusting the illumination parameters to optimize the light dose for the entire tumour volume. Development of advanced light delivery systems for advanced PDT dosimetry technologies is reported by Mang [75]. Diode lasers and LED light sources currently dominante as light sources for PDT. Fiber optic delivery devices optimize light penetration into the target and the corresponding spatial light distribution in the tumour volume [76]. Drug-light interval (DLI) can be a critical component of controlling the PDT. While early illumination after PS administration, vascular effects dominate while longer intervals will favour tumour cell effects since the photosensitizer will have leaked out of the vasculature and diffused into the cells [61].

Oxygen plays a key role in PDT. Reduced availability of oxygen within the tissue can limit direct tumour-cell destruction. Immediate oxygen reduction as a result of photochemical processes, as well as vascular occulsion occurs. High light dose rate treatment leads to transient depletion of oxygen resulting in decrease of treatment effectiveness [77]. Depending on the DLI and localization of the photosensitizer, variations in tissue oxygenation are reported [78]. Tissue oxygenation can increase if the DLI is long as the immediate response to the PDT is that the immune system is triggered with increased blood flow as a result [79, 80].

4.3 Dosimetry

Dosimetry of PDT is challenging due to the complex nature of this treatment modality in which many parameters are dynamically interdependent influencing treatment efficacy. Deficiency in any one of the parameters may reduce the efficacy of the treatment. Early studies suggested a model for the tissue response to PDT based on PDT's threshold dose [81]. In this model, the target tissue exposed to doses below the threshold survive, while at dose above the threshold necrosis takes place. The evaluation of PDT threshold is a challenge because the routes to malignant cell death are effected by numerous factors. Thus, assumptions are needed to define a dose metric to reduce the complexity which implies that light dosimetry alone will likely not be sufficient to predict clinical outcome. The rest of this chapter describes different approaches to address these challenges. Unfortunately there is no direct way to measure the tumour response during the treatment, but the response is delayed. This motivates the demand on accurate PDT dosimetry.

4.3.1 Implicit dosimetry

Oxygen is a critically important mediator in PDT [82]. Singlet oxygen is, as mentioned above, often considered the direct phototoxic module responsible for the tissue destruction after

PDT. The measurement of singlet oxygen, therefore has been investigated as a tool in determining tumour response to PDT, known also as a direct dosimetry metric [83, 84]. The amount of singlet oxygen can be quantified by detecting its luminescence signal at 1270 nm. The short lifetime and low probability for emission of the luminescent photons posses a challenge to detect this emission and discriminate it from other background luminescent signals. Another more clinically feasible dosimetry approach is to measure the photosensitizer bleaching based on the fact that many sensitizers photobleach significantly over the course of treatment and this is assumed to be caused mainly by the PS reaction with singlet oxygen generated. The chemical reactions that degrade the drug concentration are similar to those that damage the tissue. This approach is especially important for PDT treatment with ALA-PpIX as PpIX is very prone to photobleaching. Implicit dosimetry is eloquently summerized by Wilson *et al.* [85].

4.3.2 Explicit dosimetry

Most clinical dosimetry protocols use explicit dosimetry [85, 86]. The model takes into account three components responsible for inducing the PDT action, i.e light dose, as well as photosensitizer and oxygen concentrations in the target tissue. The light fluence can be measured directly when light is delivered to the treatment volume using a calibrated optical probe in or near regions of interest. To predict the total integrated light dose throughout the entire volume, computational modeling of the light dose such as diffusion theory or Monte Carlo must be considered. An even light fluence distribution is challenging, specially for larger tumour volumes. This is partly addressed by employing interstitial light delivery. In interstitial PDT dosimetry, the light distribution in various regions of the tissue must be taken into account as a primary pre-treatment planning [17, 55]. Measurement of the photosensitizer concentration can be achieved either before injection as a prescribed delivery dose or after injection through fluorescence measurement. The pre-treatment dosimetry is often not sufficient due to wide variability in photosensitizer uptake between individuals as well as within each individual. During the therapeutic illumination the photosensitizer concentration degrades as a result of interaction with ROS. Thus, measuring the fluorescence emission can be considered as a surrogate for actual tissue drug concentration. It is necessary to correct the fluorescence for tissue optical properties. A final obvious measurement in explicit dosimetry is the oxygen level in the treated tumour. Monitoring tissue oxygenation in vivo is complicated because oxygen concentration varies spatially and dynamically throughout the treatment. As presented in Section 2.2 the absorption spectra for oxy- and deoxy-hemoglobin are different, hence, tissue oxygenation can be assessed by monitoring the blood saturation using optical techniques such as diffuse reflectance spectroscopy. The main limitation in accurate implementation of explicit dosimetry is the inacurracy of the above parameters. Efforts to define dosimetry in PDT have focused primarily on integration of all PDT factors without the need to measure them separately.

In this thesis, fluorescence and reflectance spectroscopy are used as an outstanding method to measure PS concentrations *in vivo* while compensating for variation in optical properties (Papers **II**, **I**, and **V**)

Chapter 5

FLUORESCENCE AND REFLECTANCE DIAGNOSTICS

Fluorescence-based techniques have become essential tools in biology and biomedical science. They are employed to develop novel, non-invasive technologies for diagnostic purposes including early detection of malignant diseases. One motivation is to reduce the need for surgical removal of biopsy tissue samples and instead rely on spectral analysis of the tissue using an imaging system or employing a fibre probe close to the tissue to minimally-invasively record fluorescence spectra *in vivo*. Studies on fluorescence diagnostics of malignant tumours have been centred on two approaches. One is based on the detection of deviations in the fluorescence spectra of native fluorophores between normal and diseased tissue. The other approach uses the administration of exogenous biomarkers that concentrate in malignant tissues. A few of these fluorophores are introduced in Chapter 2. A fluorescence signal can be measured and analysed in various ways to extract information regarding concentration and spatial distribution within the tissue. Steady-state fluorescence techniques are the most widely used measurements since they require only simple and cheap instrumentation. Temporal properties of the fluorescence emission is another approach that can provide effective means of discrimination among fluorophores. In this chapter, fluorescence emission spectroscopy for bulk tissue diagnostics and different methods to retrieve undistorted *in vivo* fluorescence signals are discussed. Moreover, the use of quantitative *in vivo* information such as fluorophore concentration is discussed to establish dosimetry for photodynamic therapy.

5.1 Fluorescence emission spectroscopy of turbid media

Steady-state fluorescence spectroscopy consists of measurements and analysis of the wavelength distribution of various fluorophores [87]. Discrimination among distinct fluorophores is achieved on the basis of differences in their spectral shape, peak positions, and intensity. The fluorescence emission spectrum of a particular fluorophore is the fluorescence intensity measured over a range of emission wavelengths at a fixed excitation wavelength (usually at the excitation maximum for that fluorophore). The fluorescence excitation of a clear medium can be obtained using the Beer-Lambert law. However, fluorescence excitation and emission from a turbid media, such as tissue, is complex to assess as it is distorted by the absorption and scattering properties of the tissue. Fluorophores are often distributed inhomogeneously within the tissue. For instance, the layered architecture of the skin has a variable spatial distribution of blood and other chromophores. The concentration of the scatterers within the tissue can also significantly distort measured fluorescence signals. Clearly, quantitative information about fluorophore concentrations can only be assessed if proper correction techniques are exerted to compensate for the effects of tissue scattering and absorption. Despite the distorting contributions of absorption and scattering in obtaining intrinsic fluorophore concentrations in tissue, absorption and scattering properties may themselves provide valuable diagnostics information. For example, knowing the blood oxygenation level in tissue is helpful from a diagnostics perspective. Furthermore, changes in the scattering are indicative of changes in tissue structure. Diffuse reflectance spectroscopy is a suitable method to characterize absorption and scattering coefficients.

5.2 Diffuse reflectance spectroscopy

Steady-state diffuse reflectance spectroscopy (DRS) is a technique that reflects the composition and morphology of tissue by measuring the diffusely reflected light following its interactions with the tissue. To quantify the optical properties of the tissue, a model for light propagation through it is needed. This is then used to resolve the relationship between the measured spectra and optical properties in the framework of the radiative transport equation. As discussed in Chapter 2, the two most suitable forward methods are the diffusion approximation and Monte Carlo simulation. Analytical solutions from the diffuse approximation can be obtained rapidly and accurately if photons are sufficiently scattered and the geometry allows such solutions [88]. The source detector distance (SDD) is an important parameter to consider when the diffusion approximation is used. The SDD is required to be much larger than the inverse of the reduced scattering coefficient to collect multi-scattered photons deeper in tissue. Therefore, the DE is not accurate for application of superficial measurement. MC simulation is, thereby, a gold standard for this purpose since any tissue structure and range of optical properties can be modelled in different illumination-collection geometries. An inverse MC look-up table is used in Paper **V** to extract the tissue parameters from diffuse reflectance measurements.

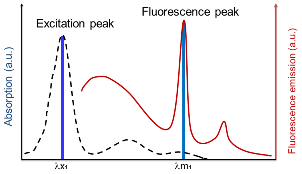

Figure 5.1. *Schematic illustration of the absorption and emission spectra for quantification of fluorophores.*

5.3 Tissue fluorescence attenuation correction

Correction techniques to retrieve the intrinsic fluorophore concentrations in turbid media are possible first if one can isolate changes in the tissue fluorophore from changes in other tissue optical properties. There have previously been several attempts to extract the intrinsic fluorescence based on fluorescence and reflectance information [89–93]. Below, the most commonly used techniques are described.

5.3.1 Reflectance utilization

The most common techniques to compensate for changes in tissue absorption are based on a ratio of fluorescence intensity to backscattered excitation light intensity [94, 95]. Figure 5.1 represents the raw uncorrected fluorescence signal $(F\lambda_{ex1}, \lambda_{em1})$. The raw uncorrected fluorescence signal is divided to the reflected signal at the excitation wavelength.

$$\frac{F(\lambda_{ex1}, \lambda_{em1})}{R(\lambda_{ex1})} \tag{5.1}$$

This technique is valid at high absorption and constant scattering. In a similar fashion, a correction factor is taken into account for the optical properties at the emission wavelength [96]. However, this method is only accurate when absorption is weak. Finlay *et al.* [97] proposed a modification of the above approaches which involves the ratio of fluorescence to reflectance at both excitation and emission wavelengths.

5.3.2 Spatially resolved reflectance

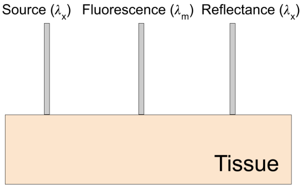

Figure 5.2. *Diagram of the measurement geometry for two distance optical fiber. Excitation light is delivered through the source optical fiber. The fluorescence and reflectance are collected with fiber in the middle and fiber in the right, respectively.*

Spatially resolved techniques rely on the monitoring of the diffuse reflectance as a function of distance away from an excitation optical fiber. The concentration of the PS has been quantified to an accuracy of about 10% by using a probe with a small source-detector separation [98]. The approach is based on the theory that the ratio of fluorescence to scattered light is linearly proportional to the absorption coefficient of the photosensitizer. Weersink *et al.* incorporated the diffuse reflectance and fluorescence measurement at two different distances [99]. A diagram of the measurement geometry is shown in Figure 5.2. They proposed that the ratio of fluorescence at a source detector distance of 0.65 mm to the reflectance at 1.35 mm is only weakly dependent on the optical properties of the tissue sample. A different technique for determining fluorophore concentration is based on the diffusion equation. A priori knowledge of the optical properties is applied in a forward model to correct for tissue attenuation. This approach has limited dynamic range of optical properties when used with a single fiber-source distance. To overcome this limitation, multiple source-collector distances can be used to expand the dynamic range of optical properties.

5.3.3 Correlation techniques

The possibility of utilizing multivariate analysis methods to extract the concentration of fluorophores from the intensity measurements has been explored in 1996 by Durkin and Richards [100]. Such techniques are constrained using training data sets which cover underlying physical parameters in all possible conditions that may occur in later measurements. A mixture of calibration constants to build the training dataset must include accurate values of tissue fluorophore concentrations and optical properties. This method is used in Papers **I**, **II**, and **V**.

It has been proven that the optical properties of cancerous lesions are different from those of normal tissue. Therefore determination of the intrinsic fluorescence and analysis of tissue scattering and absorption parameters, in combination, would provide a better understanding of the morphological changes that take place during progression of disease than only fluorescence or reflectance. One specific example is a disease to be treated using photodynamic therapy where one considerable issue is to retrieve the dosimetric values when the optical properties of the tissue

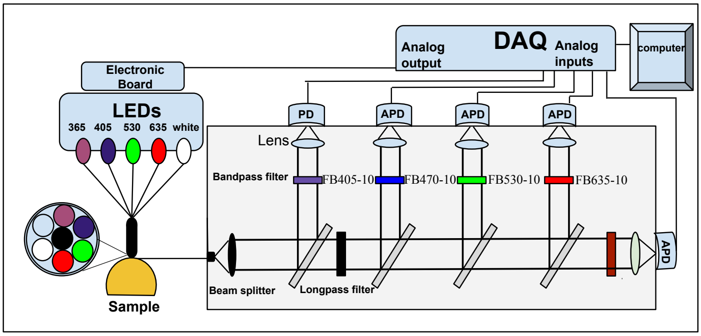

Figure 5.3. *Schematic diagram of multi-excitation multi-emission system (MEME).*

are unknown. In this thesis, a novel multi-excitation multi-emission system was used to characterize optical properties of biological tissue as well as quantitative information about PS concentration during photodynamic therapy. To achieve that, a multivariate analysis technique was employed to correlate the experimentally determined data with *in vivo* data real-time. This technique does not require *a priori* knowledge of the optical properties of the sample.

5.4 Instrumentation

The multi-excitation multi-emission (MEME) system has been primarily developed for precise tumour delineation during brain surgery [101]. The schematics diagram of the system is shown in Figure 5.3 and details of components are described in Paper **II**. The light source employed in this system consists of light-emitting diodes (LED) at different wavelengths as shown in Figure 5.3. The light sources are modulated with high frequency allowing suppression of ambient light during measurement in the clinical environment. Excitation wavelengths match the absorption of the compounds of interest. The custom-made hand-held fiber probe consists of six surrounding delivery fibers and one collecting fiber at the centre. The collected light is then routed to one photodetector (PD) and four avalanche photo detectors (APDs). A narrow-band bandpass filter was positioned in front of each APD. The real-time signal manipulation was performed by a custom LabVIEW program.

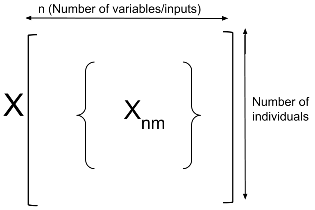

Figure 5.4. *The input matrix X, with dimension of m×n. Any row* x_n *represents the measured quantities of one individual. Any column* x_m *represents one data observation for all individuals.*

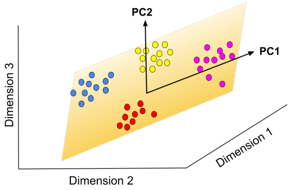

Figure 5.5. *PCA linear transformation. PC1 and PC2 are orthogonal axes which best represent the variabity in the dataset X with m=3.*

5.5 System validation

Tumour-mimicking phantoms are widely used in biomedical optics research for system validation and stability testing as well as in illumination and collection evaluation. To validate the MEME system, an aqueous suspension containing absorber and scatterer was used to emulate the optical properties of real tissue. Intralipid is a scattering agent biologically similar to the lipid membrane of cells and organelles [102]. These are the main scatterers in tissue. Intralipid is broadly used to reproduce the scattering coefficient and anisotropy factor g of real tissue. One major constituent causing absorption in biological tissue is blood. For MEME validation, bovine blood purchased from a local supermarket was used as an absorber in the tissue phantoms. The MEME system was used for two pre-clinical trials employing two different photosensitizers as described in Section 2.3.1. Validation of the system for both specific fluorophores used in the studies was required. The stock solutions of the fluorophores were prepared and a tissue phantom study was performed by altering the concentration of Intralipid, blood and fluorophore in order to render different optical properties and fluorophore concentration for the studies.

5.6 Multivariate analysis

Multivariate analysis (MVA) methods have been applied as an alternative to other statistical methods in modern data analysis for predicting, identifying, and decision making [103]. MVA is quickly evolving in the medical industry for data analysis purposes without the need for human involvement. Medical records of patients contain many variables often interrelated to one another, and the most interesting trends are hidden within a combination of dependent variables. Using conventional methods, it is not possible to analyze this significant volume of information. Therefore, MVA is developing various algorithms to interpret complex data quickly and confidently. There are several different MVA methods that can be used for extracting the most significant data in a data set, as well as for regression and classification purposes. Methods include principal component analysis (PCA), partial least squares (PLS), and support vector machines (SVM). PCA is a very useful algorithm that simplifies the complexity in a large set of variables within a dataset, while still retaining as much information as possible. A typical dataset is usually represented as a matrix X consisting of n rows and m columns and is organized as shown in Figure 5.4. Each input n can be represented as a point in an m-dimensional coordinate system. PCA transforms the large number of variables in measurements X into a number of uncorrelated variables called principal components (PC:s) (Figure 5.5). The first principal component accounts for as much of the variability in dataset X as possible. PCA is an unsupervised learning technique in which the datasets are not labelled and there is no response value (Y matrix in supervised learning). Therefore, PCA captures only the characteristics of the predictive variables (X variables) and it does not consider the correlation between the so called dependent and independent variables (Y variables). PLS as a supervised dimension reduction takes into account the correlation between dependent and independent variables. This technique extracts factors from both X and Y such that the covariance between the extracted factors is maximized. SVM is another supervised learning algorithm which has been proved highly effective in data classification. The principle is similar to PLS in reduction of data to a simpler form and considers the correlation between X and Y. This learning algorithm finds an optimal hyperplane in-between different classes of data which could best separate the data. The vectors in the data set that define the optimum hyperplane are the support vectors. Support vectors are closer to the hyperplane and influence the position and orientation of the hyperplane (support vectors are indicated by circles in Figure 5.7).

The SVM is also a predictive data-regression algorithm that assigns new data elements to a given labelled training data set (supervised learning). In SVM regression, the data set of training data includes predictor variables and observed response values. The aim is to learn the mapping function from the input X variable to the output Y variable. This transformation can be done using some linear algebra; the Kernel function. Kernel functions approximate the mapping function as accurately as possible such that when there is new input data, the output variable for the dataset can be predicted. As a consequence, the SVMs model can be used for predicting the outcome of feature measurements. The principle is depicted in Figure 5.8. Usually the performance of an SVM model in terms of maximum prediction precision and stability is evaluated by a cross validation approach (CV) in a way that the dataset is divided into training and testing sets. Then, the training set is used to test the model. The correlation coefficient for the training and testing datasets are calculated to evaluate the prediction performance.

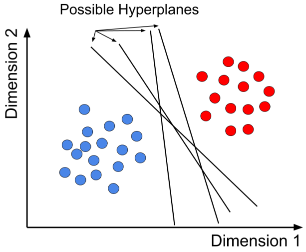

Figure 5.6. *The linear classifier for SVM modelfor two group classification problem.*

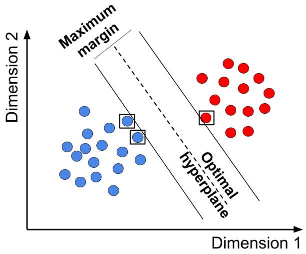

Figure 5.7. *SVMs learn an optimal separating hyperplane which maximizes the margin distance. The support vectors are in squares.*

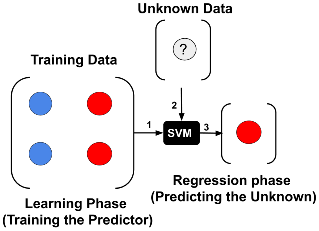

Figure 5.8. *The principle of SVM for prediction an known data by using a model created from a training dataset.*

The Least Squares formulation of SVM, called LS-SVM, is a recent, simplified version of standard SVM. Standard SVM uses optimized quadratic programming methodology while LS-SVM solves linear equations by replacing the inequality with equality constrains. In this work, PLS was used in Paper **I** to validate the instrument performance in quantification of fluorophore concentration. LS-SVM is used in Papers **II** and **V** to predict the optical properties and fluorophore concentration in *in vivo* measurements.

Chapter 6

UPCONVERTING NANOPARTICLES

The use of exogenous luminescent biomarkers enables non-invasive detection and real-time visualization of biological processes from subcellular structures to the organ level. Upconverting nanoparticles (UCNPs) are a type of luminescent particles doped with lanthanide ions featuring a wealth of electronic transitions within 4f electronic shells. The UCNPs possess a number of attractive and unique properties that make them highly interesting for the purpose of luminescence imaging in biological applications. This chapter introduces photon upconversion processes followed by a description of the properties and applications of UCNPs.

6.1 Upconversion process

Upconversion refers to a non-linear optical process involving two or more excitation photons being absorbed and converted into one emitted photon with higher energy. UCNPs are thus able to convert near-infra-red excitation into visible and ultraviolet emission. Upconversion can be achieved through a number of different mechanisms. For UCNPs, three basic routes have been determined: excited state absorption (ESA), also known as sequential two-photon absorption, energy transfer upconversion (ETU), and photon avalanche effect (PA). The principles of these upconversion processes are schematically presented and discussed in several articles [104, 105].

Excited state absorption. In ESA (Illustrated in Figure 6.1 a)) an activator ion is first excited to an excited state (E_1) and then absorbs a second photon and is further excited to an emitting level (E_2). Subsequently, the ion relaxes back to the ground state providing the upconverted emission. Lanthanide ions, including Er^{3+}, Tm^{3+}, and Ho^{3+} possess a ladder-like arrangement of the energy states, so that ESA can be easily observed in these ions. ESA is the least efficient of the UC processes discussed here.

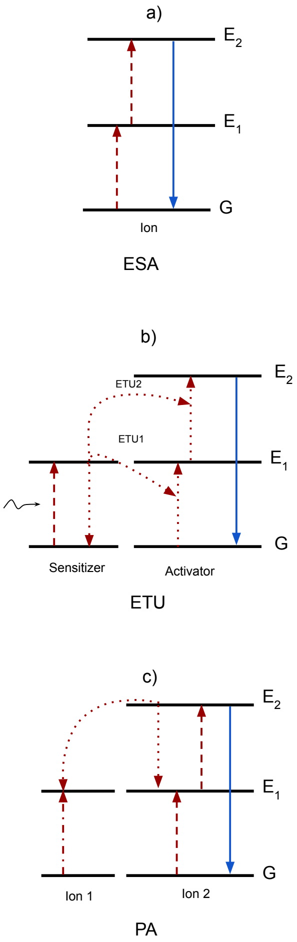

Figure 6.1. *Schematic of the upconverion process. a) excited state absorption (ESA), b) energy transfer upconversion (ETU), and photon avalanche (PA). Dashed, solid and dotted lines represent photon absorption, photon emission and energy transfer processes, respectively.*

Energy transfer upconversion (ETU) is considered the most efficient upconversion process in UCNP crystals. In this process, successive energy transfer between neighbouring ions at different sites in the crystal promote the excitation of an ion to a highly excited state. In particular, the sensitizer absorbs a photon and is excited to an excited state. The energy transformation takes place in a non-radiative manner to an activator ion not only between ground state and the first excited (ETU1 in Figure 6.1 b)) but also between excited states (ETU2). Yb^{3+} is typically used as a sensitizer due to a large absorption cross-section in the NIR region and long luminescence lifetime. The energy separation of the Yb^{3+} ground and excited states match the transitions of the activator ions well which results in significant energy transfer between ions. This energy transfer occurring between identical ions resulting in the population of an intermediate level of the activator ion is known as cross relaxation (CR). UC emission of different colour can be obtained with different sensitizer and activator combinations. In this thesis, ETU has been employed.

Photon avalanche (PA) is also based on sequential energy transfer between ions. It is a looping process that requires a pump intensity above a certain threshold value. The PA process involves weak non-resonant ground state absorption (GSA), followed by resonant ESA to populate the E2 level ultimately. An efficient cross relaxation energy transfer occurs between the excited ion and neighbouring ground state ions, and results in strong UC emission as an avalanche process [106].

6.2 Composition

An upconversion system typically consists of three components including an inorganic host, absorber (sensitizer) and an emitter (activator). It is essential to carefully engineer crystals with lanthanide dopant for upconversion processes as it totally depends on the energy transfer between sensitizer and activator within a suitable proximity. A description of each component is presented here.

6.2.1 Host materials

The crystal structure and the optical properties of the host material play important roles in the UC process and in particular dictate the luminescence efficiency. An ideal host material needs to be transparent, chemically stable and possess low lattice phonon energies to avoid deexcitations or phonon excitation processes. To date, amongst different crystalline host lattice materials, $NaYF_4$ and $NaGdF_4$ have gained significant attention, particularly for biological applications. Regarding crystal structure of host matrices, several studies have shown that hexagonal $NaYF_4$ is favourable and exhibits UC emission with efficiencies of about one order of magnitude greater than a cubic $NaYF_4$ [107–110]. Beside the crystal structure, crystal decomposition [111] and core/shell structure have been applied to increase the efficiency of UCNPs [112, 112].

6.2.2 Lanthanide dopants

The Lanthanide (Ln) ions, also known as rare-earth (RE) metals, with multiple metastable energy level structure are the most commonly used luminescent centres for this application. Their special electron configuration with a partially filled 4f electron shell and completely filled $5s^2$, $5p^2$ and $6s^2$ subshells results in sharp and narrow f-f transition bands and a stable excitation state. The choice of sensitizer-activator pair amongst all possible combinations of Lanthanide ions is based on efficient energy transfer between them as well as the emission wavelength of interest for a specific application. As a sensitizer ytterbium Yb^{3+} and as an activator erbium Er^{3+} or thulium Tm^{3+} are the most commonly used pairs since they provide visible optical emission under low pump power densities. The widely accepted energy level diagram of Yb-Er and Yb-Tm is shown in Figure 6.2. The Yb-Tm doped are of particular interest due to their NIR-to-NIR conversion. The particles absorb light at 980 nm and emit upconverted light at 800 nm allowing for autofluorescence-free biodetection [113]. The UC efficiency is influenced by the dopant concentration [114]. The sensitizer concentration must be high enough to optimize energy transfer between sensitizer and activator, but not too high to move the activator ions in too much proximity to induce quenching by CR.

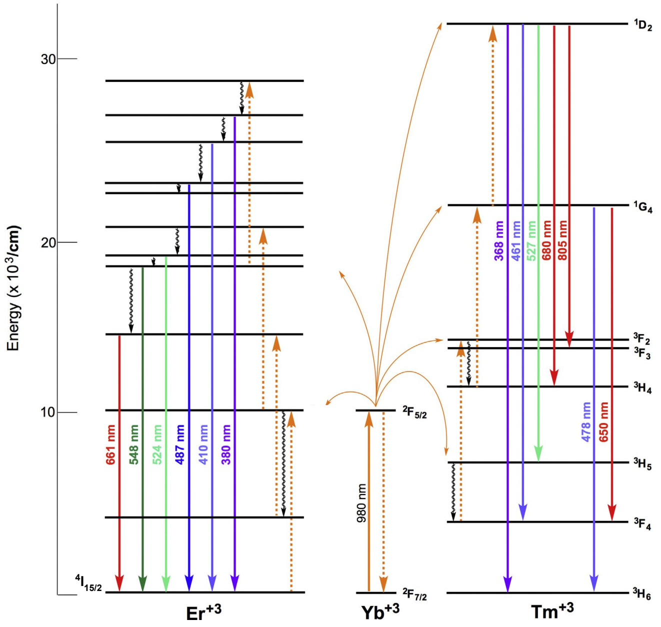

Figure 6.2. *Energy level diagram and upconversion scheme for the Yb-Er and Yb-Tm pairs are shown. The figure is taken with permission from [115].*

6.3 Optical properties of UCNPs

The use of NIR light in biomedical applications has provided numerous opportunities with great potential for bioimaging. UCNPs have the capability to convert near infra-red radiation (NIR) into visible light resulting in deep tissue penetration. The anti-Stokes emission makes UCNPs attractive candidates for a variety of broad applications, spanning from background-free biological sensing and drug delivery to super-resolution microscopy [116, 117]. Compared to other conventional fluorescent dyes, UCNPs shows high photostability and non-blinking behaviour. These nanoparticles contain individual and variable absorption and emission centres. It is feasible to dope multiple types of lanthanide ions into a host matrix for customized multimodal imaging probes. The advantage of the UCNPs as imaging probes stems also from the need of a modest CW NIR laser source for exciting UCNPs. The upconversion process requires sequential absorption of two or more excitation photons by sensitizer lanthanide ions to transfer energy to the activator ions. Consequently, the optical luminescence and the quantum yield are excitation power dependent [112, 118]. Despite the enormous potential that UCNPs offer for different applications, a number of limitation still need to be addressed. Compared to conventional contrast agents such as organic dyes and semiconductor probes, the quantum yield of UCNPs, a parameter proportional to brightness, is relatively low. Nowadays, one of the greatest trends in the field of UNCPs research is the quest to enhance the luminescence brightness of UCNPs. Different methods to synthesize UCNPs have been proposed and reviewed in detail in various articles [119, 120] as well as in Paper **VI**.

6.4 Excitation wavelength optimization

Most commonly used Yb^{3+}-sensitized UCNPs have an excitation band centred at 980 nm (the peak absorption of Yb^{3+} ions), overlapping an absorption peak of water molecules. This causes heat generation in tissue and poor penetration depth for biomedical applications. Tuning the excitation wavelength to a region with less water absorption in tissue is possible by designing new UCNPs where RE^{3+} ions provide new excitation pathways. Zhan *et al.* reported a continuous wave laser at 915 nm to excite $Tm^{3+}/Er^{3+}/Ho^{3+}$-doped $NaYF_4$ to avoid overheating of tissue [121]. However, water absorption has remained a challenge. A novel class of UCNPs are engineered by cascade sensitization employing Nd^{3+}as an 800 nm photo co-sensitizer [122]. In this thesis, a core-shell structure with Nd^{3+} ions in the shell with excitation at 808 nm and $Nd^{3+}/Yb^{3+}/Er^{3+}$ dopants in the core with emission at 650 nm was designed and used in measurements described in Paper **III**.

6.5 Power density dependence and quantum yield characterization

The power dependenece of the UCNPs is governed by the competition between the ETU rates from the sensitizer ion to the activator ion and the linear decay rate for depletion of the intermediate states of the activator ions involved in the UC process. This nonlinear behaviour results in non-linear power dependent curves for core and core-shell nanoparticles. Under low excitation intensities, the depopulation from the intermediate state is dominating over the ETU rate causing low luminescence efficiency with a slope of 2.0, indicating a two-photon absorption process. Increasing the excitation intensity leads to saturation of the upconversion process where the curve appears with a slope of 1.0. Figure 6.3 represents this trend in an experimentally determined quantum yield for the core NaYF$_4$:Yb^{3+}/Tm^{3+} and core/shell NaYF$_4$:Yb^{3+}/Tm^{3+}@NaYF$_4$ UCNPs over a power density interval from 0 to 20 W/cm^2. Recently, a theoretical investigation based on a simplified steady state rate equation model was derived to well characterize the quantum yield of UCNPs in different excitation power density regions. H.C. Liu proposed a balancing power density point, at which the ETU rate and the linear decay rate equally contribute to depopulate the intermediate level of activator ion [123]. The QY can be well characterized by two parameters: the balancing power density behaviour for an arbitrary excitation power density and QY at the power density. This approach was used to characterize the quantum yield of UCNPs in Papers **IV** and **VII**.

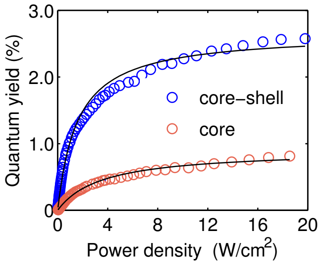

Figure 6.3. *Experimentally determined QYs for the core* NaYF$_4$:Yb^{3+}/Tm^{3+} *and core/shell* NaYF$_4$:Yb^{3+}/Tm^{3+}@NaYF$_4$.

6.6 Beam profile compensation in quantum yield measurement

Determining the QY of UCNPs can be accomplished with an integrating sphere or a fluorometer [124, 125]. Due to nonlinear dependency on excitation irradiance, it is important to characterize the distribution of the excitation power within the cross-sectional area of the excitation beam. Typically, unmodified laser beams introduce an inhomogeneous distribution of the excitation light on the sample, usually close to a Gaussian distribution. For a linear excitation process, the beam profile is not a serious concern while for an upconversion process the luminescence intensity depend on P^n, where P is power density of the laser beam and n is the number of photons required for the excitation process. In an integrating sphere, the excitation light passes through the sample many times after reflecting from the sphere wall. It is therefore difficult to precisely determine the actual excitation profile that contributes to the detected luminescence signal. Experimental characterization of the beam profile can be accomplished with a suitable camera in a fluorometer setup (without the reflections in an integrating sphere). In a fluorometer-based setup, a reference standard sample is required to conduct a relative quantum yield measurement as light is only collected in a limited solid angle. Beam profile compensated quantum yield measurements are described in Papers **IV** and **VII**.

CHAPTER 7

OUTLOOK

Luminescence spectroscopy has become a crucial tool in biomedical applications. In particular, fluorescence spectroscopy provides a simple, fast, and inexpensive method to determine the concentration of fluorophores in biological tissues. However, improvements in instrumentation and methodologies are still needed to obtain accurate information from highly scattering media. PDT dosimetry based on steady-state fluorescence measurement has been proposed to improve real-time monitoring of treatment efficacy, while the intrinsic measurement of fluorescence concentration remains a challenge. Toward the goal to extract fluorophore concentration in highly scattering media, we develop a novel combined fluorescence/reflectance system to measure photosensitiser concentration as well as optical properties in tissue during photodynamic therapy. These studies have provided encouraging results and show the potential to become a valuable tool in evaluation of treatment outcomes in real time. A goal for the future is to miniaturise the system and improve its performance for various specific medical applications. Extending the number of light sources will increase the amount of data measured and will enable the retrieving of information about fluorophore concentrations in biological tissue. This in turn will help to extract diagnostic information in addition to obtaining the absolute PS concentration. In the precise quantitative measurement of optical properties and PS concentration, multivariate analysis of datasets with a specific focus on data exploration and dimension reduction is a useful technique. A robust multivariate model can be constructed with special attention to predictive performance when the variable selection is considered carefully. These improvements will lead to improved PDT dosimetry in individual patients. Therefore, PDT will gain further acceptance by becoming a reliable tool for controlled therapeutic outcome.

Upconverting nanoparticles have proven to be effective in biological applications due to their unique optical and chemical properties. In spite of the many merits of UCNPs, their efficiency is restricted and quantum yield is low. Therefore, a main focus remains to develop UCNPs with enhanced brightness and emission efficiency. Amongst possible paths towards improved UCNPs properties are the engineering of the surfaces and the modification of luminescence pathways. In spite of recent efforts and progress, more research is needed and is underway. A complication is that it is often difficult to compare the optical performance of UCNPs in different studies, and standardised procedures are required to quantify the performance of the different UCNPs developed. As the field is growing out of its infancy and develops toward biomedical applications, the quantum efficiency becomes a key factor to compare different UCNPs. Therefore, standardize protocols and robust systems are of great importance to build a foundation in the field, and thereby enable the accurate measurement of luminescence efficiency. We have in this work developed a multi-modal UCNP characterisation instrumentation and measurement protocol for accurate determination of UCNP properties relevant for biomedical applications. We believe that this work can contribute to a standardisation of UCNP characterisation and comparisons. I hope this can be of great benefit to the field moving forward.

As a personal note, this PhD has developed me as a person. The experiences gained first being a new team member in a larger research group, and then increasingly working more independently has been great for my development both as a person and as a researcher, although frustrating at times. Managing to complete this interesting and challenging PhD work and at the same time being part of raising an amazing and supporting family, with husband, two fantastic children and a playful dog, has boosted my self-confidence enormously and is for me a proof that I am now, if not fully, at least partially assimilated in this new world (academically and culturally). After completing this part of my life and education, I am very inspired and feel very ready for new challenges.

THE AUTHOR'S CONTRIBUTIONS

I **Development of a novel combined fluorescence and reflectance spectroscopy system for guiding high-grade glioma resections: confirmation of capability in lab experiments**

M. Mousavi, H. Xie, Zh. Xie, M. Brydegaard, J. Axelsson, S. Andersson-Engels

In this study, a hand-held fiber optic probe instrument was developed to assist the surgeon in distinguishing tissue types during brain tumour resection. The system performance is based on fluorescence and reflectance spectra collected from the probed sample. It was required to validate the instrument capabilities in the lab before being used in the clinic. Measurements were performed on tissue-equivalent phantoms with a variety of optical properties that mimic biological tissues. I was the main responsible person for the design of the phantom experiment, I took an active part in the preparation of the phantoms and in acquiring data, as well as in data evaluation using multivariate analysis. I wrote the manuscript.

II **Design and validation of a fiber optic point probe instrument for therapy guidance and monitoring**

H. Xie, Zh. Xie, M. Mousavi, M. Brydegaard, J. Axelsson, S. Andersson-Engels

In this study, a clinically adapted fiber optic system was used to measure fluorescence and reflectance spectra from patients with skin tumours. The system was validated on tissue phantoms and showed a good correlation with true fluorophore concentration. I contributed substantially to the phantom measurement. I've been involved in preparing the system to be used in the clinic, and I have took part in the *in vivo* measurements. I wrote minor parts of the manuscript.

III **Increasing depth penetration in biological tissue imaging using 808-nm excited $Nd^{3+}Yb^{3+}Er^{3+}$-doped upconverting nanoparticles**

H. Söderlund, M. Mousavi, H. Liu, S. Andersson-Engels

In general, upconverting nanoparticles are excited at 975 nm, where the water absorption is strong dominantly. In this study, a new type of UCNPs was synthesised to increase the depth penetration of the excitation light in biological tissue by shifting the excitation light from 975 nm to 808 nm wavelength. The experiment was carried out mainly by Hugo Söderlund. I made substantial contributions to the preparation of the manuscript.

IV **Beam-profile-compensated quantum yield measurements of upconverting nanoparticles**

M. Mousavi, B. Thomasson, M. Li, M. Kraft, Ch. Wurth, U. Resch-Genger, S. Andersson-Engels

The characterization of the quantum yield of upconverting nanoparticles is a crucial issue in developing upconverting materials. In this study, the quantum yield of upconverting nanoparticles was measured considering the influence of the beam profile. The quantum yield measurement was based on a simple relationship between the quantum yield and excitation intensity for two-photon upconversion emission. I took part in the development of the experimental set-up and contributed substantially to all experiment. I supervised a bachelor student to perform the experimental work and data evaluation. I prepared the manuscript.

V **Real-time photodynamic therapy dosimetry using multi-excitation, multi-emission wavelengths: towards accurate prediction of treatment outcome**

M. Mousavi, L. Moriyama, C. Grecco, M. Nogueira, K. Svanberg, C. Kurachi, S. Andersson-Engels

A hand-held fiber optic probe instrument based on fluorescence and reflectance spectroscopy is used to measure the intrinsic fluorescence signal during photodynamic therapy. The design employs multiple light sources, enabling to compensate for optical property effects on quantification of Chlorine E6. The project was conducted in Brazil. The system was developed in Lund and transported to the Sao Carlos institute and measurements were performed *in vivo*. I was involved in all the experimental work. I was responsible for data analysis and manuscript preparation.

VI **Potential biomedical use of diode-laser-induced luminescence from upconverting nanoparticles**

M. Mousavi, S. Andersson-Engels

This paper is a chapter in the book 'Handbook of Semiconductor Lasers and Diode-based light sources in Biophotonics'. This chapter presents the potential biomedical use of diode-laser-induced luminescence from upconverting nanoparticles. I made substantial contribution to the preparation of this book chapter.

VII Multi-variable compensated quantum yield measurements of upconverting nanoparticles with high dynamic range: A systematic approach

S. Konugolu, J. Matias, G. Dumlupinar, L. Niemitz, M. Mousavi, K. Komobilus, S. Andersson-Engels

The excitation-intensity-dependent quantum yield of upconverting nanoparticles makes them challenging to characterize using commercial quantum yield systems. In this study, a modified multimodal system is developed to measure UCNPs quantum yield compensated for various distorting parameters, significantly, beam profile influence. This system provides an accurate high dynamic range quantum yield curves. At the start of the project, I provided valuable information regarding the optical arrangement and data analysis. I travelled to Cork for final stabilization of the system and also to conduct last measurements to finalize the manuscript.

ACKNOWLEDGEMENTS

I wish to express my sincere gratitude to all those who supported me throughout my PhD studies. I would like to take this opportunity to thank all of you and particularly the following people who have been especially helpful and important for my studies:

First and foremost, I would like to thank my supervisor Professor Stefan Andersson-Engels for the continuous support, guidance and constant encouragement that you offered me from the first to the last day. It is my pleasure and honour to be your student.

I would like to thank my co-supervisors: Sune and Katarina Svanberg for all your help during my PhD, and Nina Reistad, for our enlightening discussions. I would also like to thank my ex-co-supervisor Johan Axelsson who taught me a lot during the first part of my PhD, when he still worked at the university.

I am grateful to all of my co-authors and research partners and above all, my dear friend, Jason Beech for his support when it was very much needed. This thesis would not have been possible without your contribution and support.

I reserve my deepest gratitude for my beloved mother and father for their unconditional love and for my sister, Atefeh, and her family, Behzad and Hannah, for all their moral support during these years. Also thanks to all my beloved relatives and friends in my life.

Finally, I would like to express my love and gratitude to my husband, Vahid. You have no idea how much of an inspiration you've been to me. For you and our children, Elin and Kevin, I am forever grateful.

BIBLIOGRAPHY

1. Z. Huang, K. Y. Ho, M. S. Bergholt, W. Zheng, K. G. Yeoh and S. Duraipandian. *Methods related to real-time cancer diagnostics at endoscopy utilizing fiber-optic Raman spectroscopy* (2018). US Patent 9,931,039.
2. M. Sharma, E. Marple, J. Reichenberg and J. W. Tunnell. *Design and characterization of a novel multimodal fiber-optic probe and spectroscopy system for skin cancer applications.* Review of Scientific Instruments **85**, 083101 (2014).
3. J. Z. Zhang. *Biomedical applications of shape-controlled plasmonic nanostructures: a case study of hollow gold nanospheres for photothermal ablation therapy of cancer.* The Journal of Physical Chemistry Letters **1**, 686–695 (2010).
4. P. Matousek and M. Morris. *Emerging Raman applications and techniques in biomedical and pharmaceutical fields.* Springer Science & Business Media (2010).
5. A. Garcia-Uribe, J. Zou, M. Duvic, J. H. Cho-Vega, V. G. Prieto and L. V. Wang. *In vivo diagnosis of melanoma and nonmelanoma skin cancer using oblique incidence diffuse reflectance spectrometry.* Cancer research **72**, 2738–2745 (2012).
6. A. L. Vahrmeijer, M. Hutteman, J. R. Van Der Vorst, C. J. Van De Velde and J. V. Frangioni. *Image-guided cancer surgery using near-infrared fluorescence.* Nature reviews Clinical oncology **10**, 507 (2013).
7. R. Etzioni, N. Urban, S. Ramsey, M. McIntosh, S. Schwartz, B. Reid, J. Radich, G. Anderson and L. Hartwell. *Early detection: The case for early detection.* Nature reviews cancer **3**, 243 (2003).
8. M. Ilic and I. Ilic. *Epidemiology of pancreatic cancer.*

World journal of gastroenterology **22**, 9694 (2016).

9. K. Doi. *Diagnostic imaging over the last 50 years: research and development in medical imaging science and technology.* Physics in Medicine & Biology **51**, R5 (2006).
10. S. S. Gambhir. *Molecular imaging of cancer with positron emission tomography.* Nature Reviews Cancer **2**, 683 (2002).
11. L. Martí-Bonmatí, R. Sopena, P. Bartumeus and P. Sopena. *Multimodality imaging techniques.* Contrast media & molecular imaging **5**, 180–189 (2010).
12. L. Gao and L. V. Wang. *A review of snapshot multidimensional optical imaging: measuring photon tags in parallel.* Physics reports **616**, 1–37 (2016).
13. T. E. De Carlo, A. Romano, N. K. Waheed and J. S. Duker. *A review of optical coherence tomography angiography (OCTA).* International journal of retina and vitreous **1**, 5 (2015).
14. D. Grosenick, H. Rinneberg, R. Cubeddu and P. Taroni. *Review of optical breast imaging and spectroscopy.* Journal of biomedical optics **21**, 091311 (2016).
15. R. Raghunathan, M. Singh, M. E. Dickinson and K. V. Larin. *Optical coherence tomography for embryonic imaging: a review.* Journal of biomedical optics **21**, 050902 (2016).
16. H. Gursoy, C. Ozcakir-Tomruk, J. Tanalp and S. Yılmaz. *Photodynamic therapy in dentistry: a literature review.* Clinical oral investigations **17**, 1113–1125 (2013).
17. G. Shafirstein, D. Bellnier, E. Oakley, S. Hamilton, M. Potasek, K. Beeson and E. Parilov. *Interstitial photodynamic therapy—A focused review.* Cancers **9**, 12 (2017).
18. F. Vohra, A. A. Al-Kheraif, T. Qadri, M. I. A. Hassan, A. Ahmed, S. Warnakulasuriya and F. Javed. *Efficacy of photodynamic therapy in the management of oral premalignant lesions. A systematic review.* Photodiagnosis and photodynamic therapy **12**, 150–159 (2015).
19. C. A. Robertson, D. H. Evans and H. Abrahamse. *Photodynamic therapy (PDT): a short review on cellular mechanisms and cancer research applications for PDT.* Journal of Photochemistry and Photobiology B: Biology

96, 1–8 (2009).

20. V. V. Tuchin. *Tissue optics and photonics: biological tissue structures.* Journal of Biomedical Photonics & Engineering **1** (2015).
21. C. L. Evans, E. O. Potma, M. Puoris' haag, D. Côté, C. P. Lin and X. S. Xie. *Chemical imaging of tissue in vivo with video-rate coherent anti-Stokes Raman scattering microscopy.* Proceedings of the national academy of sciences **102**, 16807–16812 (2005).
22. D. Pappas, B. W. Smith and J. D. Winefordner. *Raman spectroscopy in bioanalysis.* Talanta **51**, 131–144 (2000).
23. E. Hanlon, R. Manoharan, T. Koo, K. Shafer, J. Motz, M. Fitzmaurice, J. Kramer, I. Itzkan, R. Dasari and M. Feld. *Prospects for in vivo Raman spectroscopy.* Physics in Medicine & Biology **45**, R1 (2000).
24. S. L. Jacques. *Optical properties of biological tissues: a review.* Physics in Medicine & Biology **58**, R37 (2013).
25. X. Wang, B. W. Pogue, S. Jiang, X. Song, K. D. Paulsen, C. Kogel, S. P. Poplack and W. A. Wells. *Approximation of Mie scattering parameters in near-infrared tomography of normal breast tissue in vivo.* Journal of biomedical optics **10**, 051704 (2005).
26. A. Sassaroli and S. Fantini. *Comment on the modified Beer–Lambert law for scattering media.* Physics in Medicine & Biology **49**, N255 (2004).
27. J. R. Lakowicz. *Principles of fluorescence spectroscopy.* Springer Science & Business Media (2013).
28. B. Valeur. *Molecular fluorescence.* digital Encyclopedia of Applied Physics pages 477–531 (2003).
29. Y. Wu and J. Y. Qu. *Autofluorescence spectroscopy of epithelial tissues.* Journal of biomedical optics **11**, 054023 (2006).
30. D. De Veld, M. Witjes, H. Sterenborg and J. Roodenburg. *The status of in vivo autofluorescence spectroscopy and imaging for oral oncology.* Oral oncology **41**, 117–131 (2005).
31. M. Monici. *Cell and tissue autofluorescence research and diagnostic applications.* Biotechnology annual review **11**, 227–256 (2005).
32. R. R. Allison, G. H. Downie, R. Cuenca, X.-H. Hu, C. J.

Childs and C. H. Sibata. *Photosensitizers in clinical PDT.* Photodiagnosis and photodynamic therapy **1**, 27–42 (2004).

33. N. Patel, P. Pera, P. Joshi, M. Dukh, W. A. Tabaczynski, K. E. Siters, M. Kryman, R. R. Cheruku, F. Durrani, J. R. Missert et al. *Highly effective dual-function near-infrared (NIR) photosensitizer for fluorescence imaging and photodynamic therapy (PDT) of cancer.* Journal of medicinal chemistry **59**, 9774–9787 (2016).
34. N. Ferraro, E. Barbarite, T. R. Albert, E. Berchmans, A. H. Shah, A. Bregy, M. E. Ivan, T. Brown and R. J. Komotar. *The role of 5-aminolevulinic acid in brain tumor surgery: a systematic review.* Neurosurgical review **39**, 545–555 (2016).
35. S. Kaneko and S. Kaneko. *Fluorescence-guided resection of malignant glioma with 5-ALA.* International journal of biomedical imaging **2016** (2016).
36. R. Szeimies, C. A. Morton, A. Sidoroff and L. R. Braathen. *Photodynamic therapy for non-melanoma skin cancer.* ACTA DERMATOVENEREOLOGICA-STOCKHOLM- **85**, 483 (2005).
37. R. F. V. Lopez, N. Lange, R. Guy and M. V. L. B. Bentley. *Photodynamic therapy of skin cancer: controlled drug delivery of 5-ALA and its esters.* Advanced drug delivery reviews **56**, 77–94 (2004).
38. D. Jocham, H. Stepp and R. Waidelich. *Photodynamic diagnosis in urology: state-of-the-art.* European urology **53**, 1138–1150 (2008).
39. I. Kausch, M. Sommerauer, F. Montorsi, A. Stenzl, D. Jacqmin, P. Jichlinski, D. Jocham, A. Ziegler and R. Vonthein. *Photodynamic diagnosis in non–muscle-invasive bladder cancer: a systematic review and cumulative analysis of prospective studies.* European urology **57**, 595–606 (2010).
40. M.-A. D'Hallewin, L. Bezdetnaya and F. Guillemin. *Fluorescence detection of bladder cancer: a review.* European urology **42**, 417–425 (2002).
41. D. Zaak, R. Sroka, M. Höppner, W. Khoder, O. Reich, S. Tritschler, R. Muschter, R. Knüchel and A. Hofstetter. *Photodynamic therapy by means of 5-ALA induced PPIX in human prostate cancer–preliminary results.* Medical Laser Application **18**, 91–95 (2003).

42. S.-C. Chang, G. A. Buonaccorsi, A. J. MacRobert and S. G. Brown. *Interstitial photodynamic therapy in the canine prostate with disulfonated aluminum phthalocyanine and 5-aminolevulinic acid-induced protoporphyrin IX.* The Prostate **32**, 89–98 (1997).
43. https://omlc.org ().
44. F. Asllanaj, S. Contassot-Vivier, A. Liemert and A. Kienle. *Radiative transfer equation for predicting light propagation in biological media: comparison of a modified finite volume method, the Monte Carlo technique, and an exact analytical solution.* Journal of biomedical optics **19**, 015002 (2014).
45. L. Wang, S. L. Jacques and L. Zheng. *MCML—Monte Carlo modeling of light transport in multi-layered tissues.* Computer methods and programs in biomedicine **47**, 131–146 (1995).
46. E. Alerstam, T. Svensson and S. Andersson-Engels. *Parallel computing with graphics processing units for high-speed Monte Carlo simulation of photon migration.* Journal of biomedical optics **13**, 060504 (2008).
47. C. B. Simone II and K. A. Cengel. *Photodynamic therapy for lung cancer and malignant pleural mesothelioma.* In *Seminars in oncology* volume 41 pages 820–830. Elsevier (2014).
48. A. Chiaviello, I. Postiglione and G. Palumbo. *Targets and mechanisms of photodynamic therapy in lung cancer cells: a brief overview.* Cancers **3**, 1014–1041 (2011).
49. N. Ikeda, J. Usuda, H. Kato, T. Ishizumi, S. Ichinose, K. Otani, H. Honda, K. Furukawa, T. Okunaka and H. Tsutsui. *New aspects of photodynamic therapy for central type early stage lung cancer.* Lasers in surgery and medicine **43**, 749–754 (2011).
50. S. R. Lucena, N. Salazar, T. Gracia-Cazaña, A. Zamarrón, S. González, Á. Juarranz and Y. Gilaberte. *Combined treatments with photodynamic therapy for non-melanoma skin cancer.* International journal of molecular sciences **16**, 25912–25933 (2015).
51. R. Darlenski and J. W. Fluhr. *Photodynamic therapy in dermatology: past, present, and future.* Journal of biomedical optics **18**, 061208 (2012).
52. M. C. Choi, S. G. Jung, H. Park, S. Y. Lee, C. Lee,

Y. Y. Hwang and S. J. Kim. *Photodynamic therapy for management of cervical intraepithelial neoplasia II and III in young patients and obstetric outcomes.* Lasers in surgery and medicine **45**, 564–572 (2013).

53. L. M. de Freitas, C. P. Soares and C. R. Fontana. *Synergistic effect of photodynamic therapy and cisplatin: A novel approach for cervical cancer.* Journal of Photochemistry and Photobiology B: Biology **140**, 365–373 (2014).

54. C. M. Moore, M. Emberton and S. G. Bown. *Photodynamic therapy for prostate cancer—an emerging approach for organ-confined disease.* Lasers in surgery and medicine **43**, 768–775 (2011).

55. K. Svanberg, N. Bendsoe, S. Svanberg and S. Andersson-Engels. *Clinical and technical aspects of photodynamic therapy–superficial and interstitial illumination in skin and prostate cancer.* Handbook of biophotonics pages 259–287 (2013).

56. K. Svanberg, N. Bendsoe, J. Axelsson, S. Andersson-Engels and S. Svanberg. *Photodynamic therapy: superficial and interstitial illumination.* Journal of biomedical optics **15**, 041502 (2010).

57. T.-Y. Lin, Y. Li, Q. Liu, J.-L. Chen, H. Zhang, D. Lac, H. Zhang, K. W. Ferrara, S. Wachsmann-Hogiu, T. Li et al. *Novel theranostic nanoporphyrins for photodynamic diagnosis and trimodal therapy for bladder cancer.* Biomaterials **104**, 339–351 (2016).

58. K. Inoue. *5-Aminolevulinic acid-mediated photodynamic therapy for bladder cancer.* International Journal of Urology **24**, 97–101 (2017).

59. G. Jori. *Factors controlling the selectivity and efficiency of tumour damage in photodynamic therapy.* Lasers in Medical Science **5**, 115–120 (1990).

60. H. Abrahamse and M. R. Hamblin. *New photosensitizers for photodynamic therapy.* Biochemical Journal **473**, 347–364 (2016).

61. R. R. Allison and K. Moghissi. *Photodynamic therapy (PDT): PDT mechanisms.* Clinical endoscopy **46**, 24 (2013).

62. M. Ethirajan, Y. Chen, P. Joshi and R. K. Pandey. *The role of porphyrin chemistry in tumor imaging and*

photodynamic therapy. Chemical Society Reviews **40**, 340–362 (2011).

63. I. Yoon, J. Z. Li and Y. K. Shim. *Advance in photosensitizers and light delivery for photodynamic therapy.* Clinical endoscopy **46**, 7 (2013).
64. V. G. Schweitzer. *PHOTOFRIN-mediated photodynamic therapy for treatment of early stage oral cavity and laryngeal malignancies.* Lasers in Surgery and Medicine: The Official Journal of the American Society for Laser Medicine and Surgery **29**, 305–313 (2001).
65. I. Georgakoudi, M. G. Nichols and T. H. Foster. *The mechanism of Photofrin photobleaching and its consequences for photodynamic dosimetry.* Photochemistry and photobiology **65**, 135–144 (1997).
66. Z. Ji, G. Yang, V. Vasovic, B. Cunderlikova, Z. Suo, J. M. Nesland and Q. Peng. *Subcellular localization pattern of protoporphyrin IX is an important determinant for its photodynamic efficiency of human carcinoma and normal cell lines.* Journal of Photochemistry and Photobiology B: Biology **84**, 213–220 (2006).
67. P. Cramers, M. Ruevekamp, H. Oppelaar, O. Dalesio, P. Baas and F. Stewart. *Foscan® uptake and tissue distribution in relation to photodynamic efficacy.* British journal of cancer **88**, 283 (2003).
68. M. O. Senge and J. C. Brandt. *Temoporfin (Foscan®, 5, 10, 15, 20-tetra (m-hydroxyphenyl) chlorin)—a second-generation photosensitizer.* Photochemistry and photobiology **87**, 1240–1296 (2011).
69. A. Juzeniene. *Chlorin e6-based photosensitizers for photodynamic therapy and photodiagnosis.* Photodiagnosis and photodynamic therapy **2**, 94–96 (2009).
70. L. V. Kostryukova, V. N. Prozorovskiy, N. V. Medvedeva and O. M. Ipatova. *Comparison of a new nanoform of the photosensitizer chlorin e6, based on plant phospholipids, with its free form.* FEBS Open Bio **8**, 201–210 (2018).
71. I. Yankovsky. *Evaluation of photodynamic activity of chlorine-type photosensitizers with β-cyclodextrins nanovectors.* PhD thesis (2016).
72. J. H. Woodhams, A. J. MacRobert, M. Novelli and S. G. Bown. *Photodynamic therapy with WST09 (Tookad):*

quantitative studies in normal colon and transplanted tumours. International journal of cancer **118**, 477–482 (2006).

73. T. S. Mang. *Light sources and delivery devices for photodynamic therapy.* Photodiagnosis and Photodynamic Therapy **2**, 147 (2009).
74. L. Wyld, M. Reed and N. Brown. *Differential cell death response to photodynamic therapy is dependent on dose and cell type.* British journal of cancer **84**, 1384 (2001).
75. T. S. Mang. *Lasers and light sources for PDT: past, present and future.* Photodiagnosis and photodynamic therapy **1**, 43–48 (2004).
76. B. C. Wilson and M. S. Patterson. *Light delivery and optical dosimetry in photodynamic therapy of solid tumors.* In *Photodynamic therapy, basic principles and clinical applications.* Marcel Dekker, Inc New York (1992).
77. I. Van Geel, H. Oppelaar, J. Marijnissen and F. Stewart. *Influence of fractionation and fluence rate in photodynamic therapy with Photofrin or mTHPC.* Radiation research **145**, 602–609 (1996).
78. B. W. Pogue, J. A. O'Hara, I. A. Goodwin, C. J. Wilmot, G. P. Fournier, A. R. Akay and H. Swartz. *Tumor pO2 changes during photodynamic therapy depend upon photosensitizer type and time after injection.* Comparative Biochemistry and Physiology Part A: Molecular & Integrative Physiology **132**, 177–184 (2002).
79. G. Yu, T. Durduran, C. Zhou, H.-W. Wang, M. E. Putt, H. M. Saunders, C. M. Sehgal, E. Glatstein, A. G. Yodh and T. M. Busch. *Noninvasive monitoring of murine tumor blood flow during and after photodynamic therapy provides early assessment of therapeutic efficacy.* Clinical cancer research **11**, 3543–3552 (2005).
80. A. L. Maas, S. L. Carter, E. P. Wileyto, J. Miller, M. Yuan, G. Yu, A. C. Durham and T. M. Busch. *Tumor vascular microenvironment determines responsiveness to photodynamic therapy.* Cancer research **72**, 2079–2088 (2012).
81. J. Van Gemert, M. Berenbaum and G. Gijsbers. *Wavelength and light-dose dependence in tumour phototheraphy with haematoporphyrin derivative.* British journal of cancer **52**, 43 (1985).

82. K. R. Weishaupt, C. J. Gomer and T. J. Dougherty. *Identification of singlet oxygen as the cytotoxic agent in photo-inactivation of a murine tumor.* Cancer research **36**, 2326–2329 (1976).

83. *Direct Near-infrared Luminescence Detection of Singlet Oxygen Generated by Photodynamic Therapy in Cells In Vitro and Tissues In Vivo¶* ().

84. M. J. Niedre, A. J. Secord, M. S. Patterson and B. C. Wilson. *In vitro tests of the validity of singlet oxygen luminescence measurements as a dose metric in photodynamic therapy.* Cancer research **63**, 7986–7994 (2003).

85. B. C. Wilson, M. S. Patterson and L. Lilge. *Implicit and explicit dosimetry in photodynamic therapy: a new paradigm.* Lasers in medical science **12**, 182–199 (1997).

86. B. W. Pogue, J. T. Elliott, S. C. Kanick, S. C. Davis, K. S. Samkoe, E. V. Maytin, S. P. Pereira and T. Hasan. *Revisiting photodynamic therapy dosimetry: reductionist & surrogate approaches to facilitate clinical success.* Physics in Medicine & Biology **61**, R57 (2016).

87. N. Ramanujam. *Fluorescence spectroscopy in vivo.* Encyclopedia of analytical chemistry (2000).

88. T. J. Farrell, M. S. Patterson and B. Wilson. *A diffusion theory model of spatially resolved, steady-state diffuse reflectance for the noninvasive determination of tissue optical properties in vivo.* Medical physics **19**, 879–888 (1992).

89. I. Georgakoudi, B. C. Jacobson, J. Van Dam, V. Backman, M. B. Wallace, M. G. Müller, Q. Zhang, K. Badizadegan, D. Sun, G. A. Thomas et al. *Fluorescence, reflectance, and light-scattering spectroscopy for evaluating dysplasia in patients with Barrett's esophagus.* Gastroenterology **120**, 1620–1629 (2001).

90. Z. I. Volynskaya, A. S. Haka, K. L. Bechtel, M. Fitzmaurice, R. Shenk, N. Wang, J. Nazemi, R. R. Dasari and M. S. Feld. *Diagnosing breast cancer using diffuse reflectance spectroscopy and intrinsic fluorescence spectroscopy.* Journal of biomedical optics **13**, 024012 (2008).

91. S. C. Kanick, S. C. Davis, Y. Zhao, T. Hasan, E. V. Maytin, B. W. Pogue and M. S. Chapman.

Dual-channel red/blue fluorescence dosimetry with broadband reflectance spectroscopic correction measures protoporphyrin IX production during photodynamic therapy of actinic keratosis. Journal of Biomedical Optics **19**, 075002 (2014).

92. P. A. Valdes, F. Leblond, K. D. Paulsen, A. Kim, B. C. Wilson, O. M. Conde, B. T. Harris and D. W. Roberts. *Combined fluorescence and reflectance spectroscopy for in vivo quantification of cancer biomarkers in low-and high-grade glioma surgery.* Journal of Biomedical Optics **16**, 116007 (2011).

93. R. S. Bradley and M. S. Thorniley. *A review of attenuation correction techniques for tissue fluorescence.* Journal of the royal society Interface **3**, 1–13 (2005).

94. J. Coremans, C. Ince, H. Bruining and G. Puppels. *(Semi-) quantitative analysis of reduced nicotinamide adenine dinucleotide fluorescence images of blood-perfused rat heart.* Biophysical journal **72**, 1849–1860 (1997).

95. J. Beuthan, O. Minet and G. Muller. *Quantitative optical biopsy of liver tissue ex vivo.* IEEE Journal of selected topics in quantum electronics **2**, 906–913 (1996).

96. X. Chen, H. Xie, Z. Xu and D. Yu. *Correction of tissue autofluorescence by reflectance spectrum.* In *Optics in Health Care and Biomedical Optics: Diagnostics and Treatment* volume 4916 pages 441–444. International Society for Optics and Photonics (2002).

97. *Porphyrin Bleaching and PDT-induced Spectral Changes are Irradiance Dependent in ALA-sensitized Normal Rat Skin In Vivo¶* ().

98. M. Canpolat and J. R. Mourant. *Optical measurement of photosensitizer concentration using a probe with a small source-detector fiber separation.* In *Biomedical Diagnostic, Guidance, and Surgical-Assist Systems II* volume 3911 pages 10–18. International Society for Optics and Photonics (2000).

99. R. Weersink, M. S. Patterson, K. Diamond, S. Silver and N. Padgett. *Noninvasive measurement of fluorophore concentration in turbid media with a simple fluorescence/reflectance ratio technique.* Applied optics **40**, 6389–6395 (2001).

100. A. J. Durkin and R. Richards-Kortum. *Comparison of methods to determine chromophore concentrations from*

fluorescence spectra of turbid samples. Lasers in Surgery and Medicine: The Official Journal of the American Society for Laser Medicine and Surgery **19**, 75–89 (1996).

101. H. Xie, Z. Xie, M. Mousavi, N. Bendsoe, M. S. Brydegaard, J. Axelsson and S. Andersson-Engels. *Design and validation of a fiber optic point probe instrument for therapy guidance and monitoring.* Journal of biomedical optics **19**, 071408 (2014).
102. S. T. Flock, S. L. Jacques, B. C. Wilson, W. M. Star and M. J. van Gemert. *Optical properties of Intralipid: a phantom medium for light propagation studies.* Lasers in surgery and medicine **12**, 510–519 (1992).
103. H. Seal et al. *Multivariate statistical analysis for biologists.* Multivariate statistical analysis for biologists. (1964).
104. F. Auzel. *Upconversion and anti-stokes processes with f and d ions in solids.* Chemical reviews **104**, 139–174 (2004).
105. D. R. Gamelin and H. U. Güdel. *Design of luminescent inorganic materials: new photophysical processes studied by optical spectroscopy.* Accounts of chemical research **33**, 235–242 (2000).
106. F. Wang and X. Liu. *Recent advances in the chemistry of lanthanide-doped upconversion nanocrystals.* Chemical Society Reviews **38**, 976–989 (2009).
107. G. S. Yi and G. M. Chow. *Synthesis of hexagonal-phase NaYF4: Yb, Er and NaYF4: Yb, Tm nanocrystals with efficient up-conversion fluorescence.* Advanced Functional Materials **16**, 2324–2329 (2006).
108. J.-H. Zeng, J. Su, Z.-H. Li, R.-X. Yan and Y.-D. Li. *Synthesis and upconversion luminescence of hexagonal-Phase NaYF4: Yb, Er3+ phosphors of controlled size and morphology.* Advanced Materials **17**, 2119–2123 (2005).
109. D. Chen, P. Huang, Y. Yu, F. Huang, A. Yang and Y. Wang. *Dopant-induced phase transition: a new strategy of synthesizing hexagonal upconversion NaYF4 at low temperature.* Chemical Communications **47**, 5801–5803 (2011).
110. D. T. Klier and M. U. Kumke. *Analysing the effect of the crystal structure on upconversion luminescence in Yb 3+, Er 3+-co-doped NaYF 4 nanomaterials.* Journal of

Materials Chemistry C **3**, 11228–11238 (2015).

111. D. R. Gamelin and H. U. Gudel. *Upconversion processes in transition metal and rare earth metal systems.* In *Transition metal and rare earth compounds* pages 1–56. Springer (2001).
112. F. Vetrone, R. Naccache, V. Mahalingam, C. G. Morgan and J. A. Capobianco. *The active-core/active-shell approach: A strategy to enhance the upconversion luminescence in lanthanide-doped nanoparticles.* Advanced Functional Materials **19**, 2924–2929 (2009).
113. C. T. Xu, N. Svensson, J. Axelsson, P. Svenmarker, G. Somesfalean, G. Chen, H. Liang, H. Liu, Z. Zhang and S. Andersson-Engels. *Autofluorescence insensitive imaging using upconverting nanocrystals in scattering media.* Applied Physics Letters **93**, 171103 (2008).
114. R. Lei, D. Deng, X. Liu, F. Huang, H. Wang, S. Zhao and S. Xu. *Influence of excitation power and doping concentration on the upconversion emission and optical temperature sensing behavior of Er 3+: BaGd 2 (MoO 4) 4 phosphors.* Optical Materials Express **8**, 3023–3035 (2018).
115. M. V. DaCosta, S. Doughan, Y. Han and U. J. Krull. *Lanthanide upconversion nanoparticles and applications in bioassays and bioimaging: A review.* Analytica chimica acta **832**, 1–33 (2014).
116. S. Wilhelm. *Perspectives for upconverting nanoparticles.* ACS nano **11**, 10644–10653 (2017).
117. C. Wang, L. Cheng and Z. Liu. *Drug delivery with upconversion nanoparticles for multi-functional targeted cancer cell imaging and therapy.* Biomaterials **32**, 1110–1120 (2011).
118. Y. Wang, L. Tu, J. Zhao, Y. Sun, X. Kong and H. Zhang. *Upconversion luminescence of β-NaYF4: Yb3+, Er3+@ β-NaYF4 core/shell nanoparticles: excitation power density and surface dependence.* The Journal of Physical Chemistry C **113**, 7164–7169 (2009).
119. M. Lin, Y. Zhao, S. Wang, M. Liu, Z. Duan, Y. Chen, F. Li, F. Xu and T. Lu. *Recent advances in synthesis and surface modification of lanthanide-doped upconversion nanoparticles for biomedical applications.* Biotechnology advances **30**, 1551–1561 (2012).

120. M. Wang, G. Abbineni, A. Clevenger, C. Mao and S. Xu. *Upconversion nanoparticles: synthesis, surface modification and biological applications.* Nanomedicine: Nanotechnology, Biology and Medicine **7**, 710–729 (2011).

121. Q. Zhan, J. Qian, H. Liang, G. Somesfalean, D. Wang, S. He, Z. Zhang and S. Andersson-Engels. *Using 915 nm laser excited Tm3+/Er3+/Ho3+-doped NaYbF4 upconversion nanoparticles for in vitro and deeper in vivo bioimaging without overheating irradiation.* ACS nano **5**, 3744–3757 (2011).

122. J. Shen, G. Chen, A.-M. Vu, W. Fan, O. S. Bilsel, C.-C. Chang and G. Han. *Engineering the upconversion nanoparticle excitation wavelength: cascade sensitization of tri-doped upconversion colloidal nanoparticles at 800 nm.* Advanced Optical Materials **1**, 644–650 (2013).

123. H. Liu, C. T. Xu, D. Lindgren, H. Xie, D. Thomas, C. Gundlach and S. Andersson-Engels. *Balancing power density based quantum yield characterization of upconverting nanoparticles for arbitrary excitation intensities.* Nanoscale **5**, 4770–4775 (2013).

124. J.-C. Boyer and F. C. Van Veggel. *Absolute quantum yield measurements of colloidal NaYF 4: Er3+, Yb3+ upconverting nanoparticles.* Nanoscale **2**, 1417–1419 (2010).

125. S. Balabhadra, M. Debasu, C. Brites, R. Ferreira and L. Carlos. *A cost-effective quantum yield measurement setup for upconverting nanoparticles.* Journal of Luminescence **189**, 64–70 (2017).

PAPERS

PAPER I

Development of a novel combined fluorescence and reflectance spectroscopy system for guiding high-grade glioma resections: confirmation of capability in lab experiments

M. Mousavi, H. Xie, Zh. Xie, M. Brydegaard, J. Axelsson,
S. Andersson-Engels.

SPIE Proceeding **9032**, (2013).

Development of a novel combined fluorescence and reflectance spectroscopy system for guiding high-grade glioma resections _ Confirmation of capability in lab experiments

Monirehalsadat Mousavi, Haiyan Xie, Zhiyuan Xie, Mikkel Brydegaard, Johan Axelsson, and Stefan Andersson-Engels
Lund University, Department of Physics, P.O. Box 118, SE-221 00, Lund, Sweden

ABSTRACT

Total resection of glioblastoma multiform (GBM), the most common and aggressive malignant brain tumor, is challenging among other things due to difficulty in intraoperative discrimination between normal and residual tumor cells. This project demonstrates the potential of a system based on a combination of autofluorescence and diffuse reflectance spectroscopy to be useful as an intraoperative guiding tool. In this context, a system based on 5 LEDs coupled to optical fibers was employed to deliver UV/visible light to the sample sequentially. Remitted light from the tissue; including diffuse reflected and fluorescence of endogenous and exogenous fluorophores, as well as its photobleaching product, is transmitted to one photodiode and four avalanche photodiodes. This instrument has been evaluated with very promising results by performing various tissue-equivalent phantom laboratory and clinical studies on skin lesions.

1. INTRODUCTION

Surgical resection of glioblastoma tumors, the most common and aggressive type of malignant brain tumor, is difficult due to its similarity in appearance to surrounding brain tissue and its infiltrative growth pattern. The standard method used today for tissue discrimination during surgical resections is visual inspection and palpation. Ultrasound and MR images are also taken before and after surgery in order to locate the tumor, delineate the borders between malignant and healthy tissue, as well as to verify the result of the resection. This information is not always sufficient for optimal surgical results. Several previous studies have been made to utilize various optical guidance techniques to guide brain tumor resections, mainly based on fluorescence [1-9]. The aim is here to develop an in-contact hand-held system with improved sensitivity that can guide surgeries.

The main idea of this project is to develop a system that can assist the surgeon in distinguishing tissue types during brain tumor resection. This system is based on an optical fiber probe, enabling *in vivo* fluorescence and reflectance spectroscopy during surgery. The tissue discrimination in the fluorescence signals is based on both endogenous fluorescence and contrast agents, while the reflectance correlates with optical properties of the tissue. The contrast agent employed is 5-aminolevulinic acid (ALA)-induced protoporphyrin IX (PpIX). It is assumed that the PpIX concentration is well correlated with the malignant transformation of the tissue. The ALA is administered orally to the patient prior to surgery. Malignant glial tumor tissue will then build up a higher concentration of Protoporphyrin IX, providing a fluorescence peak at 635 nm following 405 nm light excitation. The primary goal is obviously to provide a signal with high sensitivity and specificity for malignant tissue.

The idea for the system is thus to combine multi-wavelength diffuse reflection and fluorescence signals to obtain information related to PpIX concentration, independent on the amount of blood in the tissue. This would be an improvement to the previous generation of this setup, called optical touch pointer (OTP) [4], which was also somewhat sensitive to ambient light during the measurements, such as microscope lamp and room light in the operating room. In that system laser was as a source for fluorescence excitation illumination and a spectrometry method was used to detect fluorescence signals during tumor resection. The suppression capability of background light was not fully optimal, mainly due to that the signal integration time was rather long. The ambition was to reduce this sensitivity in the now presented system. By pulsing the light sources and employing lock-in type detection, this ambient light can very efficiently be suppressed in the detection. This method has in lab tests proven to detect very low PpIX fluorescence

Biophotonics—Riga 2013, edited by Janis Spigulis, Ilona Kuzmina, Proc. of SPIE Vol. 9032,
90320M · © 2013 SPIE · CCC code: 1605-7422/13/$18 · doi: 10.1117/12.2044480

concentrations in tissue phantoms, with insignificant influence of ambient light. An *in vivo* elaborate test on skin tumor was conducted with this specific system to demonstrate its full capability, before the systems will be taken into use in the ongoing clinical research program for glioblastoma tumors.

2. MATERIALS AND METHODS

2.1 System specification

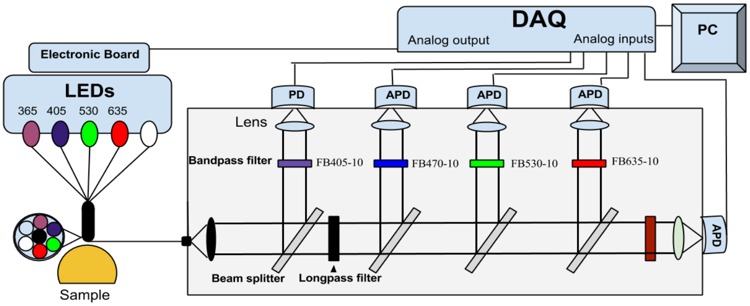

Figure 1. Schematic representation of the system

The system developed with the purpose to be useful for guiding brain tumor resections is outlined in Figure 1, including a schematic illustration of the distal end of the fiber-optic probe. It has three main parts: A light source, a fiber optical probe and a detector unit. The light source (Prizmatix Ltd.) is constructed of LEDs with four different wavelengths: 365nm, 405nm, 530nm, 635nm as well as a white light LED. The UV light (365nm) is used to excite endogenous fluorophores in tissue, while the violet light (405 nm) serves as an excitation source for PpIX. The other wavelengths and the white light are used to provide reflection data and thus signals correlating with optical properties from the tissue at these wavelengths. The light source is controlled by the output ports of a 16-bit data acquisition (DAQ) board (National Instrument, Type No. USB6351). A labview program controls the light generation sequences and time intervals between the on (high voltage) and off (low voltage) mode of the LEDs. For this purpose, a custom made electrical board was designed and connected to the Digital Clock (CTR) output channel of the DAQ board.

The hand-held fiber-optical probe delivers light to the sample by five optical fibers each with a core diameter of 750 µm, a numerical aperture of 0.5 and a length of 4 meters suitable for the operating room. The optical fiber located in the center of probe is used to collect fluorescence and diffusely reflected light from the sample and guides the collected light to the detection unit. There is a fiber collimator (Edmund Optics; 64770) in front of the detection unit. The collimated light is split into five different light paths by means of four dichroic beam splitters (BS) (Thorlabs; DMPL425, 505, 567, and 638, respectively). The detector after the first beam splitter is a silicon photodiode (PD) (Edmund Optics; 53378). This is employed to detect diffusely reflected UV and violet light from the probed tissue. Four avalanche photodiodes (APD) (Hamamatsu; S9075), are used to detect the collected endogenous fluorescence light, exogenous PpIX-fluorescence and its photobleaching products, and also reflectance from the red, green and white LED. To suppress the strong diffusely reflected light from reaching the APDs, a long pass cutoff filter (3 mm Edmond optics GG-435) is mounted after the first elastic channel. Bandpass filters (Edmund Optics; FB405-10, FB470-10, FB530-10, FB-635-10, and FB-660-10, respectively) are mounted in front of each detector to transmit only the desired spectral band of light to each detector. The bandpass filters are followed by a lens to focus the light onto the center of the active area of the detector. The photocurrents from the photodetectors are first converted to voltages by five trans-impedance amplifiers, one for each detector, transmitted to five analogue inputs of the DAQ board and then sent to the computer. Real-time control and initial data analysis is performed in LabView (Version 2012, National Instruments).

2.2 Signal processing

Light intensity modulation has been employed in the data acquisition for two reasons. Firstly, it was important to measure the signals generated for the five LEDs independently. Secondly it was essential to enable measurements in strong ambient light conditions. The periodic square-wave modulation has been evaluated to modulate the light from the source in this system. This modulation is based on a TTL signal generated from the CTR port of the DAQ board. A series of square wave pulses is created with a varied voltage sequence with square wave voltage pulses between 0 (low) and 5V (high) at a frequency of 777 Hz. The resulting waveform from the square wave modulation consists of a 777 Hz repeated time sequence of 11 time slots. This sequence includes one time slot where each of the LEDs is on at maximum and reduced power, respectively, and one where they are all switched off. The main reason to apply voltage in high and low power is to monitoring the power fluctuation resulted from temperature variation of LEDs. For each detection channel, the average signal value within each of these time slots is calculated and the background from ambient light measured with all LEDs switched off is subtracted from all signals. In order to increase the signal-to-noise ratio, this sequence is repeated over 70 cycles and an average value was calculated, corresponding to a 90 ms integration time.

2.3 Samples

In order to validate and test the system performance, water-based tissue phantoms were prepared. The tissue phantom employed in this study was based on three major ingredients, an absorber, a scatterer and a fluorophore. Diluted Intralipid (Fresenius Kabi, Sweden; 200 mg/ml), which is a fat emulsion, was added to provide the required scattering properties, while bovine blood (purchased from a local supermarket) or diluted India ink (Pelican Fount, Germany; 1:100 stock solution prepared in our lab), were used as absorbers. The Protoporphyrin IX (PpIX, Fisher Scientific) was served as a fluorophore. In order to better control and suppress any aggregation of PpIX in the phantom, the surfactant tween (Scharlau Chemie) was mixed into the phantom. The phantoms were designed to mimic the optical properties of gray matter of brain tissue.

3. RESULT

3.1 System linearity assessment

Several sets of experiments were carried out to validate our setup. First only 405nm excitation light was used for studies on system validation of linearity response and background light suppression capabilities in a dark room as well as under well controlled ambient light conditions. In the first series of experiments liquid phantoms were prepared by mixing 3.5% volume of Intralipid, 0.5% of Ink (1:100 stock solution) and 96% water. PpIX powder (0.056 g) was dissolved in 20 mL of DMSO and 80 mL of distilled water was added to obtain a 1 mM PpIX stock solution. The fluorophore concentration

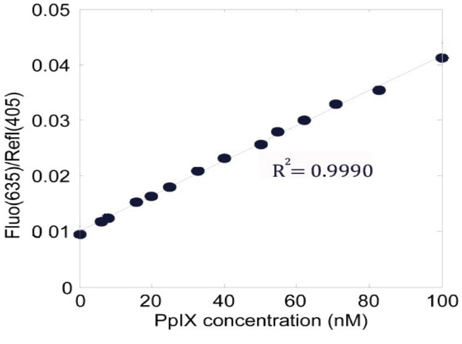

Figure 2. PpIX quantification using violet light. The solid line indicates a linear fit to the data

in the tissue phantom was, in this series of measurements, varied between 10 to 100 nM. The phantom with the highest fluorophore concentration was prepared in a glass cylinder container. The lower concentrations have subsequently been prepared by diluting with the initial tissue phantom, without any fluorophore. A gentle stirring of the sample during measurement was employed to prevent the fluorophores from aggregation and to minimize the photobleaching so that the bleached dye molecules directly under the tip of the delivering fiber were continuously replaced by fresh fluorophores.
The measured data need to be corrected to account for any small variation in source power. For this purpose, the ratio between fluorescence and reflection signals was formed. Figure 2 shows the results from the first set of measurements. The ratio has a very linear dependence on the fluorophore concentration using 405 nm LED as an excitation source. The work has shown that very low fluorescence concentration is detectable by this system, much lower concentrations than is expected in brain tissue during clinical use [10].

3.2 Ambient light suppression

As mentioned in the Introduction, the previous generation of this setup (OTP) [4] was sensitive to the ambient light during the measurements, such as fluorescence microscope lamp and room light in the operating room. In order to evaluate the capability of suppressing ambient light with the present system, measurements were conducted with tissue phantoms under well controlled ambient light conditions. In this study we used a white light ring-lamp from a microscope with similar emission spectrum to the surgical operating microscope, to examine the influence of different light conditions on the recorded signals. A tissue phantom with 100 nM PpIX concentration was prepared and the ring light was located at varying distances vertically above the sample to provide an even illumination of different intensities. A light-meter was used to quantitatively determine the ring light intensity at the surface of the tissue phantom. The experiment started with a 60 centimeter distance from the sample. The distance was then decreased to obtain a stronger ambient light condition.

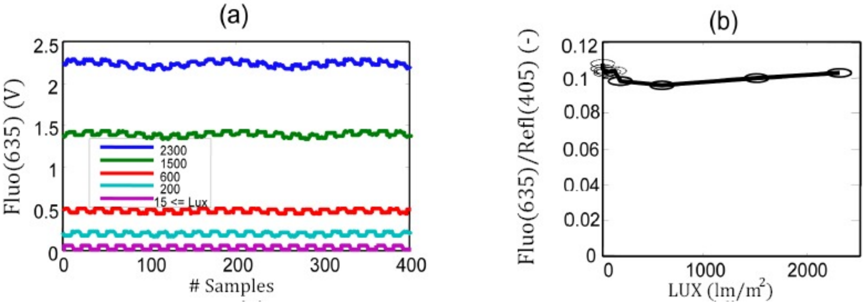

Figure 3. Sensitivity of the system to the ambient light level for a fixed PpIX concentration of 100 nM. Figures (a) shows the raw data when the violet light was modulated by a square waves and (b) demonstrates the fluorescence vs reflection ratio (i.e. the evaluated signal corresponding to the PpIX concentration) in different ambient light conditions.

Figure 3(a) illustrates the results, including raw data, for different ambient light conditions. Since the ambient light has the modulations in the low frequency range (0-100 Hz), the detected signal with a modulation at 777 Hz is totally related to the light from the LED source. In The low frequency wavy shape of the raw data curves is related to the ring light while the relatively small pulses were produced from the 777 Hz frequency-modulated LED. Figure 3(b) illustrates the evaluated signal level as a function of the ambient light intensity. Here, the on-off lock-in type of subtraction was performed for the 777 Hz modulation to remove the influence of the ambient light. As mentioned in the experimental setup chapter, the average signal value was for these plots calculated over 70 cycles to increase the signal-to-noise ratio. The results clearly indicate that the measured signal is almost completely dominated by the ambient light, while the fluorescence signal could be recovered almost uninfluenced by the ambient light when the lock-in type of subtraction was performed.

3.3 Evaluation protocol

Now, after having been able to successfully demonstrate the capability of suppressing any influence of ambient light on the detected signal using one 405 nm excitation source, all channels were connected. The multiple LEDs were run sequentially using an electrical board (multiplexer) connected to the DAQ board. In order to evaluate the experimental data, multivariate analysis is used in the data processing. The partial least squares (PLS) method was employed to develop a linear model of sample fluorescence and optical properties from 269 different samples varied in known dependent variables such as absorption, scattering and fluorescence. Intralipid concentration varies between 3% -8% of the whole phantom volume, while 0%-4% of the blood concentration was considered as an absorption variation. Protoporphyrin concentration was varied between 0 to 1000 nM. The samples were prepared through several dilution steps starting from the highest concentration. It was diluted into the lowest concentration and the last sample was measured in a separate container without any fluorophore. The measurement process occurs similarly to the previous experiment. For the PLS model regression, data normalization was done and a data matrix was created. This model can be used to predict the fluorescence concentration in unknown samples in the future, as long as the absorption, scattering and fluorescence properties fall into the interval of this set of samples. Leave-one-out methodology was used to evaluate the accuracy of predicting the fluorophore concentrations. LOO-CV split the dataset into two groups, it left one observation as the validation data, and the remaining observations were used to build the PLS regression model and this was repeated so that each variable was used as validation data.

Linear regression analysis was performed using the data from all sample measures to correlate between predicted and true properties for different variables.

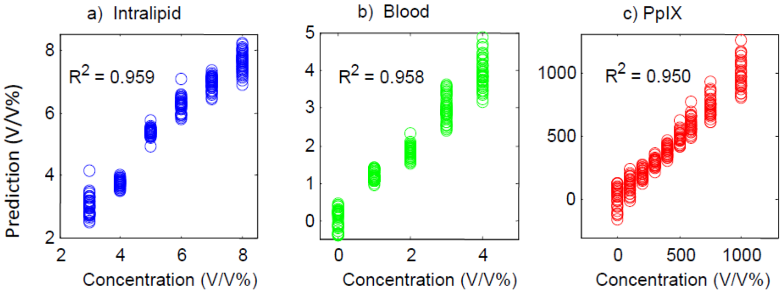

Figure 4. PpIX quantification in liquid phantom with various optical properties. a) Predicted Intralipid concentration b) Predicted blood concentration and c) Predicted PpIX concentration.

Figure 4 illustrates the relation between these values and also indicates their coefficient of determination. This coefficient denotes the goodness of linear relation between responds and predicted values. As can be seen, the estimated blood and intralipid concentration are highly correlated with correlation coefficient of 0.96 and 0.96, respectively. For fluorescence concentration, the correlation coefficient is 0.95. The result shows the viability of PLS regression for intralipid/scattering, blood/absorption, and PpIX fluorescence concentration estimation using the multi-LEDs arrangement.

3.4 *In vivo* experiments

In order to ensure that the system will work in complex living systems, an *in vivo* clinical human trial was performed. Skin tumors are easily accessible and such tumors were used in this first clinical trial. The whole setup was packed on to a portable case for outpatient clinical data acquisition and carried to the clinic of Dermatology at Skåne University Hospital in Lund.

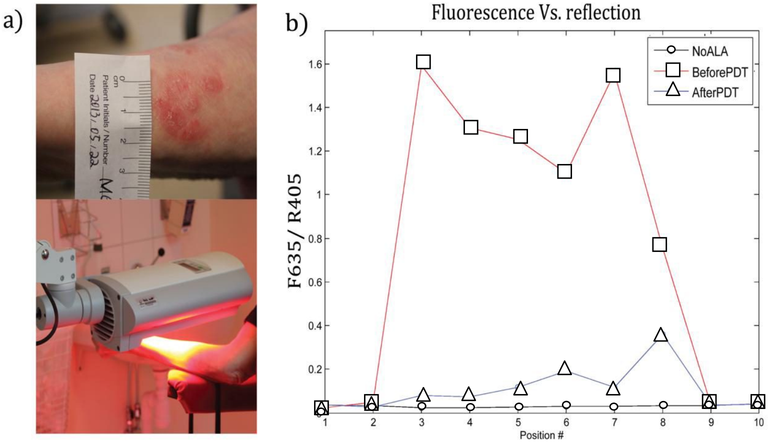

Figure 5. a) A typical skin tumor under treatment .b) In vivo fluorescence reflectance spectroscopy of a patient with a skin tumor before ALA administration before PDT and after PDT.

Figure 5(a) presents one of the eight measurements of the different experiments conducted on patients with skin tumor undergoing PDT. The PpIX accumulation at the site of application in the skin tumor is obvious from the results presented in the Figure 5(b). In this case it was straight forward to detect the lesion in the turbid tissue with a robust distinction. The curve after PDT evidences PpIX existence after treatment which indicates a somewhat prolonged photosensitivity of this drug in the lesion.

4. CONCLUSION

A novel combined fluorescence reflectance spectroscopy system based on LED-excitation and APD-detection has been developed and evaluated. The system is built as an intraoperative guiding tool for resection of glioblastoma, the most frequent and complex to treat malignant brain tumor. The LEDs as diagnostic light sources are interesting in respect of their compactness and low cost. As well, it provides sufficient intensity at the desired wavelengths, and any wavelength desired for the diagnostics. The main advantage for the present application of APDs as detectors, instead of a spectrometer used in the previous generation of the system [4] is the short integration time. This makes it possible to correctly subtract any ambient background light in a noise-free manner.

The combined use of reflectance and fluorescence, using different wavelength of interest, optimizes the diagnostic capabilities. The UV light excitation source provides information about tissue autofluorescence properties. The other light sources are employed to compensate for any variations of optical properties of the examined tissue. The use of multiple detection wavelengths in parallel allows to also compensating for any small fluctuations in the LED output by forming dimensionless ratios of detection signals. The violet light is also utilized to induce PpIX fluorophore. Accurate extraction of intrinsic fluorescence could potentially provide better diagnostic accuracy.

The linearity study conducted demonstrates that very low fluorescence signal can be detected in the presence of strong ambient light with the developed system. The ambient light suppression, as a main challenge in previous study, is successfully achieved for improved clinical applicability. Multivariate analysis of the signals has proved a great potential in separating the contributions to the signal from fluorescence, absorption and scattering in a serious of tissue phantom measurements.

The clinical trials on skin tumors were performed in order to test the instrument and its performance. While the data are promising, future work will focus on improving the system performance and preparing the setup to carry out real-time measurement in collaboration with Linköping University for ALA-guided brain tumor resections.

5. ACKNOWLEDGMENT

The authors warmly acknowledge fruitful discussions and collaborations with Karin Wårdell, Neda Haj-Hosseini, Johan Richter, Malin Svensson, Jonas Gårding, Ola Svärm, and Niels Bendsoe. The project was financially supported by the Swedish Research Council (VR); the Swedish Foundation for Strategic Research (SSF); the Swedish Governmental Agency for Innovation Systems (VINNOVA); as well as by the Linneus Centre at Lund Laser Centre.

References:

[1] Andersson-Engels, S., Elner, A., Johansson, J., Karlsson, S., Salford, L., Strlomblad, L., Svanberg, K. and Svanberg, S., "Clinical recording of laser-induced uorescence spectra for evaluation of tumor demarcation feasibility in selected clinical specialities," Laser in Medical Science, 6:415-424, (1991).

[2] Novotny, A., Stummer, W., Pichlmeier, U., Meinel, T., Wiestler, O. D., Zanella, F. and Reulen, H. J., "ALA-Glioma Fluorescence-guided surgery with 5-aminolaevulinic acid for resection of malignant glioma: a randomised controlled multicentre phase III study," Lancet Oncol, 7, 392–401, (2006).

[3] Utsuki, S., Oka, H., Sato, S., Shimizu, S., Suzuki, S., Tanizaki, Y., Kondo, K., Miyajima, Y. and Fujii, K., "Histological examination of false positive tissue resection using 5-aminolevulinic acid-induced fluorescence guidance, " Neurol Med Chir (Tokyo), 47(5):210-214, (2007 May).

[4] Haj-Hosseini, N., Richter, J., Andersson-Engels, S. and Wårdell, K., "Optical Touch Pointer for Fluorescence Guided Glioblastoma Resection Using 5-Aminolevulinic Acid," Laser Surg Med, 42(1), 9-14 (2010).

[5] Pogue, B. W., Gibbs-Strauss, S. L., Valde’s, P. A., Samkoe, K. S., Roberts, D. W. and Paulsen, L. D., "Review of neurosurgical fluorescence imaging methodologies," IEEE J. Sel. Topics Quantum Electron, 16(3), 493-505, (May/Jun. 2010).

[6] Kim, A., Roy, M., Dadani, F. and Wilson, B. C., "A fiberoptic reflectance probe with multiple source-collector separations to increase the dynamic range of derived tissue optical absorption and scattering coefficients," Opt Express, 18(6), 5580-5594 (2010).

[7] Kim, A., Khurana, M., Moriyama, Y. and Wilson, B. C. "Quantification of in vivo fluorescence decoupled from the effects of tissue optical properties using fiber-optic spectroscopy measurements," J Biomed Opt, 15(6), (2010).

[8] Richter, J. C., Haj-Hosseini, N., Andersson-Engel, S. and Wårdell, K., "Fluorescence spectroscopy measurements in ultrasonic navigated resection of malignant brain tumors," Laser Surg Med, 43(1), 8-14 (2011).

[9] Brydegaard, M., Haj-Hosseini, N., Wårdell, K. and Andersson-Engels, S., "Photobleaching-Insensitive Fluorescence Diagnostics in Skin and Brain Tissue," IEEE Photon J, 3(3), 407-421 (2011).

[10] Johansson, A., Palte, G., Schnell, O., Tonn, J. C., Herms, J. and Stepp, H., "5-Aminolevulinic Acid-induced Protoporphyrin IX Levels in Tissue of Human Malignant Brain Tumors," Photochem Photobiol, 86(6), 1373-1378 (2010).

PAPER II

Design and validation of a fiber optic point probe instrument for therapy guidance and monitoring

H. Xie, Zh. Xie, M. Mousavi, M. Brydegaard, J. Axelsson, S. Andersson-Engels.

Journal of Biomedical Optics **19(7),071408**, (2014).

Journal of Biomedical Optics 19(7), 071408 (July 2014)

Design and validation of a fiber optic point probe instrument for therapy guidance and monitoring

Haiyan Xie,[a,*] Zhiyuan Xie,[a] Monirehalsadat Mousavi,[a] Niels Bendsoe,[b] Mikkel Brydegaard,[a] Johan Axelsson,[a] and Stefan Andersson-Engels[a]
[a]Lund University, Department of Physics, P.O. Box 118, SE-221 00 Lund, Sweden
[b]Skåne University Hospital, Department of Dermatology and Venereology, Lasarettsgatan 15, SE-221 85 Lund, Sweden

Abstract. Optical techniques for tissue diagnostics currently are experiencing tremendous growth in biomedical applications, mainly due to their noninvasive, inexpensive, and real-time functionality. Here, we demonstrate a hand-held fiber optic probe instrument based on fluorescence/reflectance spectroscopy for precise tumor delineation. It is mainly aimed for brain tumor resection guidance with clinical adaptation to minimize the disruption of the standard surgical workflow and is meant as a complement to the state-of-the-art fluorescence surgical microscopy technique. Multiple light sources with fast pulse modulation and detection enable precise quantification of protoporphyrin IX (PpIX), tissue optical properties, and ambient light suppression. Laboratory measurements show the system is insensitive to strong ambient light. Validation measurements of tissue phantoms using nonlinear least squares support vector machines (LS-SVM) regression analysis demonstrate an error of <5% for PpIX concentration ranging from 400 to 1000 nM, even in the presence of large variations in phantom optical properties. The mean error is 3% for reduced scattering coefficient and 5% for blood concentration. Diagnostic precision of 100% was obtained by LS-SVM classification for *in vivo* skin tumors with topically applied 5-aminolevulinic acid during photodynamic therapy. The probe could easily be generalized to other tissue types and fluorophores for therapy guidance and monitoring. [DOI: 10.1117/1.JBO.19.7.071408]

Keywords: fluorescence spectroscopy; fiber optic sensors; reflectance; tissue; light-emitting diodes.

Paper 130832SSRR received Nov. 20, 2013; revised manuscript received Feb. 6, 2014; accepted for publication Feb. 11, 2014; published online Mar. 12, 2014.

1 Introduction

Optical techniques provide powerful means for tissue diagnostics in a wide variety of biomedical applications. Extensive efforts have been made in developing optical diagnostic tools which are noninvasive, inexpensive and could be applied *in vivo* and in real time. Fiber optic probes for biomedical optical spectroscopy enable clinical use in endoscopy, surgery, and neurological imaging.[1] Typically, such a probe incorporates a light source, fiber optic cables for light transport, and an optical detector integrated with spectroscopic devices. Different spectroscopic fiber optic probes have long since been developed and used to substantially improve clinical diagnostic capability for different purposes,[2,3] such as surgical guidance during brain tumor resection,[4–6] determination of tissue optical property for optical biopsy of brain tissue[7] and for interstitial photodynamic therapy (PDT),[8] treatment monitoring during PDT,[9,10] lung cancer staging of mediastinal lymph nodes,[11] diagnosis of nonalcoholic fatty liver disease,[12] detection of metastatic breast cancer in sentinel lymph nodes,[13] and tumor oxygenation monitoring and tissue optical properties evaluation for breast cancer diagnosis.[14,15] These probes have the flexibility that they can be manufactured into either cavities or tubular structures, put in contact with epithelial surfaces, or inserted into structures, punctured by rigid devices such as needles.[1]

Most of the spectroscopic fiber optic probes for biomedical applications are performing reflectance and/or fluorescence spectroscopy of turbid tissue. These probes are capable of providing quantitative molecular and functional information to distinguish normal from abnormal human tissue. For example, Kanick et al.[11] employed a single-fiber reflectance spectroscopy system for lung cancer staging. They developed a data evaluation model to extract information about the physiological and morphological properties of lymph tissue. Austwick et al.[13] developed a scanning elastic scattering spectroscopy system, combined with statistical discrimination analysis. It was used to detect metastatic breast cancer in sentinel lymph nodes. Fluorescence spectroscopic probes are a different approach, where either endogenous tissue fluorescence (i.e., tissue autofluorescence) or exogenous fluorescence from contrast agents is used for tissue discrimination. For instance, a fiber optic fluorosensor was developed to measure the fluorescence signal from 5-aminolevulinic acid (ALA)-induced protoporphyrin IX (PpIX) for tumor resection guidance during open brain surgery.[4,5] To correct for tissue autofluorescence superimposed on the PpIX fluorescence peak, a dimensionless fluorescence ratio was taken between these two spectral bands. To further improve the data evaluation, a photobleaching-insensitive method was developed based on a dynamic model together with multivariate analysis.[16] Valdes et al. reported a combined fluorescence and reflectance spectroscopy system for *in vivo* quantification of PpIX in low- and high-grade glioma surgery. They conducted model based evaluation to correct the detected fluorescence spectra for tissue optical properties from the reflectance.[6,17] Foscan® concentration in rat liver *in vivo* was measured by Kruijt et al. with fluorescence differential path length spectroscopy, based on the

---

*Address all correspondence to: Haiyan Xie, E-mail: haiyan.xie@fysik.lth.se fluorescence intensity corrected for absorption from the differential reflectance spectra.[18]

Fluorescence biochemical probes have been extensively applied to fluorescence-guided surgery (FGS) of malignant brain tumors.[5,19–21] In this area, 5-ALA–induced PpIX accumulates in malignant tumors and inflamed brain tissue because of the blood–brain barrier.[20,21] The resulting increased tumor tissue fluorescence is used to enhance the contrast between the tumors and surrounding healthy tissue. It could thus assist the surgeon in deciding which tissue to remove or spare in open brain surgery and improve surgical outcomes. By this technique, brain tumors have been visualized using two types of fluorescence probes: Type I, point spectroscopic tools (such as fiber optic probes) for measuring at one region at a time, and Type II, imaging systems (such as *in vivo* fluorescence microscopy, modified surgical microscopes, commercial neurosurgical operating fluorescent microscopes) for displaying every point in the area of resection. The noncontact surgical microscopy instruments are implemented as a standard in surgical resection today. However, they suffer from only being useful for identifying tumor subtypes with relatively high PpIX accumulation due to low sensitivity from the limited capture of light.[6,19,22] The imaging modalities are also limited to very superficial tissue as a result of the limited penetration depth for the excitation light. In contrast, a point probe can provide spectroscopy with better spectral information and usually higher overall sensitivity. It can be incorporated into hand tools used by the surgeon, such as ultrasonic vacuum suction devices, scalpels, and navigation systems.[5] Therefore, it can proceed to underlying regions and be able to probe the tissue to be removed. Further, this may allow penetration beyond the exposed superficial cell layer, which is of critical importance in resecting the infiltrative tumors. The previous point monitoring systems have mainly used fluorescence spectroscopy based on spectrometers. Despite many wavelength channels, those systems only provide at most three spectral components among several individuals and measurement locations,[16] thus providing limited diagnostic information for tissue diagnostics of complex tissue structures. In addition, a slight limitation with both current imaging and fiber-based FGS systems is their high sensitivity to the surrounding light sources in the operating room (OR). This results from the fact that the integration time of the detector has to be long enough to detect the weak fluorescence signal. The light fluctuation within the relatively long measurement time could also lead to imprecise measurements. Dim lighting conditions or shading the measurement region from the direct light required by current FGS systems are obviously disruptive to standard surgical workflow. There exists a need for an intraoperative FGS fluorescence spectroscopic system capable of suppressing ambient light in the OR while high fluorescence sensitivity and larger probing depth could be achieved.

In this paper, we demonstrate a clinically adapted hand-held fiber optic probe system based on fluorescence/reflectance spectroscopy with pulse modulation in combination with the light detection of the signal strength only at the modulation frequency. The probe was validated by tissue phantom measurements and *in vivo* clinical measurements on patients with skin tumors. It demonstrates insensitivity to ambient light as well as accurate assessment of both fluorophore concentration and tissue optical properties. It is mainly aimed for brain tumor resection guidance, by providing the operating surgeon with an intuitive and real-time surgical guidance tool. The probe is applicable to other tissue types and fluorophores for therapy guidance and monitoring in a general sense.

2 Materials and Methods

2.1 *System Description*

The fiber optic probe instrument described here was configured to quantify PpIX using fluorescence/reflectance spectroscopy for therapy guidance and monitoring under surgical conditions during open brain surgery. The schematic diagram of the probe system is shown in Fig. 1. It consists of a light source with five fiber-coupled light-emitting diodes (LEDs), a source/detector fiber optic probe, a detection unit, a data acquisition (DAQ) board, electronic circuits, and a laptop computer. The entire system was assembled on a trolley with a dimension of $80 \times 50 \times 100\ \text{cm}^3$ and a total weight of 15 kg, to facilitate flexibility in use in the examination room or OR.

2.1.1 *Light source*

The light source comprises five fiber-coupled LEDs (Prizmatix Ltd., Israel; FC5-LED) at four different wavelengths: 365, 405, 530, and 635 nm, as well as a white light LED (450 to 700 nm). The 405-nm and 365-nm LED were chosen to provide a strong signal from PpIX fluorescence at 635 nm and tissue autofluorescence with a broad spectrum in the visible range, respectively. The other three LEDs were used to monitor tissue optical properties from the reflectance measurements at wavelengths of interest. When running in the continuous mode, all LEDs had a maximal output power of approximately 13 mW through a polymer optical fiber (POF) of 750-μm core diameter and

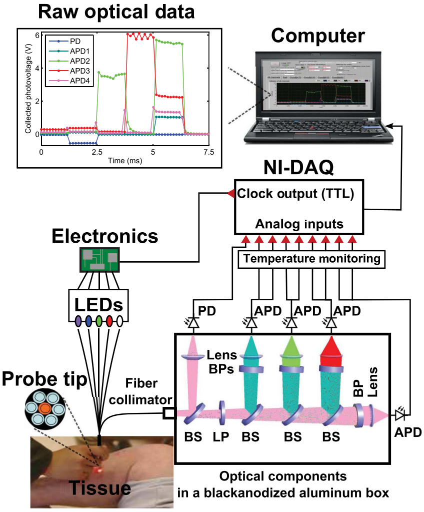

Fig. 1 Schematic diagram of the fiber optic point probe system, illustrating *in vivo* measurement of a skin lesion on the right leg of a patient. The subplot on the top left shows the real-time raw optical data detected by the five photodetectors, including the PpIX fluorescence, tissue autofluorescence, and reflectance spectra. Here, the abbreviations in this figure are BS, dichroic beam splitter; LP, long-pass filter; BP, bandpass filter; PD, photodiode; and APD, avalanche photodiode.

a numerical aperture (NA) of 0.5. The power could be adjusted with a potentiometer located on the front panel.

All LEDs were multiplexed to work sequentially, driven by a transistor-transistor logic (TTL) pulse at 777 Hz with a duty cycle of 8.3% for each LED. The source multiplexing module consists of a counter (CD40193) and a demultiplexer (CD4514). There were six pulses within one period: each LED was lit up in turn within the first five pulses, followed by one pulse with all LEDs switched off. This allowed the measurement of ambient light level.

2.1.2 *Fiber optic probe*

The custom-made hand-held fiber probe (Prizmatix Ltd., Givat-Shmuel, Israel; Y-shaped fiber patch cord bundle) consists of six surrounding delivery fibers (one spare fiber during the measurement) and one collection fiber at the center. All fibers were made of POFs (750-μm core diameter, 0.50 NA, 4-m long), which could be sterilized with ETO gas in clinical practice. They were bundled together into a stainless steel tube (5 cm long and with a 4-mm diameter), and the other end of the fibers was assembled to an SMA905 connector. The distance between two adjacent cores is almost the same as the fiber core diameter, as the cladding of POF is <15 μm. The probe tip was held perpendicular to and in contact with the sample surface.

2.1.3 *Detection unit*

The collected light from the sample was detected by the detection unit, mounted in a compact black anodized aluminum box (designed in-house using CAD). Collected light from the central fiber was collimated (Edmund Optics Inc., Barrington, New Jersey; 64770) and split into five different light paths by four dichroic beam splitters (BS) (Thorlabs Inc., Newton, New Jersey; DMPL425, 505, 567, and 638). On each path, light was detected either by a silicon photodiode (PD) (Edmund Optics; 53378) with a UV enhanced response, or an avalanche photodiode (APD) (Hamamatsu, Hamamatsu City, Japan; S9075, ϕ 1.5-mm active area). All four APDs were working at a reversed bias voltage of approximately -160 V, generated from an APD bias voltage power supply module (Hamamatsu; M6017). To suppress the back-reflected elastic violet light from reaching the APDs, a long-pass cutoff filter (Edmund Optics; GG-435) was positioned after the first elastic channel. In front of each detector, there is a light-focusing lens (Edmund Optics; 47884). For each APD, a 10-nm full width at half maximum (FWHM) narrowband bandpass filter (Edmund Optics; FB470-10, FB530-10, FB-635-10, and FB-660-10, respectively) was assembled. The photocurrent in each detector was converted to voltage with a larger dynamic range by an in-house transimpedance amplifier, consisting of an Operation Amplifier and RC feedbacks. The entire box has a dimension of $200 \times 120 \times 104\ \mathrm{mm}^3$ together with the components.

2.1.4 *Pulse generation and data acquisition*

The TTL pulse to modulate the light source was generated from the digital clock output of a 16-bit DAQ board (National Instruments Corp., Austin, Texas; NI USB-6351). The photovoltages in the PD and APDs were recorded by the analog inputs of the DAQ.

2.1.5 *Intensity calibration*

The intensity of each detection band was calibrated with a high-power quartz tungsten halogen lamp (Oriel Instruments, Stratford, Connecticut; 63355), powered by a current power supply (Oriel; 68830) with an output current of 6.5 A. Light from the calibration lamp was guided by an optic fiber (Thorlabs Inc., Newton, New Jersey; 600-μm core diameter, 0.39 NA, positioned 5 m away from the lamp) and entered the detection box without any sample. The voltage outputs on the photodetectors were normalized to the known intensity spectrum of the lamp for all five detection channels.

Unless otherwise stated, all calibration measurements were conducted in a dark laboratory room.

2.1.6 *Thermal calibration*

To compensate for the gain variation with temperature, each APD was glued with a thermistor (PTC 60-323-30, Elfa Distrelec, Järfälla, Sweden) on the rear surface so that the APD temperature could be monitored. Thermal calibration measurement was performed in a similar way as described in Sec. 2.1.5 but mounting all detection units in a mobile car fridge (Mobicool Ltd., Shenzhen, China; TC-16-12/230), which could be cooled down to +14°C. The measured photovoltage on each APD (V_{APD_i}) versus the voltage on each thermistor (V_{Therm_i}) was fitted by an exponential equation

$$V_{\mathrm{Therm}_i} = a e^{b V_{\mathrm{Therm}_i}} (i = 1 - 4), \tag{1}$$

where a and b are the fitting coefficients. Both V_{APD_i} and V_{Therm_i} were averaged over all samples within the integration time. For each photovoltage measured later on, it was multiplied by a thermal calibration factor, $F_{\mathrm{Calib}}(V_{\mathrm{Therm}_i})$, calculated from the corresponding thermal voltage with Eq. (1)

$$F_{\mathrm{Calib}}(V_{\mathrm{Therm}_i}) = 1/(a e^{b V_{\mathrm{Therm}_i}})(i = 1 - 4). \tag{2}$$

2.1.7 *Software*

Pulse generation, DAQ, and real-time signal manipulation were performed by a custom LabVIEW® (National Instruments Corp., Austin, Texas; Version 2012) application running on a laptop computer. Off-line data analysis was performed in the Matlab® environment (Mathworks™, Inc., Natick, Massachusetts; version R2012a) on a conventional PC. LS-SVMlab (version 1.8),[23] a MATLAB toolbox for least squares support vector machines (LS-SVM) was employed for multivariate regression and tissue classification analysis.

2.2 *Experimental Procedure*

2.2.1 *Phantom preparation*

Phantom experiments were carried out to test the system performance. A set of well-controlled tissue-like liquid phantoms were prepared by mixing water, intralipid (Fresenius Kabi, Uppsala, Sweden; 200 mg/ml), and India ink (Pelican Fount, Hannover, Germany; 1:100 stock solution prepared in our laboratory) or bovine blood (purchased from a local supermarket). The optical properties were chosen to have a good correspondence to real biological tissue. PpIX stock solution was prepared by dissolving 0.056 g PpIX powder (Fisher Scientific, Pittsburg, Pennsylvania) in 20 ml dimethyl sulfoxide (DMSO) (Merck, Darmstadt, Germany) and 80 ml distilled water, resulting in a PpIX concentration of 1 mM. When diluting the PpIX solution in the phantom, 2% volume of Tween (Scharlau Chemie S.A., Barcelona, Spain) was added to prevent PpIX from aggregation. The ink phantom contained 3.75% volume of intralipid, 0.25% volume of ink, and 100 nM PpIX. In total 270 blood phantoms were prepared containing different concentrations of intralipid (3%, 4%, 5%, 6%, 7%, and 8%, v:v), bovine blood (0%, 1%, 2%, 3%, and 4%, v:v), and PpIX (0, 100, 200, 300, 400, 500, 600, 750, and 1000 nM), respectively. Each phantom was placed in a cylindrical glass container. The phantoms were stirred for 4 h prior to the measurements using a magnetic stirrer (to ensure that the temperature of each APD was stable) and kept stirred during the measurements.

The reduced scattering coefficient of each phantom, in $\text{cm}^{-1}/(\text{ml}/\text{l})$, was estimated from the expression[24]

$$\mu_s'(\lambda) = C \cdot [0.58 \cdot (\lambda/1\ \mu\text{m}) - 0.1] \cdot 0.32 \cdot (\lambda/1\ \mu\text{m})^{-2.4}, \tag{3}$$

where C is the concentration of intralipid-20% in ml/l and λ is the light wavelength in μm.

The absorption coefficient at 635 nm, $\mu_a(635)$, and reduced scattering coefficient, $\mu_s'(635)$, of the phantoms were measured with a time-of-flight (TOF) spectroscopy system employing a supercontinuum white light source, described in detail elsewhere.[25]

2.2.2 *In vivo clinical validation measurements of skin cancer*

The performance of the system was validated on a total of eight patients (all of skin phototypes I–III) with skin cancers at the Department of Dermatology and Venereology, Skåne University Hospital, Sweden. The study was conducted with the approval of the Local Ethics Committee and in accordance with the ethical principles of the Declaration of Helsinki. Patients were assessed and recruited by the clinical team at outpatient clinics and were going to receive PDT after the spectral measurements. Three hours prior to PDT, all patients were topically applied with either Ameluz® (78 mg/g gel, Biofrontera AG, Germany) or Metvix® (160 mg/g, Galderma, France) to the lesion as an approximately 1-mm-thick layer including 5 mm of the surrounding normal tissue. The lesions are summarized in Table 1.

The spectral measurements on patients were performed just prior to PDT. For each lesion, a couple of locations were measured on both the tumor and neighboring tissue. The number of measurements, depending on the lesion size, is illustrated in an example image in Fig. 2 and listed in Table 1. After the measurements, the patients received PDT for 14 min.

2.3 *Evaluation Protocol*

2.3.1 *Data preprocessing*

The collected pulses on all detectors were preprocessed following the procedure as illustrated by the flowchart in Fig. 3. Within each pulse from one detector, the first and the last two data points were excluded and then an average signal value was calculated. The background, measured as the average value from the time slot when all LEDs were turned off, was then subtracted from all the other measured values of the remaining five time slots. To increase the signal-to-noise ratio, the signal was averaged over 70 light cycles, corresponding to a total integration time of 90 ms. Thereafter, the APD data were divided by the corresponding PD data for the UV, blue, and white light LED cycle, in order to compensate for the source fluctuation and tissue attenuation. Such a data preprocessing procedure would result in a data vector of size 1 × 25 for measurement on one sample spot.

Table 1 Summary of the skin lesions in this study. Eight patients were involved in the clinical study, each with one lesion. For each lesion, a number of spots on both the tumor and surrounding normal tissue were measured.

Lesion type	Patient No.	Number of locations: Lesions	Number of locations: Normal tissue
Squamous cell carcinoma *in situ*	1	6	4
Actinic keratosis	2, 8	11	8
Basal cell carcinoma	3, 7	9	8
Parapsoriasis	4	6	4
Alopecia mucinosa	5	6	4
Actinic cheilitis	6	6	4
Total measurements	8	44	32

For multiple samples, the data vector was joined to generate a matrix, M, each row representing the data vector for one measurement location.

2.3.2 *Least squares support vector machines*

A milestone of the SVMs algorithm was proposed by Cortes and Vapnik for solving two-group classification problems in 1995.[26] In short, the principle can be interpreted as the idea that the observations in the input space are transformed nonlinearly to a high-dimensional feature space, where an optimal linear

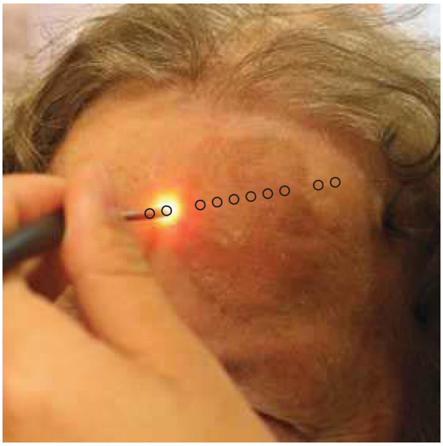

Fig. 2 Example of image showing the measured locations (circles) of a skin tumor (squamous cell carcinoma *in situ*) on the patient's forehead.

separating hyperplane (with a maximized distance between the margins) is constructed with the training data to achieve good separation. The kernel trick realizes the nonlinear feature transformation without explicitly computing the feature mapping function, if given the kernels (i.e., inner product of data point pairs in the feature space). Usually, a quadratic optimization problem (QOP) needs to be solved to determine the optimal hyperplane. SVMs have now been developed also for multiclass separation and function estimation (or regression).[23]

LS-SVM is a simplified and recent derivative version of the standard SVMs,[27] which suffer from a major drawback of high-computational burden for the constrained QOP programming.[28] Instead of solving a QOP, LS-SVM works with solving linear equations. This makes LS-SVM much faster than the standard SVMs.[23,28] In this work, LS-SVM was thus chosen for both regression (quantification of PpIX concentrations and tissue optical properties) and classification of tissue types (optical diagnostics of skin tumors) from the spectroscopic measurements. The readers are referred to the literature elsewhere[23,26,27,29] for the details of the theory of SVMs and LS-SVM.

For LS-SVM, a Gaussian radial basis function kernel was used. Despite the data matrix M containing the spectral observations, there are two additional input parameters needed. They are (1) the kernel parameter, σ, defining the kernel width, and (2) a regularization parameter, γ, determining the trade-off between the training error minimization and smoothness. A simplex algorithm was applied to tune and optimize these two model hyperparameters.[30]

2.3.3 *Ambient light rejection*

The ability to suppress any influences from ambient light was tested with intralipid ink phantoms at a fixed PpIX concentration of 100 nM in the laboratory measurements. Light from a halogen lamp (Photonic Optische Geräte GmbH & Co KG, Vienna, Austria; PL2000) was guided by a fiber optic microscope illuminator, composed of an optical fiber bundle with a ring-light-shaped distal end (Photonics Optische Geräte GmbH & Co KG, Vienna, Austria; PL1000) onto the phantom. To obtain various illumination conditions, the position of the ring-light was adjusted up and down above the sample at a distance of maximal 60 cm, while the sample and probe were kept fixed. The fluence rate of the ambient light at the top surface of the phantoms was measured with a Panlux 2 Electronic Lux Meter (Gossen Foto-u. Lichtmesstechnik GmbH).

2.3.4 *System quantification calibration*

For quantification of PpIX in intralipid ink phantoms under the test on ambient light rejection, the ninth value in the data vector in Fig. 3 was used, which is a ratio

$$R_F = F_{635}/R_{405}, \tag{4}$$

where F_{635} denotes PpIX fluorescence intensity detected from the 635 nm APD channel, indicating the PpIX fluorescence peak under 405-nm excitation. Correspondingly, the reflectance from the 405-nm channel is denoted by R_{405}.

LS-SVM regression was employed to create three nonlinear models to predict $\mu_s'(635)$, blood volume fraction (denoted by [Blood]) and PpIX molar concentration (denoted by [PpIX]) in the intralipid blood phantoms. Each model was made from the preprocessed data matrix M and a corresponding data column

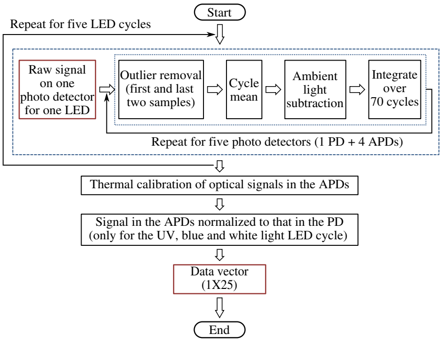

Fig. 3 The flowchart of data preprocessing to retrieve the spectral data for one measurement location on a sample.

consisting of true values. In the data analysis, 269 phantoms were included and one phantom was excluded because of obvious misoperation. Each prediction model was validated by the twofold cross-validation (CV) methodology: the phantom dataset was split into one subset for calibration (training) and the other one for validation (testing). The correlation coefficient, R^2 for the training set, and Q^2 for the testing set, both percent coefficient of variation (Cov, defined as SD/mean), and the percent error (mean ± SD) for each set of predicted quantities were calculated to evaluate the precision of the validation model.

2.3.5 *Clinical quantification validation*

The signals measured from the skin were preprocessed and the APD signals were temperature calibrated prior to normalization with reflectance. The [PpIX], $\mu_s'(635)$, and [Blood] for the tissue samples were predicted by three LS-SVM regression models, where all the phantom datasets were used for training with leave-one-out cross-validation (LOOCV), following the procedure described in Sec. 2.3.4.

2.3.6 *Clinical tissue classification*

The discrimination between normal tissue and tumor lesion was performed on the clinical data using LS-SVM classification for tissue diagnostic purposes. Here, in the classification model, the tissue type was assigned to logical 1 for tumor lesions and 0 for the surrounding healthy tissue according to the histological diagnosis. The model was trained and tested with LOOCV due to the limited number of measurements in the dataset (44 spots on lesions and 32 on normal tissues). No threshold is needed for LS-SVM since the algorithm provides the discrimination automatically.

3 Results

3.1 *Optical Properties of Phantoms*

For the phantoms with 3% to 8% intralipid, $\mu_s'(635)$ was calculated to be 7.7 to 20.4 cm^{-1} from Eq. (3). From the TOF measurement, $\mu_s'(635)$ was determined to be 8.9 cm^{-1} for 3.75% intralipid and $\mu_a(635) = 0.020\ \text{cm}^{-1}$ for 0.25% ink or 0.11 cm^{-1} for 3% blood.

3.2 *Ambient Light Rejection*

How much the performance of the system is affected by the ambient light level is shown in Fig. 4. The raw fluorescence signal in (a) clearly shows increasing levels of disturbance due to the ambient light from the white light lamp for an increased light fluence rate. The light level can be represented by the direct current (DC) level of the fluorescence intensity. The ratio in (b) takes the source power fluctuation into account. For a large variation in the ambient light level (from 15 to 2300 lm/m), the ratio in (c) only exhibits a variation of approximately 12%, showing that our probe system is significantly insensitive to the ambient light with a much higher light level than the scenarios from operation lamps.

3.3 *System Quantification Calibration*

The quantification responses of the LS-SVM regression model with twofold CV to predict $\mu_s'(635)$, [Blood], and [PpIX] for the phantoms are shown in Fig. 5. The correlation coefficients for the training and testing datasets are calculated to exceed 0.990 and 0.983, respectively. The mean percentage error (mPE) of the predicted values is 3% with a maximum of 4% for $\mu_s'(635)$ and 5% with a maximum of 8% for [blood]. For PpIX, the mPE is 8% for all [PpIX] involved and 5% for relatively high [PpIX] ranging from 400 to 1000 nM. Correspondingly, the mean Cov was calculated to be 3% for $\mu_s'(635)$, 7% for [Blood], 11% for all [PpIX], and 6% for higher [PpIX]. It indicates in general a very good quantification performance for a large variation of optical properties and low fluorophore concentrations in the nM regime.

3.4 *Clinical Quantification Validation*

Using the LS-SVM regression model created from the data of the entire phantom dataset, the reduced scattering coefficient at the emission wavelength, blood volume fraction, and PpIX molar concentration of the skin under investigation are shown in Fig. 6. The model predicts in general a higher blood content and higher PpIX concentration for the tumor lesions than the normal skin. The two clusters could be employed to classify tissue types for diagnostic purposes.

3.5 *Clinical Tissue Classification*

The classification responses for discrimination between normal tissue and tumor lesions involved in the clinical study are shown in Fig. 7(a). The LS-SVM model indicates a significant diagnostic capability with 100% accuracy. Figure 7(b) shows an example of fluorescence and reflectance signals at 405-nm excitation for one selected patient.

4 Discussions

One of the particular benefits of our probe is that it has overcome the challenge for the fluorescence spectroscopy system to be used in the operating theater with strong ambient light always present. In the case of brain tumor resection surgery, the surrounding light sources include fluorescence tubes, surgical lamps, and the high-power surgical microscope.[16] The suppression of ambient light of our instrument was achieved by a fast pulse modulation of the excitation source in combination with the detection at the modulation frequency. In this way, the ambient light level is monitored simultaneously and then subtracted from the detected optical signals. This design has two major advantages; first, it significantly improves the signal-to-background ratio in the analyzed signals. A recently published work by Sexton et al. has demonstrated that pulsed excitation light and time-gated detection technique provides superior sensitivity *in vivo* and can realize fluorescence imaging in room light for FGS.[31] However, our system is less expensive, simpler, and safer for the eyes compared to LEDs. The modulation at a kHz frequency regime in our design allows detection of weak fluorescence signal in the presence of strong ambient light up to 2300 lm/m in our phantom experiments (see Fig. 4). An even higher signal-to-background light ratio could be expected with a faster modulation frequency, which should not be any problem to increase to orders of magnitude in-house, even though this level would be sufficient for clinical use. Second, it does not disturb the standard surgical workflow as the previous design,[4,32] as it is necessary neither to employ an umbrella-like cover on the probe shading the tip nor to take a separate background reference measurement.

APDs are employed as photodetectors for fluorescence spectroscopy with weak light signals in our system. The APDs

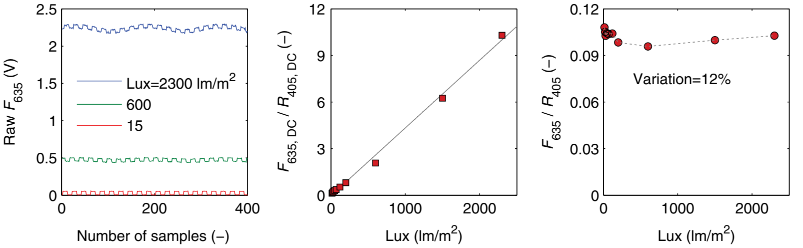

(a) (b) (c)

Fig. 4 Sensitivity of the fluorophore quantification performance to the ambient light level under the 405-nm excitation, modulated by a TTL pulse at 777 Hz, for a fixed PpIX concentration of 100 nM in an intralipid ink phantom with $\mu_a = 0.020\ \text{cm}^{-1}$ and $\mu_s' = 8.90\ \text{cm}^{-1}$ at 635 nm. (a) Example of raw fluorescence signals under different ambient light conditions. The sinusoidal pattern of the ambient light can be easily seen for a high lux. For clarity, only signals for a few of the lux levels are shown here. (b) Ratio of the DC level of F_{635} and DC level of R_{405} and (c) the ratio of F_{635}/R_{405} versus the ambient light level with a maximum variation of 12%. Solid line in (b) indicates a linear fit to the data.

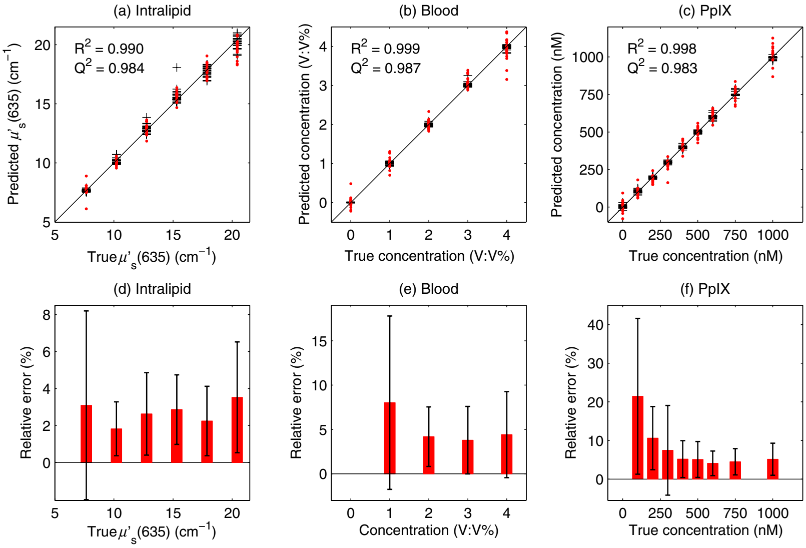

Fig. 5 (a–c) PpIX quantification in intralipid blood phantoms with various optical properties using LS-SVM regression with twofold cross-validation (135 samples for training and 134 samples for validation). The dark solid lines indicate the diagonal of best prediction (coordinates 1:1). R^2 and Q^2 are the correlation coefficients between the true parameter and model response for training and validation, respectively. (d–f) Relative error of the predicted parameters (mean ± SD). The data have not been temperature calibrated because of a long waiting time of ∼4 h prior to measurement.

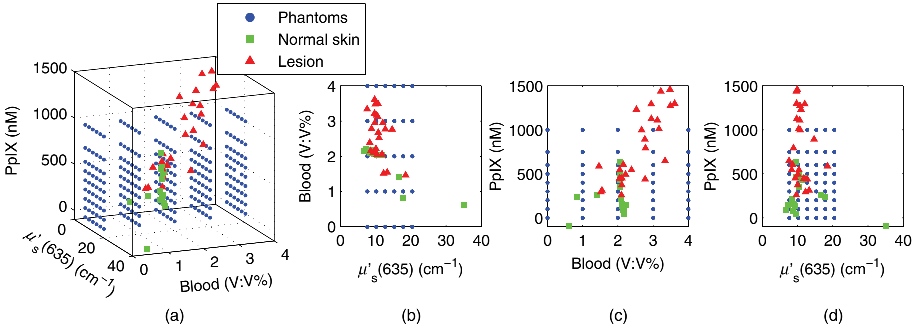

Fig. 6 System quantification validation to predict the scattering coefficient at the emission wavelength, blood content, and fluorophore concentration of the skin from the data measured at the clinic. The LS-SVM model was created and optimized by leave-one-out cross-validation (LOOCV) from 269 phantoms with different amounts of scatters, absorbers, and fluorophores (blue dots). The testing dataset includes measurements of 76 locations in total (44 skin tumor lesions and 32 normal skin). (a) Three-dimensional scatter plots and (b)–(d) are the corresponding two-dimensional projections. The model predicts in general a higher blood content and higher PpIX concentration for the tumor lesions than the normal skin.

possess high light-detection sensitivity (gain ~50) with high dynamic range as well as fast readout capability [no serial readout from a large charge-coupled device (CCD) chip]. The improved sensitivity of APDs over conventional PDs and spectrometers together with the modulation scheme enables efficient removal of the ambient light, providing an exquisite sensitivity to PpIX fluorescence. In our phantom validation study, PpIX could be precisely quantified on the order of nanomolars in the presence of high scattering and absorption. Such concentrations are far below expected tumor tissue concentrations in clinical scenarios. For example, the absolute PpIX concentration was found to be 5.8 ± 4.8 μm (mean ± SD) in the human high-grade glioma tissue and 0.2 ± 0.4 μm for grade III brain tumors.[33] For ALA-mediated skin PDT, topical application of ALA was reported to result in a PpIX concentration of 1 to 2 μm for various human skin malignancies.[34] Due to the high fluorophore sensitivity of our system, it is possible to reduce the ALA dose for intracranial tumor fluorescence purposes (commonly used at 20 mg/kg body weight[21]), and thus minimize the adverse side effects in patients undergoing surgery and avoid affecting normal brain. Owing to the higher photosensitivity of APD, it is also possible to reduce the power of the excitation light in order for less fluorophore photobleaching, which could perturb the optical diagnostics.

A slight complication with this setup is that APDs suffer from their extremely high sensitivity to temperature (the sensitivity varies typically a couple of percent per degree Celsius). This effect originates from its operation with high reverse bias voltage to achieve desired high photosensitivity. This temperature variation issue has been effectively solved in our system by thermal calibration with compact thermistors rather than direct control of APD temperature. Such a design does not significantly increase the instrument costs and complexities in surgical operation.

It is well known that one main challenge of fluorescence-based diagnostic methods comes from varying light attenuation by the tissue. Figure 7(b) shows that the optical properties vary much for different locations, leading to a change in the reflectance at the excitation wavelength. This results in the difficulties in tissue classification using a single excitation wavelength (e.g., see Location 5). In our system, multiple light sources are employed for fluorescence and reflectance spectroscopy. The monitoring of the reflectance is aimed to provide signals to compensate the detected fluorescence signals for tissue optical properties as well as to correct for source power fluctuation by normalizing the APD signals to that from the PD. In the phantom calibration experiments, a wide range of both scattering [$\mu_s'(635) = 7.7$ to $20.4\ \mathrm{cm}^{-1}$] and absorption (0% to 4% blood) have been covered. The results of the multivariate analysis (i.e., nonlinear LS-SVM regression) indicate that despite the large variation in the optical properties, the detected fluorescence signals correlate linearly to the true fluorophore concentrations (see Fig. 5). Both the significantly high correlation coefficient (>0.98) and the low percent error in the predicted [PpIX] (<5% for $400\ \mathrm{nM} \le [\mathrm{PpIX}] \le 1\ \mu\mathrm{M}$) show that the LS-SVM regression model works pretty well to accurately predict the fluorophore concentrations in the presence of large optical properties variations. Our results are in general better than those in the literature using fluorescence spectroscopy. The comparisons of the quantification performance for PpIX in tissue phantoms with the other designs reported are summarized in Table 2. Kim et al.[35] used a fiber optic probe and an analytical equation derived from the diffusion theory to estimate [PpIX]. They reported a root mean square deviation from mean of 10.1% and a Cov value of 14% at a fixed [PpIX] of 5 μg/ml (or 8.9 μM). A recently published work by Valdes et al.[36] reported a complementary metal–oxide–semiconductor (CMOS) imaging system to measure [PpIX] with a CMOS array. They obtained a mean error of 6% and a Cov of <10% for [PpIX] in the range between 36 nM and 8.9 μM. However, the optical properties of the phantoms vary less than those in our study. Moreover, slight limitations of their study include the priori knowledge of the optical properties at the excitation wavelength and the inherent limitations that certain assumptions had to be made in the diffusion model. Besides the fluorophore concentration, our LS-SVM regression model can also accurately quantify the reduced scattering coefficient and blood content of the media. Figure 5 indicates that our combined fluorescence/reflectance probe, in addition to obtaining the [PpIX] accurately, has also achieved a slightly higher quantification accuracy (relative error <3% for μ_s' and 4% for [Blood]) than another recently published study based on spatially resolved diffuse reflectance.[9] In their study, the mPE of μ_s' and μ_a values was accurate to 4.3% and 5.4%, respectively, when compared with integrating sphere estimates.

Other challenges of the fluorescence technique include its superimposition with tissue autofluorescence and complex tissue structures, which may also aggravate the problem of inaccurate fluorophore quantification and thereby tissue diagnostics. There is apparently no doubt that adequate information should

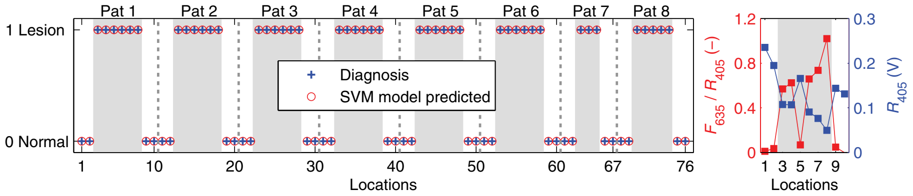

(a) (b)

Fig. 7 (a) Classification performance of the diagnoses of skin lesions using LS-SVM with LOOCV. The model discriminates successfully in 100% of the cases. (b) As an example, the reflectance signal and the ratio of drug fluorescence peak and reflectance at the 405-nm excitation for one selected patient (Pat 2) are shown. Note that Location 5 has a low normalized fluorescence signal, which might be a result of low blood content (high reflectance) rather than a low PpIX concentration.

Table 2 Comparison of the quantification performance for PpIX in tissue phantoms in this work and the other designs reported.

	This work		Kim et al. (Ref. 35)	Valdes et al. (Ref. 36)
System design	Fiber optic probe		Fiber optic probe	CMOS camera
Quantification approach	Multivariate analysis (LS-SVM)		Diffusion theory	Diffusion theory
Number of phantoms	134	75	54	54
[PpIX] (nM)	100 to 1000	400 to 1000	8900	36 to 8900
mPE[a] (%)	8	5	—	6
mCov[b] (%)	11	6	14	<10
R^2[c]	0.983	—	0.976	0.92
$\mu_s'(635)$ (cm^{-1})	7.7 to 20.4	—	8.7 to 14.5	

[a] mPE stands for mean percent error.

[b] Cov stands for mean coefficient of variation.

[c] R^2 is the correlation coefficient.

be provided for diagnostics in clinical practice. In our design, 365 and 405 nm can excite tissue autofluorescence which has the potential to provide extra tissue structure information. Meanwhile, the drug fluorescence is superimposed with tissue autofluorescence at the 405-nm excitation wavelength. All the factors mentioned above have been taken into account by the multivariate analysis of the clinical data, where no hypothesis for the light model needs to be made. As shown in Fig. 6, generally very realistic quantification results have been achieved in terms of a higher blood content and higher PpIX concentration for the tumor lesions than the normal skin. The obtained [PpIX] is consistent with the values reported for various human skin malignancies with topically applied ALA.[34] Such clusters could be used for tissue classification purposes. However, one location for normal skin was predicted to have a much higher $\mu_s'(635)$ (>30 cm^{-1}) than the others, which is obviously not likely to be true. In principle, a much larger calibration dataset is required to cover all the possible parameters to be studied in order to improve the quantification performance of the probe for clinical *in vivo* studies.

When the *in vivo* clinical data from the skin lesions were employed to train the nonlinear LS-SVM model for tissue classification, 100% diagnostic accuracy was obtained, as can be seen in Fig. 7(a). It again indicates complicated nonlinear dependency of the drug fluorescence signal of many other factors rather than only the fluorophore concentration. A similar study on skin basal cell carcinomas by Thompson et al. using fluorescence/diffuse reflectance spectroscopy together with a linear singular value decomposition analysis yielded diagnostic accuracy of 87%.[37] Such a comparison suggests the potential of using the probe with multiple sources and nonlinear analysis of the spectral data to aid tissue diagnosis.

The results of the clinical data shown in this paper (Figs. 6 and 7) are still somewhat preliminary as the database is still small and under development. A large and representative calibration dataset is a common prerequisite for all multivariate analysis–based methods. The presented results, however, already give a good indication of what might be achievable. Figure 7 indeed shows significant discrimination ability even with the small dataset collected so far. The obtained clusters in Fig. 6, if combined with a proper classification method, could most certainly also provide valuable diagnostic information. Again, the values obtained cannot be considered very accurate though, in this case due to some differences in the tissue phantoms used for the training set and human tissue with different types of tumors used in the evaluation. The identified differences include tissue autofluorescence and blood oxygen saturation (the ratio between oxy- and deoxyhemoglobin concentrations). Therefore, we did not proceed to discriminate tissue type in this study beyond what is presented in Fig. 6, illustrating its potential for quantification of both fluorophore concentration and tissue optical properties. To fully evaluate the potential of the technique, future studies will be based on clinical data for both training and evaluation. Such a study will, in addition, require a much increased set of data to ensure fully representative data.

A slight limitation of our instrument is that the delivery fibers for different light sources at the fiber probe tip are aligned in a circle with a diameter of approximately 2.3 mm. This means that the interrogation volume is not exactly the same for each light source. In case of inhomogeneous tissue, especially tumors of small size and irregular tissue structure, it would lead to an inaccurate quantification of fluorophores and thus wrong optical diagnosis. In future clinical studies, it would be good to replace the current probe with dual fibers at the probe tip in order to minimize the probe volume.

From a light source perspective, there might be other reasons for the quantification error in our probe system. A white LED is employed to measure the diffuse reflectance at wavelengths of interest, in order to compensate for tissue optical properties. Despite the detection bands at 405, 530, and 635 nm, one of the other two bands at 470 nm allows to monitor a strong tissue autofluorescence following 365-nm excitation, while 660 nm provides a possibility to monitor photobleaching of porphyrins through the photoproducts. In fact, the white LED consists of a blue LED peaked at 470 nm with a Ce:YAG crystal in front, emitting broadband yellow light from 500 to 700 nm. It is possible that this elastic light tail toward long wavelengths leaks into the fluorescence bands. To minimize such leakage, the white LED should have a short-pass filter, e.g., UG1 or UG11.

In addition, the fluorescence of the Ce:YAG crystal is extremely efficient and sometimes not negligible. Therefore, when the 365- and 405-nm LEDs are lit up, the elastic violet light will scatter into both the collection fiber and the fiber connecting the white LED. The latter could convert to yellow light by the crystal, travel back to the tissue sample, and then superimpose on the tissue and drug fluorescence. Ideally this potential issue could be solved in the future by equipping the white LED with a long-pass GG475 filter.

Further improvements could be made to explore the diagnostic potential of the probe system. An electric high-pass alternating current (AC) filter could be added in each transimpedance amplifier, making the system blind to the DC signal level prior to the analog-to-digital conversion in the DAQ board. This would thus take use of the full dynamic range of the DAQ without saturating the detector for high signal levels. Furthermore, the green and red LEDs could be easily replaced with additional excitation bands (e.g., at 445 nm) to evaluate the effects of tissue oxygenation over the UV–visible spectrum[38] and/or acquire multiexcitation fluorescence in order to form a two-dimensional excitation emission matrix.[39] It has the potential to improve cancer diagnostics by providing absorption and fluorescence characteristics of normal and abnormal tissues.[39,40]

Point measurements are usually time consuming. However, the probe presented in this work is not intended for tumor delineation for the entire tumor border, especially in open brain surgery. It is instead meant to be used in combination with other systems, for instance, an intraoperative ultrasonic navigation system and fluorescence surgical microscope.[5] This is to say, it is meant as a complement to microscopy to check only those uncertain sites which emit very weak fluorescence signals from the tumor tissue (often invisible to the surgeon's eyes).

In conclusion, we present a fiber optic probe instrument with fluorescence/reflectance spectroscopy for therapy guidance and monitoring. It is meant as a complement to the state-of-the-art neurosurgical fluorescence microscopy for FGS of brain tumor using 5-ALA–induced PpIX as a fluorescence contrast agent. The probe is clinically adapted to minimize the disruption of the standard surgical workflow. Multiple sources using LEDs with fast pulse modulation and detection of the signal strength only at the modulation frequency enable precise quantification of the fluorophore concentration, tissue optical properties, and ambient light suppression. We have shown that the probe system is insensitive to strong ambient light up to $2300\ \mathrm{lm/m^2}$. Validation measurements of tissue phantoms using LS-SVM regression demonstrate that even with large variations in phantom optical properties, a low quantification error of <5% has been obtained for PpIX concentration ranging from 400 to 1000 nM, which is far below the concentration in the high-grade human brain tissue samples. The LS-SVM classification model yields 100% diagnostic accuracy for *in vivo* skin tumors with topically applied ALA. In principle, the probe is generic to quantify fluorophores other than PpIX in many tissue types.

Acknowledgments

The authors gratefully acknowledge Professor Karin Wårdell, Dr. Neda Haj-Hosseini, and M.D. Johan Richter for the critically important discussions on the clinical adaptions. We also thank Sören Johansson and Alfi Shaharin for conducting the TOF measurements of tissue phantoms. We also thank Professor Katarina Svanberg for her valuable discussions and Åke Johansson for his advice and efforts on the electronic components. This work was supported by the Swedish Foundation for Strategic Research (SSF), the Swedish Research Council (VR), the Swedish Governmental Agency for Innovation Systems (Vinnova) under Grant No. 331-2006-7661, a Linnaeus Research Grant to the Lund Laser Center, LaserLab Europe JRA project Biopthical (Contract No. EC-GA 284464), and Elekta AB, Stockholm, Sweden.

References

1. U. Utzinger and R. R. Richards-Kortum, "Fiber optic probes for biomedical optical spectroscopy," *J. Biomed. Opt.* **8**(1), 121–147 (2003).
2. S. Andersson-Engels et al., "Clinical recording of laser-induced fluorescence spectra for evaluation of tumour demarcation feasibility in selected clinical specialities," *Lasers Med. Sci.* **6**(4), 415–424 (1991).
3. C. af Klinteberg et al., "Compact medical fluorosensor for minimally invasive tissue characterization," *Rev. Sci. Instrum.* **76**(3), 034303 (2005).
4. N. Haj-Hosseini et al., "Optical touch pointer for fluorescence guided glioblastoma resection using 5-aminolevulinic acid," *Laser Surg. Med.* **42**(1), 9–14 (2010).
5. J. C. Richter et al., "Fluorescence spectroscopy measurements in ultrasonic navigated resection of malignant brain tumors," *Laser Surg. Med.* **43**(1), 8–14 (2011).
6. P. A. Valdes et al., "Combined fluorescence and reflectance spectroscopy for in vivo quantification of cancer biomarkers in low- and high-grade glioma surgery," *J. Biomed. Opt.* **16**(11), 116007 (2011).
7. D. J. Cappon et al., "Fiber-optic probe design and optical property recovery algorithm for optical biopsy of brain tissue," *J. Biomed. Opt.* **18**(10), 107004 (2013).
8. T. M. Baran, M. C. Fenn, and T. H. Foster, "Determination of optical properties by interstitial white light spectroscopy using a custom fiber optic probe," *J. Biomed. Opt.* **18**(10), 107007 (2013).
9. A. Kim et al., "A fiberoptic reflectance probe with multiple source-collector separations to increase the dynamic range of derived tissue optical absorption and scattering coefficients," *Opt. Express* **18**(6), 5580–5594 (2010).
10. J. Swartling et al., "System for interstitial photodynamic therapy with online dosimetry: first clinical experiences of prostate cancer," *J. Biomed. Opt.* **15**(5), 058003 (2010).
11. S. C. Kanick et al., "Integration of single-fiber reflectance spectroscopy into ultrasound-guided endoscopic lung cancer staging of mediastinal lymph nodes," *J. Biomed. Opt.* **15**(1), 017004 (2010).
12. V. R. Sauvage et al., "Multi-excitation fluorescence spectroscopy for analysis of non-alcoholic fatty liver disease," *Laser Surg. Med.* **43**(5), 392–400 (2011).
13. M. R. Austwick et al., "Scanning elastic scattering spectroscopy detects metastatic breast cancer in sentinel lymph nodes," *J. Biomed. Opt.* **15**(4), 047001 (2010).
14. G. M. Palmer et al., "Monte Carlo-based inverse model for calculating tissue optical properties. Part II: application to breast cancer diagnosis," *Appl. Opt.* **45**(5), 1072–1078 (2006).
15. G. M. Palmer et al., "Quantitative diffuse reflectance and fluorescence spectroscopy: tool to monitor tumor physiology in vivo," *J. Biomed. Opt.* **14**(2), 024010 (2009).
16. M. Brydegaard et al., "Photobleaching-insensitive fluorescence diagnostics in skin and brain tissue," *IEEE Photonics J.* **3**(3), 407–421 (2011).
17. P. A. Valdes et al., "Quantitative fluorescence in intracranial tumor: implications for ala-induced ppix as an intraoperative biomarker," *J. Neurosurg.* **115**(1), 11–17 (2011).
18. B. Kruijt et al., "In vivo quantification of chromophore concentration using fluorescence differential path length spectroscopy," *J. Biomed. Opt.* **14**(3), 034022 (2009).
19. B. W. Pogue et al., "Review of neurosurgical fluorescence imaging methodologies," *IEEE J. Sel. Top. Quantum Electron.* **16**(3), 493–505 (2010).
20. M. Hefti et al., "Fluorescence-guided surgery for malignant glioma: a review on aminolevulinic acid induced protoporphyrin IX photodynamic diagnostic in brain tumors," *Curr. Med. Imaging Rev.* **6**(4), 254–258 (2010).

21. M. J. Colditz, K. V. Leyen, and R. L. Jeffree, "Aminolevulinic acid (ALA)-protoporphyrin IX fluorescence guided tumour resection. Part 2: theoretical, biochemical and practical aspects," *J. Clin. Neurosci.* **19**(12), 1611–1616 (2012).
22. W. Stummer et al., "Fluorescence-guided resection of glioblastoma multiforme by using 5-aminolevulinic acid-induced porphyrins: a prospective study in 52 consecutive patients," *J. Neurosurg.* **93**(6), 1003–1013 (2000).
23. K. Pelckmans et al., "LS-SVMlab: LS-SVMlab: a MATLAB/C toolbox for Least Squares Support Vector Machines," (2011), http://www.esat.kuleuven.be/sista/lssvmlab/ (16 August 2011).
24. S. T. Flock et al., "Optical properties of intralipid: a phantom medium for light propagation studies," *Laser Surg. Med.* **12**(5), 510–519 (1992).
25. E. Alerstam, S. Andersson-Engels, and T. Svensson, "White Monte Carlo for time-resolved photon migration," *J. Biomed. Opt.* **13**(4), 041304 (2008).
26. C. Cortes and V. Vapnik, "Support-vector networks," *Mach. Learn.* **20**, 273–297 (1995).
27. J. A. K. Suykens, T. Van Gestel, and J. De Brabanter, *Least Squares Support Vector Machines*, World Scientific, Singapore (2002).
28. H. Wang and D. Hu, "Comparison of SVM and LS-SVM for regression," *IEEE Int. Conf. Neural Networks Brain*, Vol. 1, 279–283 (2005).
29. V. N. Vapnik, *Statistical Learning Theory*, 1st ed., Wiley, New York (1998).
30. K. De Brabanter, J. Suykens, and B. De Moor, "Nonparametric regression via StatLSSVM," *J. Stat. Software* **55**(2), 1–21 (2013).
31. K. Sexton et al., "Pulsed-light imaging for fluorescence guided surgery under normal room lighting," *Opt. Lett.* **38**(17), 3249–3252 (2013).
32. M. A. Ilias et al., "Evaluation of a fiber-optic fluorescence spectroscopy system to assist neurosurgical tumor resections," *Proc. SPIE*, **6631**, 66310W (2007).
33. A. Johansson et al., "5-aminolevulinic acid-induced protoporphyrin IX levels in tissue of human malignant brain tumors," *Photochem. Photobiol.* **86**(6), 1373–1378 (2010).
34. C. Fritsch et al., "Optimum porphyrin accumulation in epithelial skin tumours and psoriatic lesions after topical application of delta-aminolaevulinic acid," *Br. J. Cancer* **79**(9–10), 1603–1608 (1999).
35. A. Kim et al., "Quantification of in vivo fluorescence decoupled from the effects of tissue optical properties using fiber-optic spectroscopy measurements," *J. Biomed. Opt.* **15**(6), 067006 (2010).
36. P. A. Valdes et al., "System and methods for wide-field quantitative fluorescence imaging during neurosurgery," *Opt. Lett.* **38**(15), 2786–2788 (2013).
37. A. J. Thompson et al., "In vivo measurements of diffuse reflectance and time-resolved autofluorescence emission spectra of basal cell carcinomas," *J. Biophotonics* **5**(3), 240–254 (2012).
38. G. M. Palmer et al., "Optimal methods for fluorescence and diffuse reflectance measurements of tissue biopsy samples," *Laser Surg. Med.* **30**(3), 191–200 (2002).
39. M. Brydegaard et al., "Versatile multispectral microscope based on light emitting diodes," *Rev. Sci. Instrum.* **82**(12), 123106 (2011).
40. R. A. Zângaro et al., "Rapid multiexcitation fluorescence spectroscopy system for in vivo tissue diagnosis," *Appl. Opt.* **35**(25), 5211–5219 (1996).

Haiyan Xie is currently a PhD student in the biophotonics group at the Department of Physics, Lund University, Lund, Sweden. Her research interests include development of optical spectroscopy and multispectral imaging systems for cancer diagnostics.

Zhiyuan Xie got her master's degree from the Department of Physics, Lund University, in 2013. The majority of this work was performed during her diploma work at the biophotonics group.

Monirehalsadat Mousavi obtained her master's degree from Lund University in 2013. She is currently a PhD student under the supervision of professor Stefan Andersson Engels. Her research is focused on using upconverting nanoparticles for diffuse optical imaging of turbid media.

Niels Bendsoe received his PhD degree in medical science, dermatology, and venereology in 2003 and became an associate professor at the Department of Dermatology at Skåne University Hospital in 2012. He has been working at the Dermatology Clinic, Lund University Hospital, since 1981 and is the chief consulting dermatologist. He has been involved in the development of photodynamic therapy and tumor detection both in experimental studies as well as in the clinic. He is a board member in the Lund University Medical Laser Centre.

Mikkel Brydegaard received his master's degree in electrical engineering in 2007 and doctorate at atomic physics from Lund University in 2013. Since 2001, he persistently worked in developing countries developing realistic instrumentation for applied optical spectroscopy. During doctoral studies he specialized in broadband biomedical fluorescence and interpretation with multivariate and chemometrics. Recently, he has worked part time with laser radar diagnostics of atmospheric fauna at Lund University and part time with hyperspectral imaging at Norsk Elektro Optikk.

Johan Axelsson received his PhD in atomic physics in 2010 from the Department of Physics, Lund University. He is currently a research associate in the biophotonics group at Atomic Physics, Lund University. His research focuses on biomedical optics, medical imaging, optical tomography, and Cerenkov emission imaging with applications in radiation treatment monitoring.

Stefan Andersson-Engels received his MSc and PhD degrees in engineering physics and physics from Lund University in 1985 and 1990, respectively. He was a postdoctoral at McMasters University in Canada from 1990 to 1991. He has since been at Lund University and became a full professor in 1999. He is presently the director of Lund University Medical Laser Centre and the deputy head of the Atomic Physics Division at Lund University. His research interest includes tissue optics as well as applications of light in biomedical diagnostics and treatments.

PAPER III

Increasing depth penetration in biological tissue imaging using 808-nm excited $Nd^{3+}Yb^{3+}Er^{3+}$-doped upconverting nanoparticles

H. Söderlund, M. Mousavi, H. Liu, S. Andersson-Engels.

Journal of Biomedical Optics **20(8),086008**, (2015).

Journal of Biomedical Optics 20(8), 086008 (August 2015)

Increasing depth penetration in biological tissue imaging using 808-nm excited $Nd^{3+}/Yb^{3+}/Er^{3+}$-doped upconverting nanoparticles

Hugo Söderlund,[†] Monirehalsadat Mousavi,[†] Haichun Liu, and Stefan Andersson-Engels*
Lund University, Biophotonics Group, Department of Physics, P.O. Box 118, SE-22100 Lund, Sweden

Abstract. Ytterbium (Yb^{3+})-sensitized upconverting nanoparticles (UCNPs) are excited at 975 nm causing relatively high absorption in tissue. A new type of UCNPs with neodymium (Nd^{3+}) and Yb^{3+} codoping is excitable at a 808-nm wavelength. At this wavelength, the tissue absorption is lower. Here we quantify, both experimentally and theoretically, to what extent Nd^{3+}-doped UCNPs will provide an increased signal at larger depths in tissue compared to conventional 975-nm excited UCNPs. *© 2016 Society of Photo-Optical Instrumentation Engineers (SPIE)* [DOI: 10.1117/1.JBO.20.8.086008]

Keywords: upconverting nanoparticles; tissue optics; deep tissue imaging.
Paper 150191RR received Mar. 23, 2015; accepted for publication Jul. 15, 2015; published online Aug. 13, 2015.

1 Introduction

Upconverting nanoparticles (UCNPs) are becoming highly interesting in the field of biophotonics due to their upconverting properties supporting minimal autofluorescense background under near-infrared excitation.[1] Other beneficial aspects of UCNPs include high-imaging resolution and relatively large penetration depth in tissues of both excitation and emission light, as well as the absence of photobleaching and photoblinking.[2] However, there are still challenges with UCNPs, such as low quantum yield compared to traditional downconverting fluorophores and a nonoptimal attenuation of the excitation light in tissue.[2] Thus it is beneficial to improve these aspects of the UCNPs to increase overall efficiency.

In most UCNPs, there is a sensitizer and an activator, where the sensitizer absorbs the excitation photons and transfers the energy to the activator in order to achieve upconversion. As of today, ytterbium (Yb^{3+})-sensitized and Tm^{3+}- or Er^{3+}- activated $NaYF_4$ UCNPs are promising contrast agents for bioimaging and are being intensively studied.[2–5] They both exhibit several strong luminescence emission bands. In tissue imaging, the emission bands at 800 and 650 nm are preferentially used as they are within the tissue optical window enabling good light penetration in tissue. Both these bands can be excited with 975-nm light due to the Yb^{3+} absorption. These wavelengths all match the optical window for biological tissue, well known to be between 600 and 1300 nm.[6] While the Yb^{3+}/Tm^{3+} $NaYF_4$ UCNPs (Yb:UCNPs) operate within this region, Yb^{3+} cannot be considered as an optimal sensitizer for deep tissue imaging due to the increased absorption of light in tissue due to water within the tissue optical window around 975 nm.[7] Recently, Nd^{3+}/Yb^{3+}-cosensitized and Er^{3+}-activated $NaYF_4$ UCNPs (Nd:UCNPs) have been introduced with an excitation wavelength at 808 nm and emission at 650 nm.[8] The motivation for the neodymium (Nd^{3+}) codoping is to provide better light penetration of the excitation light and provides possibilities to excite the UCNPs deeper into tissue. The water absorption is greatly reduced at the excitation wavelength of 808 nm as compared to at the excitation wavelength of 975 nm which is used for the conventionally employed UCNPs.[7] Since the upconversion process requires two or more excitation photons,[9] it should be more essential to minimize the attenuation of the excitation than the emission light in order to optimize the strength of the detected signal. Thus, by using an excitation wavelength with reduced absorption in tissue, it should be possible to increase the signal from deep locations in tissue.

The Nd:UCNPs allow Nd^{3+} to absorb the incoming photons and transfer the energy to the second sensitizer, Yb^{3+}, which subsequently transfers the energy to the activator in order to achieve upconversion.[8] The energy transfer efficiency between the Nd^{3+} and Yb^{3+} ions has been reported to be as high as 70%.[10] Meanwhile, Nd^{3+} has a larger absorption cross-section at 808 nm compared to that of Yb^{3+} at 975 nm. Furthermore, by using Nd:UCNPs in a core-shell structure, quenching of the UC emission due to unwanted energy transfer from the activator to Nd^{3+} ions is reduced, resulting in an optimal upconversion efficiency comparable to that of the Yb:UCNPs.[8] Most interestingly, the excitation wavelength at 808 nm will have a greatly reduced water absorption compared to that at 975 nm ($0.02\ \mathrm{cm}^{-1}$ compared to $0.46\ \mathrm{cm}^{-1}$ for 100% water).[11]

In addition to reducing imaging depth, there have also been several reports stating that 975-nm excited UCNPs cause overheating due to the relatively high absorption by water for this wavelength.[2,10,12,13] Nd:UCNPs will drastically reduce any heating due to the reduced water absorption at 808 nm compared to at 975 nm.[8] The present report is intended to quantify the advantages in tissue penetration for Nd:UCNPs compared to that of Yb:UCNPs. Here, we thoroughly investigate the imaging depth advantages of $NaYF_4:Yb^{3+}/Er^{3+}/Nd^{3+}$ UCNPs compared to using $NaYF_4:Yb^{3+}/Tm^{3+}$ UCNPs by performing

---

*Address all correspondence to: Stefan Andersson-Engels, E-mail: stefan.andersson-engels@fysik.lth.se

[†] Authors contributed equally on this paper.

measurements in tissue phantoms in addition to Monte Carlo (MC) simulations for varying tissue compositions.

2 Experiment

2.1 *Materials*

The core-shell UCNPs used in the study were synthesized in-house. They are characterized in detail elsewhere.[14] The measurements conducted for this report were performed in tissue phantoms, containing 3% bovine blood, 3% intralipid-20%, and the remaining 94% tap water. The blood was purchased at the local supermarket in a frozen container and was stored in the refrigerator prior to the measurements. The blood was used within a week after purchase. The intralipid was of the brand Fresenius Kabi and contained intralipid 200 mg/ml. It was stored in the refrigerator in sealed containers before use. The water used in the tissue phantom was regular tap water. A cylindrical container made of glass with a diameter of 140 mm was used for the tissue phantom. The measurements were performed in transillumination geometry, as seen in Fig. 1. The thickness of the tissue phantom was 18 mm. Diode lasers (Thorlabs L808P1WJ for the 808-nm laser and Thorlabs L975P1WJ for the 975-nm laser) were used for excitation. The diode lasers were powered and temperature controlled by Thorlabs LDC 220 C and Thorlabs TED 200 C, respectively. The laser light was coupled into a 400 μm optical fiber and guided to the tissue phantom. The distal end of the optical fiber was imaged on the bottom surface of the tissue phantom by a 2.0 cm focal length lens to obtain a top-hat profile of the illumination spot. The diameter of the illumination spot was 5.0 and 7.0 mm for 808 and 975 nm, respectively. A bandpass filter (Omega Optical, NC 146753 Z800/40X for the 808-nm laser and 712M000040 BP-0975-056 for the 975-nm laser) was placed in front of the collimation lens in order to remove unwanted sidelobes of the laser light. The two samples containing the Nd:UCNPs and the Yb:UCNPs particles, respectively, were prepared by adding UCNPs into approximately 15 μl epoxy glue to create 3-mm diameter spherical samples. These UCNPs-containing glue-samples were cured on 0.148-mm transparent fishing thread and later attached to a custom-made metal holder, attached to a translator stage, allowing for positioning the UCNPs at different depths with a resolution of 20 μm. Above the container, the emitted light was collected by a lens (25-mm focal length and $f/0.95$, Xenon, Schneider-Kreuznach, Germany) connected to a filter tube which, in turn, was attached to an air-cooled CCD camera (Andor iXon$_+$, Belfast, Ireland). The filter tube used two achromatic doublet $f = 75$-mm lenses (Thorlab, ARC: 650 to 1050 nm) to create parallel light through the filters, in order to effectively block out unwanted light while transmitting the emission light.[15,16] For the Nd:UCNPs 650-nm emission, the filters, SP OD4—750 nm (Edmund Optics), BP 650 nm × 50 nm OD4 (Edmund Optics), and RED-50S (Chroma), were used to clean the emission while for the Yb:UCNPs 800-nm emission, the 900-nm short pass filter (Omega Optical, BSP 156613) and two 800 nm (Omega Optical, BP50 156612) were employed. These filters ensured that only the emission light from the selected bands contributed to the recorded signal.

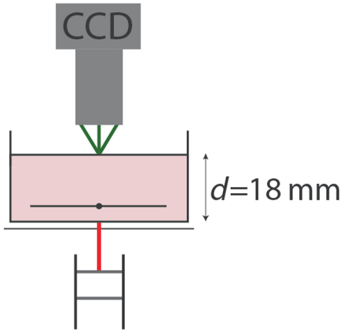

Fig. 1 Instrumental setup for the transillumination measurements. From bottom to top, fiber-coupled excitation laser (808 or 975 nm), collimation lens with bandpass filter, glass container with 18-mm thick tissue phantom, containing an upconverting nanoparticle (UCNP) inclusion, objective lens, filter tube, and camera.

2.2 *Methods*

For a comparison of two different UCNPs, it is necessary to ensure they both operate in an unsaturated regime in all measurements in order to enable general conclusions from the comparison. The aim of the first measurements was to find an excitation intensity regime in which the particles were not saturated. When a nonsaturated region was found, depth measurements were performed with the corresponding nonsaturated excitation intensity. Here, the excitation intensity was kept constant while the depth of the sample into the tissue phantom was increased in a stepwise manner. An image was taken for each step, with a corresponding background image without the UCNP sphere subtracted.

2.2.1 *Power dependence*

A power dependence measurement was performed at a depth of 3.0 mm into the phantom, the same as the initial depth for the following depth measurements. Here, zero depth is established when the sample is just in contact with the bottom of the container. The power was varied from 50 to 140 mW with a factor of 1.1 between each step for the Nd:UCNPs. The spotsize at the surface of the phantom was 5.0 mm in diameter. For the Yb:UCNPs, the power was varied from 20 to 73 mW with a factor of 1.1 between each step with a spotsize of 7.0 mm in diameter. The exposure time was set to 9.9 s for each image for both sample measurements; an electron-multiplying (EM) gain of 10 for the Nd:UCNPs and an EM gain of 100 for the Yb:UCNPs were employed. A binning of 8 × 8 pixels was used for both samples. A final image without any UCNP sample was recorded in order to effectively subtract the background from each recorded image. The images were analyzed in MATLAB where the value of each pixel was summed up for each image and plotted as a function of excitation intensity (mW/cm^2).

2.2.2 *Depth measurements*

Depth measurements were conducted under nonsaturation excitation conditions, as confirmed by the power dependence measurements. The samples were positioned at a starting depth of 3.0 mm into the 18-mm deep tissue phantom, and the depth was increased stepwise with 0.5 mm per step until a total depth of 10 mm was reached. The zero depth was as defined above as when the sample was just in contact with the bottom of the glass container. The excitation power was 70 mW for both lasers, corresponding to an intensity of 407 and 207 $\mathrm{mW/cm^2}$ for the 808- and 975-nm lasers, respectively. The spotsize was again 5.0 and 7.0 mm in diameter for the 808- and 975-nm lasers, respectively. For each depth position, an image was recorded. Directly after completing the measurements at all depths, a sample-free image was recorded in order to enable subtraction of the background from each recorded image. The same setup as in the power dependence measurements was used. Every image was recorded using an acquisition time of 9.9 s. A binning of 8×8 pixels was employed and the EM gain was set to 300 at the camera for all recordings. The images were analyzed in MATLAB and a square of 10×10 pixels was summed up, with the largest value pixel in the center of the square.

2.2.3 *Monte Carlo simulations*

To investigate how the potential signal gain for the Nd:UCNPs versus the Yb:UCNPs was influenced by the tissue composition, MC simulations of the transport of excitation and emission light in tissue were employed. The MC code used for this purpose was CUDAMCML.[17] The absorption coefficients for the chromophores used in the measurements, i.e., blood, fat, water, and melanin, were extracted from relevant publications.[7,18–20] The wavelengths of interest were 975, 808, and 650 nm, which include the excitation and emission wavelengths for both UCNPs employed.

The first simulation was performed aiming for the same optical properties as the tissue phantom in the experimental measurements, i.e., a phantom with a volume fraction of 3% blood, 3% intralipid (20% stock solution), and 94% water. The blood was assumed to be 75% oxygenated. For the simulation, the absorption properties of 20% intralipid stock solution were considered as those from 20% pure fat and 80% water. The reduced scattering was assumed to only depend on intralipid, and the values were obtained according to the equation from Aernouts et al.:[21]

$$\mu_s' = -76.7 + 1.71 \cdot 10^5 \cdot \lambda^{-0.957},$$

where λ is the wavelength (nm) and μ_s' is the reduced scattering coefficient [$\mathrm{cm^{-1}}$]. The g-factor was set to 0.85. This resulted in the following optical properties: μ_a (650 nm) $= 0.20\ \mathrm{cm^{-1}}$, μ_a (800nm)$=0.15\mathrm{cm^{-1}}$, μ_a (975nm)$=0.60\mathrm{cm^{-1}}$, μ_s (650nm)$=$ $54\mathrm{cm^{-1}}$, μ_s (800 nm) $= 41\ \mathrm{cm^{-1}}$, and μ_a (975 nm) $= 32\ \mathrm{cm^{-1}}$. In the simulations, 50 million photon packets were injected into the 18-mm thick tissue. One simulation was conducted for the excitation wavelength and one for the emission wavelength. The light was injected from opposite sides in the two simulations to simulate a transillumination measurement. This resulted in two fluence distributions in the tissue. A Jacobian, describing the probabilities for generating a signal at various positions in the tissue, was calculated as the excitation fluence squared times the emission fluence.

Next, the fat volume fraction was varied from 5% to 30% in the simulations while keeping the blood volume fraction constant at 3%, leaving the water volume fraction to vary from 92% to 67%. The scattering was assumed to be constant in these simulations and the same as above. The results were presented as the ratio of the signals simulated for the two types of UCNPs.

Another simulation included a variation of blood content in the tissue. In this simulation, the volume fraction of blood was gradually increased from 1% to 10% in steps of 0.5%. Here, a constant fat volume fraction of 5% was used and the water volume fraction varied from 94% to 85%. Again, the scattering was kept constant with values as above.

Finally, in order to simulate a realistic *in vivo* measurement, a thin layer of melanin was added at the tissue surface to simulate skin. The layer was 0.1-mm thick and had a varying melanin volume fraction of 1% to 45%, with a step-size of 1% and a constant fat concentration of 5%. In the simulations, the thin melanin layer contained no blood chromophores, and the remaining volume fraction was water. Below the 0.1-mm thick skin layer, the tissue contained 3% blood (75% oxygenation), 5% lipid, and 92% water. The entire tissue had constant scattering properties equal to previous simulations.

3 Results and Discussion

The results of the slope efficiency measurements of emission signal versus excitation intensity for the samples at a depth of 3.0 mm are shown in Fig. 2. This clearly shows a slope efficiency of 2.0 for both types of UCNPs, meaning the excitation relies on two photons and thus the UCNPs operate in a nonsaturated regime. Such dependence is expected for these UCNPs,[1] and secures that all measurements are conducted at low enough intensities such that no saturation takes place. As these measurements are conducted at the position closest to the excitation source in the following measurements, this ensures that all measurements were in the nonsaturated excitation regime and thus allowed straightforward comparisons. In addition, the graph shows that the excitation intensities differ for the two UCNPs samples. Data, not published here, suggest that the Yb:UCNPs sample used saturated at lower power densities than the Nd: UCNPs studied. Thus, we conducted the measurements at different intensities by using two beam size diameters, 5.0 and 7.0 mm. The difference in excitation intensities between the samples is not of primary interest in this study as we have not optimized the samples for efficiency. The particles may have different quantum yields as this is strongly dependent on the synthesis and neither is fully optimized nor measured for these particles. The concentration of the UCNPs may also vary between the two samples as this was difficult to control at the preparation. In Fig. 3, the signal as a function of sample depth is plotted for the two types of UCNPs. The signals are plotted both in linear and semilogarithmic scales to clearly visualize the gain in signal for the Nd:UCNPs. Under the used conditions, the UCNPs had an equal signal at 3.0-mm depth (not shown). In the figure, the signals are instead normalized to a value of 1 at a 3.0-mm depth to clearly illustrate the variation of signals with depth for the two types of UCNPs. The comparison of the two different particle signals as a function of depth yields significant improvement in the emission signal intensity for the Nd codoped particles.

The Nd:UCNPs showed a gain of about 7 times as compared to the Yb:UCNPs at a depth of 10 mm in the tissue phantom.

Figure 4 presents one set of MC simulations for the excitation and emission light. The probability map for detecting the emitted light is simulated in a reverse-path strategy.[22] A homogeneous sample of 18-mm thickness is studied in the simulations. The Jacobian generated from these simulations is also presented. This shows that most of the signals are generated close to the source. This can be understood as two excitation

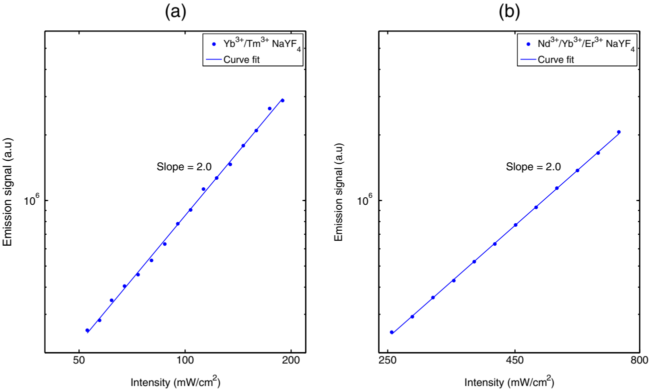

Fig. 2 Power dependence illustrated in a log–log plot of (a) $NaYF_4$:Yb^{3+}/Tm^{3+} and (b) $NaYF_4$:$Nd^{3+}/Yb^{3+}/Er^{3+}$. The intensity refers to excitation intensity at the surface of phantom.

photons are required per event, while only one emission photon is emitted. Thus, the attenuation of the excitation light is becoming dominant over the attenuation of the emission light, and the Jacobian will be clearly asymmetric. This shape suggests that it is more efficient to optimize the measured signal by reducing the attenuation of the excitation than the emission light. In Fig. 5, the experimentally measured signals from a sample at various depths in the tissue phantom are plotted together with MC results. The signal was again normalized to the value of 1.0 for a depth of 3.0 mm to enable a direct comparison on the relative slope of the MC modeled curve with experimental data. The comparison illustrates a good agreement between measurement and simulations. These modeled results deviate less than 20% for any measured data point. This is as good as one can expect with the values of the optical properties as taken from literatur with the samples being extended to 3.0 mm in diameter. MC simulations are known to provide accurate results and the CUDAMCML code has been benchmarked previously.[17]

Encouraged by the good agreement for the results of MC simulations, modeled results of the gain in signal by using Nd:UCNPs are presented for different optical properties in Fig. 6. The gain ratios, i.e., the ratios of the signals for the Nd:UCNPs and the Yb:UCNPs, are illustrated as a function of position in tissue and tissue composition. A gain ratio above the value 1 means that the Nd:UCNPs provide a stronger signal than the Yb:UCNPs—a signal gain, only due to the effect of less attenuation in the tissue. Gain values below the value 1 mean

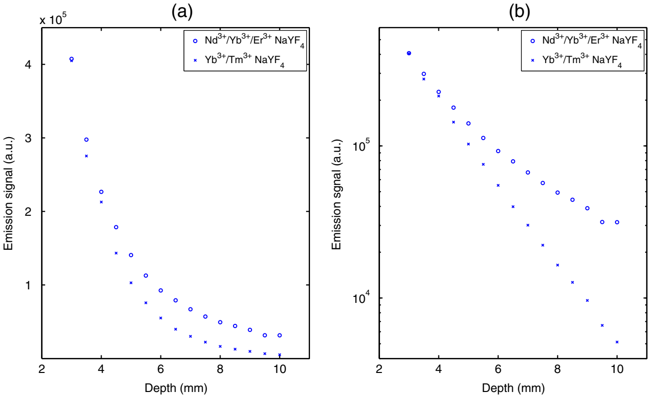

Fig. 3 Depth measurements of Yb^{3+}/Tm^{3+} and $Nd^{3+}/Yb^{3+}/Er^{3+}$: (a) a linear scale, and (b) a plot in semilogarithmic scale.

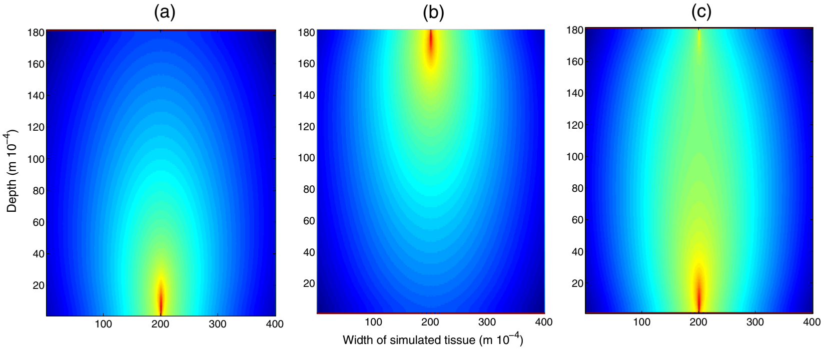

Fig. 4 An MCML simulation showing (a) the excitation fluence distribution in the tissue, (b) a probability map for detecting the emitted light as a function of position, and (c) the Jacobian of the excitation fluence distribution squared times the emission fluence distribution. The Jacobian represents a value of the detected signal strength at the detector for different localizations of the UCNP-sample within the tissue.

a signal loss, i.e., a lower signal for the Nd:UCNPs than for the the Yb:UCNPs, and are achieved for regions close to the source where the attenuation of the emitted light dominates the total light attenuation in tissue.

The lipid simulation shows that varying the lipid fraction has little impact on signal gain. The blood simulations show that for larger amounts of blood, the Nd:UCNPs have less gain compared to low blood volumes. For the simulations containing a thin melanin layer, it is shown that the gain for the Nd: UCNPs is higher for low quantities of melanin in the tissue.

For certain compositions of tissue, the signal will be weaker due to either a large absorption for the emission wavelength or for the excitation wavelength, or both. This is clear in the melanin simulation where melanin has a larger absorption for lower wavelengths, which greatly penalizes the Nd:UCNPs for both excitation and emission wavelengths, reducing the gain obtained from the remainder of the volume. This has important practical consequences, as the skin contains melanin, and this effectively reduces the gain in the signal for these particles. However, for large amounts of lipid, both the excitation and emission wavelengths of the Nd:UCNPs are beneficial compared to the 975-nm excitation in the Yb:UCNPs. Thus, large amounts of lipid will cause the Nd:UCNPs to be beneficial over the Yb: UCNPs. Blood has a larger absorption at 650 nm compared to the other wavelengths, again causing a reduction in gain for large amounts of blood.

Another important aspect to bring forward is that the measurements and simulations were performed in transillumination.

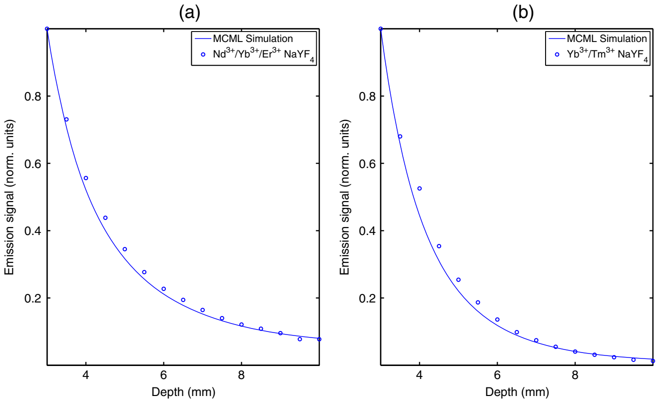

Fig. 5 Comparison of MCML simulation and experimental values: (a) Nd^{3+}/Yb^{3+}/Er^{3+}, and (b) Yb^{3+}/Tm^{3+}.

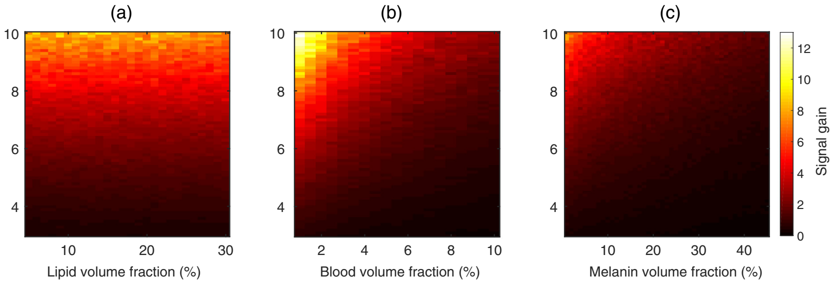

Fig. 6 MCML simulations with varying tissue compositions in an 18-mm thick tissue. The gain ratio of the signals for the Nd:UCNPs versus Yb:UCNPs is plotted as a function of tissue composition and sample depth inside the tissue: (a) simulates a varying lipid volume fraction from 5% to 30% with a step-size of 1%, (b) simulates a varying blood volume fraction from 1% to 10%, and (c) contains a 0.5-mm layer of skin including a melanin variation.

This means that for larger depths, the emission signal has a short path length. This is beneficial for the Nd:UCNPs in cases where the emission wavelength experiences a large absorption. It will at the same time penalize the signal for the same particles at lower depths, due to the much longer emission path length.

While there have been reports of other kinds of cosensitized upconversion using an organic dye as a cosensitizer in order to increase the spectral region of the absorption,[23] this report focuses on the Nd^{3+}/Yb^{3+} cosensitized UCNPs with an absorption peak at 808 nm. Any advantages for these particles in terms of improved signals for deep tissue regions should be directly transferable to dye–particles complexes.

The upconversion process in UCNPs is complex and differs depending on the rare-earth ions involved. It has been shown that a two-photon upconversion process will have a quadratic power dependence when not saturated.[24] Thus, the generated emission will depend quadratically on the fluence rate of the excitation light. A higher-excitation intensity will lead to saturation in some energy levels, causing the power dependence to gradually decrease from quadratic to linear.[24]

This study concerns deep tissue imaging, consequently at a very low excitation fluence rate, most likely far from any saturation effects. While comparing two kinds of UCNPs, it is necessary to confirm that they both are in the same region of saturation, in this case nonsaturated, to enable a generally valid comparison.

4 Conclusion

In conclusion, the Nd:UCNPs show a gain in signal at larger depths for most compositions of optical properties, mainly due to the reduced water absorption at 808 nm. The gain typically can be as high as 10 times for a depth of 10 mm. Melanin in the skin may to some extent reduce this gain in practical use. The gain suggests the Nd:UCNPs to be a promising substitution-for the Yb:UCNPs when performing deep tissue imaging in certain compositions of tissue.

Acknowledgments

The authors gratefully acknowledge Gökhan Dumlupinar for the help with the synthesis of the nanoparticles. This work was supported by a Swedish Research Council grant (VR).

References

1. C. T. Xu et al., "Autofluorescence insensitive imaging using upconverting nanocrystals in scattering media," *Appl. Phys. Lett.* **93**(17), 171103 (2008).
2. Q. Zhan et al., "Using 915 nm laser excited $Tm^{3+}/Er^{3+}/Ho^{3+}$-doped $NaYF_4$ upconversion nanoparticles for in vitro and deeper *in vivo* bioimaging without overheating irradiation," *ACS Nano* **5**(5), 3744–3757 (2011).
3. J.-H. Zeng et al., "Synthesis and upconversion luminescence of hexagonal-phase $NaYF_4$:Yb, Er^{3+} phosphors of controlled size and morphology," *Adv. Mater.* **17**(17), 2119–2123 (2005).
4. J.-C. Boyer et al., "Synthesis of colloidal upconverting $NaYF_4$ nanocrystals doped with Er^{3+}, Yb^{3+} and Tm^{3+}, Yb^{3+} via thermal decomposition of lanthanide trifluoroacetate precursors," *J. Am. Chem. Soc.* **128**(23), 7444–7445 (2006).
5. F. Wang and X. Liu, "Recent advances in the chemistry of lanthanide-doped upconversion nanocrystals," *Chem. Soc. Rev.* **38**(4), 976–989 (2009).
6. R. R. Anderson and J. A. Parrish, "The optics of human skin," *J. Invest. Dermatol.* **77**(1), 13–19 (1981).
7. G. M. Hale and M. R. Querry, "Optical constants of water in the 200-nm to 200-μm wavelength region," *Appl. Opt.* **12**(3), 555–563 (1973).
8. X. Xie et al., "Mechanistic investigation of photon upconversion in Nd^{3+}-sensitized core–shell nanoparticles," *J. Am. Chem. Soc.* **135**(34), 12608–12611 (2013).
9. F. Auzel, "Upconversion and anti-stokes processes with f and d ions in solids," *Chem. Rev.* **104**(1), 139–174 (2004).
10. Y.-F. Wang et al., "Nd^{3+}-sensitized upconversion nanophosphors: efficient in vivo bioimaging probes with minimized heating effect," *ACS Nano* **7**(8), 7200–7206 (2013).
11. W. M. Irvine and J. B. Pollack, "Infrared optical properties of water and ice spheres," *Icarus* **8**, 324–360 (1968).
12. Y. Zhao et al., "Optically investigating Nd^{3+}-Yb^{3+} cascade sensitized upconversion nanoparticles for high resolution, rapid scanning, deep and damage-free bio-imaging," *Biomed. Opt. Express* **6**, 838–848 (2015).
13. G. Chen et al., "Light upconverting core-shell nanostructures: nanophotonic control for emerging applications," *Chem. Soc. Rev.* **44**, 1680–1713 (2015).
14. G. Dumlupinar, "Crystal structure and luminescence studies of upconverting nanoparticles," Master's Thesis, Department of Physics, Lund University (2015).
15. B. Zhu et al., "Reduction of noise floor for molecular, fluorescence-enhanced optical imaging," *Proc. SPIE* **7891**, 789104 (2011).
16. B. Zhu et al., "Reduction of excitation light leakage to improve near-infrared fluorescence imaging for tissue surface and deep tissue imaging," *Med. Phys.* **37**(11), 5961–5970 (2010).
17. E. Alerstam et al., "Next-generation acceleration and code optimization for light transport in turbid media using GPUs," *Biomed. Opt. Express* **1**(2), 658–675 (2010).

18. S. Prahl, *Optical Absorption of Hemoglobin*, Oregon Medical Laser Center, Portland, OR (1999).
19. R. L. van Veen et al., "Determination of VIS-NIR absorption coefficients of mammalian fat, with time- and spatially resolved diffuse reflectance and transmission spectroscopy," presented at *Biomedical Topical Meeting, SF4* (2004).
20. S. L. Jacques et al., "Internal absorption coefficient and threshold for pulsed laser disruption of melanosomes isolated from retinal pigment epithelium," *Proc. SPIE* **2681**, 468–477 (1996).
21. B. Aernouts et al., "Supercontinuum laser based optical characterization of intralipid phantoms in the 500-2250 nm range," *Opt. Express* **21**(26), 32450–32467 (2013).
22. J. Swartling et al., "Accelerated Monte Carlo models to simulate fluorescence spectra from layered tissues," *J. Opt. Soc. Am. A* **20**(4), 714–727 (2003).
23. W. Zou et al., "Broadband dye-sensitized upconversion of near-infrared light," *Nat. Photonics* **6**(8), 560–564 (2012).
24. H. Liu et al., "Balancing power density based quantum yield characterization of upconverting nanoparticles for arbitrary excitation intensities," *Nanoscale* **5**(11), 4770–4775 (2013).

Biographies for the authors are not available.

Paper IV

Beam-profile-compensated quantum yield measurements of upconverting nanoparticles

M. Mousavi, B. Thomasson, M. Li, M. Kraft, Ch. Wurth,
U. Resch-Genger, S. Andersson-Engels.

Royal Society of Chemistry **19,22016**, (2017).

PCCP

PAPER

View Article Online
View Journal | View Issue

Check for updates

Cite this: *Phys. Chem. Chem. Phys.*, 2017, **19**, 22016

Received 5th June 2017, Accepted 1st August 2017

DOI: 10.1039/c7cp03785f

rsc.li/pccp

Beam-profile-compensated quantum yield measurements of upconverting nanoparticles†

Monirehalsadat Mousavi, *[a] Björn Thomasson,[a] Meng Li,[a] Marco Kraft,[b] Christian Würth,[b] Ute Resch-Genger[b] and Stefan Andersson-Engels[ac]

The quantum yield is a critically important parameter in the development of lanthanide-based upconverting nanoparticles (UCNPs) for use as novel contrast agents in biological imaging and optical reporters in assays. The present work focuses on the influence of the beam profile in measuring the quantum yield (ϕ) of nonscattering dispersions of nonlinear upconverting probes, by establishing a relation between ϕ and excitation light power density from a rate equation analysis. A resulting 60% correction in the measured ϕ due to the beam profile utilized for excitation underlines the significance of the beam profile in such measurements, and its impact when comparing results from different setups and groups across the world.

Lanthanide-based upconverting nanoparticles (UCNPs) exhibit significant promise as contrast agents in biological applications[1–6] and reporters in complex matrices like whole blood.[7] These UCNPs emit visible light following sequential absorption of several near-infrared photons. The sequential absorption scheme for UCNPs significantly reduces the need for high intensities of the excitation light as compared to conventional two-photon absorbing dyes.[8] This absorption-emission process precludes background fluorescence in the detection band and drastically reduces light attenuation and scattering in biological materials. Other advantages of UCNPs include their photostability, long fluorescence lifetime, sharp emission bands, as well as lack of photobleaching and photoblinking. One remaining challenge in the use of UCNPs is the still relatively low efficiency of the upconverting process. This issue is being addressed by researchers in the design of enhanced UCNPs upconversion efficiency through several approaches such as lattice manipulation[9] and surface modification.[10,11]

In developing optimised UCNPs, an objective measure of the efficiency of the light upconversion from the actual luminescent material is required. This is provided by the quantum yield (ϕ), defined as the ratio of the number of photons emitted to the number of photons absorbed.[12] Several studies have measured the ϕ of UCNPs absolutely, see *e.g.* ref. 13–18. Two central contributions have been completely devoted to how to measure ϕ in absolute numbers for UCNPs.[19,20] In the case of upconversion, the ϕ determination must consider the nonlinear power dependence of the excitation process. Other groups focused on measuring ϕ relatively and its variation with excitation power density.[21,22] Two different experimental setups known as fluorometer-based setup and an integrating-sphere-based setup have been employed in these measurements. When it comes to nonlinear luminescence emitters, however, another publication describes the difficulties in assessing the beam size when employing an integrating sphere,[23] and as a result we have chosen to use the fluorometer based setup in obtaining the ϕ as a function of excitation power density.

It has been reported that the ϕ of an upconversion luminescence has a linear dependence on the excitation power density (ρ) for a two-photon process at low excitation intensities and gradually becomes constant at high excitation intensities where the excitation process is saturated.[24] This behaviour has been modelled with rate equations and the ϕ can be expressed as a simple relation that depends on two parameters;[25]

$$\phi = 2 \cdot \phi_b \cdot \frac{\rho/\rho_b}{1+\rho/\rho_b}, \qquad (1)$$

Here $\phi[-]$ is characterized by the balancing power density, ρ_b [W m^{-2}], and its corresponding quantum yield, $\phi_b[-]$. The value of ϕ_b is precisely half of the maximum ϕ at very high excitation intensity. This relation helps in providing the means to compare results from different studies and facilitates to correct for the beam profile in a measurement as used below.

Due to the non-linear behaviour, and different from linear fluorescent dyes and quantum dots, quantum yield measurements of UCNPs are influenced by the intensity distribution of the excitation light in the sample. The unmodified laser beam

---

[a] *Department of Physics, Lund University, Lund, Sweden. E-mail: arefeh.mousavi@fysik.lth.se*

[b] *Federal Institute for Materials Research and Testing (BAM), Division Biophotonics (1.10), Richard-Willstaetter-Str. 11, D-12489 Berlin, Germany*

[c] *IPIC, Tyndall National Institute and Department of Physics UCC, Cork, Ireland*

† Electronic supplementary information (ESI) available. See DOI: 10.1039/c7cp03785f

introduces a non-uniform intensity distribution, usually close to a Gaussian distribution. This Gaussian beam profile of an excitation beam implies that particles at different positions within the laser beam experience different excitation power densities and consequently yield different ϕ. This effect has, to our knowledge, not previously been taken into consideration in the determination of the ϕ for UCNPs, and is not included in the published protocols for how to measure the ϕ of UCNPs.[13–18]

The aim of the current study is to investigate the importance in considering the beam profile in the assessment of ϕ from UCNPs in suspension. This will be conducted in two ways, firstly by estimating the beam intensity distribution in the probed volume with a Gaussian spatial density distribution of the beam, and secondly, by measuring the actual beam distribution; followed by compensating for the power density distribution in assessing ϕ for a particular power density of the excitation light. This paper is based on the idea first published in the Masters thesis of Björn Thomasson.[26]

1 Materials and method

1.1 The quantum yield measurement system

The system developed for relative measurements of ϕ is designed based on a conventional fluorometer. A schematic illustration of the fluorometer design is given in Fig. 1.

The fluorometer setup consists of one excitation and three detection paths oriented in a transmission and at 90° angle arrangements, respectively. Two laser diodes at 975 nm (Thorlabs, L975P1WJ) and 785 nm (Thorlabs, L785P090) were employed, well matching the optimal excitation wavelengths of the UCNPs and reference NIR dye, respectively. The two diode lasers are driven by benchtop laser diode current controllers (Thorlabs LDC220C) and controlled by Thorlabs temperature controllers (Thorlabs LDC200C). The excitation light generated by the laser diode is guided to the free-space fluorometer arrangement using a 600 µm core diameter step index optical fibre with a numerical aperture of NA = 0.22. The excitation path includes two convex lenses, a polariser (Thorlabs, LPNIRE200-B) and a beam splitter (Thorlabs, CM1-BP108). These components are mounted in a 60 mm cage system to align the components and direct the beam along a common optical axis into the sample cuvette. The first convex lens L1 ($f = 9$ cm) creates a parallel light beam with a diameter of 40 mm. The beam is vertically polarised with a linear polariser, then focused with a second convex lens L2 ($f = 22$ cm) to a focal point located in the center of the sample cuvette. This long focal length ensures that the beam width in a first approximation remains the same within the probe volume. Furthermore, the expanded beam design is used to prevent any damage of the polariser due to a too high light power density. A beam splitter is placed before the cuvette and it splits 8% of the light onto a CCD camera (Thorlabs, DCU224M), to measure the beam profile as it is in the focal point. An adjustable rectangular stepwise increasingly dense neutral density filter (Thorlabs, NDL-25S-4) is located in front of the camera to avoid saturation for ϕ measured at high light intensities. The sample cuvette, a 10 mm UV fused quartz cuvette with four polished windows (Thorlabs, CV10Q3500F) containing the sample to be measured, is placed in a cuvette holder (Thorlabs, CVH100/M), with its centre equidistant to the CCD camera from the beam splitter. A power meter (Thorlabs, PM16-121) is mounted next to the cuvette holder in line with excitation path to record the excitation power as well as to provide the absorption data for the sample.

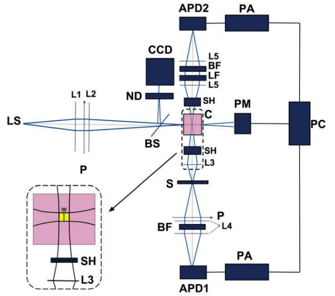

Fig. 1 Illustration and optical arrangement of the fluorometer. Acronyms used: LS – laser source, L – convex lens, P – linear polariser, BS – beam splitter, ND – neutral density filter, CCD – CCD camera, C – sample cuvette, SH – shutter, PM – photo diode power meter, S – slit, BF – bandpass filter, LF – longpass filter, APD – avalanche photo diode, PA – preamplifier, PC – personal computer, W – beam width.

The induced luminescence is measured at a 90° angle to the excitation path. Two luminescence paths were employed, one for the UCNPs (APD1) and one for the reference dye (APD2). Five functions are included in UCNPs luminescence arm – a shutter, a spatial filter, a polarising filter, a wavelength filter and a detector. All components in this luminescence arm are mounted with light-shielding tubes to block any light not generated in the focal probe to reach the APD detector. A shutter next to the cuvette, is followed by a convex lens L3 ($f = 2.5$ cm), focusing the collected light on a 1.0 mm wide vertical slit (S, Thorlabs VA100C/M). The slit suppresses light originating from volumes other than the excitation focal probe, thus ensuring that detected signals are generated within the beam waist of the excitation beam. The light transmitted through the slit is then collimated by a 7.5 cm focal length lens (L4, Thorlabs AC508-075-B). Right before this lens, a polariser identical to the one in the excitation path, oriented at a magic angle (54.7°) with respect to the first polariser located in the excitation path, is placed. This polariser thereby makes measurement results independent on any anisotropy in the sample. A bandpass filter is placed right after L4, followed by an identical focusing lens (L4, Thorlabs AC508-075-B). The 800 nm bandpass filter (Omega Optics, XB135-800BP50) is placed between these two lenses to ensure that only the luminescence light is detected. An avalanche photo diode detector (APD1, Thorlabs APD410A/M) with an active area diameter of 1.0 mm is mounted to collect the emitted luminescence originated from the focal probe in the sample. The measured probe volume is determined by the beam width and the detector size in the 90° detection arm.

(The slit is an intermediate spatial filter of the same effective width as the detector, used to avoid any stray light).

The reference dye luminescence detection arm consists of a shutter, two wavelength filters, two lenses and an APD detector. The wavelength filters consist of one 830 nm bandpass filter (Thorlabs, FL830-10) and one 830 nm longpass filter (Thorlabs, FGL830) located between two lenses L5 (f = 2.5 cm). By connecting the two identical APDs in the luminescence arms to a computer *via* a preamplifier (Stanford research system, SR560, gain setting 10^3) and DAQ board (National Instruments, NI-DAQ, USB-6501), the signal data can be collected and processed by using a custom designed Labview code.

1.2 Spectrometer setup

The luminescence emission spectrum of the probed UCNP samples (Fig. 2) was measured with a spectrometer setup. For this measurement a 600 μm core diameter optical fibre was used to collect the emission from the top of the cuvette in the setup in Fig. 1. A fibre optic spectrometer (Ocean Optics, QE65000) was employed for this measurement.

1.3 Samples

During relative ϕ measurements, it is customary to measure the quantum yield (ϕ_x) of a target sample and to compare it to that of a standard sample with a known quantum yield (ϕ_{st}). The target sample in this study is hexagonal core–shell $\mathrm{NaYF_4{:}Yb^{3+},Tm^{3+}}$ UCNPs synthesized and prepared in-house by Liu *et al.*[25] through a reported protocol[27] and is well characterized in ref. 28. The sample emission spectrum is shown in Fig. 2. The UCNPs were dispersed in cyclohexane (Sigma-Aldrich). The concentration of the UCNPs was selected such that 15% of the light was absorbed in the cuvette as measured with the power meter. This concentration ensures good accuracy by providing a sufficiently strong absorption signal, while the light attenuation was low enough to avoid any significant light attenuation along the beam within the measured probe volume. The sample used as ϕ standard is DY-781-01 (Dyomics GmbH) dissolved in ethanol (Sigma-Aldrich 95% pure ethanol). In order to determine the amount of energy absorbed by the UCNPs and the standard dye molecules, two extra sample cuvettes containing cyclohexane and ethanol only were also prepared.

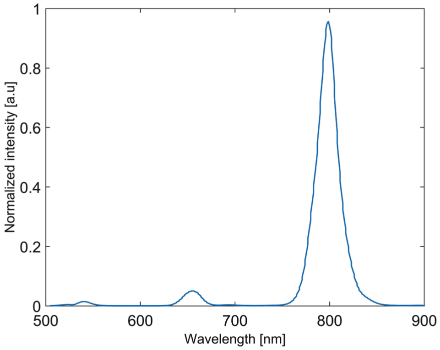

Fig. 2 The luminescence spectra of the core–shell $\mathrm{NaYF_4{:}Yb^{3+},Tm^{3+}}$ UCNPs excited with excitation power density of 200 W $\mathrm{cm^{-2}}$ at 975 nm.

1.4 Measurement procedure

Unless stated otherwise, the procedure follows the protocol by Würth *et al.*[20] The measurement procedure is divided into three ϕ measurement parts: procedure 1.1 and 1.2 for the reference DY-781 dye, absolute and relative ϕ measurements, and procedure 1.3 for the UCNPs relative ϕ measurements; all detailed in ESI† Section S1. The quantum yield was measured in a power series of 16 different excitation power. The individual signals were obtained by taking an average value of the 65 s long recordings.

1.5 Data analysis

The following raw data were used in the analysis: raw data acquired from the power meter for both absorption and excitation light power data signals, and luminescence data acquired by APDs, as well as images recorded by the CCD camera for beam profile data. An example of these data are shown in ESI† Section S1. The transmission spectra of the optical filters were obtained from the suppliers to determine their contribution on blocking the luminescence signals. To also account for scattering caused by UCNPs, the scattering compensation factor (6.7%) is calculated with a method described in ESI† Section S5.

The absorption coefficient (μ_a) of a sample was obtained as,

$$\mu_\mathrm{a} = \frac{1}{1.0\,\mathrm{cm}} \cdot \ln\frac{P_0}{P}, \tag{2}$$

where P_0 and P represent the power of the excitation radiation when there is not any cuvette in the cuvette holder and when the sample cuvette is placed, respectively. The absorption coefficient required for obtaining the ϕ was measured for both fluorophores (UCNPs and DY-781) and their solvent (cyclohexane and ethanol). The net absorption coefficient is obtained by subtracting the value of the dye and its solvent. This subtraction provides the absorption coefficient due to the fluorophore only, without any superimposed solvent absorption. The power in the centre of the cuvette, P_c, was estimated as $P_\mathrm{c} = \sqrt{PP_0}$. The number of photons absorbed per unit volume per second at a distance r from the optical axis in the focus would then be $N_\mathrm{a}(r) = \mu_\mathrm{a}\rho_\mathrm{c}(r)/(hc/\lambda)$ $\mathrm{cm^{-3}\ s^{-1}}$. Here $\rho_\mathrm{c}(r)$ is the excitation beam intensity in the focus plane of the excitation light in the cuvette, such as:

$$P_\mathrm{c} = \int_0^\infty \rho_\mathrm{c}(r)2\pi r\mathrm{d}r \tag{3}$$

Therefore, the absorbed power per unit length in the probe volume is $P_{\mathrm{abs}} = \mu_\mathrm{a}P_\mathrm{c}$ mW $\mathrm{cm^{-1}}$. The net luminescence signal of the sample was, in the same way as for the absorption, calculated by subtracting the signal measured for the solvent from that of the fluorophore solution. An experimentally number of the quantum yield, $\phi_{x,\mathrm{exp}}$, was calculated from the measured uncorrected luminescence signal divided by the number of absorbed photons in the probe volume.

$$\phi_{x,\text{exp}}(r) = \frac{L_x(r)}{N_{\text{a},x}(r)}\frac{1}{T_x}, \tag{4}$$

where L is the detected luminescence signal from the APD, proportional to the number of emitted photons; $N_{\text{a},x}(r)$ is the number of photons absorbed per unit volume per second in the probe volume of the sample; and the T_x is the spectrally integrated transmission of the wavelength filters (see Complementary materials, Section S4 (ESI†), for details how this is calculated). The subscripts x refer to the luminescence upconverting particles with unknown ϕ.

Initially in the data evaluation we will, as conventionally done and for reference purpose, ignore the influence of the beam profile of the excitation light. This is effectively in our evaluation the same as by considering a uniform profile with an intensity of the measured power across the beam area. The beam width (w) is selected as the width for which the intensity within the beam profile has dropped to half of the peak value, meaning the full width half maximum (FWHM). The intensity is set to zero outside this radius. The excitation power density ρ, is the variable that depends on the beam profile in this uniform beam-profile case, calculated according to eqn (5), where P_c is the total measured power over the beam profile and w is the measured FWHM as illustrated in the inset in Fig. 1.

$$\begin{aligned} \rho(r) &= \frac{P_\text{c}}{\pi\left(\frac{w}{2}\right)^2}, \quad |r| \le \frac{w}{2} \\ \rho(r) &= 0, \quad |r| > \frac{w}{2} \end{aligned} \tag{5}$$

As the excitation light intensity is constant across and along the beam within the probe volume with this approximation, the ϕ would be independent on location within this volume and eqn (4) can be simplified as:

$$\phi_{x,\text{exp}} = \frac{L_x}{N_{\text{a},x}}\frac{1}{T_x}, \tag{6}$$

The ϕ for each excitation power density in a measurement series was calculated using eqn (6), and a curve fit was made for all 16 power density values in the measurement series based on the expression in eqn (1), with the two parameters ρ_b and ϕ_b used as fitting parameters. This fitting was carried out with the *lsqnonlin* nonlinear fitting algorithm in MatLab.

The next step is to calculate the ϕ more correctly as a function of excitation power density across the beam profile. During each ϕ measurement a distribution of power densities is present across the beam profile of the excitation beam. In order to calculate the ϕ for a certain power density, two assumptions are made in the data analysis. Firstly, we assume that the distribution of the UCNPs is homogeneous across the measured probe volume, so that the signal from each position across the beam profile only is related to the excitation light power density in that position. Secondly we assume eqn (1) as a valid relation between the ϕ and the power density.

A fitting was made by assuming the profile from a perfect Gaussian beam. For this a 2D Gaussian profile was fitted to the recorded beam profile. For each measurement within the series, the total power of the Gaussian profile was normalised to the excitation power P_c. A detailed description of the fitting procedure is described in the ESI† Section S6. Briefly, the gross resulting ϕ assessed from the measurements according to eqn (6) was compared to a weighted sum of all contributions within the beam profile. The weight for each position within the Gaussian profile is the fraction of the total power contributed. The two parameters ρ_b and ϕ_b valid for any position in the beam and any excitation power was then calculated by fitting the 16 measurements in a measurement series to eqn (1), using the same *lsqnonlin* nonlinear fitting algorithm in MatLab. Finally, a correspondent fitting of ρ_b and ϕ_b was also performed by using the measured beam profile itself in the fitting. Again the profile was normalised to have the total power P_c used for each measurement.

Finally, in order to obtain relative value of the ϕ of the UCNP sample, the absolutely measured $\phi_{\text{st,abs}}$ for the reference dye was multiplied by the ratio of the experimentally obtained values for the UCNPs and reference dye, respectively. The probe volume was assumed to be the same for the measurements of the two samples. The following expression was thereby obtained in assessing the ϕ for the UCNPs sample:

$$\phi_{x,\text{rel}} = \phi_{\text{st,abs}} \cdot \phi_{x,\text{exp}}\frac{N_{\text{a,st}}}{L_\text{st}}\frac{{n_x}^2}{{n_\text{st}}^2}\frac{T_\text{st}}{C}. \tag{7}$$

It is necessary to include the refractive index in the equation due to reflection losses of the light when it goes from one medium to another. In our case this effect comes in twice, both when the excitation light enters the sample solution and when the luminescence light leaves the medium before detected. The factor C corresponds to the relative sensitivity of the two luminescence arms. This value is compensating for any differences in the sensitivity of the two detection arms. The value is measured be recording the luminescence signal of a standard dye sample in both arms simultaneously. The subscripts *st* refer to the reference fluorophore standard of known ϕ.

2 Result

The ϕ for the reference dye DY-781-01 in ethanol (emission from 720 to 940 nm) was determined absolutely at BAM to (12.4 ± 0.1)%. This value is used in assessing the ϕ of the UCNPs sample examined.

The luminescence signals measured from the UCNPs and reference dye cuvettes are plotted *versus* the absorbed power per unit length of the sample in the probe volume (P_abs) in Fig. 3. The absorption coefficient for the reference dye and for UCNPs was measured to be 0.25 and 0.15 cm^{-1}, respectively. The signal generated by the reference dye and the UCNPs, with any signal from the pure solvent subtracted is shown. The signals were measured in a power density range of 0.2–30 W cm^{-2}. The abscissa is illustrating how much energy is absorbed in the focal

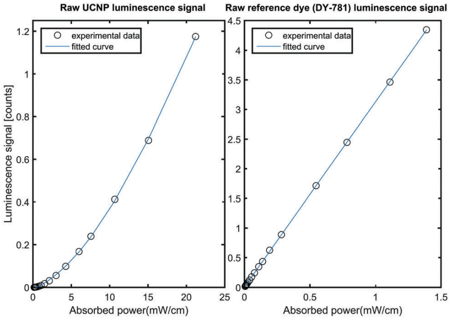

Fig. 3 The luminescence signals from the UCNPs and reference dye as a function of absorbed power in the probe volume. The UCNPs exhibit a nonlinear behaviour, while the reference dye generates a linear relation.

volume per unit time and unit depth. This value is calculated as $P_{\text{abs}} = (\mu_{\text{a}}, \text{sample} - \mu_{\text{a}}, \text{blanck})P_{\text{c}}$ mW cm^{-1}.

Using the data in Fig. 3, the ϕs are presented in the lowest full power density series in Fig. 4 (the blue curve fitting to eqn (1) is provided as a guidance for the eyes). These ϕs are thereby not considering the profile of the excitation beam. The plot illustrates the excitation power density dependency of the upconversion process. The fitting has been made using by eqn (1) based on readings from the power meter and spot size measured with the beam profiler as the full width at half maximum, FWHM = 0.076 cm. The fitting parameters for this curve are, ϕ_{b} = 0.25% and ρ_{b} = 14 W cm^{-2}. Five repeated measurements yielded a measurement precision of 99% in the evaluated experimental ϕ.

To explain the influence of the beam profile distribution in the evaluation of UCNPs ϕ in a simple figure, the difference in the luminescence signal from a uniform top hat beam and a Gaussian beam is modelled in MatLab and demonstrated in ESI† Section S3 and Fig. S2, S3 for a 2D and 1D model, respectively. This example shows that two beam profiles with the same total power and beam width can give rise to different measured ϕ values. The analysis clearly illustrate the importance of the beam profile in the simplified case of very low power density, when the ϕ is dependent on the power density squared for all parts of the beam. The measurements in Fig. 4 indeed include also values beyond where saturation is becoming important, as seen from its non-linear shape, clearly motivating the need for the next level of model sophistication provided by eqn (1).

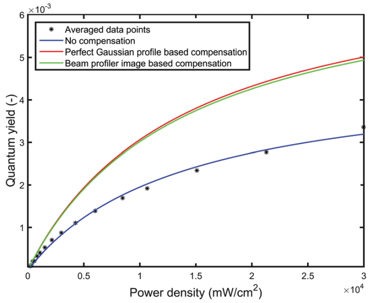

Fig. 4 The ϕ of NaYF$_4$:Yb^{3+},Tm^{3+} UCNPs at 800 nm emission band (black stars) at various excitation power densities. The blue lines stand for fitted data for the ϕ not compensated for the excitation light beam profile. The dotted red curve presents the ϕ compensated for a perfectly Gaussian beam profile, while the green curve gives the ϕ compensated for the measured beam profile.

In a final data analysis step, the measured ϕ was corrected for the beam profile. Two approaches were taken as described above, firstly by assuming a Gaussian beam profile and secondly employing the direct measured beam profile. These evaluations result in the two remaining curves in Fig. 4. As a consequence of the fact that laser beams in practice are not perfectly Gaussian, reduces the ϕ value slightly for the beam profile used in our experiments. All these three curves are plotted together to indicate that the measured ϕ of the sample varies depending on the excitation radiation profile. At the balancing power density ρ_{b} = 14 W cm^{-2}, the beam profile compensated ϕ of the UCNPs is ϕ_{b} = 0.4% for perfect Gaussian and ϕ_{b} = 0.39% for measured beam profile.

3 Discussion

In practice, the measurement of ϕ is a complex procedure because it must take into account a number of parameters that can effect the ϕ value determination. These considerations are documented in previous researches and are beyond of scope in this study. The overall goal of this study is to improve the accuracy of ϕ assessments of UCNPs by considering the influence of the excitation beam profile. It is valuable to measure ϕ of UCNPs, but also to measure it as a function of excitation power density. The reason for this is that particles more efficient in transferring absorbed photons into luminescence emission, also tend to saturate the excitation process at lower power densities, as the pathways yielding losses are minimised.

For that reason it is not sufficient to measure the ϕ at one power density only, but more information is necessary to characterise the luminescence efficiency of the particles, as is also obvious from eqn (1). With a standardised protocol to measure the ϕ as a function of power density, it would be much more straight forward to compare qualities of UCNPs developed by different research teams.

The results clearly illustrate that any absolute ϕ measurement of nonlinear chromophores needs to consider the power density of the excitation light. The influence of the light distribution within the excitation beam has, until now, not been accounted for in determinations of the ϕ of various UCNPs. Even if one considers the beam size, our results suggest that the evaluated ϕ can be wrong by a factor of 1.60. Even if one assumes a Gaussian beam profile and conduct the calculations in the best possible way, the errors can be considerable as shown in the results.

Thus, it is important to measure the actual beam power distribution in order to get an accurate absolute value of the ϕ.

The excitation power density in this study is limited by the laser power to 30 W cm^{-2}. This means that the measurements never reached the fully saturated region in Fig. 4. This also will obviously influence the two parameters we reach by fitting eqn (1) to the measured values. The curves in Fig. 4 is merely the predicted ϕ values for the parameters studied as a function of power density obtained from these fitted values. We estimate that by extending the measurement series to higher laser powers in the recordings would help provide better estimates of the fitted parameters and would possible reduce the correction factor obtained here and thereby also slightly the importance of measuring the accurate beam profile. In the limit of infinite excitation power all nanoparticles will be saturated, also in the beam wings, and the beam profile will have no influence on the luminescence signal, and the measured ϕ. That said, we always need to measure a sufficiently large fraction of the entire power series to enable the extraction of both parameters characterizing the ϕ for the transition studied in this manuscript.

The model employed to describe the luminescence process is simplified and is in its present form designed for a 2 photon excitation scheme for low power densities, to become a one photon process at full saturation (according to eqn (1)). Even for such a scheme, the rate equation derivation used for this model is only considering the minimum number of possible energy levels possible, and even for those neglect certain de-excitation paths. Despite this, the expression obtained fits experimental data for the ϕ as a function of power density rather well. As the evaluation is designed, it requires this type of relation in order to facilitate the fitting. If other transitions in UCNPs are to be considered where more energy levels are needed, the model can be modified and this method is still valid. Such development would be straight forward.

The optical arrangement was designed to minimise the influence of as many uncertainties as possible in the measurements. The robust system developed, minimising the number of steps necessary in the measurements and the recording time proved to be very easy to work with. Especially the simultaneous measurements of the absorption and luminescence makes the system relatively insensitive to any temporal instabilities in the system (in particular in the diode laser). This was important in order to secure repeatability in the measurements.

We made an assumption that beam waist is the same along the excitation beam within the detection volume for the luminescence signal (see inset in Fig. 1). We estimate that this provides an uncertainty of a maximum of 5% in the evaluated ϕ, considering how much the beam waist is actually altering within a distance of 0.5 mm from the focal plane.

Protocols for measuring ϕs suggest a concentration giving an absorbed fraction of the excitation light of 4–5%. This is typically balancing so that the luminescence and absorption signals are sufficiently strong to provide a good signal-to-noise ratio, and avoiding filtering effects within the cuvette. In the evaluation conducted here, the filtering of the excitation light has in the first order been accounted for by estimating the intensity in the centre of the cuvette and multiplying this number by the calculated absorption coefficient. Any variation within the 1 mm long probe volume still remains an issue, as does any filtering of the detected emission light. With this approach an absorption as high as 20% could thus be permitted providing a better signal-to-noise ratio.

Other experimental uncertainties in the values we obtained include any uncertainty in the absolute ϕ of the reference dye. With careful consideration of all other potential sources of errors, the proposed method seem to us justified in measuring the ϕ of UCNPs as a function of excitation power density.

4 Conclusions

The study clarifies the importance of the power density distribution of the excitation beam in measuring the ϕ of UCNPs, as well as its dependence on the excitation intensity. By modelling the ϕ as a function of power density using rate equation analysis, it is possible to utilize all measurements at different power densities, including all pats of the beam profile, to extract the two parameters characterizing the ϕ for the UCNPs sample studied. This averaging procedure provides good precision in the evaluation. The results suggest that the presently used protocols for measuring the quantum yield of upconverting nanoparticles should be updated to consider this effect. This finding also indicates the importance for selecting a suitable method for the measurement of the upconversion luminescence efficiency of UCNPs and other nonlinear luminescence materials and evaluating the obtained results regarding the proper consideration of the effective excitation power distribution in the sample. This results might become important in the work of developing novel UCNPs with improved characteristics, and in standardising the protocols for their characterisation.

Acknowledgements

Discussions with Haichun Liu, Can Xu, Anders Persson and Johan Axelson are greatly acknowledged. Especially the discussion with Haichun Liu and Can Xu in the initial idea generation phase has been instrumental for this paper. The work was financially supported by the Swedish Research Council (VR) grant number 2014-31612 and Science Foundation Ireland (SFI) grant number 15/RP/2828. Financial support from the German Research Council (German Research Foundation (DFG); grants RE 1203/18-1 and RE 1203/20-1) and from the COST Action CM1403 "The European Upconversion Network: From the Design of Photon-Upconverting Nanomaterials to Biomedical Applications" are gratefully acknowledged.

References

1 J. Wang, T. Wei, X. Li, B. Zhang, J. Wang, C. Huang and Q. Yuan, *Angew. Chem.*, 2014, **126**, 1642–1646.
2 H. Chen, B. Qi, T. Moore, D. C. Colvin, T. Crawford, J. C. Gore, F. Alexis, O. T. Mefford and J. N. Anker, *Small*, 2014, **10**, 160–168.

3 Q. Liu, W. Feng, T. Yang, T. Yi and F. Li, *Nat. Protoc.*, 2013, **8**, 2033–2044.

4 Y. Dai, H. Xiao, J. Liu, Q. Yuan, P. Ma, D. Yang, C. Li, Z. Cheng, Z. Hou and P. Yang, *et al.*, *J. Am. Chem. Soc.*, 2013, **135**, 18920–18929.

5 M. Wang, Z. Chen, W. Zheng, H. Zhu, S. Lu, E. Ma, D. Tu, S. Zhou, M. Huang and X. Chen, *Nanoscale*, 2014, **6**, 8274–8282.

6 Q. Xiao, X. Zheng, W. Bu, W. Ge, S. Zhang, F. Chen, H. Xing, Q. Ren, W. Fan and K. Zhao, *et al.*, *J. Am. Chem. Soc.*, 2013, **135**, 13041–13048.

7 R. Arppe, L. Mattsson, K. Korpi, S. Blom, Q. Wang, T. Riuttamäki and T. Soukka, *Anal. Chem.*, 2015, **87**, 1782–1788.

8 R. K. Benninger and D. W. Piston, *Curr. Protoc. Cell Biol.*, 2013, 4–11.

9 M. D. Wisser, M. Chea, Y. Lin, D. M. Wu, W. L. Mao, A. Salleo and J. A. Dionne, *Nano Lett.*, 2015, **15**, 1891–1897.

10 F. Vetrone, R. Naccache, V. Mahalingam, C. G. Morgan and J. A. Capobianco, *Adv. Funct. Mater.*, 2009, **19**, 2924–2929.

11 G.-S. Yi and G.-M. Chow, *Chem. Mater.*, 2007, **19**, 341–343.

12 R. H. Page, K. I. Schaffers, P. A. Waide, J. B. Tassano, S. A. Payne, W. F. Krupke and W. K. Bischel, *J. Opt. Soc. Am. B*, 1998, **15**, 996–1008.

13 M. Pokhrel, A. Kumar Gangadharan and D. K. Sardar, *Mater. Lett.*, 2013, **99**, 86–89.

14 G. Kumar, M. Pokhrel and D. Sardar, *Mater. Lett.*, 2013, **98**, 63–66.

15 S. Fischer, R. Marttin-Rodriguez, B. Fröhlich, K. W. Krämer, A. Meijerink and J. C. Goldschmidt, *J. Lumin.*, 2014, **153**, 281–287.

16 M. Ferreira and V. Piscitelli, *Proc. SPIE*, 2016, 988422.

17 A. Jain, G. Hirata, M. Farias and F. Castillon, *Nanotechnology*, 2015, **27**, 065601.

18 L. C. Mimun, G. Ajithkumar, C. Rightsell, B. W. Langloss, M. J. Therien and D. K. Sardar, *J. Alloys Compd.*, 2017, **695**, 280–285.

19 J.-C. Boyer and F. C. Van Veggel, *Nanoscale*, 2010, **2**, 1417–1419.

20 C. Würth, M. Grabolle, J. Pauli, M. Spieles and U. Resch-Genger, *Nat. Protoc.*, 2013, **8**, 1535–1550.

21 C. T. Xu, P. Svenmarker, H. Liu, X. Wu, M. E. Messing, L. R. Wallenberg and S. Andersson-Engels, *ACS Nano*, 2012, **6**, 4788–4795.

22 J. Suyver, J. Grimm, M. Van Veen, D. Biner, K. Krämer and H. Güdel, *J. Lumin.*, 2006, **117**, 1–12.

23 D. O. Faulkner, J. J. McDowell, A. J. Price, D. D. Perovic, N. P. Kherani and G. A. Ozin, *Laser Photonics Rev.*, 2012, **6**, 802–806.

24 M. Pollnau, D. R. Gamelin, S. R. Lüthi, H. U. Güdel and M. P. Hehlen, *Phys. Rev. B: Condens. Matter Mater. Phys.*, 2000, **61**, 3337–3346.

25 H. Liu, C. T. Xu, D. Lindgren, H. Xie, D. Thomas, C. Gundlach and S. Andersson-Engels, *Nanoscale*, 2013, **5**, 4770–4775.

26 B. Thomasson, High Accuracy Relative Luminescence Quantum Yield Measurements of Upconverting Nanoparticles, MSc thesis, Lund University, 2016.

27 H.-S. Qian and Y. Zhang, *Langmuir*, 2008, **24**, 12123–12125.

28 H. Liu, C. T. Xu, G. Dumlupinar, O. B. Jensen, P. E. Andersen and S. Andersson-Engels, *Nanoscale*, 2013, **5**, 10034–10040.

PAPER V

Real-time photodynamic therapy dosimetry using multi-excitation, multi-emission wavelengths: towards accurate prediction of treatment outcome

M. Mousavi, L. Moriyama, C. Grecco, M. Nogueira, K. Svanberg, C. Kurachi, S. Andersson-Engels.

(September 2019) *Submitted to Journal of Biomedical Optics.*

Real-time photodynamic therapy dosimetry using multi-excitation multi-emission: towards accurate prediction of treatment outcome

Monirehalsadat Mousavi[a,*], **Lilian Tan Moriyama**[b], **Clovis Grecco**[b], **Marcelo Saito Nogueira**[c,d], **Katarina Svanberg**[a], **Cristina Kurachi**[b], **Stefan Andersson-Engels**[a,c,d]
[a]Lund University, Biophotonics group, Department of Physics, Box 118, SE-22100 Lund, Sweden
[b]University of São Paulo, Optics Group, São Carlos Institute of Physics, Av. Trabalhador São Carlense 400, São Carlos/SP, Brazil, 13566-590
[c]Biophotonics@Tyndall, IPIC, Tyndall National Institute, Lee Maltings, Dyke Parade, Cork, Ireland, T12 R5CP
[d]University College Cork, Department of Physics, College Road, Cork, Ireland, T12 R5CP

Abstract. Evaluating the optical properties of biological tissues is needed to achieve accurate dosimetry during photodynamic therapy (PDT). Currently, accurate assessment of the photosensitizer concentration by fluorescence measurements during PDT is typically hindered by the lack of information about tissue optical properties. In the present work, a hand-held fiber-optic probe instrument monitoring fluorescence and reflectance is used for assessing blood volume, reduced scattering coefficient and photosensitizer concentration facilitating accurate dosimetry for PDT. System validation was carried out on tissue phantoms using non-linear least squares support machine regression analysis. It showed a high correlation coefficient (>0.99) in the prediction of the photosensitizer concentration upon a large variety of phantom optical properties. *In vivo* measurements were conducted in a PDT Chlorine E6 dose escalating trial involving 36 male Swiss mice with Ehrlich solid tumors in which fluences of 5, 15, 40 J/cm^2 were delivered at two fluence rates; 100 and 40 mW/cm^2. Remarkably, quantitative measurement of fluorophore concentration was achieved in the *in vivo* experiment. A diffuse reflectance spectroscopy system was also used to independently measure the physiological properties of the target tissues for result comparisons. Then blood volume and scattering coefficient measured by the fiber-optic probe system were compared with the corresponding result measured by DRS and showed agreement. Additionally, tumors hemoglobin oxygen saturation were measured using DRS system. Overall, the system is capable of assessing the implicit photodynamic dose to predict the PDT outcome.

Keywords: biomedical optics, fluorescence, photodynamic therapy, optical properties, dosimetry, *in vivo measurement*, fiber-optic probe.

***Monirehalsadat Mousavi**, arefeh.mousavi@fysik.lth.se

1 Introduction

Advances in optical techniques have provided non-invasive diagnostics and treatment and effective mean to improve clinical outcome.[1–3] Fiber-optic probes have been increasingly utilized to provide a minimally invasive approach in tissue characterization for various biomedical applications such as cancer diagnostics or surgical guidance and treatment response monitoring.[4–7] Photodynamic therapy (PDT) in conjunction with fiber-optic probing is a promising modality to achieve optimal therapeutic efficiency for cancer treatment.[8–10] PDT is a viable minimally-invasive treatment, involving the administration of photosensitizer (PS), incubation time to allow the adequate accumulation of the drug in the tumor and activation by light of appropriate wavelength. This process results in the generation of highly active oxygen radicals that cause tumor necrosis, apoptosis and autophagy.[11–13]

Although PDT has proven to be a promising modality for a variety of malignant and pre-malignant conditions, customized dosimetry is in high demand, and development of such advanced techniques are under clinical evaluation.[14–16] Most PDT clinical protocols utilize the explicit dosimetry based on the light and photosensitizer parameters as well as the incubation time and treatment interval to create a dose model. These parameters are dynamically interdependent and additional factors may influence the PDT outcome. One considerable issue is to know how the light is transported within the tissue to enable optimization of the treatment results. It is well known that a primary challenge of many diagnostics as well as treatment methods stems from spatial and temporal alterations in light attenuation caused by inter- and intra-patient variation of the optical properties in the tissue. Also, due to individual tumor and patient variations, including intra- and inter-individual optical properties distributions and photosensitizer accumulation, a single and efficient PDT irradiation protocol is many times considered unfeasible.

Evaluation of photosensitizer concentration during PDT treatment is an important implicit dosimetry metric that incorporates photosensitizer uptake as well as photobleaching during the treatment. Several investigators have proposed ways to monitor photosensitizer levels during PDT. Depending on the type of optical instrumentation used for illumination and detection, fiber-optic probes that measure both fluorescence and diffuse reflectance signals enable assessment of endogenous and exogenous fluorophores, as well as photobleaching products. Fiber-optic probes are placed in direct contact with the tissue to mitigate the influence of scattering and absorption on the measured fluorescence signal. Such compact fluorescence spectrometer was developed by Nadeau *et al.*[17] to monitor the photobleaching of ALA-induced protoporphyrin IX (PpIX) and to quantify the photobleaching rates in the skin of healthy volunteers. The instrument employs blue and red light sources and shows that the photobleaching rate for a fixed excitation fiber is wavelength dependent. It also allows to quantify the PpIX fluorescence photobleaching rates for the two excitation wavelengths. However, as their probe is designed to interrogate fluorescence with a single fiber, it is not suitable for sampling photosensitizer from beneath the superficial tissue. In another study,[18] a dynamic model was developed to describe the photobleaching process of the involved chromophores in the probed tissue. This model can be used to achieve a photobleaching-insensitive method to improve the fluorophore quantification. Kanick *et al.*[16] have reported on a spectroscopic dosimeter that combines two-channel excitation fluorescence system (blue and red excitation wavelength, respectively) with a broadband reflectance spectroscopic correction to quantify PpIX signals originating from different depths. In a similar approach, Kim *et al.*[19] have combined fluorescence and reflectance spectroscopy for *in vivo* quantification of cancer biomarkers in low and high-grade glioma surgery based on multivariate analysis. The optical fiber was an intra-operative tool that allowed the neurosurgeon to rapidly switch between blue and white light. This group has also proposed an analytical model to extract the quantitative fluorescence signal from PpIX in guided resection surgery of brain tumors.[20]

Quantitative measurements of fluorescence emission *in vivo* can still not be accurately performed when the optical properties of the turbid media are unknown. Variation in the absorption and scattering coefficients may be mistaken for variations in fluorophore concentration. Therefore, an instrument that robustly assesses absorption, scattering, and fluorescence concentration could improve the irradiation dosimetry planning and treatment outcome. In this study, a compact still advanced novel fiber-optic probe system earlier described in[21] was used to quantify parameters of dosimetric importance during PDT. The multichannel dosimeter is based on fluorescence and reflectance spectroscopy, and consists of five excitation wavelengths to assess fluorophore concentration and reduced scattering and absorption coefficients of the probed tissue. Multi-excitation sources have the potential to improve the accuracy of quantitative fluorescence measurements in highly distorted media, while compensating for absorption caused by endogenous chromophores and blood content. The system performance was validated by tissue phantom measurements followed by multivariate analysis. An *in vivo* study on Ehrlich solid tumor model was conducted. The objective of the present work is to evaluate the feasibility of using a hand-held fiber-optic probe to characterize optical properties of biological tissue during PDT treatment. Real-time dosimetry is important for accurate prediction of the PDT outcome and the presented system has capability to measure all relevant PDT parameters in a short time and independent of the ambient light conditions. The evaluation of these parameters allows to retrieve the dosimetric value when the physical properties of the tissue are unknown. In a previous study conducted with this system, insensitivity to ambient light was demonstrated as well as the capability of detection of very low concentrations of the fluorophore in range of nM.[21]

2 Materials and Methods

2.1 Animals and Tumor Induction

Thirty-six male Swiss mice weighting around 30 grams were subcutaneously inoculated with a suspension of 2 x 10^6 Ehrlich carcinoma cells on their backs.[22] The tumor grew for 10 days until the tumor reached about 10 mm in diameter. The animals were then divided into two experimental groups and treated using two fluence rates; 40 mW/cm^2 and 100 mW/cm^2 of a diode laser at 660 nm. The treatment procedure was carried out according to the protocol shown in Table 1. The study was approved by the Ethics Committee for the Use of Animals of the São Carlos Institute of Physics of the University of São Paulo, in compliance with the laws on experimental animals. The study was performed at the São Carlos Institute of Physics of University of São Paulo.

Table 1 The protocol of the study

Fluence rate mW/cm^2 (at 660 nm)	Dose J/cm^2	Number of mice (all=36)
100 (Group I) (3 subgroups)	5 5, 15 5, 15, 40	18 12 6
40 (Group II) (3 subgroups)	5 5, 15 5, 15, 40	18 12 6

2.2 Procedures for In vivo measurements

A stock solution of Chlorine E6 (synthesized at the Department of Chemistry of Federal University of São Carlos)[23] was prepared using 1 mg of the photosensitizer in powder diluted in 1 µl DMSO (LabSynth® Ltda, Diadema, SP, Brazil) and distilled water was added up to 1 ml, obtaining a 1 mg/ml solution. The animals were anesthetized using inhalation anesthesia (isoflurane, 2% in oxygen) and the hair of an area around the tumour about 2 cm in diameter was removed, then a dose of 2 mg/kg of Chlorine E6 was injected via the tail vein with a 4 hours drug-light interval (DLI) according to the protocol. During the DLI, the animals were kept in their cages protected from ambient light. For the PDT procedure, the mice were anesthetized again and a mask made of aluminum foil covered with white bandage tape with a 5 mm in diameter hole was used to delimitate the treatment area. As a PDT light source, a 660 nm diode laser was used (QuantumTech, São Carlos, SP, Brazil) and the light was delivered through an optical fiber tip with a uniform circular illumination spot (FD Frontal Light Distributor, Medlight, Switzerland). The fluence was checked with a power meter, keeping the fiber at a fixed distance from the power meter. The animals were euthanized directly after completion of PDT irradiation and subsequent dosimetry measurements. The group of 36 animals was divided into two experimental groups as shown in Table 1 categorized based on two different PDT fluence rates. Each of these group was divided into three subgroups for three different total light doses. All mice in each main group (18 mice) received 5 J/cm^2 dose. From then on, 12 of them, received an additive of 10 J/cm^2 and thereafter, 6 mice received an additive of 25 J/cm^2 dose (Table 1). The two monitoring optical systems described below were used to measure the reflection and fluorescence spectra before and after PDT treatment using an optical fiber probe in gentle contact with the surface of the tumors. An initial measurement series was performed on all mice before the photosensitizer injection. The PDT light source illuminated through a hole in an aluminum foil placed on the mice skin. The consecutive optical measurements were performed at five sites on each tumour by repositioning the fiber between measurements. The measured optical properties from the five sites in each tumour were averaged. The same measurements were then repeated at the same locations immediately after each stage of the PDT light delivery.

2.3 System description

Two systems described in detail below were used in this study. The first is a probe dosimeter system with five excitation sources and five detection units. This multi-excitation multi-emission system (MEME) has been primarily developed for precise tumor delineation in brain surgery and is capable of suppressing ambient light as well as accurate assessment of both fluorophore concentration and tissue optical properties of tissue samples. The system has been described in detail elsewhere.[21] The second is a diffuse reflectance spectroscopy system. This system is in this study used for *in vivo* validation of the diffuse reflectance results obtained by the MEME probe dosimeter system.

2.3.1 Multi Excitation Multi Emission (MEME) system

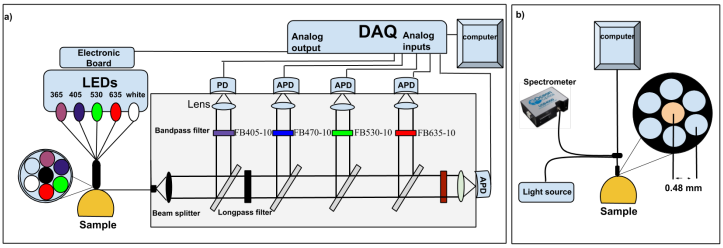

Fig 1 Schematics diagram of a) multi excitation multi emission system (MEME) and b) the optical setup for diffuse reflectance spectroscopy (DRS).

The schematic diagram of the Multi Excitation Multi Emission (MEME) system is shown in Fig. 1a. The light source assembly consists of five light-emitting diodes (LED); four of different wavelengths: 365 nm, 405 nm, 530 nm, 635 nm, and one white light LED (450 nm to 700 nm). The two LED emitting light at the shortest wavelengths were chosen to excite tissue autofluorescence. Additionally, the 405 nm LED provides a strong excitation signal for Chlorine E6 fluorescence. The main tissue absorber interfering with the PDT process is blood. This is primarily absorbing the violent and green LED radiation. The present system is designed to be used in other studies employing PpIX as a photosensitiser, thus, in this study the 635 nm LED channel is used for diffuse reflectance measurements only. All LEDs were multiplexed sequentially by rapid switching between channels, as driven by a transistor-transistor logic (TTL) pulsing at 777 Hz. One measurement period contains six pulse sequences. The first five sequences were used to take measurements once each LED is sequentially switched on while the ambient light level is acquired during the sixth pulse. A hand-held fiber-optical probe delivers light to the sample by means of six illumination fibers in a circular arrangement and with a single collection fiber at the center, each with a core diameter of 750 µm, cladding distance of $< 15\mu$m, a numerical aperture of 0.5, and a length of 4 meters. The center-to-center distance between two adjacent cores is the same as the fiber cladding diameter. During the measurements, the probe tip was held perpendicularly in gently contact (with minimum pressure on the tissue) with the tissue surface. The collected light from the sample was guided to the detection unit and split into five different light paths by means of four dichroic beam splitters. The first detector is a silicon photodiode (PD) (Edmund Optics; 53378) was used to detect diffusely reflected UV and violet light from the probed tissue. Four avalanche photodiodes (APD) (Hamamatsu; S9075) were utilized to collect fluorescence light arising from tissue endogenous substances, exogenous Chlorine E6 fluorescence and also reflectance from the red, green and white LED.

2.3.2 Pulse generation and data analysis

A digital clock output of a 16-bit DAQ board (National Instrument Corp., NIUSB-6351) was used to modulate the light source and record the signal voltages in the PD and APDs. As described above, light intensity modulation was employed, first, to measure the signal generated for the five LEDs independently and second, to enable measurements in strong ambient light conditions by means of precise background light subtraction. A full measurement cycle including all 20 measurement channels is presented in Fig. 2a. The used excitation-emission combinations defined in Fig. 2b is such a cycle. For a typical measurement case, the pulse generation, DAQ, real-time control and initial data analysis are performed by a custom-made LabVIEW application. A MATLAB toolbox for least-squares support vector machines (LS-SVM) was employed for multivariate regression and analysis.

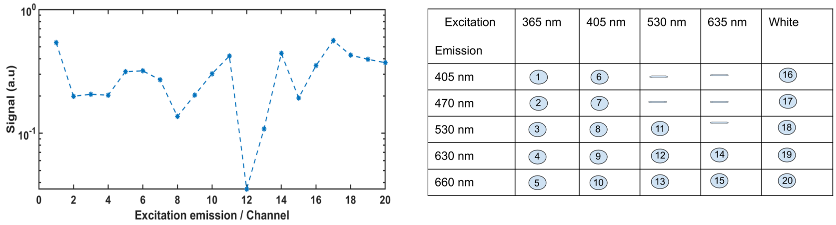

a) Channels

Excitation Emission	365 nm	405 nm	530 nm	635 nm	White
405 nm	①	⑥	—	—	⑯
470 nm	②	⑦	—	—	⑰
530 nm	③	⑧	⑪	—	⑱
630 nm	④	⑨	⑫	⑭	⑲
660 nm	⑤	⑩	⑬	⑮	⑳

b) Excitation and emission wavelengths

Fig 2 a) Typical optical data collected by the MEME system is shown for each pair of excitation and emission wavelengths. These pairs are shown in Table b)

2.3.3 System validation

Phantom experiments were carried out to construct a data set used for evaluation of the MEME system performance. A set of tissue-like phantoms was prepared by mixing water, Intralipid®

(Sigma-Aldrich, 200 mg/ml), and bovine blood (purchased from a local supermarket). Chlorine E6 stock solution was prepared by dissolving 0.3 g Chlorine E6 powder in 2 µl dimethyl sulfoxide (DMSO) (Merck, Darmstadt, Germany) and 80 µl distilled water to make a Chlorine E6 concentration of 5 µM. In total 112 phantoms were prepared containing different amounts of Intralipid (2%, 4%, 6%, 8%), bovine blood (1%, 2%,3%, 4%) and Chlorine E6 (0-5 µM). These concentrations were chosen to have a good correspondence to real biological tissue. The phantom with the highest fluorophore concentration (5 µM) was placed in a cylindrical glass container and stirred for 4 h prior and during the measurements. The lower concentration was subsequently prepared by diluting the initial liquid tissue phantom, without any fluorophore. The reduced scattering coefficient of each phantom was estimated by the Staveren *et al.*[24] relation:

$$\mu_s'(\lambda) = C.[0.58.(\lambda/1\mu m) - 0.1].0.32.(\lambda/1\mu m)^{-2.4}, \tag{1}$$

where C denotes the concentration of 20%-Intralipid in the phantom and λ refers to the light wavelength in µm.

2.4 *Diffuse reflectance spectroscopy*

2.4.1 *System description*

Diffuse reflectance spectra were collected using an optical measurement system shown in Fig. 1 b), consisting of a halogen lamp (HL-2000, Ocean Optics) used as a light source, and a fiber-optic based spectrometer (USB4000, Ocean Optics) used to acquire diffuse reflectance spectra from 400 nm to 650 nm. The fiber-optic probe (Avantes, Reflection Probe (FCR-7IR400-2-ME)) consists of six surrounding collection fibers and one illumination fiber located at the center. The numerical apertures of the illumination fiber and the detection fibers are 0.22. The core diameters of the fibers are 400 µm while cladding is 480 µm . The distance between the centers of the illumination and the collection fibers is 0.48 mm.

2.4.2 *Data acquisition*

The spectra were obtained from the same location on samples as specified for the MEME system. A spectrally flat white reflectance standard (Spectralon, absphere, Inc., SRS-99-010) was used as a reflectance standard and all spectra were normalized to the calibration spectrum. The background signal was recorded and subtracted from all measurements including the reference spectra to correct for dark current and stray light.

2.4.3 Inverse Monte Carlo spectral fitting

The spectral fitting was performed by using an inverse Monte Carlo algorithm. This algorithm allows the retrieval of optical properties (scattering and absorption) by relating them to reflectance values of a database generated by using forward Monte Carlo simulations (performed by using a CUDAMCML code[25]). The simulations assume a given geometric configuration of the illumination and collection fibers, as well as the refractive index of the fibers and tissue. Details about the calculation of the blood volume fraction are described elsewhere.[26]

3 Results

3.1 MEME system calibration

The calibration responses, based on a least-squares support vector machines (LS-SVM) regression model to predict reduced scattering coefficient (μ'), blood volume and photosensitizer concentration, are shown in Fig. 3. The performance of each experiment was evaluated by using a two-fold cross-validation methodology: the phantom dataset was split into one subset for training and another for testing. The solid line indicates supreme prediction and the black, red, and green dots represent the predicted points. The results obtained show calibration curves with correlation coefficient exceeding 0.999. It indicates an excellent performance of the MEME system for estimation of a large range of optical properties and low fluorophore concentrations in the μM range.

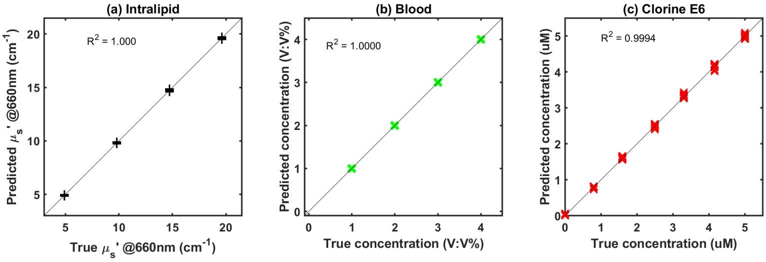

Fig 3 System validation plot by means of Intralipid phantoms with various optical properties using a 2-fold LS-SVM regression method (112 samples). Each graph shows the prediction values versus true values for a) reduced scattering coefficient (set by Intralipid concentration) b) Blood as absorption coefficient (set by blood volume fraction) and c) Chlorine E6 concentration (set by the photosensitizer fluorescence) to quantify photosensitizer concentration.

3.2 Spectral fitting

Figure 4 shows comparison between an example of an experimental spectrum and the inverse Monte Carlo spectral fitting. The blue line indicates measured spectra and the corresponding model fit is shown in the red line. The chromophore parameters for the spectral fitting algorithms are hemoglobin, deoxyhemoglobin, lipid, water and bilirubin. In addition to scattering and absorption parameters, the tissue oxygenation was also calculated by using the output values of the fitting algorithm. Error percentage is calculated as the difference between two spectra divided by the experimental reflectance is below 3.0 %

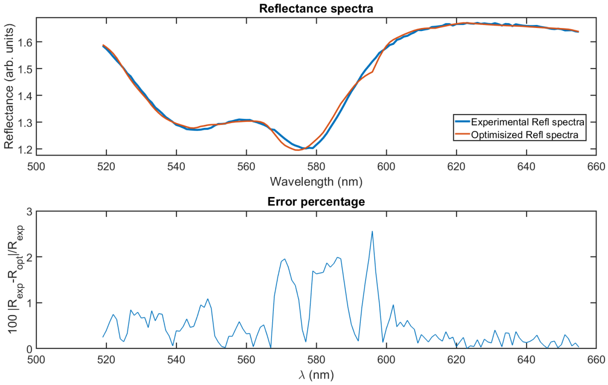

Fig 4 DRS spectrum and inverse Monte Carlo fitted spectrum (top) and error percentage (bottom) for the fitting algorithm.

3.3 In vivo quantification

The SVM model created from phantom validation measurements is applied to the mice data for predicting the optical properties and fluorophore concentration in tumors. Since one of the main aims of this experiment was to quantitatively measure the photosensitizer accumulation in the tumors, the pre-injection tissue autofluorescence, pre-PDT, and post-PDT Chlorine E6 fluorescence signals were analysed to extract the Chlorine E6 concentration (Fig. 5). Box-plots are used to show the median and interquartile range of data in the figures. A low initial presence of red fluorescence signal is observed before PS injection. Accumulation of the photosensitizer is obvious after injection with three times increase in signal ($p\text{-value}<0.01$) from the initial red fluorescence intensity for group I and seven times increase ($p\text{-value}<0.01$) for group II. The photosensitizer intensity decreased for both groups after 5 J/cm^2 treatment step. There is no remarkable difference after 15 J/cm^2 delivered dose.

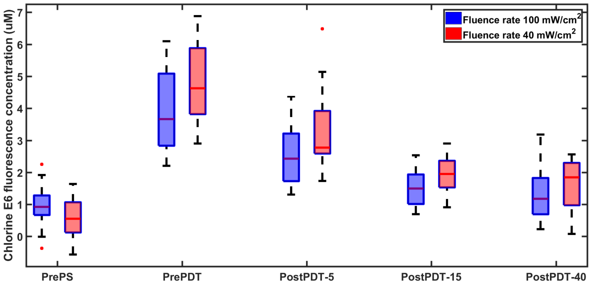

Fig 5 Chlorine E6 level in tumor tissues evaluated by the MEME system before drug injection, pre-PDT and post-PDT. PrePS stands for before photosensitizer injection, PrePDT for 4h after injection and before PDT treatment, and Post PDT-5, 15, or 40 for the three different treatment procedures after light delivery. First three box-plots on the left represent measurements on 36 animals divided into two groups of PDT fluence rate (18 animals in each group). The two last box-plots show 24 treated animals with 15 J/cm^2 (12 animals in each group) and 12 treated animals with 40 J/cm^2(6 animals in each group). All data is based on training set obtained from tissue phantoms.

Figures 6 and 7 illustrate the blood volume and the reduced scattering coefficient variation at different treatment procedures. Data before the photosensitizer injection were assessed to investigate whether the tumor physiology properties changed due to the drug injection. For the MEME system the blood volume fraction is evaluated at the two fluence rates of 100 mW/cm^2 (group I) and 40 mW/cm^2 (group II) with median values of 2.2 % and 2.3 %, respectively before injection. Median relative value of the blood content at group I after injection is 1.2% and 1.1%, 1.1%, 1.0% respectively after treatment stages with 5, 15, and 40 J/cm^2. For group II, median relative blood content is 1.2% after injection, and 1.2%, 1.0%, 1.0% after the three stages of treatment. For the DRS system, the median relative changes in the blood absorption for group I is 1.0% for all four measurement procedures relative to the blood absorption value before PS injection. For group II the median relative blood volume is 1.0%.

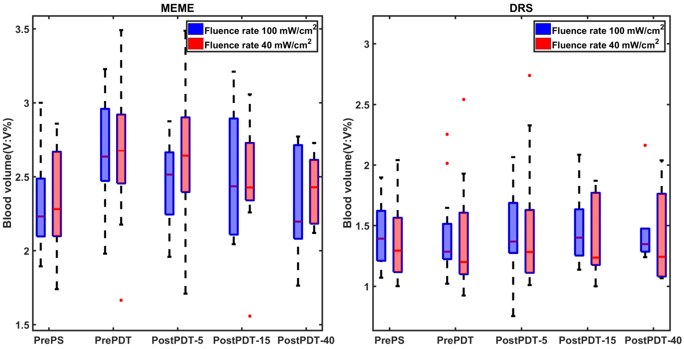

Fig 6 Blood volume variation of tumor tissues evaluated by the MEME and DRS system before drug injection, pre-PDT and post-PDT. PrePS stands for before photosensitizer injection, PrePDT for 4h after injection and before PDT treatment, and PostPDT-5, 15, or 40 for the three different treatment procedures after light delivery. First three box-plots on the left represent measurements on 36 animals divided into two groups of PDT fluence rate (18 animals in each group). The two last box-plots show 24 treated animals with 15 J/cm^2 (12 animals in each group) and 12 treated animals with 40 J/cm^2(6 animals in each group).

For the MEME system, the reduced scattering coefficients before PS injection were evaluated as 10.7 cm^{-2} for group I and 9.0 cm^{-2} for group II. Comparison of reduced scattering coefficient at two different light doses shows significantly lower value at 40 mW/cm^2 before PDT and during subsequent treatment. All measurements procedures demonstrated relative median values of around 1 for optical properties variation. The optical properties did not change substantially before and after PDT treatment. The reduced scattering coefficient had rather high standard deviations compared to the blood volume fraction variations. The reduced scattering coefficient exhibited a slight tendency to increase during treatment.

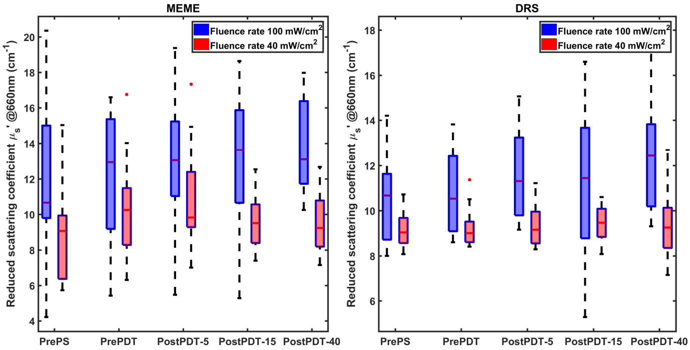

Fig 7 Reduced scattering coefficients of tumor tissues evaluated by MEME and DRS before drug injection, pre-PDT and post-PDT. PrePS stands for before photosensitizer injection, PrePDT for 4h after injection and before PDT treatment, and PostPDT-5, 15, or 40 for the three different treatment procedures after light delivery. First three box-plots on the left represent measurements on 36 animals divided into two groups of PDT fluence rate (18 animals in each group). The two last box-plots show 24 treated animals with 15 J/cm^2 (12 animals in each group) and 12 treated animals with 40 J/cm^2(6 animals in each group).

Blood oxygenation changes in tissue were determined by fitting the diffuse reflectance spectra based on the concentrations of oxyhemoglobin and deoxyhemoglobin. A typical fitted result for the optical parameters is depicted in Fig. 4.

In contrast to findings that reveal insignificant optical parameters variation during PDT, blood oxygenation showed a high variation during PDT (Fig. 8). Lowest mean oxygenation was seen before PS injection and it was 9% for group I and 13% for group II. Tissue oxygenation raised to 26% after drug injection and before treatment with P value$<$0.01 for both groups. The tissue oxygenation increased to 33% (p-value$<$0.01) after treatment using light with 5 J/cm^2 fluence for group I and reached to 41% (p-value$<$0.04) for group II. No appreciable difference in PDT effect on oxygen saturation was observed for the rest of the process (non-significant p-value$>$0.2). Similar trend is shown in Fig. 5, when the photobleaching rate was constant in the last two stages of treatment.

A histological analysis was planned in order to evaluate tissue changes related to the PDT protocols. However, there were not any significant results from histological analysis likely due

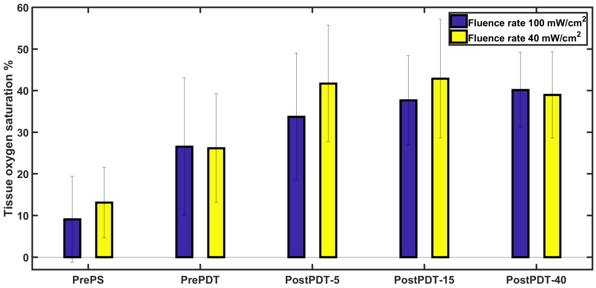

Fig 8 Tumor hemoglobin oxygen saturation measured by the DRS system before drug injection, pre-PDT and post-PDT. PrePS stands for before photosensitizer injection, PrePDT for 4h after injection and before PDT treatment, and PostPDT-5, 15, or 40 for the three different treatment procedures after light delivery. First three box-plots on the left represent measurements on 36 animals divided into two groups of PDT fluence rate (18 animals in each group). The two last box-plots show 24 treated animals with 15 J/cm^2 (12 animals in each group) and 12 treated animals with 40 J/cm^2(6 animals in each group).

to short time with the samples preparation which did not allow us to get any relevant information from the slides.

4 Discussion

In this study, the change of the important dosimetric parameters for PDT *in vivo*, namely the tissue optical properties and photosensitizer level in tissue were evaluated with a novel combined fluorescence reflectance system with Multi Emission Multi Excitation (MEME) functionality. Measurements of the optical properties of the tissue are of great interest for some medical applications, particularly for PDT as used for dosimetry during the treatment sessions. Dosimetry has potential to predict treatment outcomes by taking into account non-homogeneous distribution of photosensitizer within the tumour and inter- and intra- animal variability in tissue optical properties. The fiber optic point probe is designed to quantitative tissue fluorescence measurement *in vivo* using separate source-detector fibers. The modulation at a kHz frequency regime in this design allows detection of weak fluorescence signals with a variety of illumination sources in the presence of the ambient light. Multi LED sources are employed for fluorescence and reflection spectroscopy. The monitoring of the reflectance is aimed to correct the fluorescence signal from the tissue optical properties as well as to compensate for source power fluctuation.

Previous studies have shown that the choice of fluence rate in PDT can affect the physiological and cytotoxic response and consequently the treatment outcome.[27,28] Therefore, 36 mice received a light dose escalating from 5 J/cm^2 to 15 and 40 J/cm^2 at two fluence rates of 100 and 40 mW/cm^2. Diffuse reflectance spectroscopy was conducted concurrently to measure tissue optical properties and oxygenation level.

In this study, least-squares support vector machines (LS-SVM) were used to evaluate the fluorophore concentration, blood volume, and reduced scattering coefficient. In the phantom calibration experiments, a wide range of absorption and scattering values have been provided to cover a large variation in the optical properties. The photosensitizer used in this study was Chlorine E6, and it was added to the liquid phantom to validate the accuracy and robustness of the system in the prediction of fluorophore concentration in the presence of large optical variations. The results show that the LS-SVM model can predict the photosensitizer concentration in tissues with different optical properties. In addition, the detected signals - blood volume, reduced scattering coefficient and fluorophore concentration - correlate linearly to the actual concentrations (see Fig. 3). The phantom results were used as a training set in evaluating the same parameters in the *in vivo* measurements. There is a significant variation in optical properties between tumors and within any of the tumors caused by the heterogeneity in tissue. We observed that clear fluctuations are present in blood volume and reduced scattering coefficient in the animals before drug injection prior to the PDT. Such fluctuations would be imperative to consider in PDT treatments, as they indicate that individual tumors can respond differently to PDT.

The intensity of the PS-related signal in tissue was measured with the optical fiber system. The photosensitizer level was highly variable among tissues. There is some statistical difference between individual mice, but consistency in average values is clear (Fig. 5). A significant photosensitizer uptake is clear after drug administration. A substantial reduction of tissue Chlorine E6 after PDT is observed after first and second treatment due to the photobleaching. There are challenges to estimate the photosensitizer concentration from fluorescence signals in the presence of endogenous fluorophores. This stems from the background signal from such fluorophores not related to the photosensitizer concentration. This could have be avoided by adding these fluorophores in the tissue phantom training set to correctly the presence of tissue autofluorescence in tissue.

Our results from both systems show insignificant changes in blood volume and reduced scattering coefficients during the treatment procedure for all light doses and both fluence rates. Such responses have been observed earlier, even though previous studies have investigated other time periods of the post PDT, possibly explaining differences in the observations.[29–31] In most of the studies, the optical properties evaluation has been performed for a longer period after PDT, sometimes exceeding 24 months.[29] These different interrogation times will definitely result in different tumor optical properties, arising from different tumor response stages. For instance, Ahn *et al.*[29] presented no appreciable differences in the PDT effect on blood volume as a function of the light dose after PDT, while significant changes were reported up to 24 months after treatment.

The hemoglobin oxygen saturation was measured with only diffuse reflectance spectroscopy to investigate the local tissue oxygenation. In general, most PDT dosimetry studies perform the first oxygenation measurement after drug delivery and before PDT. In this study, we measured the tissue oxygenation before drug injection. Interestingly, a slight ,yet significant increase in the oxygenation is observed following drug delivery before any light illumination to the tissue. One explanation could be that after administration of the drug, there might be a physiological response to the drug administration. This trend is also observed after the first treatment stage when tumours were treated with 5 J/cm^2 light fluence. Understanding the mechanisms of tumor destruction may explain the increase in blood oxygenation after first light delivery. One immediate response to PDT is an acute inflammatory reaction in the targeted site and tumor bed, as well as in the normal microvasculature.[11] Increase in tissue oxygen saturation while the blood volume is constant can be explained by increased blood flow (not measured here). Previous reports on blood flow responses due to PDT showed great variability most likely due to differences in tumor characteristics and treatment protocols.[32,33] Monitoring of blood flow has been studied with several different techniques including laser Doppler technique and Doppler optical coherence tomography and diffuse correlation spectroscopy.[34–36] In these studies, an initial increase in relative blood flow velocity followed by a reduction is indicated. Kushan *et al* attributed this increase due to the narrowing of the lumen following vasoconstriction. The same trend in vascular response to PDT is observed in a study by Maas *et al*.[37] It is also reported that tumor oxygenation change during photodynamic therapy depend on photosensitizer type and time after injection.[38] Increase in tissue oxygenation was observed for PDT with verteporfin and aminolevulinic acid-induced protoporphyrin IX (ALA-

PPIX) with 3 hours between injection and irradiation. The result reported here are encouraging, but more studies are required to translate into clinical use. The significant decrease observed in photosensitizer concentration together with a great variation in optical properties can be used to be predictive of response. However, additional interventions may need to be applied to improve the outcome, such as extending the trial time to observe the treatment influence on tumors. Tissue necrosis, apoptosis, and autophagy need longer time to become visible in histological analysis, therefore, further experiments need to be performed with longer evaluation time to get a better understanding of the PDT outcome.

5 Conclusions

In conclusion, a fiber-optic probe instrument based on fluorescence and reflectance spectroscopy was used for the purpose of diagnostic and monitoring measurement of tissue. In this study, this system is a complement to PDT as a mean of dosimetry. The PDT treatment outcome depends on many variables including PS concentration, oxygen saturation, and optical properties variation in tissue. An accurate and reliable dosimetry method to take all these variables into account is essential to allow PDT outcome to become predictable. In this novel fiber probe system, multiple sources using LEDs enable precise quantification of the fluorophore concentration and tissue optical properties. System performance was validated using LS-SVM regression analysis on phantom with a large variation of optical properties and showed a correlation of $> 99\%$ between true concentration and predicted value. The quantitative measurement of fluorescence signals was accomplished *in vivo*. Results from this study, together with the results from a previous clinical study,[21] show encouraging observation for real-time photosensitizer quantification during PDT. However, this study was somewhat limited by variation in blood volume concentration, causing changes in absorption and scattering parameters not being significant. Therefore, the future plans include optimization of the system to be utilized for better PDT planning with a more controlled treatment procedure. The longer time interval between irradiation and measurement will be necessary to observe PDT-induced changes in tumors.

Disclosures

The authors have no relevant or material financial interests that relates to the research described in this article and no potential conflicts of interest to disclose.

Acknowledgments

The authors greatly acknowledge the support of Professor Sune Svanberg. This work was supported by Joint Brazilian-Swedish Research Collaboration STINT and Swedish Research Council (VR) grant number CAPES 23038.003781/2014-76. Further support was obtained from Science Foundation Ireland (SFI) grant number SFI/15/RP/2828.

References

1 E. Alarousu, J. T. Hast, M. T. Kinnunen, *et al.*, “Noninvasive glucose sensing in scattering media using oct, pas, and tof techniques,” in *Saratov Fall Meeting 2003: Optical Technologies in Biophysics and Medicine V*, **5474**, 33–42, International Society for Optics and Photonics (2004).

2 H. Sorvoja, T. Myllylä, M. Y. Kirillin, *et al.*, “Non-invasive, mri-compatible fibreoptic device for functional near-ir reflectometry of human brain,” *Quantum Electronics* **40**(12), 1067 (2010).

3 B. W. Pogue, J. D. Pitts, M.-A. Mycek, *et al.*, “*In Vivo* nadh fluorescence monitoring as an assay for cellular damage in photodynamic therapy,” *Photochemistry and Photobiology* **74**(6), 817–824 (2001).

4 U. Utzinger and R. R. Richards-Kortum, “Fiber optic probes for biomedical optical spectroscopy,” *Journal of Biomedical Optics* **8**(1), 121–148 (2003).

5 S. Andersson-Engels, Å. Elner, J. Johansson, *et al.*, “Clinical recording of laser-induced fluorescence spectra for evaluation of tumour demarcation feasibility in selected clinical specialities,” *Lasers in Medical Science* **6**(4), 415–424 (1991).

6 C. af Klinteberg, M. Andreasson, O. Sandström, *et al.*, “Compact medical fluorosensor for minimally invasive tissue characterization,” *Review of Scientific Instruments* **76**(3), 034303 (2005).

7 N. N. Mutyal, A. Radosevich, B. Gould, *et al.*, "A fiber optic probe design to measure depth-limited optical properties in-vivo with low-coherence enhanced backscattering (lebs) spectroscopy," *Optics Express* **20**(18), 19643–19657 (2012).

8 P. Agostinis, K. Berg, K. A. Cengel, *et al.*, "Photodynamic therapy of cancer: an update," *CA: A Cancer Journal for Clinicians* **61**(4), 250–281 (2011).

9 C. A. Robertson, D. H. Evans, and H. Abrahamse, "Photodynamic therapy (pdt): a short review on cellular mechanisms and cancer research applications for pdt," *Journal of Photochemistry and Photobiology B: Biology* **96**(1), 1–8 (2009).

10 M. S. Thompson, A. Johansson, T. Johansson, *et al.*, "Clinical system for interstitial photodynamic therapy with combined on-line dosimetry measurements," *Applied Optics* **44**(19), 4023–4031 (2005).

11 T. J. Dougherty, C. J. Gomer, B. W. Henderson, *et al.*, "Photodynamic therapy," *JNCI: Journal of the National Cancer Institute* **90**(12), 889–905 (1998).

12 B. W. Henderson and T. J. Dougherty, "How does photodynamic therapy work?," *Photochemistry and photobiology* **55**(1), 145–157 (1992).

13 D. E. Dolmans, D. Fukumura, and R. K. Jain, "Photodynamic therapy for cancer," *Nature Reviews Cancer* **3**(5), 380 (2003).

14 M. T. Jarvi, M. S. Patterson, and B. C. Wilson, "Insights into photodynamic therapy dosimetry: simultaneous singlet oxygen luminescence and photosensitizer photobleaching measurements," *Biophysical Journal* **102**(3), 661–671 (2012).

15 A. Johansson, J. Axelsson, S. Andersson-Engels, *et al.*, "Realtime light dosimetry software tools for interstitial photodynamic therapy of the human prostate," *Medical Physics* **34**(11), 4309–4321 (2007).

16 S. C. Kanick, S. C. Davis, Y. Zhao, *et al.*, "Dual-channel red/blue fluorescence dosimetry with broadband reflectance spectroscopic correction measures protoporphyrin ix production during photodynamic therapy of actinic keratosis," *Journal of Biomedical Optics* **19**(7), 075002 (2014).

17 V. Nadeau, M. O'Dwyer, K. Hamdan, *et al.*, "In vivo measurement of 5-aminolaevulinic acid-induced protoporphyrin ix photobleaching: A comparison of red and blue light of various intensities," *Photodermatology, Photoimmunology & Photomedicine* **20**(4), 170–174 (2004).

18 M. Brydegaard, N. Haj-Hosseini, K. Wardell, *et al.*, “Photobleaching-insensitive fluorescence diagnostics in skin and brain tissue,” *IEEE Photonics Journal* **3**(3), 407–421 (2011).

19 P. A. Valdes, F. Leblond, K. D. Paulsen, *et al.*, “Combined fluorescence and reflectance spectroscopy for in vivo quantification of cancer biomarkers in low-and high-grade glioma surgery,” *Journal of Biomedical Optics* **16**(11), 116007 (2011).

20 A. Kim, M. Khurana, Y. Moriyama, *et al.*, “Quantification of in vivo fluorescence decoupled from the effects of tissue optical properties using fiber-optic spectroscopy measurements,” *Journal of Biomedical Optics* **15**(6), 067006 (2010).

21 H. Xie, Z. Xie, M. Mousavi, *et al.*, “Design and validation of a fiber optic point probe instrument for therapy guidance and monitoring,” *Journal of Biomedical Optics* **19**(7), 071408 (2014).

22 K. Kuroda, M. Akao, M. Kanisawa, *et al.*, “Inhibitory effect of capsella bursa-pastoris extract on growth of ehrlich solid tumor in mice,” *Cancer Research* **36**(6), 1900–1903 (1976).

23 M. P. Uliana, L. Pires, S. Pratavieira, *et al.*, “Photobiological characteristics of chlorophyll a derivatives as microbial pdt agents,” *Photochemical & Photobiological Sciences* **13**(8), 1137–1145 (2014).

24 S. T. Flock, S. L. Jacques, B. C. Wilson, *et al.*, “Optical properties of intralipid: a phantom medium for light propagation studies,” *Lasers in Surgery and Medicine* **12**(5), 510–519 (1992).

25 E. Alerstam, T. Svensson, and S. Andersson-Engels, “Parallel computing with graphics processing units for high-speed monte carlo simulation of photon migration,” *Journal of biomedical optics* **13**(6), 060504 (2008).

26 M. S. Nogueira, M. Raju, J. Gunther, *et al.*, “Diffuse reflectance spectroscopy for determination of optical properties and chromophore concentrations of mice internal organs in the range of 350 nm to 1860 nm,” in *Biophotonics: Photonic Solutions for Better Health Care VI*, **10685**, 106853G, International Society for Optics and Photonics (2018).

27 E. Angell-Petersen, S. Spetalen, S. J. Madsen, *et al.*, “Influence of light fluence rate on the effects of photodynamic therapy in an orthotopic rat glioma model,” *Journal of Neurosurgery* **104**(1), 109–117 (2006).

28 T. M. Busch, X. Xing, G. Yu, *et al.*, “Fluence rate-dependent intratumor heterogeneity in physiologic and cytotoxic responses to photofrin photodynamic therapy,” *Photochemical & Photobiological Sciences* **8**(12), 1683–1693 (2009).

29 P. H. Ahn, J. C. Finlay, S. M. Gallagher-Colombo, *et al.*, “Lesion oxygenation associates with clinical outcomes in premalignant and early stage head and neck tumors treated on a phase 1 trial of photodynamic therapy,” *Photodiagnosis and Photodynamic Therapy* **21**, 28–35 (2018).

30 N. Honda, K. Ishii, T. Terada, *et al.*, “Determination of the tumor tissue optical properties during and after photodynamic therapy using inverse monte carlo method and double integrating sphere between 350 and 1000 nm,” *Journal of biomedical optics* **16**(5), 058003 (2011).

31 H.-W. Wang, T. C. Zhu, M. P. Putt, *et al.*, “Broadband reflectance measurements of light penetration, blood oxygenation, hemoglobin concentration, and drug concentration in human intraperitoneal tissues before and after photodynamic therapy,” *Journal of biomedical optics* **10**(1), 014004 (2005).

32 T. L. Becker, A. D. Paquette, K. R. Keymel, *et al.*, “Monitoring blood flow responses during topical ala-pdt,” *Biomedical Optics Express* **2**(1), 123–130 (2011).

33 T. A. Middelburg, S. C. Kanick, E. R. de Haas, *et al.*, “Monitoring blood volume and saturation using superficial fibre optic reflectance spectroscopy during pdt of actinic keratosis,” *Journal of biophotonics* **4**(10), 721–730 (2011).

34 G. Yu, T. Durduran, C. Zhou, *et al.*, “Noninvasive monitoring of murine tumor blood flow during and after photodynamic therapy provides early assessment of therapeutic efficacy,” *Clinical cancer research* **11**(9), 3543–3552 (2005).

35 M. Khurana, E. H. Moriyama, A. Mariampillai, *et al.*, “Intravital high-resolution optical imaging of individual vessel response to photodynamic treatment,” *Journal of biomedical optics* **13**(4), 040502 (2008).

36 I. Wang, S. Andersson-Engels, G. Nilsson, *et al.*, “Superficial blood flow following photodynamic therapy of malignant non–melanoma skin tumours measured by laser doppler perfusion imaging,” *British Journal of Dermatology* **136**(2), 184–189 (1997).

37 A. L. Maas, S. L. Carter, E. P. Wileyto, *et al.*, “Tumor vascular microenvironment determines responsiveness to photodynamic therapy,” *Cancer research* **72**(8), 2079–2088 (2012).

38 B. W. Pogue, J. A. O'Hara, I. A. Goodwin, *et al.*, "Tumor po2 changes during photodynamic therapy depend upon photosensitizer type and time after injection," *Comparative Biochemistry and Physiology Part A: Molecular & Integrative Physiology* **132**(1), 177–184 (2002).

List of Figures

List of Tables

Paper VI

Potential biomedical use of diode-laser-induced luminescence from upconverting nanoparticles

M. Mousavi, S. Andersson-Engels.

(2018) *Handbook of Semiconductor Lasers and Diode-based Light Sources in Biophotonics, Institution of Engineering and Technology.*

Chapter 9

Potential biomedical use of diode-laser-induced luminescence from upconverting nanoparticles

Monirehalsadat Mousavi[1] *and*
Stefan Andersson-Engels[2,3]

9.1 Introduction

The intention with this chapter is to briefly review the capabilities made possible in the field of biomedical diagnostics and treatment by employing upconverting nanoparticles (UCNPs), as well as the importance of appropriate light sources for such applications. The field of UCNPs in biomedicine has grown rapidly the last decade, since they first were made sufficiently small and bright to be of real interest for biomedical applications. This research has been reviewed previously (see, e.g., [1–7], while this chapter will focus on recent advances in the use of UCNPs for preclinical applications and diagnostic assays using laser diode excitation.

9.1.1 Present challenges in biomedical imaging

The development of novel imaging modalities is of high importance in the field of medicine, for the purposes of clinical diagnostics and therapy [8]. It is of equally importance for preclinical studies in biomedical research and for screening of pharmaceutical drugs. The ability to visualise morphological structures of various sizes, from subcellular structures to organs, can provide essential diagnostic and prognostic information for a diseased patient, such as the cause, extent and prognosis of a disease. In clinical care, and also to an increased extent in preclinical studies, diagnostic information is today provided by amongst other techniques various diagnostic imaging modalities (*in vivo* or *ex vivo*). These modalities include optical X-ray, magnetic resonance imaging (MRI), ultrasound and histopathological examinations. In particular, the quickly growing incidence of detected malignancies will require further extensive development and refinement of various imaging techniques, both *in vivo* and for histopathological samples, to facilitate adequate care [9]. It would for these patients be of particular interest to benefit from

[1] Department of Physics, Lund University, Sweden
[2] IPIC, Tyndall National Institute, Cork, Ireland
[3] Department of Physics, University College Cork, Ireland

improved possibilities for visualisation of the confinement and spread of the malignant cells in the treatment planning and prognostic assessments. In 2008, malignant deceases became the leading cause of death in the world and lead to 13% of deaths (equal to 7.6 million deaths annually) [9,10]. Furthermore, the trend is that the death toll of malignant deceases will continue to grow and is expected to become 13.1 million deaths annually by the year 2030.

A key prognostic factor for malignant deceases is the time of initiating adequate treatment. Early treatments require early detection – yielding that improved diagnostic potential provides a potential to significantly reduce mortality and morbidity of malignancies. Thus, malignant deceases alone motivates the development of improved imaging and other diagnostic tools, both in terms of sensitivity and specificity of malignant decease at a very early stage [11]. Today the most used anatomical imaging modalities for deep tissue imaging includes primarily X-ray computed tomography (CT), MRI, ultrasonography (US), positron emission tomography (PET) and single-photon emission computed tomography (SPECT) [12,13]. So far, optical imaging (OI) has mainly been used for endoscopic and microscopic imaging. Subsurface imaging is much more challenging due to the high light scattering and absorption properties of tissue, limiting the imaging depths [14,15]. However, with the development of much improved clinically adapted sources and detectors, imaging beyond millimetres and even centimetres has today become possible. As shown in Figure 9.1, OI techniques have proven to be significantly faster, more compact and cost effective, and possess excellent molecular

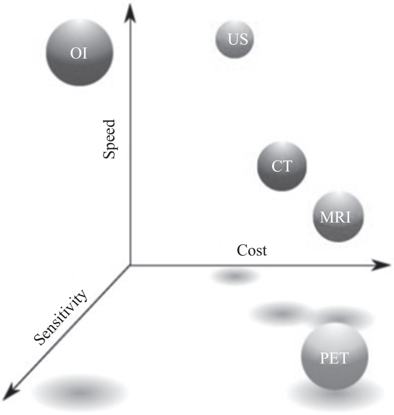

Figure 9.1 This image illustrates how optical imaging (OI) is compared to conventional biomedical imaging techniques in terms of sensitivity, acquisition speed and cost. The illustration is reprinted with permission from the PhD thesis of Can Xu [23]

sensitivity through the use of fluorescent contrast agents, as compared to conventional non-optical techniques [12,15,16]. Today, diffuse optical imaging (DOI), diffuse optical tomography and diffuse optical spectroscopy (DOS) are used to, for example, monitor and visualise tumour protease activity [17], apoptosis [18], brain activity [19,20], breast cancer [21] and to control photodynamic therapy treatments of cancer [22].

In a similar way, preclinical, often whole-body, imaging has rapidly grown in use and importance. This is primarily in an effort to make preclinical studies less expensive and time-consuming. The vision and trend is to adhere to the 3R principle (replace, reduce and refine) animals studies by designing an increasingly fraction of longitudinal studies, where each individual animal is followed throughout the study. This strategy would facilitate studies of any disease development or treatment response based on few subjects only.

9.1.2 Motivation of interest for optical bioimaging

Despite the many merits of OI techniques, several challenges and limitations exist, in particular related to the spatial resolution and limited penetration depths in certain tissues illustrated in Figure 9.1. There exists a general ambition to find ways to improve the OI and spectroscopy techniques by employing novel contrast agents known as UCNPs, as well as models for light-tissue interaction. This may potentially enhance several aspects of current optical techniques, including the sensitivity, depth penetration, spatial resolution, quantitative accuracy and system complexity. The OI techniques can provide excellent spatial maps of quantities of interest, however, this is often at the cost of little to no spectral information. DOS can be used to obtain spectral information and has already been used heavily in numerous tissue diagnostics applications [24–26].

When employing OI, one can rely on a number of different contrast mechanisms. OI employs typically molecular contrast rather than morphological structures for imaging. The molecular contrast can either be through absorption (such as in DOI), luminescence or scattering (such as in various Raman-based techniques). This chapter will concern luminescence-based techniques. The luminescence emission is generally originating in molecules present in the tissue, either tissue endogenous molecules present naturally in the tissue, or exogenous agents used as contrast agents for improved imaging qualities. The exogenous drugs used for imaging are often based on fluorescence dyes that are preferentially located in the tissue structures to be imaged. Important characteristics for the contrast agent is that it should provide a characteristic signal easily discriminated from tissue autofluorescence, it should not bleach easily when illuminated and obviously be selectively bound to the tissue structures to image. The excitation and emission wavelengths are also important as they define the probe volume and spatial resolution that will be obtained in the image. Also genetically encoded markers are used, such as fluorescence proteins. These contrast agents are produced by genetically modified cells, and will thus label these cells very uniquely. The drawback with this technique is that the cells labelled are genetically modified, and thus only applicable in specially engineered preclinical studies.

9.1.3 Genetically modified and exogenous molecular labelling

Controlled activation of biomolecules is very crucial in medicine, for example, controllable gene delivery/knockdown in gene therapy and anti-cancer drug delivery in cancer chemotherapy. Photoactivation provides an elegant approach for on-demand site-specific molecule release with high spatio-temporal precision. Unfortunately, photoactivable molecule vectors mostly respond to ultraviolet (UV) and blue radiation, which has very limited penetration depths and light toxicity to biological tissues. This makes direct-UV-irradiation-based photoactivation method unrealistic in deep tissues in *in vivo* systems. A very unique and recently suggested photoactivation approach, employing lanthanide doped UCNPs as energy transducers, opens the possibility of implementing light-controlled biomolecule activation in deep tissues [27,28]. UCNPs, upon near-infrared (NIR) excitation, can generate UV emission, which acts as a switch to activate biomolecules in vicinity. The NIR excitation guarantees maximised penetration depth and minimised adverse effects of excitation light in tissues, while the localisation of UV or blue emission vanishes its toxic effect on non-targeted tissues.

9.1.4 Motivation of interest for UCNPs for bioimaging

With photon upconversion we mean a process in a medium where energy of the photons emitted are higher than for those absorbed. Typically two or more photons are absorbed and their combined energy is higher than the emitted photon they generate through the upconverting process. This reduction in number of photons makes the process possible as it guarantees conservation of energy. The process is schematically shown in Figure 9.2(b). The generated, the so-called upconverted, emission is also known as anti-Stokes shifted emission. The upconversion phenomenon was first observed by Bloembergen in 1959. He proposed that the concept could be used for infrared quantum counters [29]. Today, upconversion is, for example, used in infrared markers to visualise near-infrared light, otherwise invisible for the human eyes. While the upconversion mechanism proposed by Bloembergen relied on meta-stable real states in crystal hosts, with the availability of lasers, upconversion is today routinely realised in multiphoton microscopy [30], triplet–triplet annihilation [31–33] and other nonlinear effects in crystals and gases [34]. The processes of upconversion were thoroughly investigated by Auzel [35–37]. The interest of these materials came with the development of these materials in form of nanoparticles. Faris *et al.* pioneered this early biomedical research of UCNPs [38]. The field gained increased interest once UCNPs were produced with considerable improved quantum yield (QY) [39–48]. The UCNPs used today for biomedical applications include mainly rare-earth metal doped nanocrystals. Frequently $NaYF_4$ is used as a host material in these nanoparticles, due to the low losses of the emission in these materials. The UCNPs have been demonstrated to provide unique properties, clearly providing potentials for improved optical bioimaging, as reviewed in this chapter. These advantages will be discussed in more detail under the *Photophysical properties* and *Applications* subchapters below.

9.1.5 Use of diode lasers for upconversion nanoparticle-based bioimaging

In order to gain full interest of UCNP-based imaging for the biomedical community, it has to be safe, provide better results than other markers and also be cost-effective. As far as the community so far has been observing, the particles are biocompatible, in the sense that they can be administered systemically without complication. No toxicity at concentrations of biomedical interest has been observed [49], while more studies in this topic obviously are necessary before any use in human studies. Such studies are underway.

Cost-effectiveness is ensured by availability of commercial particles, either coated with specified functional material to specifically bind to a number of predefined and identified tissue targets, or as bare particles, that can be coated by the users with their own specific targeting coating. Instrumentation-wise the technique can also be kept at low cost through the use of inexpensive diode lasers for excitation and conventional laboratory cameras for detection. An intention with this chapter is also to discuss the specific properties of the excitation sources to enable optimised detection possibilities. In particular, wavelength, power and pulse duration properties are essential. For many applications, the possibility to couple the light into large core-size multi-mode optical fibres is crucial. The most important identified properties of the excitation source are discussed in the subchapter *Sources*. In this respect, both the spectral and temporal properties of the light source is of importance, as will be further discussed below.

9.1.6 Organisation of chapter

The organisation of this chapter is as follows. After the introduction, a subchapter entitled *Photophysical properties* is provided. Here the main properties of the particles are discussed, together with a brief description of the unique possibilities these properties provide for biomedical imaging. This subchapter is relatively more extensive than the others, as most of our own research has been within characterising UCNPs for biomedical applications, and identify the unique properties, so they can be utilised as well as possible.

Next follows a subchapter briefly discussing some of many potential biomedical applications, where UCNPs can become an enabler for successful studies or biomedical procedures. This subchapter will review selected applications, to illustrate the vast possibilities with UCNPs for biomedical use.

Before the final summary of the chapter, being a part of *Handbook of Semiconductor Lasers and Diode-Based Light Sources in Biophotonics*, we will also discuss the essential properties for the sources to generate as useful information as possible. These properties are primarily wavelength, pulse-length, power and beam properties. In addition, the importance of short- and long-term stability will be addressed.

9.2 Optical properties of UCNPs

The interaction between light and tissue is strong, making the depth of light penetration limited to a rather shallow region. The interaction is due to both absorption and scattering. The light-tissue interaction and thus light penetration is dependent on its wavelength. The near-infrared wavelength region is beneficial for deep light penetration, due to low absorption and scattering for light in this wavelength range. Selecting the best contrast agent and light source thereby ensures that the light penetrates the furthest through tissue, enabling that deeply located target cells can be investigated. Furthermore, in luminescence imaging employing UCNPs as a contrast agent, the signals also clearly depends on the concentration of UCNPs, their absorption cross section and QY. Techniques for characterisation and synthesis of UCNPs and various factors for optimisation of their luminescence efficiency are addressed in this subchapter.

9.2.1 Upconversion process

The photophysical pathway associated with upconversion (UC) photoluminescence is relatively well understood. UC refers to non-linear optical processes in which sequential absorption of two or more low-energy photons results in higher-energy emission. It is thereby described as an anti-Stokes mechanism. There are three main processes causing upconversion (shown in Figure 9.2): Excited state absorption (ESA), also known as sequential two photon absorption; energy transfer upconversion (ETU); and photon avalanche effect (PA). The principles of them are all schematically presented and discussed in several review articles [37,50–52]. In ESA (illustrated in Figure 9.2(a)) is a pumping mechanism suitable for single-doped materials for which the emitting ion first absorbs one photon of proper energy to be prompted from the ground to the first excited state (E1). Sequentially it is then excited again now from E1 to emitting level (E2) by absorption of another pump photon. The two pump photons can be generated from the same source if the

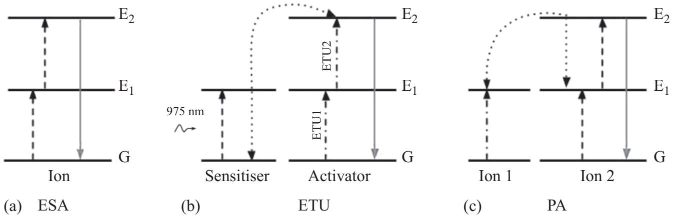

Figure 9.2 This image shows simplified energy diagram of the upconversion photoluminescence mechanism: (a) excited state absorption (ESA); (b) energy transfer upconversion (ETU); and (c) photon avalanche (PA). Dashed, solid and dotted lines represent photon absorption, photon emission and energy transfer processes, respectively

two energy gaps are equal. UC emission achieved via ETU follows a similar principle as those of ESA, whilst the UC process involves a non-radiative energy transfer between neighbouring ions in the crystal (sensitiser and activator), as depicted in Figure 9.2(b). In the ETU process, the sensitiser absorbs a photon and is excited to an excited state. The activator is through the energy transfer in a first step excited to an intermediate level (E1), and then, following a second absorbed photon by the sensitiser, sequentially transferred to a higher excited level (E2). The photon avalanche effect, is also based on sequential energy transfers between ions as result of cross relaxation process, simplified in Figure 9.2(c). All of these mechanisms take advantage of employing real intermediate energy levels. These intermediate levels also possess a relatively long lifetime (in the order of milliseconds). Therefore, the simultaneous absorption of two and more photons is not required, and the excitation intensity for observing upconversion can be achieved by using low-cost lasers suitable for biological applications. This is in sharp contrast to the mechanisms employed in multiphoton photoluminescence, requiring very intense excitation (typically femtosecond lasers) as all excitation photons need to be present simultaneously due to the virtual intermediate energy level unable to store the absorbed photon energy. Competition for the depopulation of the intermediate state of the involved activator governs the power density dependence of the upconversion luminescence intensity and consequently, the QY.

9.2.2 Lanthanide-doped UCNPs

The Lanthanide (Ln) ions, also known as rare-earth metals, with a ladder-like energy level structure are the most commonly used luminescent centres for upconversion luminescence, owning their special electron configuration with a filled outer 4f electron shell and stable excitation state. Ln-doped ions generally comprise a nanoscale inorganic host, doped with sensitiser and activator ions [53]. The most popular UCNP represents $NaYF_4$ as inorganic crystal matrix, co-doped with lanthanide ions in the form of the sensitiser ytterbium Yb^{3+} and activator Er^{3+} or thulium Tm^{3+}. The widely accepted energy level diagram of $NaYF_4$:Yb^{3+}, Er^{3+} is shown in Figure 9.3. The sensitisers absorb energies from NIR photons and then transfer their excitation energy to the activators from where radiation can be emitted.

Apart from the upconversion phenomena, UCNPs benefit from their unique properties including, sharp emission bandwidth, long lifetime, high photostability and low cytoxicity, all being very desirable properties in biotechnology. Since the optical properties of lanthanide ions are greatly determined by the f-f electron transitions, their forbidden nature (Laporte rule) [54] leads to a long lifetime – in the order of milliseconds. Distinguished from traditional fluorescent labelling agents, RE-doped UCNPs can be excited by sequential absorption of two or more NIR photons and emit light at shorter wavelengths (range of NIR-UV to NIR). This upconversion mechanism possesses several advantages which include: (i) high signal-to-background ratio and thereby high detection sensitivity due to the absence of autofluorescence; (ii) deep penetration of NIR light into biological tissue and less photo damage to biological samples. In contrast to direct two photon absorption, upconversion processes are often related to energy stepwise transfer between a

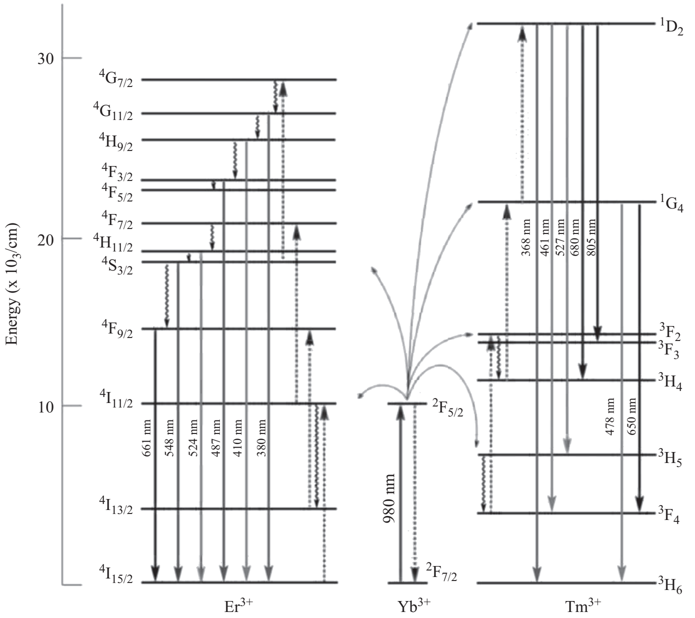

Figure 9.3 Energy-level diagram and upconversion scheme for the Yb^3+-sensitized Er^3+ and Tm^3+ systems is shown. The figure is taken from [7] with permission

sensitiser and activator. This results in much higher efficiency of upconversion, excitation can be achieved at substantially lower power continues wave diode laser. Individual UCNPs have been spectroscopically investigated and no photobleaching or photodamage was reported after 1 h of continues laser illumination [55]. Moreover, UCNPs showed non-blinking behaviour since the upconversion process accruing among numerous randomly positioned ions in a single UCNPs which produce steady-state emission after continues exposure to a high excitation energy level.

The absorption probability of UCNPs is determined by the doped lanthanide ions. The majority of lanthanide ions exhibit low absorption cross sections leading to poor excitation efficiency. To enhance upconversion efficiency, co-doping with a second ion as a sensitiser with a high absorption cross section in NIR region is generally utilised. Among the lanthanides, Yb^{3+} (1.2×10^{-20} cm^2 at 980 nm) and Nd^{3+} (1.2×10^{-19} cm^2) have relatively large absorption cross section. The absorption band of Yb^{3+} is due to ${}^2F_{\frac{7}{2}}$–${}^2F_{\frac{5}{2}}$ transition and well resonant with f-f transition of many activator ions, such as Er^{3+}, Tm^{3+} and Ho^{3+} [56,57]. The selection of different emitters in terms of combinations of lanthanide dopants is a novel approach to generate tunable multicolour conversion emission [56,58]. It is notable that the emission spectrum of an UCNP is associated with the host composition, particle size and particle surface properties. Contrary to the Yb which has a very narrow band absorption and only one excited state $({}^2F_{\frac{5}{2}})$, Nd has multiple NIR excitation bands at wavelength 730, 808 and 865 nm corresponding to transitions from ${}^4I_{\frac{9}{2}}$ to ${}^4F_{\frac{7}{2}}, {}^4F_{\frac{5}{2}}$ and ${}^4F_{\frac{4}{2}}$, respectively. The absorption by water around these excitation wavelengths is much lower than that at 980 nm, allowing not only light to penetrate deeper into biological tissue, but also minimising tissue damage due to heating effect. Additionally, the large absorption cross section and efficient energy transfer from excited Nd^{3+} to Yb^{3+} ions suggest Nd as a promising candidate for bioimaging applications [59–62]. Another interesting novel approach to address overheating by shifting the excitation to shorter wavelengths is to utilise an organic broadband dye-sensitised antenna molecules to increase the absorptivity and broadens the absorption spectrum of upconverter as well as enhance the overall upconversion efficiency by a factor of 3.3 [63].

While many Lanthanide-doped host materials have been observed to exhibit upconversion luminescence, a significant effort has been focused on the optimal selection of host material, dopant ions and dopant concentration to achieve most efficient UC luminescence with controllable emission profiles. The choice of host lattice determines the distance between ions and consequently, concentration of ions. In the case of sensitised UC luminescence the average distance between dopant ions significantly influence the upconversion efficiency. The sensitiser concentration must be high enough to optimise energy transfer between sensitiser and activators, but not so high to be influenced by deleterious cross-relaxation effects. The three-dimensional lattice structure of host material brings the luminescence centres into the optimal position with respect to the ion-to-ion distance and spatial distribution of dopant ions. An ideal host material should be optically transparent, chemically and thermally stable and possess low phonon cut-off energies [64]. The local structure of lattice is known to have an impact on its optical properties. It was found that the intensity of the upconversion luminescence in hexagonal-phase $NaYF_4$:Yb^{3+}, Er^{3+} is approximately 10 times stronger than that in cubic one for otherwise identical particles [65]. The emission intensity of an upconverting material depends also on its dimension. Although the small nanoparticles are advantageous to the biological applications, the reduced particles size leads to an increase of surface-to-volume ratio of materials and thus more defects on the nanoparticles surface is introduced [66]. There are now many methodologies to synthesise nanoparticles with desired size and chemical compositions.

9.2.3 Synthetic methods of UCNPs

In the use of UCNPs as luminescent labels in biological applications, suitable size and uniform shape of the nanocrystals and high aqueous solubility are the primary prerequisites for imaging. The size of the particles plays a key role in the uptake, biodistribution and clearance of nanoparticles in living organisms. Sizes comparable to the biomolecules are required so as not to interfere with cellular systems. Great efforts have been dedicated to exploring the efficiency of various methods for the synthesis of UCNPs [57,67,68]. The thermal decomposition and hydro(solvo)thermal synthesis have become the most popular methods as they provide excellent control over shape, particle size and phase of fluoride UCNPs.

The thermal composition method. Thermal composition method was first employed by Yan and colleagues for fluoride-based nanocrystals via the co-thermolysis of the trifluoroacetate precursors in a solution of surface ligands, octadecene (ODE), and capping ligands, oleic acid (OA), at high temperature ($\approx$300 °C) [69]. In this reaction, the octadecene was used as the primary high boiling surface solvent to provide high temperature environment. Oleic acid acted as a capping ligand to control the particles growth and stabilise the growing particles in solution. Yi replaced the ODE and OA by a single olelyamine (OM) and produced uniform and small size $NaYF_4:Yb^{3+}$, Er^{3+} and $NaYF_4:Yb^{3+}$, Tm^{3+} [70]. In addition, Mai *et al.* synthesised monodisperse high-quality cubic-(α) and hexagonal-(β) phase particles with controllable size in OA/OM/ODE mixture [71]. The thermal decomposition synthesis procedure has been refined by several groups and now is a general route to synthesis monodisperse and well-defined size nanocrystals in different phases. So far, a series of UCNPs based on $NaYF_4$ [67,70–72], $NaGdF_4$ [71,73], $NaYbF_4$ [74], $LiYF_4$ [75,76] and $BaGdF_5$ [77] hosts have been synthesised through this particular method. The thermal decomposition method requires expensive and toxic air-sensitive metal precursors and control of high reaction temperature. The need for non-polar capping ligands on the surface of UCNPs entails further surface modification to make them water-soluble.

Hydro(solvo)thermal synthesis. The solvothermal techniques operate at much lower temperatures and produce fewer toxic by-products than the thermal decomposition methods. This approach utilises a solvent in a sealed environment under pressure and temperature above their critical point to facilitate the interaction of precursors during synthesis. Typically, the reaction takes place in specialised vessels known as autoclave involving mixing of lanthanide and fluoride precursors in an aqueous solution. Li and co-workers reported hydrothermal synthesis of $\beta{-}NaYF_4:Yb^{3+}$, Er^{3+} UCNPs of controlled size and morphology in different solvents aided by cetyltrimethylammonium bromide (CTAB) and ethylenediaminetetraacetic acid (EDTA) [78]. It was observed that the NPs size and their morphology is not easy to control when water is used as a solvent (hydrothermal). However, spherical nanoparticles on the order of 20–30 nm are produced in acetic acid and uniform size of 50 nm were generated in ethanol (solvothermal). A “one pot process” with heat-resistant organic polymer (e.g., PVP, PEI) added to the solvent and polyacrylic acid (PAA) as capping ligands was reported by Wang *et al.* [79]. The pure hexagonal phase UCNPs with a uniform size of about 40 nm β-$NaYF_4$, with the capability of readily dispersing in aqueous media, was fabricated. The feasibility of this method has been demonstrated by several groups.

Coprecipitation is another friendly and convenient approach for synthesising lanthanide doped $NaYF_4$ UCNPs [80]. The benefits of this method are operational simplicity, easy control of particle size and composition, and the lack of toxic by-products.

In addition to discussed methods, also other less well known synthetic routes such as sol-gel [81], microemulsion [82,83] and flame synthesis [84] have also been employed for the generation of luminescence non-crystalline nanoparticles of varying host materials.

9.2.4 Surface modification

The UCNPs fabricated by many of these available methods are prepared using an organic environment, such as oleic acid, and are surrounded by hydrophobic capping ligands. A preparation with hydrophilic nanoparticle surfaces is required for biomedical applications (or they will aggregate immediately after in vivo administration to the water rich tissue [85–88]. Therefore, surface modification is necessary to convert the hydrophobic UCNPs into hydrophilic ones. In addition to hydrophilicity, surface functionality is required to facilitate the conjugation between UCNPs and biomolecules. Surface modification of UCNPs can be classified into two broad categories: (1) coating with an inorganic shell layer and (2) modification with organic capping ligands. The most frequently employed method in inorganic surface functionalisation is surface silanisation of silicon. Silica is an attractive coating with a negligible influence on the luminescence properties of UCNPs. The surface silanisation technique can be used to modify the surface of both hydrophobic and hydrophilic UC nanocrystals. The Stöber method has been widely used to apply a uniform coating of silica on hydrophilic NPs while UCNPs with hydrophobic ligands surface are coated with well-established reverse microemulsion method. Li and Zhang reported a uniform size (10 nm) silica-coated polyvinylpyrrolidone (PVP) stabilised $NaYF_4$:Yb, Er/Tm nanoparticles in a mixture of ethanol-water solution via Stöber method [89]. The thickness of silica shell can be adjusted within 1–3 nm by varying the initial amount of tetraethoxysilane (TEOS), see Figure 9.4. Silica-coated UCNPs are highly stable, biocompatible and well dispersible in aqueous buffers [90,91]. Silanisation method provides a core shell structure which creates an easily accessible platform for introducing the various functional group (e.g., $-NH_2$, –COOH or –SH, etc.) for the further conjugation

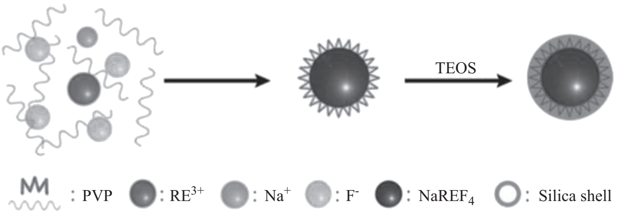

Figure 9.4 Schematic illustration of the $NaYF_4$:Yb,Er@PVP silica-coated. The concentration of TEOS controls the size of silica shell thickness [92]

with biological molecules. Another inorganic surface modification scheme is core-shell concept discussed in Section 9.2.5.

The most common surface modification strategies with organic capping ligands investigated are ligand-exchange, oxidation, absorption and free modification, as well as what is called the layer-by-layer (LbL) method. In the ligand exchange process, bifunctional organic molecules are utilised to replace the original hydrophobic OA ligands. To date, hexanedioic acid [93], 1,10-Decanedicarboxylic acid [94], 11-mercaptoundecanoic acid [94], citric acid [55,73,95], poly(ethyleneglycol)-phosphate [96], polyacrilic acid (PAA) [72,97,98] and polyvinylpyrrolidone (PVP) [99] are the most common acids and polymers used in a ligand exchange process. The ligand oxidation is an alternative method based on the chemical reaction of surface ligands [100]. The capped OA ligands of UCNPs are oxidised into azelaic acid and nonanoic acid with the Lemieux–von Rudloff reagent. This results in the generation of free carboxylic acid group on the surface due to the cleavage of unsaturated carbon-carbon bonds. In the OA ligands, the oxidised UCNPs modified with carboxylic acids exhibit the same size, shape and luminescence properties as the original UCNP. The transformation of hydrophobic UCNPs to hydrophilic materials can be achieved also through the absorption of an amphiphilic polymer onto the surface of the nanoparticles as a result of hydrophobic-hydrophobic van-der-Waals interactions. Chow *et al.* [101] reported modifying the coating of $NaYF_4$:Yb,Er@$NaYF_4$ to become an amphiphilic layer consisting of 25% octylamine and 40% isopropylamine modified PAA. Speghini *et al.* reported that the formation of an oleate double layer around colloidal CaF_2:Yb,Er/Ho/Tm nanoparticles rendered stable water suspension [102]. Wang *et al.* modified this strategy and developed a method of depositing LbL to successfully generate water-soluble UC nanoparticles. This technique involved the electrostatic attraction between oppositely charged species [103]. The LbL assembly technique permits the preparation of coated colloids of different size and shape with high stability and biocapability.

9.2.5 The core-shell concept

The dopant ions distributed at the surface of UCNPs are readily quenched through non-radiative decay pathway due to the presence of surface ligands with high vibrational oscillators, weakly bound surface impurities and crystal imperfections, as well as solvent molecules. The luminescence quenching can be reduced by forming a uniform core without sensitiser ions with small lattice mismatch around the core, to protect the host lattice and greatly minimise the surface quenching-induced emission losses. The most straightforward choice for the shell materials is the same pure host materials of the core particles with no optical active ions, called as active core/inert shell. Chow *et al.* [101] reported a significant luminescence enhancement of nearly 30 times by 1.5 nm tick shell of undoped shell materials on the surface of $NaYF_4$ Yb,Tm core particles and 7.4 times for $NaYF_4$:Yb,Er core particles. These small core/shell nanoparticles (11 nm) were rendered hydrophilic with an amphiphilic layer of polymer. A heterogeneous core-shell nanostructure can also be synthesised with different core and shell materials. In this case, the quality of core-shell structure can be characterised in transfer electron microscopy (TEM) as the core and shell will differ. To further enhance upconversion luminescence and also tunability of the upconversion luminescence, optically active centres have been introduced in the shell layers, fabricating active core/active shell structure. For example, Capobianco and co-workers have demonstrated a significant increase in the intensity of upconversion in $NaGdYF_4$:Yb^{3+}, Er^{3+} active core $NaGdYF_4$:Yb^{3+} active shell compared to $NaGdYF_4$:Yb^{3+}, Er^{3+} active core $NaGdYF_4$ inert shell and $NaGdYF_4$:Yb^{3+} active core only nanoparticles [104].

9.2.6 *Quantum yield*

The luminescence QY determines the efficiency of the conversion of absorbed photons into emitted fluorescence photons. Since the intensity of an upconversion process has a nonlinear dependency on absorbed pump power, the QY will be power dependence. As will be seen below, this will be a linear dependence for a 2-photon process below saturation excitation levels, gradually going towards a constant value for saturating power densities. Thus, it is critical to measure the exact excitation power density to evaluate the QY precisely. Determination of QY of conventional fluorophore has been carried out via two widely used experimental setups: a fluorometer and integrating sphere. However, there have not been any report on measuring the absolute QY of UCNPs until recently where Boyer *et al.* have successfully designed a setup based on integrating sphere using a basic spectrometer and an inexpensive diode laser [105]. In their study, they have measured the QY of $NaYF_4$ UCNPs in various sizes ranging from 10 to 100 nm. QY was measured to be in the range of 0.005% to 0.3% for particles and 3% for bulk material. A fluorometer can also be utilised to measure relative QY of UCNPs through careful optical characterisation by comparison to a reference fluorophore with known QY. Xu *et al.* reported a QY of the 800 nm emission of hexagonal-phase core-shell $NaYF_4$:Yb^{3+}, Tm^{3+} $NaYF_4$ using spectrofluorometer-based setup. A QY of 3.2% was measured under an excitation intensity of 78 W/cm^2. They theoretically compared the QY of the UCNPs with the most efficient two-photons dye under the same experimental conditions. It was observed that the two-photon dye is 8 orders of magnitude less bright for realistic power densities a few centimetres deep in tissue.

In almost all reports so far, QY values are published without consideration of their complex dependency to the power density. This ignorance leads to incomparable results from different studies. Thus, a standard protocol for QY measurement of UCNPs to provide complete information about UC is desirable. Liu *et al.* proposed a simple approach to fully describe the QY of UCNPs for arbitrary excitation power densities. In this method, a simplified steady-state condition for the population of excited energy state of Yb^{3+} is considered from a rate-equation analysis. As depicted in Figure 9.2(b)) the activator is described by a quasi-three-level model including ground state G, the intermediate state E1 and the emitting state E2. The incoming photons excite the sensitiser ground state which is well populated. The laser power (photon flux) (ρ), dopant concentration and absorption cross sections (σ)

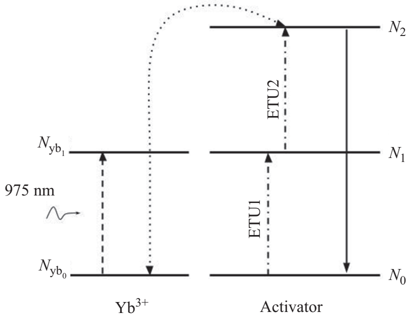

Figure 9.5 Simplified energy levels model used for the rate equation modeling

determine the ground state excitation rate. As shown in Figure 9.5, these parameters can be indicated in the following steady-state rate equations:

$$\frac{dN_{\mathrm{Yb}_1}}{dt} = \sigma\rho N_{\mathrm{Yb}_0} - \frac{N_{\mathrm{Yb}_1}}{\tau_{\mathrm{Yb}_1}} = 0 \tag{9.1}$$

$$\frac{dN_1}{dt} = C_0 N_0 N_{\mathrm{Yb}_1} - C_1 N_1 N_{\mathrm{Yb}_1} - \frac{N_1}{\tau_1} = 0 \tag{9.2}$$

$$\frac{dN_2}{dt} = C_1 N_1 N_{\mathrm{Yb}_1} - \frac{N_2}{\tau_2} = 0 \tag{9.3}$$

Where τ_{Yb_1}, τ_1 and τ_2 are the lifetimes of sensitiser excited level, activator intermediate level and activator emission level, respectively. In this equation, a term representing the depletion of the population of sensitiser excited state due to ETU is neglected since the linear decay is the dominant depletion mechanism [106]. This is also the case for the population depletion of activator emission state E2 due to ETU to even higher energy levels. After rearranging and solving the above system of equations, the QY of two-photon upconversion emission can be obtained as follows:

$$\eta \equiv \frac{P_{\mathrm{lum}}}{\sigma N_{\mathrm{Yb}_0}\rho h v} = \eta_s \cdot \frac{\frac{\rho}{\rho_b}}{1 + \frac{\rho}{\rho_b}} \tag{9.4}$$

with

$$\rho_{\mathrm{b}} = \frac{hv}{\sigma\tau_1\tau_{\mathrm{Yb}_1}N_{\mathrm{Yb}_0}C_1} \tag{9.5}$$

and

$$\eta_s = C_0 N_0 \tau_2 \tau_{\mathrm{Yb}_1}/\tau_2^{\mathrm{rad}} \tag{9.6}$$

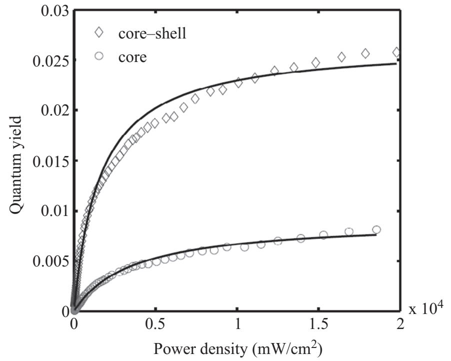

Figure 9.6 Experimentally determined QYs for the 800 nm upconversion emission band of core NaYF$_4$:Yb^{3+}/ Tm^{3}+ and core-shell NaYF$_4$: Yb^{3+}/Tm^{3+}@NaYF$_4$ UCNPs. The solid lines are the fitted curves using (9.4). The fitting parameters used for the core particles are $\rho_b = 3{,}800$ mW/cm^2 and $\eta_s = 0.91\%$, and for the core-shell particles they are $\rho_b = 1{,}300$ mW/cm^2 and $\eta_s = 2.6\%$. Reproduced from ref [107] with permission from The Royal Society of Chemistry

where ρ_b is referred as balancing point when the ETU rate and linear decay rate equally contribute to the depopulation of the intermediate state E1, i.e., $\frac{N_1}{\tau_1} = C_1 N_1 N_{\mathrm{Yb}_1}$. The η_s is the maximum attainable QY of the system when the pump power density is at the saturation level and τ_2^{rad} is the radiative lifetime of excited state E2. When the excitation intensity is at the balancing power density, $\rho = \rho_\mathrm{b}$, the QY, η, is the half of the maximum QY, η_s. As can be seen in Figure 9.6, experimental QY data acquired from measurement on core NaYF$_4$:Yb^{3+},Tm^{3+} and core-shell NaYF$_4$:Yb^{3+}, Tm^{3+} NaYF$_4$ is well fitted by the expression in (9.4).

The power density dependence of the QY can be extracted by the derivative of luminescence power, P_lum, over excitation photon flux, ρ, in a double log scale.

$$k \equiv \frac{d\log P_\mathrm{lum}}{d\log\rho} = 1 + \frac{1}{1 + \tau_1 \cdot C_1 \tau_{\mathrm{Yb}_1} \sigma N_{\mathrm{Yb}_0} \rho} \tag{9.7}$$

The slope efficiency, *k*, has a value of 1.5 at the balancing power density point. Under low excitation intensities, where the linear decay from E1 to G state is dominant over the ETU rate, the slope efficiency will be close to 2, indicating a quadratic dependence on the excitation intensity. An extra consideration needs to be applied in UCNPs QY measurement where non-uniform excitation spatial radiation, typically with a Gaussian profile, is illuminating the sample. A CCD-based detector was used to record the intensity distribution of a laser beam cross-section in real time to compensate for change on excitation power density to provide accurate QY information [108,109].

9.3 Applications

The advantages of UCNPs as imaging probes are derived from their unique upconverting luminescence (UCL) properties and also from the NIR radiation used for exciting UCNPs. Compared to visible light excitation, NIR excitation for *in vivo* imaging provides several advantages such as remarkable light penetration depth, weak autofluorescence, low tissue heating and weak non-specific photo-damage to biological samples. Therefore, the Ln-doped UCNPs are an attractive choice for biomedical applications, primarily for *in vivo* imaging and assays. To date, few aspects within small animal imaging have been studied, which include whole small animal body imaging, *in vivo* tumour targeting imaging, multimodal animal imaging, immunoassay, PDT and photo-activate ions.

9.3.1 Whole body small animal imaging

An early study on imaging of small animals using Ln-doped nanoparticles is reported by Zhang *et al.* injecting 100 μl of polyethyleneimine (PEI)-coated $NaYF_4$:Yb,Er nanoparticles subcutaneously in anaesthetised Wistar rats [39]. Luminescence signals were observed up to 10 mm beneath the rat's skin. The *ex vivo* biodistribution of PEI coated nanoparticles was investigated 0.5 h, 24 h and 7 days after injection. A rapid accumulation in the lung was observed 30 min after injection while the concentration of nanoparticles in all tissues was decreased 24 h after injection with highest concentration in the spleen. The nanoparticles were undetectable by 7 days post-intravenous injection. A long-term *in vivo* distribution study of PAA-UCNPs ($NaYF_4$:Yb,Tm) with NIR-to-NIR UCNP emission was conducted by Li's group by an UCNP imaging method [97]. The distribution analysis shows a long-term retention of nanoparticles in the lungs and spleen, similar to other reports. To date, a high contrast UCL imaging of whole body small animals with a penetration depth of 20 mm has been achieved [73]. Moreover, ultra-high sensitive stem cell labelling for long-term *in vivo* tracking was generated and used to detect as few as 10 cells in a mouse [110]. Biodistribution studies are useful indicators for studying the toxicity effects of the UCNPs. The absence of short term toxicity has been proven so far in various studies, encouraging further exploration of UCNPs for *in vivo* biomedical applications.

9.3.2 Tumour targeting imaging

Development of tumour targeting molecular imaging using upconversion materials is still a great challenge due to insufficient tumour accumulation which limits their further clinical application. However, their ability to easily bind targeting molecules is one important aspects of the use of UCNPs as bioprobes for bioimaging. The utilisation of Ln-UCNPs have been documented for tumour targeting imaging in few cases based on ligand-acceptor and antigen-antibody interactions. For instance, folic acid modified UCNPs and arginine-glycine-aspartic acid (RGD) peptide have been employed as a targeting agent for *in vivo* tumour targeting. On the basis of high affinity between folic acid (FA) and folate receptors (FR), the first successful example of *in vivo* targeting imaging with mice bearing HeLa tumours was reported [87]. Strong upconversion emission signals were collected from the location of the tumour. Afterwards, several FA-modified UCNP have been employed in various studies for targeted bioimagining of tumour cells [39,111–113]. Li and co-workers also used the RGD (RGD = arginine-glycine-aspartic acid) peptide conjugated UCNPs for targeted imaging of mice bearing U87MG tumours [114]. These probes show a significant increase in the avidity of α_v/β_3 integrin receptors, being over expressed in human glioblastoma U87MG tumours. It has been well known that most antibodies have high affinity for their antigens. The antigen-antibody reaction can be widely used as a useful strategy for targeted recognition for luminescence bioimaging. For example, anti-Her2 antibody was conjugated with nanoparticles to image cancer cells over-expressed with a protein called Her2 [115]. An obvious fluoresce pattern under a modified epifluorescence microscope was observed in the tumour as a direct result of Her2 recognition, whereas no significant fluorescence could be detected in a control group. In addition, the use of UCNPs as a feasible cell tracker tool was demonstrated by Zhang *et al.* The long-term stability of UCNPs has allowed to obtain information on cell dynamics at high resolution inside living animals [116]. Multicolour *in vivo* UCNP imaging is demonstrated in multiplexed lymph node mapping and multicolour cancer cell tracking by using a series of UCNPs with three different emission colours [117]. Moreover, vascular imaging of the mouse ear was performed. The probe was clearly visible more than 2 h post injection [118].

9.3.3 Multimodal imaging

Within the vision of future medical imaging to detect life-threatening diseases long before clinical manifest, even at the time of the earliest cellular changes that define the disease, improved diagnostics are needed. Two main lines towards meeting this vision are the use of molecular and multimodal imaging. Molecular imaging is the labelling of contrast agents with tumour/tissue specific targeting agents, for example, antibodies, affibodies, peptides and aptamers, by which it is possible to detect changes that occur on a cellular or molecular level. Multi-modal imaging is the combination of several imaging technologies to extract more information by combining the advantages of each technology, such as high spatial resolution, quantification ability, and portability. Key for this would be to accomplish additional value in using a combination of techniques, not to just get the same information in a multitude of ways. This development is expected to have a major impact on the detection and individualised treatment guidance of many diseases, the development of new drugs and our understanding of how disease arises.

UCNPs can be very interesting in the context of molecular sensitivity and multimodal approach, as they offer a contrast agent that could be used for both purposes. The molecular sensitivity can be achieved by coating the particles with specific targeting agents. Appropriate modification of the surface can provide selective binding to specific molecules. For this, the size of the particles is also of interest, as this is a critically important parameter for the biodistribution and pharmacokinetics of the compound following administration. Bigger particles will not be able to reach all parts of the body, and thereby not the molecules they are aimed to target. As a consequence most molecules targeted should be localised outside or on the cell membranes, i.e., for instance, being expressed on the cell membrane of the cells to be labelled. To obtain the capabilities of multimodal approach, the nanoparticles should be active in several respects. Upconversion nanoparticles provide an ideal platform for achieving multifunction, for example, multimodal imaging, sensing and therapy. This can be accomplished primarily by combining various nanomaterials to construct complicated heterogeneous nanostructures. This can be possible in multiple ways, depending on the techniques to combine in the imaging. By exchanging the commonly used matrix from $NaYF_4$ to one with a crystal lattice with Gd ions, like for instance NaGdF4, the nanoparticles would be detectable also with MRI [119–122]. The nanoparticles can also be optimised for simultaneous upconverting and downconverting imaging [123], providing also an opportunity to dual optical imaging.

Another approach that could be considered for multifunctional particles, would be to consider developing superparagmagnetic iron oxide (SPIO) nanoparticles coated with a UCNP shell [124,125]. Such particles would be possible to detect with magnetomotive ultrasound imaging [126], and with PET/SPECT if also attached to a radionucleid [127].

9.3.4 Bioassays

Bioassays are experiments that measure the effects of the substance on a living reporter system and are essential to provide information about biochemical substance such as a drug or bioactive substance. To achieve a high sensitive detection and accurate analysis of single biomolecules, efficient bioassay methods based on Ln-doped UCNPs probes have been developed. UCNPs are photostable and exhibit long-lived emissions even in an excitation field of relatively high power. In addition, the narrow emission line width of lanthanide ions in hosts (with full width at half maximum of 10–20 nm) increases the potential of changing the lanthanide dopants concentration to achieve distinguishable emission bands, enabling a large number of multiplexed detections [128]. The currently established biological assays are generally categorised into heterogeneous and homogeneous bioassays. The first use of upconverting phosphors in heterogeneous bioassay technique was reported by Zijlman and co-workers in the year of 1999 [129]. Two UCL reporters, including a green emitting ytterbium/erbium Y_2O_2S:Yb,Er and blue-emitting ytterbium/thulium Y_2O_2S:Yb,Tm particles conjugated to NeutrAvidin were used in a model system consisting of human prostate specific antigen. Later, Tanke *et al.* used the green emitting phosphor particles (Y_2O_2S:Yb,Er) to identify human papillomavirus type 16 infection via detection of specific nucleic acid molecules sequences [130]. Cooper *et al.* used phosphor particles with a composition of Y_2O_2S:Yb,Er and Y_2O_2S:Yb,Tm in lateral flow (LF) assays on human chorionic gonadotropin (hCG) to benefit from the advantages of this assay format with those of the UC phosphors reports system [131]. A detection limit of 10pg hCG in a

100 μl sample was achieved, which represents at least a 10-fold improvement over conventional reporter systems. The possibility of detecting two different targets simultaneously on the same membrane strip colour coded with two different UC phosphors compositions was proven as a concept of assay multiplexing. This was furthermore demonstrated by Niedbala *et al.*, where they developed a lateral flow strip assay format for simultaneous detection of amphetamine, methamphetamine, phencyclidine and opiates in saliva [132]. The 400-nm diameter spherical UCP particles were covalently conjugated to antibodies and were placed into the test by premixing with the sample or dried into a sample pad. Smaller magnetic and upconversion luminescent nanoparticles were produced through magnetic-field associated biochemical separation and concentration technology [133]. The magnetic nanoparticles were approximately 150 nm and were conjugated with nucleic acid for sensitive detection of trace amounts of DNA. The possibility of printing multiple antibodies was demonstrated by Hanna Päkkila *et al.* [134]. Three model analytes, including prostate specific antigen, thyroid-stimulating hormone and luteinising hormone, were selected to be used in evaluation of the performance of array-based immunoassay using a mix of secondary antibody-coated UCNP. Very recently, Kale has demonstrated spectrally and spatially multiplexed array-in-wall immunoassay for simultaneous classification and detection of serological samples utilising green-emitting IgG-coated UCNPs and blue emitting IgM coated to detect human IgG and IgM, respectively [135]. In this method, the differentiation between antigen specificity and antibody class was achieved based on the position and the colour of the signal, respectively. UCNP-based bioassays can achieve much more sensitive detection than conventional ones due to their desirable photophysical properties. Moreover, they are inexpensive and allow for multiplexing and quantitative detection. The development of new optical encoding strategies for multiple analyte detection is well established endowing the unique properties of UCNPs. Tunable luminescence lifetime of UCNPs in the microseconds region is an additional attractive parameter that can be used for optical encoding. By manipulating the luminescence decay lifetime, one can create a temporal coding dimension from the micro to milliseconds range in a single colour band [136]. Each code can be well-separated at this time scale to avoid overlapping of the signals.

A homogeneous assay platform generally utilises a sandwich structure to measure the analyte concentration and biological activities in biological fluid based on sensitive and reliable fluorescence resonance energy transfer (FRET) technique. In a conventional FRET process, the labelled donor and acceptor molecules are capable to interact in the presence of analyte through a luminescence energy transfer. UC luminescence resonance energy transfer (LRET) biodetection utilises UC nanoparticles as ideal energy donor insomuch as the noise of the autofluorescence background can be thoroughly removed as a result of NIR excitation. Moreover, unwanted detection signal due to direct excitation of acceptor can be completely ruled out, thus offering high detection sensitivity and signal-to-noise ratio. In 2005, Soukka's group has successfully demonstrated the sensitive detection of biotin with a limit of detection (LOD) of 0.7–9 nM by utilising Y_2O_2S:Yb,Er phosphors as a donor and a fluorescent phycobiliprotein (bio-PBE) as an acceptor [137]. Subsequently, they applied this technology for simultaneous detection of multiple analyte without interference from autofluorescence by using sub-micrometre-sized particles which produce multiple narrow emission band at visible wavelength under IR excitation [138]. However, due to the strong distance dependency of the energy transfer efficiency the use of large size particles limits the detection sensitivity. A highly sensitive bio-sensor to quantitatively detect target DNA with LOD of 1.3 nM has been exploited [139]. In addition to organic dyes to be used as acceptor, metallic NPs such as gold NPs and graphene oxide have also been utilised as superior quenchers of UC donor. For instance, Amino-functionalised $NaYF_4$:Yb, Er UCNPs and gold NPs (Au NPs) were prepared and conjugated with the human immunoglobulin G (IgG) and rabbit anti-goat IgG, respectively. This sandwich-type LRET-based approach can reach a low detection limit (0.88 μg/mL) of goat antihuman IgG [140]. Recently, Chu and co-workers designed a bio-sensor comprising the peptide-functionalised $NaYF_4$:Yb, Er UCNPs as energy donor and graphene oxide as energy quencher for the sensitive and selective determination of human immunodeficiency virus (HIV) antibody [141]. A detection limit of 2 nM was reported. For the detection of cholesterol level in human body, Ding and co-workers developed a upconversion nanocomposite composed of β-cyclodextrin (β-CD) derivative-modified $NaYF_4$:Yb, Er UCNPs and Rhodamine B [142]. It was observed that the detection accuracy reaches down to approximately 3.0 μM in the concentration range of 10–110 μM. Latterly, these efforts clearly demonstrate that Ln-doped UCNPs are excellent donor labels in homogeneous LRET and are capable to extend the application of FRET techniques to be engaged in clinical, food and environmental monitoring.

9.3.5 Photo-activation

There is a great potential in activating molecular reactions with light as it enables another means to remotely control molecular events in tissue. A slight complication is that many reactions only can be initiated with short, energy-rich wavelengths. An issue with this is that such short wavelengths do not penetrate tissue well, limiting the activation capability to superficial locations. For deeper tissue activations, UCNPs can be employed as mediators, facilitating local conversion of NIR-to-violet light. As NIR light penetrates much deeper into tissue, UCNP can provide the means to conduct non-invasive photo-activation below the very first superficial cell layers without artificially guiding the light into the tissue. The idea of using UCNPs for this purpose was generated already about 10 years ago, when UCNPs started to become efficient for biomedical use. Zhou *et al.* demonstrated then an NIR-controllable luminescence switch based on UCNPs. They were utilising intermolecular energy transfer within a photochromic diarylethene derivative and UCNPs loaded in a poly(methyl methacrylate) (PMMA) film [143]. The use of UCNPs for *in vivo* photo-activation has since gained a considerable interest. Many studies have been conducted in the development and evaluation of the potential of UCNP-based photo-activated chemical reactions. Examples of such research projects include activation of carboxylic acid, therapeutic nitric oxide, chlorambucil (an anti-cancer drug), doxorubicin (another anti-cancer drug) [144–147].

Besides small molecules, complex biomolecules like proteins and nucleic acids have also been photo-caged and photo-activated using UCNPs. The ability to use of UCNPs for uncaging biomolecules has been shown both *in vitro* and *in vivo* [148]. In that study thiolated silane-modified $NaYF_4$:Yb,Tm@$NaYF_4$ core-shell UCNPs were caged with D-luciferin. When incubated with the enzyme luciferase, uncaging of D-luciferin occurred and produced bioluminescence. This type of research was advanced by the group of Zhang, successfully demonstrating the use of NIR-to-UV UCNPs for light-controlled gene expression and knockdown [149]. In that study, plasmid DNA and siRNA were first converted to a non-active form by chemically photo-caging. The nucleic acids were bound to $NaYF_4$:Yb,Tm UCNPs coated with mesoporous silica. By exciting the UCNPs with NIR light, they demonstrated it is possible to locally generate sufficient amount of UV light to photo-reactivate the nucleic acids and expressed green fluorescent protein in B16F0 cells (a melanoma cell line). This was demonstrated both on a cell culture and when the cells were located in tissue at depths down to 4 mm. In a next step, this group successfully showed the use of UCNPs as mediators for gene therapy [150]. A similar methodology as above was employed. They managed to accomplish an efficient tumour reduction in a mouse model following NIR excitation. The idea behind the project was to employ NIR light to knock down the expression of the STAT3 (signal transducer and activator of transcription 3) gene. To accomplish such an activation, NIR-to-UV converting UCNPs were co-loaded with STAT3 photo-morpholino (a UV-triggered short nucleic acid analogue) and delivered into B16F0 cells. These cells were then used to induce tumours in the C57BL/6 mice model. The results illustrate the potential of utilising UCNPs for efficient photoactivation deep in tissue for gene therapy purposes. Further another study illustrated the possibility for employing UCNPs in optogenetics, to optically activate the channel Rhodopsin 2 modified mechanosensory neurons in *Caenorhabditis elegans* [151]. The activation was conducted using NIR excitation of UCNPs. The locally emitted blue light following the NIR absorption in the UCNPs stimulated the channel Rhodopsin in the neurons, triggering the *C. elegans* to change direction in its movement, see Figure 9.7. These studies provide hopes that NIR diode-laser excited UCNPs can be used as a tool to photo-activate vital chemical reactions, useful in fundamental biological research as well as in the future potentially also in medical applications.

9.3.6 Photodynamic therapy

Photodynamic therapy constitutes a special branch of photo-activation, and is given a special subchapter here because of its potential and special academic challenges in fully understanding the processes involved, as well as in optimising the treatment parameters. Photodynamic therapy is a non-thermal treatment modality involving a catalysing photosensitiser in combination with light to initiate a photochemical reaction involving oxygen. The aim of this photochemical reaction is to cause selective tissue ablation or cell death. Photodynamic therapy has mainly been utilised as a treatment option for malignant tumour destruction, but is increasingly frequented also in the management of infections. The latter capability is of particular

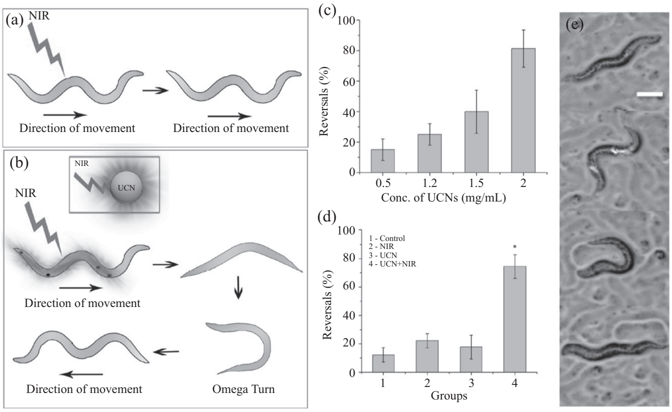

Figure 9.7 This image illustrates how it is possible to trigger a C. elegans to change direction of movement with light. This figure is reproduced with permission from Bansal et al. [151]. Here follows a slightly modified figure caption from the paper: Schematic showing differences in movement behaviour in worms expressing ChR2 in their mechanosensory neurons (a) when exposed to NIR light alone (no UCNPs) and (b) when exposed to NIR light in the presence of UCNPs. The worms move fluidly without drastic changes in direction in panel (a). However in panel (b), the worms show a drastic change in direction akin to being touched due to the activation of the mechanosensory neurons caused by the activation of ChR2 via the blue light produced by UCNPs upon NIR irradiation. (c) Effect of varying UCNP concentration on percentage of worms showing reversal phenotype when irradiated with NIR light at 50% duty cycle and peak power 4 W. $n = 20$ per group. (d) Percentage of worms showing the reversal phenotype upon incubation with UCNPs and subsequent NIR irradiation, along with the controls (untreated worms, worms exposed to NIR light alone, or worms exposed to UCNPs alone). p-value = 0.0004 between the control and UCNP + NIR groups. $n = 90$ per group. (e) Representative images (video stills) showing the reversal process in the UCNP+NIR group

interest in view of the increase in methicillin-resistant *Staphylococcus aureus* infections. Photodynamic therapy provides a new tool with the potential to be efficient also for resistant antibacterial and anti-fungal infections. A reason for that is that the PDT mechanisms are not primarily targeting the cell nucleus, resulting in poor ability for microbes to modify themselves to develop resistance against PDT.

The potential for a unique treatment selectivity is obtained through the light delivery, photosensitiser localisation and presence of oxygen in the tissues. This multiparameter sensitivity function is valuable as it provides great means to generate a very selective treatment, while it is also making the modality complex and the treatment planning challenging. Well planned and correctly conducted, PDT can provide a treatment with high precision for optimised outcomes in each individual treatment. The modality promises a minimally invasive treatment (repeated if necessary) as no *per se* harmful substances are employed. It is thereby offering selective and efficient ablation of malignant tissue volumes or infections, while sparing surrounding tissues and yielding minimal side effects.

Typically PDT employs NIR activatable photosensitisers, as the NIR light penetrates tissue more readily, facilitating treatment of more than very superficial and thin lesions. Interstitial light delivery is another route increasingly frequently employed to be enable treatment of deeply located treatment volumes or thick lesions. A remaining challenge is that the photosensitisers utilised today still have rather limited absorption cross sections and QYs, requiring high fluence to achieve the desired treatment. This is in particular challenging away from the location of light delivery, when light has been attenuated in the tissue in passing to the target volume. Also, the photosensitisers are typically activated at a still non-ideal wavelength in light penetration aspects, as in the selection of appropriate wavelength to employ, one has to balance the light penetration with the absorption properties of the photosensitiser used. An unmet need is consequently to develop a photosensitiser with properties as close as possible to what is desired in terms of efficiency and wavelength for the activation with optimal light penetration properties. Employing UCNPs as local wavelength converters could be a means to accomplish these needs, as it provides a tool to somewhat uncouple the absorption wavelength (influencing the light penetration) and the quantum efficiency in the subsequent photochemical reaction generating the cell depth. The efficiency can also be addressed by modifying the mechanistic reactions involved. One such very interesting development of PDT is what is called photochemical internalisation (PCI) [152,153].

The intention with using UCNPs as mediators in PDT is simple, they will convert far NIR to violet light locally inside the tissue to treat. In this way NIR light at a wavelength that penetrates tissue well can be utilised to convert the absorbed light to a wavelength that is optimal for the photosensitiser. Gain can be achieved as the treatment absorption cross section multiplied with treatment QY for the conventionally used photosensitisers are generally much higher for violet light than for the most used red or NIR wavelengths. This gain has to overcome the losses we have in the absorption cross section times the QY for the violet emission by the UCNPs employed. This might be non-trivial to accomplish as the QY for the UCNPs is generally low (in the per cent range) and also dropping for low light fluence rates. For that reason one needs to critically evaluate the potential gain before proposing this as a general tool to improve PDT treatment at deep locations in tissue. Figure 9.8 illustrates this issue, presenting a back-of-an-envelope calculation for which the condition that the QY is unaltered for the photosensitiser for the two treatment scenarios, meaning it is independent whether it is excited at red

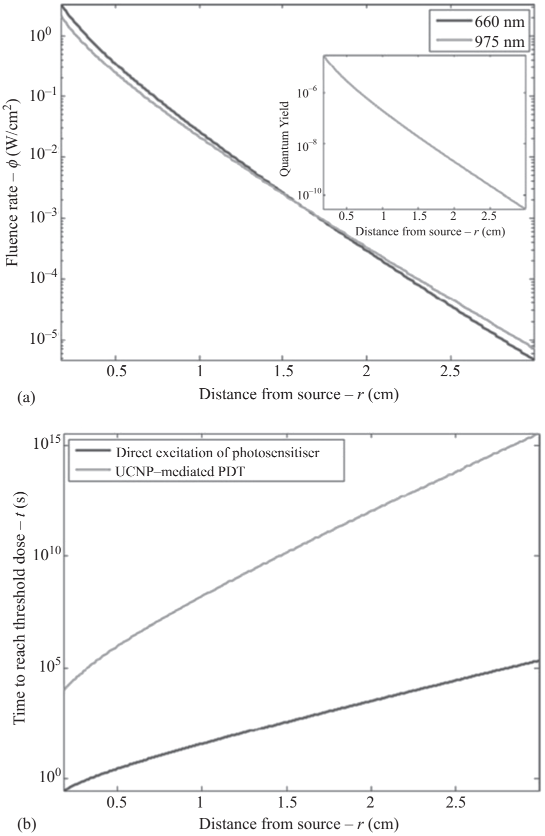

Figure 9.8 The panels are used with permission from Xu et al. [4], and illustrates plots from simple estimates of light fluence rates and treatment times versus depth in simulated prostate tissue. (a) Calculated fluence rates within human prostate tissue following 660 nm and 975 nm excitation, respectively. The modelling is based on light diffusion theory using the optical properties of the tissue detailed in the reference. The inset shows the corresponding QY for the UCNPs (the QY for the photosensitiser at 660 nm is constant) as a function of depth. (b) The treatment time needed to reach the light threshold dose of 1 J/cm^2

or violet wavelengths. In this case the necessary light energy density for reaching the treatment threshold is much higher for the UCNPs-mediated treatment than for the conventional photosensitiser.

The reality is obviously more complex than the simple model used to present Figure 9.8. This is clearly illustrated by the results presented by the group of Zhang [154–157] and others, see, for example [158]. They demonstrate enhanced treatment response by employing UCNPs mediated PDT as compared to conventional photosensitisers. To obtain these results they used UCNPs coated with a thin layer of TiO_2 as a photosensitiser. This method avoids the previously identified limitation with leaking and uneven loading of the photosensitising molecules, as well as the possibility for the generated radicals can reach the critical cellular target structures.

As for the other photoactivation ideas, there are still many remaining challenges and questions, before this modality of PDT will gain clinical interest. Such questions include:

- How efficient is the singlet oxygen production?
- How far away from a structure can the particles be to still be able to destroy critical cellular structures? Does this constitute a challenge? Where do you need to have the particles located in order to obtain optimal damage?
- Treatment at depth:
  - How is the treatment depth normally limited in conventional PDT?
  - What are the properties to compare for the photosensitiser and UCNP construct to be able to predict their efficiency for treating deep tissue locations?
  - What are the mechanisms that potentially will make the use of UCNP-mediated PDT at deep tissue locations favourable?

That said, it is remarkable promising results, given the doubts of the potential given in Figure 9.8. We are looking forward to follow the future development of UCNP-mediated photoactivation and PDT.

9.4 Sources

In order to make the UCNPs tools attractive and user-friendly, the optical arrangements employed must be acceptable both in terms of size and costs. Semiconductor sources would thereby be ideal to use as they are both small and cost efficient. What are then the additional desired properties of the light source to efficiently excite the UCNPs, sometimes located deeply into tissues?

- Wavelength – the light needs to penetrate tissue well and cause minimal tissue heating. It should also be efficiently absorbed by the UCNPs.
- Temporal profile – due to the multiphoton stepwise excitation, the pulse length should match the lifetime of the intermediate state.
- Optical integration – the light source should allow that the light can be efficiently delivered to the target tissue
- Power stability – the source should be sufficiently stable to provide a robust signal. This includes both short and long-term stability.

Firstly, for the wavelength considerations the near infrared region yields the best light tissue penetration between 700 and 900 nm. With low absorption comes also minimal tissue heating, as the heating is generated by the light absorbed in the tissue. There are a number of strategies for obtaining good absorption of the UCNPs as described above. Most frequent is to use Yb as sensitiser ion. This ion absorbs best at 975 nm. Alternatively Nd ions can be employed, absorbing around 808 nm. Some studies have also proposed to use molecular dyes in the UCNP coating to increase the absorption cross section. This scheme relies on transferring the absorbed energy from the dye to the rare-earth ions, yielding that also these should absorb in the NIR wavelength range. The benefit would be a higher absorption cross section of the dye as compared to the rare-earth ion, and also more flexibility in the absorption wavelength as compared to the discrete number of lines available for rare-earth ions.

Secondly, the light pulse length has to match the intrinsic lifetime of the UCNPs. This is because following the first excitation event in an ETU process, the second should provide an energy transfer to an already excited ion. This timing has been understood by using rate-equation analysis [107,159]. The first energy transfer must thus have been completed and the intermediate state been populated, and at the same time it should not have been depopulated through other spontaneous relaxations. This process is thus quite different from how one can employ chromophores for multi-photon excitations, as such excitation does not rely on an intermediate state, but the various photons yielding the multi-photon excitation must be present simultaneously, within the temporal uncertainty determined by the line width of the light. Typically, the intermediate state is best populated within the timeframe of milliseconds. Thus, the optimal light pulse is of that pulse length. Longer pulses will dilute the photon density within the active excitation process, while shorter pulses will provide a considerable fraction of the photons before the intermediate state is populated. Following this reasoning, longer pulses should be employed the more energy transfer process used in the excitation – meaning three or more photon processes. The pulse energy and repetition rate is then limited by the permitted tissue exposure limits. For skin at 975 nm, this is 200 mWcm^{-2} average power. This also provides a relation between pule energy and repetition frequency. Here it is an advantage to maximise the peak power, on the expense of low repetition rate, as the upconversion process is characterised by a non-linear behaviour up to a saturation limit.

Thirdly, for most applications, the light will be guided through an optical fibre. This means the beam quality from the source should be efficiently coupled into the fibre. The diameter of the fibre is usually of less importance. Frequently 400–600 μm core diameter fibres are used. One part of the reason for this is to allow simple and efficient coupling of the light source into the fibre. Another reason is that one typically will illuminate a larger area of the tissue with some known, usually top-hat illumination profile to just balance the illumination to what is permitted. Therefore, the tip of the fibre is frequently imaged with a lens on the tissue surface, with a magnification that provides the desired illumination beam size. For practical reasons a larger core fibre diameter makes such magnification optics simpler and, most of all, more compact.

Lastly, the light source needs to be sufficiently stable to secure reliability and repeatability in measurements or photoactivation. Short-term stability means the power profile within a millisecond pulse. The source needs to provide a controllable power profile within each pulse. The first intention would naturally be to provide a constant power throughout each light pulse. This is what the relatively course rate-equation analysis suggests. With improved rate-equation analysis we do not exclude that it may be better to design the temporal pulse profile differently to further improve the possibility to generate as high populations in the desired energy level in the activator ion as possible, within the limits presented by the light economy determined by the permitted light exposure, as well as by the properties of the light source employed. The long term stability is obvious to guarantee repeatability. When discussing repeatability one need to understand that this is a multiphoton process, sometimes with many photons involved. The results can thus be very sensitive to the excitation power.

In order for UCNP-based technique to become translated to become well-adopted scientific tools, these requirements must be fulfilled and especially affordable instruments need to be developed. With the great promise in the techniques UCNPs can mediate, our strong believe is that instrumentation will be developed to fully facilitate the potential of the techniques described above as well as techniques yet to be invented. The instruments obviously include appropriate excitation sources. Here cost effective diode lasers seem to be very appropriate.

9.5 Summary

We have in this chapter tried to provide a brief overview of the field of UCNPs for biomedical applications and given a flavour of its promising potential and future. Our interpretation is that UCNPs will become a valuable agent for several applications, some of them still to be invented/studied. For imaging it has great promises mainly due to the possibility to avoid any background from tissue autofluorescence, as well as the ability to simultaneously label several targets by UCNPs with different dopants. In this chapter we have not discussed applications within immunohistochemistry and digital pathology, as these fields have not been studied in any details. We believe these fields could become important application areas of UCNP labelling. Furthermore, we predict a very rapidly rising and fascinating field in general UCNP-photoactivation, with the demonstrated possibility to employ UCNPs as mediators to convert NIR light to violet light *in vivo,* and the rapidly growing interest in photo-activation in basic research in situations where one easily can access the tissue location of interest with NIR light. Here is, in our opinion, a promise for novel applications to emerge, see, for example [27,160].

By describing not only the biomedical applications possible benefiting from the properties of the UCNPs, but also providing their photophysical properties, we hope this chapter can form a valuable source for introducing the field. We have aimed to stress properties of an optimal light source, and thereby established a clear link to the use of diode lasers and LEDs. In the field of UCNPs the excitation is particularly relevant, as the upconverting excitation scheme is a non-linear to its character, with multiple sequential excitation steps. Due to the long lived intermediate state, or states, if more than a two-photon process is employed, saturation of the excitation can easily be observed when the excitation power density increases. Also, the lifetime(s) of the intermediate state(s) determines how short pulses should be used, typically in the range of milliseconds. This means that modulated CW lasers are preferred, suggesting the use of diode lasers for small illumination areas when focussing is important. For broad field illumination LEDs might be suggested, if any emission in the detection band can be avoided.

Acknowledgement

We would like to thank several previous students in the group and other collaborators in Lund who have been central in much of our research directed towards UCNPs as novel contrast agents for bioimaging. Especially we would like to express our warmest gratitude to Haichun Liu, Pontus Svenmarker and Can X. Xu for their key contributions to our research at Lund University, forming the background for this book chapter. In addition, we very much appreciate the collaboration with Peter E Andersen and Ole B. Jensen at DTU, as well as with the group of Yong Zhang at National University of Singapore, in the area of UCNPs. The work was financially supported by the Science Foundation Ireland (SFI/15/RP/2828) and the Swedish Research Council (VR/621-2013-6038).

References

[1] Heike S Mader, Peter Kele, Sayed M Saleh, and Otto S Wolfbeis. Upconverting luminescent nanoparticles for use in bioconjugation and bioimaging. *Current Opinion in Chemical Biology*, 14(5):582–596, 2010.

[2] Daniela E Achatz, Reham Ali, and Otto S Wolfbeis. Luminescent chemical sensing, biosensing, and screening using upconverting nanoparticles. In *Luminescence Applied in Sensor Science*, pp. 29–50. Springer, 2010.

[3] Min Lin, Ying Zhao, ShuQi Wang, *et al*. Recent advances in synthesis and surface modification of lanthanide-doped upconversion nanoparticles for biomedical applications. *Biotechnology Advances*, 30(6):1551–1561, 2012.

[4] Can T Xu, Qiuqiang Zhan, Haichun Liu, *et al*. Upconverting nanoparticles for pre-clinical diffuse optical imaging, microscopy and sensing: Current trends and future challenges. *Laser & Photonics Reviews*, 7(5):663–697, 2013.

[5] Anna Gnach and Artur Bednarkiewicz. Lanthanide-doped up-converting nanoparticles: Merits and challenges. *Nano Today*, 7(6):532–563, 2012.

[6] Hans H Gorris and Otto S Wolfbeis. Photon-upconverting nanoparticles for optical encoding and multiplexing of cells, biomolecules, and microspheres. *Angewandte Chemie International Edition*, 52(13):3584–3600, 2013.

[7] Matthew V DaCosta, Samer Doughan, Yi Han, and Ulrich J Krull. Lanthanide upconversion nanoparticles and applications in bioassays and bioimaging: A review. *Analytica Chimica Acta*, 832:1–33, 2014.

[8] Frederik Maes, Andre Collignon, Dirk Vandermeulen, Guy Marchal, and Paul Suetens. Multimodality image registration by maximization of mutual information. *IEEE Transactions on Medical Imaging*, 16(2):187–198, 1997.

[9] Bernard W Stewart and Christopher P Wild. *World Cancer Report 2014*. International Agency for Research on Cancer, WHO, 2014.

[10] Ahmedin Jemal, Freddie Bray, Melissa M Center, Jacques Ferlay, Elizabeth Ward, and David Forman. Global cancer statistics. *CA: A Cancer Journal for Clinicians*, 61(2):69–90, 2011.

[11] Ruth Etzioni, Nicole Urban, Scott Ramsey, *et al*. The case for early detection. *Nature Reviews Cancer*, 3(4):243–252, 2003.

[12] Vasilis Ntziachristos, Jorge Ripoll, Lihong V Wang, and Ralph Weissleder. Looking and listening to light: The evolution of whole-body photonic imaging. *Nature Biotechnology*, 23(3):313, 2005.

[13] Ralph Weissleder and Mikael J. Pittet. Imaging in the era of molecular oncology. *Nature*, 452(7187):580–589, 2008.

[14] Simon R Arridge and John C Schotland. Optical tomography: Forward and inverse problems. *Inverse Problems*, 25(12):123010, 2009.

[15] John V Frangioni. In vivo near-infrared fluorescence imaging. *Current Opinion in Chemical Biology*, 7(5):626–634, 2003.

[16] Rebecca Richards-Kortum and Eva Sevick-Muraca. Quantitative optical spectroscopy for tissue diagnosis. *Annual Review of Physical Chemistry*, 47(1):555–606, 1996.

[17] Vasilis Ntziachristos, Ching-Hsuan Tung, Christoph Bremer, and Ralph Weissleder. Fluorescence molecular tomography resolves protease activity in vivo. *Nature Medicine*, 8(7):757–760, 2002.

[18] Vasilis Ntziachristos, Eyk A Schellenberger, Jorge Ripoll, *et al*. Visualization of antitumor treatment by means of fluorescence molecular tomography with an annexin v–cy5. 5 conjugate. *Proceedings of the National Academy of Sciences of the United States of America*, 101(33):12294–12299, 2004.

[19] Arno Villringer and Britton Chance. Non-invasive optical spectroscopy and imaging of human brain function. *Trends in Neurosciences*, 20(10):435–442, 1997.

[20] David A Boas, Anders M Dale, and Maria Angela Franceschini. Diffuse optical imaging of brain activation: Approaches to optimizing image sensitivity, resolution, and accuracy. *Neuroimage*, 23:S275–S288, 2004.

[21] Stephanie van de Ven, Sjoerd Elias, Andrea Wiethoff, *et al.* Diffuse optical tomography of the breast: Initial validation in benign cysts. *Molecular Imaging and Biology*, 11(2):64–70, 2009.

[22] Dennis EJGJ Dolmans, Dai Fukumura, and Rakesh K Jain. Photodynamic therapy for cancer. *Nature Reviews Cancer*, 3(5):380–387, 2003.

[23] Can T. Xu. Diffuse optical spectroscopy and imaging of turbid media, PhD thesis, Department of Physics, Lund University, Sweden, 2013.

[24] Bruce J Tromberg, Brian W Pogue, Keith D Paulsen, Arjun G Yodh, David A Boas, and Albert E Cerussi. Assessing the future of diffuse optical imaging technologies for breast cancer management. *Medical physics*, 35(6):2443–2451, 2008.

[25] George Zonios, Lev T Perelman, Vadim Backman, *et al*. Diffuse reflectance spectroscopy of human adenomatous colon polyps in vivo. *Applied Optics*, 38(31):6628–6637, 1999.

[26] Konstantin Sokolov, Jesse Aaron, Betsy Hsu, *et al.* Optical systems for in vivo molecular imaging of cancer. *Technology in Cancer Research & Treatment*, 2(6):491–504, 2003.

[27] Niagara Muhammad Idris, Muthu Kumara Gnanasammandhan Jayakumar, Akshaya Bansal, and Yong Zhang. Upconversion nanoparticles as versatile light nanotransducers for photoactivation applications. *Chemical Society Reviews*, 44(6):1449–1478, 2015.

[28] Emmanuel Ruggiero, Silvia Alonso-de Castro, Abraha Habtemariam, and Luca Salassa. Upconverting nanoparticles for the near infrared photoactivation of transition metal complexes: New opportunities and challenges in medicinal inorganic photochemistry. *Dalton Transactions*, 45(33):13012–13020, 2016.

[29] Nicolaas Bloembergen. Solid state infrared quantum counters. *Physical Review Letters*, 2(3):84, 1959.

[30] Warren R Zipfel, Rebecca M Williams, and Watt W Webb. Nonlinear magic: Multiphoton microscopy in the biosciences. *Nature Biotechnology*, 21(11):1369–1377, 2003.

[31] Tanya N Singh-Rachford and Felix N Castellano. Photon upconversion based on sensitized triplet–triplet annihilation. *Coordination Chemistry Reviews*, 254(21):2560–2573, 2010.

[32] Marc A Baldo, Chihaya Adachi, and Stephen R Forrest. Transient analysis of organic electrophosphorescence. ii. transient analysis of triplet-triplet annihilation. *Physical Review B*, 62(16):10967, 2000.

[33] Jianzhang Zhao, Shaomin Ji, and Huimin Guo. Triplet–triplet annihilation based upconversion: From triplet sensitizers and triplet acceptors to upconversion quantum yields. *RSC Advances*, 1(6):937–950, 2011.

[34] Thomas Brabec and Ferenc Krausz. Intense few-cycle laser fields: Frontiers of nonlinear optics. *Reviews of Modern Physics*, 72(2):545, 2000.

[35] Francois F Auzel and Dario C Pecile. Comparison and efficiency of materials for summation of photons assisted by energy transfer. *Journal of Luminescence*, 8(1):32–43, 1973.

[36] Francois F Auzel and Dario C Pecile. Absolute efficiency for ir to blue conversion materials and theoretical prediction for optimized matrices. *Journal of Luminescence*, 11(5–6):321–330, 1976.

[37] Francois F Auzel. Upconversion and anti-Stokes processes with f and d ions in solids. *Chemical Reviews*, 104(1):139–173, 2004.

[38] Xudong Xiao, Jeanne P. Haushalter, and Gregory W. Faris. Upconversion from aqueous phase lanthanide chelates. *Optical Letters*, 30(13):1674–1676, 2005.

[39] Dev K Chatterjee, Abdul J Rufaihah, and Yong Zhang. Upconversion fluorescence imaging of cells and small animals using lanthanide doped nanocrystals. *Biomaterials*, 29(7):937–943, 2008.

[40] Dev K Chatterjee and Zhang Yong. Upconverting nanoparticles as nanotransducers for photodynamic therapy in cancer cells. *Nanomedicine*, 3(1): 73–82, 2008.

[41] Christopher Salthouse, Scott Hilderbrand, Ralph Weissleder, and Umar Mahmood. Design and demonstration of a small-animal up-conversion imager. *Optics Express*, 16(26):21731–21737, 2008.

[42] Can T Xu, Niclas Svensson, Johan Axelsson, *et al*. Autofluorescence insensitive imaging using upconverting nanocrystals in scattering media. *Applied Physics Letters*, 93(17):171103, 2008.

[43] Can T. Xu, Johan Axelsson, and Stefan Andersson-Engels. Fluorescence diffuse optical tomography using upconverting nanoparticles. *Applied Physics Letters*, 94(25):251107–251107–3, 2009.

[44] Hisataka Kobayashi, Mikako Ogawa, Raphael Alford, Peter L. Choyke, and Yasuteru Urano. New strategies for fluorescent probe design in medical diagnostic imaging. *Chemical Reviews*, 110(5):2620–2640, 2010. PMID: 20000749.

[45] Hisataka Kobayashi, Mikako Ogawa, Raphael Alford, Peter L Choyke, and Yasuteru Urano. New strategies for fluorescent probe design in medical diagnostic imaging. *Chemical Reviews*, 110(5):2620–2640, 2010.

[46] Haichun Liu, Can T Xu, and Stefan Andersson-Engels. Multibeam fluorescence diffuse optical tomography using upconverting nanoparticles. *Optics Letters*, 35(5):718–720, 2010.

[47] Pontus Svenmarker, Can T Xu, and Stefan Andersson-Engels. Use of nonlinear upconverting nanoparticles provides increased spatial resolution in fluorescence diffuse imaging. *Optics Letters*, 35(16):2789–2791, 2010.

[48] Qiuqiang Zhan, Jun Qian, Huijuan Liang, *et al*. Using 915 nm laser excited $Tm^{3+}/Er^{3+}/Ho^{3+}$-doped $NaYbF_4$ upconversion nanoparticles for *in vitro* and deeper *in vivo* bioimaging without overheating irradiation. *ACS Nano*, 5(5):3744–3757, 2011.

[49] Anna Gnach, Tomasz Lipinski, Artur Bednarkiewicz, Jacek Rybka, and John A Capobianco. Upconverting nanoparticles: Assessing the toxicity. *Chemical Society Reviews*, 44(6):1561–1584, 2015.

[50] Marie-France Joubert. Photon avalanche upconversion in rare earth laser materials. *Optical Materials*, 11(2):181–203, 1999.

[51] Daniel R Gamelin and Hans U Güdel. Design of luminescent inorganic materials: New photophysical processes studied by optical spectroscopy. *Accounts of Chemical Research*, 33(4):235–242, 2000.

[52] Daniel R Gamelin and Hans U Güdel. Topics in current chemistry, vol. 214, 2000.

[53] Feng Wang and Xiaogang Liu. Recent advances in the chemistry of lanthanide-doped upconversion nanocrystals. *Chemical Society Reviews*, 38(4):976–989, 2009.

[54] Brian R Judd. Optical absorption intensities of rare-earth ions. *Physical Review*, 127(3):750, 1962.

[55] Shiwei Wu, Gang Han, Delia J. Milliron, *et al*. Non-blinking and photostable upconverted luminescence from single lanthanide-doped nanocrystals. *Proceedings of the National Academy of Sciences*, 106(27):10917–10921, 2009.

[56] Xue Teng, Yihan Zhu, Wei Wei, *et al*. Lanthanide-doped Na_xScF_{3+x} nanocrystals: Crystal structure evolution and multicolor tuning. *Journal of the American Chemical Society*, 134(20):8340–8343, 2012. PMID: 22506543.

[57] Xingchen Ye, Joshua E. Collins, Yijin Kang, *et al*. Morphologically controlled synthesis of colloidal upconversion nanophosphors and their shape-directed self-assembly. *Proceedings of the National Academy of Sciences*, 107(52):22430–22435, 2010.

[58] Feng Wang and Xiaogang Liu. Upconversion multicolor fine-tuning: Visible to near-infrared emission from lanthanide-doped $NaYF_4$ nanoparticles. *Journal of the American Chemical Society*, 130(17):5642–5643, 2008. PMID: 18393419.

[59] Xiaomin Li, Rui Wang, Fan Zhang, *et al*. Nd^{3+} sensitized up/down converting dual-mode nanomaterials for efficient in-vitro and in-vivo bioimaging excited at 800 nm. *Scientific Reports*, 3:3536, 2013.

[60] Ye-Fu Wang, Gao-Yuan Liu, Ling-Dong Sun, Jia-Wen Xiao, Jia-Cai Zhou, and Chun-Hua Yan. Nd^{3+}-sensitized upconversion nanophosphors: Efficient in vivo bioimaging probes with minimized heating effect. *ACS Nano*, 7(8):7200–7206, 2013. PMID: 23869772.

[61] Hugo Söderlund, Monirehalsadat Mousavi, Haichun Liu, and Stefan Andersson-Engels. Increasing depth penetration in biological tissue imaging using 808-nm excited $Nd^{3+}/Yb^{3+}/Er^{3+}$-doped upconverting nanoparticles. *Journal of Biomedical Optics*, 20(8):086008, 2015.

[62] Qiuqiang Zhan, Baoju Wang, Xuanyuan Wen, and Sailing He. Controlling the excitation of upconverting luminescence for biomedical theranostics: Neodymium sensitizing. *Optical Materials Express*, 6(4):1011–1023, 2016.

[63] Wenqiang Zou, Cindy Visser, Jeremio A Maduro, Maxim S Pshenichnikov, and Jan C Hummelen. Broadband dye-sensitized upconversion of near-infrared light. *Nature Photonics*, 6(8):560–564, 2012.

[64] Guanying Chen, Hailong Qiu, Paras N Prasad, and Xiaoyuan Chen. Upconversion nanoparticles: Design, nanochemistry, and applications in theranostics. *Chemical Reviews*, 114(10):5161–5214, 2014.

[65] Karl W. Kramer, Daniel Biner, Gabriela Frei, Hans U. Gudel, Markus P. Hehlen, and Stefan R. Luthi. Hexagonal sodium yttrium fluoride based green and blue emitting upconversion phosphors. *Chemistry of Materials*, 16(7):1244–1251, 2004.

[66] Xiaojie Xue, Shinya Uechi, Rajanish N Tiwari, *et al*. Size-dependent upconversion luminescence and quenching mechanism of $LiYF_4$:Er^{3+}/Yb^{3+} nanocrystals with oleate ligand adsorbed. *Optical Materials Express*, 3 (7):989–999, 2013.

[67] John-Christopher Boyer, Fiorenzo Vetrone, Louis A. Cuccia, and John A. Capobianco. Synthesis of colloidal upconverting $NaYF_4$ nanocrystals doped with Er^{3+}, Yb^{3+} and Tm^{3+}, Yb^{3+} via thermal decomposition of lanthanide trifluoroacetate precursors. *Journal of the American Chemical Society*, 128 (23):7444–7445, 2006. PMID: 16756290.

[68] Jingning Shan and Yiguang Ju. A single-step synthesis and the kinetic mechanism for monodisperse and hexagonal-phase $NaYF_4$:Yb, Er upconversion nanophosphors. *Nanotechnology*, 20(27):275603, 2009.

[69] Ya-Wen Zhang, Xiao Sun, Rui Si, Li-Ping You, and Chun-Hua Yan. Single-crystalline and monodisperse LaF_3 triangular nanoplates from a single-source precursor. *Journal of the American Chemical Society*, 127(10):3260–3261, 2005.

[70] Guang Shun Yi and Gan Moog Chow. Synthesis of hexagonal-phase $NaYF_4$: Yb, er and $NaYF_4$: Yb, Tm nanocrystals with efficient up-conversion fluorescence. *Advanced Functional Materials*, 16(18):2324–2329, 2006.

[71] Hao-Xin Mai, Ya-Wen Zhang, Rui Si, *et al*. High-quality sodium rare-earth fluoride nanocrystals: Controlled synthesis and optical properties. *Journal of the American Chemical Society*, 128(19):6426–6436, 2006. PMID: 16683808.

[72] Rafik Naccache, Fiorenzo Vetrone, Venkataramanan Mahalingam, Louis A Cuccia, and John A Capobianco. Controlled synthesis and water dispersibility of hexagonal phase $NaGdF_4$: Ho^{3+}/Yb^{3+} nanoparticles. *Chemistry of Materials*, 21(4):717–723, 2009.

[73] Qian Liu, Yun Sun, Tianshe Yang, Wei Feng, Chenguang Li, and Fuyou Li. Sub-10 nm hexagonal lanthanide-doped $NaLuF_4$ upconversion nanocrystals for sensitive bioimaging in vivo. *Journal of the American Chemical Society*, 133(43):17122–17125, 2011.

[74] Feng Wang, Dev K Chatterjee, Zhengquan Li, Yong Zhang, Xianping Fan, and Minquan Wang. Synthesis of polyethylenimine/$NaYF_4$ nanoparticles with upconversion fluorescence. *Nanotechnology*, 17(23):5786, 2006.

[75] Venkataramanan Mahalingam, Rafik Naccache, Fiorenzo Vetrone, and John A Capobianco. Sensitized Ce^{3+} and Gd^{3+} ultraviolet emissions by Tm^{3+} in colloidal $LiYF_4$ nanocrystals. *Chemistry–A European Journal*, 15(38):9660–9663, 2009.

[76] Bastian Henke, Bernd Ahrens, Paul-T Miclea, Christian Eisenschmidt, Jacqueline Johnson, and Stefan Schweizer. Erbium-and chlorine-doped fluorozirconate-based glasses for up-converted fluorescence. *Journal of Non-Crystalline Solids*, 355(37):1916–1918, 2009.

[77] Dongmei Yang, Chunxia Li, Guogang Li, Mengmeng Shang, Xiaojiao Kang, and Jun Lin. Colloidal synthesis and remarkable enhancement of the

upconversion luminescence of $BaGdF_5$:Yb^{3+}/Er^{3+} nanoparticles by active-shell modification. *Journal of Materials Chemistry*, 21(16):5923–5927, 2011.

[78] Jing-H Zeng, Ji Su, ZH Li, Ruoxue Yan, and Yadong Li. Synthesis and upconversion luminescence of hexagonal-phase $NaYF_4$:Yb, Er^{3+} phosphors of controlled size and morphology. *Advanced Materials*, 17(17):2119–2123, 2005.

[79] Meng Wang, Cong-Cong Mi, Jin-Ling Liu, *et al*. One-step synthesis and characterization of water-soluble $NaYF_4$: Yb, er/polymer nanoparticles with efficient up-conversion fluorescence. *Journal of Alloys and Compounds*, 485(1):L24–L27, 2009.

[80] Wilson Sacchi Peternele, Victoria Monge Fuentes, Maria Luiza Fascineli, *et al*. Experimental investigation of the coprecipitation method: An approach to obtain magnetite and maghemite nanoparticles with improved properties. *Journal of Nanomaterials*, 2014:1–10, Article ID 682985, 2014.

[81] Rakhi Gupta and Nabo K Chaudhury. Entrapment of biomolecules in sol–gel matrix for applications in biosensors: Problems and future prospects. *Biosensors and Bioelectronics*, 22(11):2387–2399, 2007.

[82] Maqsood Ahmad Malik, Mohammad Younus Wani, and Mohd Ali Hashim. Microemulsion method: A novel route to synthesize organic and inorganic nanomaterials: 1st nano update. *Arabian Journal of Chemistry*, 5(4):397–417, 2012.

[83] Anna Zielińska-Jurek, Joanna Reszczyńska, Ewelina Grabowska, and Adriana Zaleska. Nanoparticles preparation using microemulsion systems. *Microemulsions—an introduction to properties and applications.* InTech Publisher, Rijeka, Croatia, 2012.

[84] Xiao Qin, Takeshi Yokomori, and Yiguang Ju. Flame synthesis and characterization of rare-earth (Er^{3+}, Ho^{3+}, and Tm^{3+}) doped upconversion nanophosphors. *Applied Physics Letters*, 90(7):073104, 2007.

[85] Jing Hui Zeng, Zhi Hua Li, Ji Su, Leyu Wang, Ruoxue Yan, and Yadong Li. Synthesis of complex rare earth fluoride nanocrystal phosphors. *Nanotechnology*, 17(14):3549, 2006.

[86] Feng Wang, Dev K Chatterjee, Zhengquan Li, Yong Zhang, Xianping Fan, and Minquan Wang. Synthesis of polyethylenimine/$NaYF_4$ nanoparticles with upconversion fluorescence. *Nanotechnology*, 17(23):5786, 2006.

[87] Li-Qin Xiong, Zhi-Gang Chen, Meng-Xiao Yu, Fu-You Li, Chun Liu, and Chun-Hui Huang. Synthesis, characterization, and in vivo targeted imaging of amine-functionalized rare-earth up-converting nanophosphors. *Biomaterials*, 30(29):5592–5600, 2009.

[88] Cheng Chen, Ling-Dong Sun, Zhen-Xing Li, *et al*. Ionic liquid-based route to spherical $NaYF_4$ nanoclusters with the assistance of microwave radiation and their multicolor upconversion luminescence. *Langmuir*, 26(11):8797–8803, 2010. PMID: 20085339.

[89] Zhengquan Li and Yong Zhang. Monodisperse silica-coated polyvinylpyrrolidone/$NaYF_4$ nanocrystals with multicolor upconversion fluorescence emission. *Angewandte Chemie*, 118(46):7896–7899, 2006.

[90] Zhiyao Hou, Chunxia Li, Pingan Ma, *et al*. Electrospinning preparation and drug-delivery properties of an up-conversion luminescent porous $NaYF_4$: Yb^{3+}, Er^{3+}@ silica fiber nanocomposite. *Advanced Functional Materials*, 21(12):2356–2365, 2011.

[91] Meng Wang, Congcong Mi, Yixin Zhang, *et al*.. NIR-responsive silica-coated $NaYBF_4$: Er/Tm/Ho upconversion fluorescent nanoparticles with tunable emission colors and their applications in immunolabeling and fluorescent imaging of cancer cells. *The Journal of Physical Chemistry C*, 113(44):19021–19027, 2009.

[92] Meng Wang, Gopal Abbineni, April Clevenger, Chuanbin Mao, and Shukun Xu. Upconversion nanoparticles: Synthesis, surface modification and biological applications. *Nanomedicine: Nanotechnology, Biology and Medicine*, 7(6):710–729, 2011.

[93] Qingbin Zhang, Kai Song, Junwei Zhao, *et al*. Hexanedioic acid mediated surface–ligand-exchange process for transferring $NaYF_4$:Yb/Er (or Yb/Tm) up-converting nanoparticles from hydrophobic to hydrophilic. *Journal of Colloid and Interface Science*, 336(1):171–175, 2009.

[94] Jie Shen, Ling-Dong Sun, Ya-Wen Zhang, and Chun-Hua Yan. Superparamagnetic and upconversion emitting Fe_3O_4/$NaYF_4$: Yb, Er heteronanoparticles via a crosslinker anchoring strategy. *Chemical Communications*, 46(31):5731–5733, 2010.

[95] Tianye Cao, Tianshe Yang, Yuan Gao, Yang Yang, He Hu, and Fuyou Li. Water-soluble $NaYF_4$:Yb/Er upconversion nanophosphors: Synthesis, characteristics and application in bioimaging. *Inorganic Chemistry Communications*, 13(3):392–394, 2010.

[96] John-Christopher Boyer, Marie-Pascale Manseau, Jill I Murray, and Frank CJM van Veggel. Surface modification of upconverting $NaYF_4$ nanoparticles with PEG-phosphate ligands for NIR (800 nm) biolabeling within the biological window. *Langmuir*, 26(2):1157–1164, 2009.

[97] Liqin Xiong, Tianshe Yang, Yang Yang, Congjian Xu, and Fuyou Li. Long-term in vivo biodistribution imaging and toxicity of polyacrylic acid-coated upconversion nanophosphors. *Biomaterials*, 31(27):7078–7085, 2010.

[98] Stephanie J Budijono, Jingning Shan, Nan Yao, *et al*. Synthesis of stable block-copolymer-protected $NaYF_4$: Yb^{3+}, Er^{3+} up-converting phosphor nanoparticles. *Chemistry of Materials*, 22(2):311–318, 2009.

[99] Noah JJ Johnson, Neralagatta M Sangeetha, John-Christopher Boyer, and Frank CJM van Veggel. Facile ligand-exchange with polyvinylpyrrolidone and subsequent silica coating of hydrophobic upconverting β-$NaYF_4$: Yb^{3+}/Er^{3+} nanoparticles. *Nanoscale*, 2(5):771–777, 2010.

[100] Zhigang Chen, Huili Chen, He Hu, *et al*. Versatile synthesis strategy for carboxylic acid-functionalized upconverting nanophosphors as biological labels. *Journal of the American Chemical Society*, 130(10):3023–3029, 2008.

[101] Guang-Shun Yi and Gan-Moog Chow. Water-soluble $NaYF_4$: Yb, Er(Tm)/$NaYF_4$/polymer core/shell/shell nanoparticles with significant enhancement of upconversion fluorescence. *Chemistry of Materials*, 19(3):341–343, 2007.

[102] Marco Pedroni, Fabio Piccinelli, Tiziana Passuello, *et al*. Lanthanide doped upconverting colloidal CaF_2 nanoparticles prepared by a single-step hydrothermal method: Toward efficient materials with near infrared-to-near infrared upconversion emission. *Nanoscale*, 3(4):1456–1460, 2011.

[103] Leyu Wang, Ruoxue Yan, Ziyang Huo, *et al*. Fluorescence resonant energy transfer biosensor based on upconversion-luminescent nanoparticles. *Angewandte Chemie International Edition*, 44(37):6054–6057, 2005.

[104] Fiorenzo Vetrone, Rafik Naccache, Venkataramanan Mahalingam, Christopher G Morgan, and John A Capobianco. The active-core/active-shell approach: A strategy to enhance the upconversion luminescence in lanthanide-doped nanoparticles. *Advanced Functional Materials*, 19(18): 2924–2929, 2009.

[105] John-Christopher Boyer and Frank CJM Van Veggel. Absolute quantum yield measurements of colloidal $NaYF_4$: Er^{3+}, Yb^{3+} upconverting nanoparticles. *Nanoscale*, 2(8):1417–1419, 2010.

[106] Markus Pollnau, Daniel R Gamelin, Stefan R Luthi, Hans U Gudel, and Markus P Hehlen. Power dependence of upconversion luminescence in lanthanide and transition-metal-ion systems. *Physical Review B*, 61(5):3337, 2000.

[107] Haichun Liu, Can T Xu, David Lindgren, *et al*. Balancing power density based quantum yield characterization of upconverting nanoparticles for arbitrary excitation intensities. *Nanoscale*, 5(11):4770–4775, 2013.

[108] Björn Thomasson. High accuracy relative luminescence quantum yield measurements of upconverting nanoparticles, 2016. Student Paper.

[109] Monirehalsadat Mousavi, Björn Thomasson, Meng Li, *et al*. Beam-profile-compensated quantum yield measurements of upconverting nanoparticles. *Physical Chemistry Chemical Physics*, 19(33):22016–22022, 2017.

[110] Chao Wang, Liang Cheng, Huan Xu, and Zhuang Liu. Towards whole-body imaging at the single cell level using ultra-sensitive stem cell labeling with oligo-arginine modified upconversion nanoparticles. *Biomaterials*, 33(19):4872–4881, 2012.

[111] Tianye Cao, Yang Yang, Yuan Gao, Jing Zhou, Zhengquan Li, and Fuyou Li. High-quality water-soluble and surface-functionalized upconversion nanocrystals as luminescent probes for bioimaging. *Biomaterials*, 32(11):2959–2968, 2011.

[112] Liang Cheng, Kai Yang, Yonggang Li, *et al*. Facile preparation of multifunctional upconversion nanoprobes for multimodal imaging and

dual-targeted photothermal therapy. *Angewandte Chemie*, 123(32):7523–7528, 2011.

[113] Qingtao Chen, Xin Wang, Fenghua Chen, *et al*. Functionalization of upconverted luminescent $NaYF_4$:Yb/Er nanocrystals by folic acid–chitosan conjugates for targeted lung cancer cell imaging. *Journal of Materials Chemistry*, 21(21):7661–7667, 2011.

[114] Young-Hwa Kim, Jongho Jeon, Su Hyun Hong, *et al.* Tumor targeting and imaging using cyclic RGD-PEGylated gold nanoparticle probes with directly conjugated iodine-125. *Small*, 7(14):2052–2060, 2011.

[115] Guangshun Yi, Yanfen Peng, and Zhiqiang Gao. Strong red-emitting near-infrared-to-visible upconversion fluorescent nanoparticles. *Chemistry of Materials*, 23(11):2729–2734, 2011.

[116] Niagara Muhammad Idris, Zhengquan Li, Lei Ye, *et al*. Tracking transplanted cells in live animal using upconversion fluorescent nanoparticles. *Biomaterials*, 30(28):5104–5113, 2009.

[117] Liang Cheng, Kai Yang, Shuai Zhang, Mingwang Shao, Shuittong Lee, and Zhuang Liu. Highly-sensitive multiplexed in vivo imaging using pegylated upconversion nanoparticles. *Nano Research*, 3(10):722–732, 2010.

[118] Scott A Hilderbrand, Fangwei Shao, Christopher Salthouse, Umar Mahmood, and Ralph Weissleder. Upconverting luminescent nanomaterials: Application to in vivo bioimaging. *Chemical Communications*, 2009(28): 4188–4190, 2009.

[119] Jing Zhou, Mengxiao Yu, Yun Sun, *et al*. Fluorine-18-labeled $Gd^{3+}/Yb^{3+}/Er^{3+}$ co-doped $NaYF_4$ nanophosphors for multimodality PET/MR/UCL imaging. *Biomaterials*, 32(4):1148–1156, 2011.

[120] Feng Wang, Renren Deng, Juan Wang, *et al*. Tuning upconversion through energy migration in core-shell nanoparticles. *Nature Materials*, 10(12):968–973, 2011.

[121] Qiyue Shao, Lilai Ouyang, Lifei Jin, and Jianqing Jiang. Multifunctional nanoheater based on $NaGdF_4$:Yb^{3+}, Er^{3+} upconversion nanoparticles. *Optics Express*, 23(23):30057–30066, 2015.

[122] Zengxia Zhao, Yuning Han, Chenghong Lin, *et al*. Multifunctional core–shell upconverting nanoparticles for imaging and photodynamic therapy of liver cancer cells. *Chemistry – An Asian Journal,* 7(4):830–837, 2012.

[123] Dandan Ma, Xiang Xu, Min Hu, *et al*. Rare-earth-based nanoparticles with simultaneously enhanced near-infrared (NIR)-visible (vis) and NIR-NIR dual-conversion luminescence for multimodal imaging. *Chemistry – An Asian Journal*, 11(7):1050–1058, 2016.

[124] Renata Madru, Pontus Svenmarker, Christian Ingvar, *et al*. Development of a hybrid nanoprobe for triple-modality MR/spect/optical fluorescence imaging. *Diagnostics*, 4(1):13–26, 2014.

[125] Tomas Jansson, Stefan Andersson-Engels, Sarah Fredriksson, Freddy Ståhlberg, and Sven-Erik Strand. Superparamagnetic iron oxide nanoparticles as a multimodal contrast agent for up to five imaging modalities. *Clinical and Translational Imaging*, 3(3):247–249, 2015.

[126] Maria Evertsson, Pontus Kjellman, Magnus Cinthio, *et al*. Multimodal detection of iron oxide nanoparticles in rat lymph nodes using magnetomotive ultrasound imaging and magnetic resonance imaging. *IEEE Transactions on Ultrasonics, Ferroelectrics, and Frequency Control*, 61(8):1276–1283, 2014.

[127] Renata Madru, Pontus Kjellman, Fredrik Olsson, *et al*. 99m Tc-labeled superparamagnetic iron oxide nanoparticles for multimodality spect/mri of sentinel lymph nodes. *Journal of Nuclear Medicine*, 53(3):459–463, 2012.

[128] Lei Zhou, Rui Wang, Chi Yao, *et al*. Single-band upconversion nanoprobes for multiplexed simultaneous in situ molecular mapping of cancer biomarkers. *Nature Communications*, 6, Article ID 6938, 2015.

[129] HJMAA Zijlmans, Jan Bonnet, Jarrett Burton, *et al*. Detection of cell and tissue surface antigens using up-converting phosphors: A new reporter technology. *Analytical Biochemistry*, 267(1):30–36, 1999.

[130] Paul Corstjens, Michel Zuiderwijk, Antoinette Brink, *et al*. Use of up-converting phosphor reporters in lateral-flow assays to detect specific nucleic acid sequences: A rapid, sensitive dna test to identify human papillomavirus type 16 infection. *Clinical Chemistry*, 47(10):1885–1893, 2001.

[131] Johannes Hampl, Michael Hall, Naheed A Mufti, *et al*. Upconverting phosphor reporters in immunochromatographic assays. *Analytical Biochemistry*, 288(2):176–187, 2001.

[132] R Sam Niedbala, Hans Feindt, Keith Kardos, *et al*. Detection of analytes by immunoassay using up-converting phosphor technology. *Analytical Biochemistry*, 293(1):22–30, 2001.

[133] Leyu Wang and Yadong Li. Green upconversion nanocrystals for DNA detection. *Chemical Communications*, 2006(24):2557–2559, 2006.

[134] Henna Pakkila, Minna Yliharsila, Satu Lahtinen, *et al*. Quantitative multianalyte microarray immunoassay utilizing upconverting phosphor technology. *Analytical Chemistry*, 84(20):8628–8634, 2012.

[135] Vishal Kale, Henna Pakkilaa, Jiri Vainio, *et al.* Spectrally and spatially multiplexed serological array-in-well assay utilizing two-color upconversion luminescence imaging. *Analytical Chemistry*, 88(8):4470–4477, 2016.

[136] Yiqing Lu, Jiangbo Zhao, Run Zhang, *et al.* Tunable lifetime multiplexing using luminescent nanocrystals. *Nature Photonics*, 8(1):32–36, 2014.

[137] Katri Kuningas, Terhi Rantanen, Telle Ukonaho, Timo Lövgren, and Tero Soukka. Homogeneous assay technology based on upconverting phosphors. *Analytical Chemistry*, 77(22):7348–7355, 2005. PMID: 16285685.

[138] Terhi Rantanen, Marja-Leena Jarvenpaa, Johanna Vuojola, Riikka Arppe, Katri Kuningas, and Tero Soukka. Upconverting phosphors in a dual-parameter lret-based hybridization assay. *Analyst*, 134(8):1713–1716, 2009.

[139] Peng Zhang, Snezna Rogelj, Khoi Nguyen, and Damon Wheeler. Design of a highly sensitive and specific nucleotide sensor based on photon upconverting particles. *Journal of the American Chemical Society*, 128(38):12410–12411, 2006. PMID: 16984179.

[140] Meng Wang, Wei Hou, Cong-Cong Mi, *et al*. Immunoassay of goat anti-human immunoglobulin g antibody based on luminescence resonance energy transfer between near-infrared responsive $NaYF_4$:Yb, Er upconversion fluorescent nanoparticles and gold nanoparticles. *Analytical Chemistry*, 81(21):8783–8789, 2009. PMID: 19807113.

[141] Yan-Mei Wu, Yao Cen, Li-Jiao Huang, Ru-Qin Yu, and Xia Chu. Upconversion fluorescence resonance energy transfer biosensor for sensitive detection of human immunodeficiency virus antibodies in human serum. *Chemical Communications*, 50(36):4759–4762, 2014.

[142] Yujie Ding, Hao Zhu, Xiaoxia Zhang, *et al*. An upconversion nanocomposite for fluorescence resonance energy transfer based cholesterol-sensing in human serum. *Nanoscale*, 6(24):14792–14798, 2014.

[143] Zhiguo Zhou, He Hu, Hong Yang, *et al*. Up-conversion luminescent switch based on photochromic diarylethene and rare-earth nanophosphors. *Chemical Communications*, 2008(39):4786–4788, 2008.

[144] Carl-Johan Carling, Farahnaz Nourmohammadian, John-Christopher Boyer, and Neil R Branda. Remote-control photorelease of caged compounds using near-infrared light and upconverting nanoparticles. *Angewandte Chemie International Edition*, 49(22):3782–3785, 2010.

[145] Yi-Hsin Chien, Yu-Lin Chou, Shu-Wen Wang, *et al*. Near-infrared light photocontrolled targeting, bioimaging, and chemotherapy with caged upconversion nanoparticles in vitro and in vivo. *ACS Nano*, 7(10):8516–8528, 2013.

[146] John V Garcia, Jianping Yang, Dengke Shen, *et al*. Nir-triggered release of caged nitric oxide using upconverting nanostructured materials. *Small*, 8 (24):3800–3805, 2012.

[147] Lingzhi Zhao, Juanjuan Peng, Qi Huang, *et al*. Near-infrared photoregulated drug release in living tumor tissue via yolk-shell upconversion nanocages. *Advanced Functional Materials*, 24(3):363–371, 2014.

[148] Yanmei Yang, Qing Shao, Renren Deng, *et al.* In vitro and in vivo uncaging and bioluminescence imaging by using photocaged upconversion nanoparticles. *Angewandte Chemie*, 124(13):3179–3183, 2012.

[149] Muthu Kumara Gnanasammandhan Jayakumar, Niagara Muhammad Idris, and Yong Zhang. Remote activation of biomolecules in deep tissues using near-infrared-to-UV upconversion nanotransducers. *Proceedings of the National Academy of Sciences*, 109(22):8483–8488, 2012.

[150] Muthu Kumara Gnanasammandhan Jayakumar, Akshaya Bansal, Kai Huang, Risheng Yao, Bing Nan Li, and Yong Zhang. Near-infrared-light-based nano-platform boosts endosomal escape and controls gene knockdown in vivo. *ACS Nano*, 8(5):4848–4858, 2014.

[151] Akshaya Bansal, Haichun Liu, Muthu Kumara Gnanasammandhan Jayakumar, Stefan Andersson-Engels, and Yong Zhang. Quasi-continuous wave near-infrared excitation of upconversion nanoparticles for optogenetic manipulation of*C. elegans*. *Small*, 12(13):1732–1743, 2016.

[152] Kristian Berg, Pal Kristian Selbo, Lina Prasmickaite, *et al*. Photochemical internalization. *Cancer Research*, 59(6):1180–1183, 1999.

[153] Kristian Berg, Marco Folini, Lina Prasmickaite, *et al*. Photochemical internalization: A new tool for drug delivery. *Current Pharmaceutical Biotechnology*, 8(6):362–372, 2007.

[154] Hai Sheng Qian, Hui Chen Guo, Paul Chi-Lui Ho, Ratha Mahendran, and Yong Zhang. Mesoporous-silica-coated up-conversion fluorescent nanoparticles for photodynamic therapy. *Small*, 5(20):2285–2290, 2009.

[155] Niagara Muhammad Idris, Muthu Kumara Gnanasammandhan, Jing Zhang, Paul C Ho, Ratha Mahendran, and Yong Zhang. In vivo photodynamic therapy using upconversion nanoparticles as remote-controlled nanotransducers. *Nature Medicine*, 18(10):1580, 2012.

[156] Sasidharan Swarnalatha Lucky, Niagara Muhammad Idris, Zhengquan Li, Kai Huang, Khee Chee Soo, and Yong Zhang. Titania coated upconversion nanoparticles for near-infrared light triggered photodynamic therapy. *ACS Nano*, 9(1):191–205, 2015.

[157] Sasidharan Swarnalatha Lucky, Khee Chee Soo, and Yong Zhang. Nanoparticles in photodynamic therapy. *Chemical Reviews*, 115(4):1990–2042, 2015.

[158] Gan Tian, Xiao Zhang, Zhanjun Gu, and Yuliang Zhao. Recent advances in upconversion nanoparticles-based multifunctional nanocomposites for combined cancer therapy. *Advanced Materials*, 27(47):7692–7712, 2015.

[159] Haichun Liu, Can T Xu, Gökhan Dumlupinar, Ole B Jensen, Peter E Andersen, and Stefan Andersson-Engels. Deep tissue optical imaging of upconverting nanoparticles enabled by exploiting higher intrinsic quantum yield through use of millisecond single pulse excitation with high peak power. *Nanoscale*, 5(20):10034–10040, 2013.

[160] Dongmei Yang, Zhiyou Hou, Ziyong Cheng *et al.* Current advances in lanthanide ion (Ln^{3+})-based upconversion nanomaterials for drug delivery. *Chemical Society Reviews*, 44(6):1416–1448, 2015.

PAPER VII

Multi-variable compensated quantum yield measurements of upconverting nanoparticles with high dynamic range: A systematic approach

S. Konugolu, J. Matias, G. Dumlupinar, L. Niemitz, M. Mousavi, K. Komobilus, S. Andersson-Engels.

(2019) *Manuscript in preparation.*

Multi-variable compensated quantum yield measurements of upconverting nanoparticles with high dynamic range: a systematic approach

SANATHANA KONUGOLU VENKATA SEKAR,[1,*] JEAN S. MATIAS,[1,2] GOKHAN DUMLUPINAR,[1,2] LORENZO NIEMITZ,[1,2] MONIREHALSADAT MOUSAVI[3] KATARZYNA KOMOLIBUS,[1] AND STEFAN ANDERSSON-ENGELS[1,2]

[1]*Biophotonics@Tyndall, IPIC, Tyndall National Institute, Cork, Ireland*
[2]*Department of Physics, University College Cork, Cork, Ireland*
[3]*Department of Physics, Lund University, Lund, Sweden*

**sanathana.konugolu@tyndall.ie*

Abstract: Upconverting nanoparticles are an emerging technology with fast-growing applications in various fields. The power density dependence of emission quantum yield of these particles makes them a challenging material to characterize using currently available commercial quantum yield systems. We propose a multimodal system, which takes into account and compensates for various distorting parameters while providing accurate high dynamic range (1:10^4) quantum yield curves. The resulting stability and reproducibility test showed less than 4% variation for measured quantum yield values under various experimental conditions. Furthermore, quantum yield measurements on commercially available core and core-shell particles were presented. A brief outlook on future prospects is presented towards the end.

1. Introduction

The use of upconverting nanoparticles (UCNPs) has developed rapidly and today spans a wide range of research fields including, among others, molecular interactions in cell biology, specific staining of tissue slides, *in vivo* luminescence imaging, and photodynamic therapy [1-10]. Each of these avenues of research stem from the discovery of the upconversion (UC) process by Bloembergen [11] and an early series of studies conducted by Auzel [12-14]. UC is the unique energy conversion ability of the materials to generate a high energy photon as a consequence of the sequential absorption of multiple low energy photons. UC capable nanomaterials have demonstrated remarkable optical features, which has facilitated the generation of high impact findings in various fields of research in biomedicine.

Due to the varying requirements in different biomedical applications, both material design and optimization of these particles are playing key roles in framing further research. To date, numerous properties of UCNPs have been investigated, including crystal composition and structure, surface functionality, and biocompatibility [15-20]. Recently, one of the important areas of UCNP-related research has focused on luminescence efficiency. The low quantum yield (QY) nature of UCNPs has been a limiting factor in the extensive adoption of UCNPs in biomedical applications. QY is typically only in the range of a few percents at high excitation power densities and decreases dramatically in the low power density regime [21]. The power dependence of the QY is critically important, especially for deep tissue applications - where the excitation light is heavily attenuated by intrinsic biomolecules and where low power densities are required. Various factors contribute to low QY of UCNPs, including crystal properties (*e.g.* host matrix, size, phase, and dopant ratio), surface properties, and dispersion medium [22-27]. Hence, extensive research aimed at improving the QY of UCNPs to obtain a stronger signal is well motivated. Many different approaches have been applied to increase QY, including optimization of particle composition [28], engineering of the excitation source [9, 29, 30], and implementation of core-shell structures [31, 32].

The efforts in improving the luminescence efficiency of UCNPs make standardized QY measurements essential. Previous work in measuring the QY of UCNPs includes a remarkable study done by Boyer *et al*. [33]. More recently, the importance of the excitation beam profile in such measurements was reported [34-37]. Traditionally, integrating sphere instruments are used to measure the absolute QY, as these can collect emission from all directions. The alternative would be to use a detector measuring in a limited solid angle. This can then yield the QY by referring to measurements of a dye with known QY in the same measurement geometry, assuming that the spatial distribution of the emission from the two samples are identical. The advantage with the latter relative quantum yield technique for measuring QY of UCNPs is that the beam profile can be better controlled and measured, which is of significant importance as the QY depends on the power density of the excitation light. The efficient reflections within an integrating sphere, together with a complication in measuring the actual beam profile in an integrating sphere, make it difficult to control and know the exact beam profile of the excitation light in this type of setup.

Currently, it is clear that there is no complete system that adequately characterizes the QY of UCNPs. There is a high demand for a compact QY characterization system that is capable of covering a wide dynamic range of excitation power densities and a broad spectral range that includes all emission lines of interest. Such a compact system would extremely be useful for deep tissue, photodynamic therapy (PDT), and bio-imaging applications, where excitation power density varies with the specimen depth. Furthermore, a standardized QY characterization protocol would allow for direct comparisons between different UCNPs that are developed by various research groups.

In this work, we present a multi-modal QY system that compensates for various distorting parameters (scattering, beam profile, inner filter effect, the limited bandwidth of filters) and provides well-resolved high dynamic range quantum yield curves. The system provides means to measure the absorption, scattering, emission spectra of samples and the beam profile employed in the excitation. A Tm-based core and core-shell UCNPs with excitation at 976 nm and emission at 800 nm were investigated to characterized, test and validate the system. The system provides means to measure the absorption, scattering, emission spectra of samples and the beam profile employed in the excitation. Importantly, the method also eliminates the influence of uneven and uncontrolled power density distribution due to speckles of a coherent excitation laser by cleverly managing the illumination path design.

2. Material and Methods

2.1 System Setup

Figure 1 shows the schematic layout of the multi-modal quantum yield system. The system consists of 6 arms designed to shape and acquire the beam profile (arms 1, 2, 3, respectively) and characterize various optical parameters (absorption and scattering, emission spectra, and luminescence signal) of the UCNP sample (arms 4, 5, 6, respectively). Arm 1 (UCNP excitation arm) consists of temperature stabilized single-mode fiber-coupled diode Laser (Thorlabs, BL976-PAG500) and an optical arrangement to achieve speckle free beam profile of adjustable size. Two sets of optics in arm 1 (L1 f = 30 mm; L2 f = 30 mm or nil; L3 f = 6 mm or nil; and L4 f = 200 mm) were used to achieve two different spot sizes: 700 µm or 150 µm in beam diameter. The two spot sizes were chosen to achieve a high dynamic range of power densities while also having an optimal overlap of the two quantum yield curves generated. A filter (F1-

OD 2) was employed to further increase the range of quantum yield curves at low power density regions for a given spot size. Lenses L1 and L3 on arm 1 were mounted on XY stages (Thorlabs CXY1) for precise alignment of the beam spot in the middle of the cuvette holder. A pair of irises (I2 and I3) were used to align the spot in the middle of the cuvette. A polarizer P1 (Thorlabs, LPNIRE200-B) was placed in between lenses L1 and L2 to vertically polarize the light impinging on the sample. A power meter PM (Thorlabs, PM100D) was attached at the distal end of the cuvette holder to measure the power of the light passing through the sample. Arm 2 (reference dye excitation arm) is an exact replica of arm 1 with a single-mode fiber-coupled 785 nm laser (Thorlabs FPL785S-250 at 785 nm) used for excitation. The arm is enabled by flipping the flip mirror (FM2). The purpose of this arm is to acquire the luminescence signal from the dye whose emission line is similar to the emission of the UCNPs. The quantum yield value of the dye used was well known from the literature [38], which enables the relative quantum yield assessment by calibrating the experimentally obtained quantum yield values from the UCNPs.

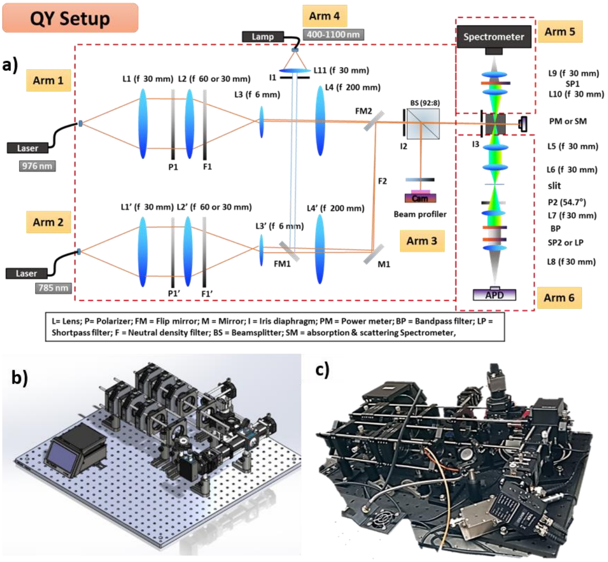

Fig. 1 a) Optical layout of multimodal quantum yield system b) CAD model of the system c) Image of the QY system in the lab

Arm 3 (beam profile arm) consists of a high-resolution camera and a set of filters to acquire the beam profile of the excitation light employed, identical to the beam profile in the cuvette. A pellicle beam splitter (Thorlabs, CM1-BP108, 92:8) was used to split the rays and the camera was placed at equidistant to the center of the cuvette holder thus acquiring a beam profile resembling the midpoint of the sample cuvette. Arm 4 (absorption and scattering spectra arm) provides a broadband light source (Ocean Optics HL 2000) to enable broadband scattering measurement of the sample. This arm is enabled by flip mirrors (FM1 and FM2) which transmit the white light through the sample in the sample holder to be measured by a spectrometer (Ocean Optics QE Pro). For this measurement, the power meter (PM) was replaced with a fiber bundle (Thorlabs BFL200HS02) which was connected to the spectrometer. The intensity and spot size of this arm is controlled using an iris (I1). Arm 5 collects the luminesce light from the sample and sends it onto the fiber-coupled (Thorlabs BFL200HS02) spectrometer (Ocean Optics QE Pro, 350-1100 nm) to measure the emission spectra of UCNP samples. The arm consists of lenses (L9, L10 = 30 mm), and a short pass filter SP1 (Thorlabs, FES0900) to remove excitation stray light at 976 nm. Arm 6 is the luminescence arm, which collects the luminescence light emitted by the sample using a set of lenses (L5, L6, L7, L8 = 30 mm) and focuses that light onto an avalanche photodiode (APD) detector (Thorlabs, APD120A). A slit (700 µm) is placed between L6 and L7 to limit the measured light to the emission generated in the center of the cuvette and also manage to avoid luminescence signals overfilling the APD. A polarizer P2 (Thorlabs, LPNIRE100-B) is kept at (53.7°) with respect to the linear polarizer in excitation arms to remove distortion caused due to any anisotropic nature of the samples. A set of two filters, a bandpass BP (Edmund Optics, FBH800) and a short pass SP2 (Thorlabs, FES0900) are placed in the path to filter excitation light and only allow the luminescence signal (800 nm) to pass and be focused on the APD active area. Similarly, a bandpass BP (Edmund Optics, FBH800) and long pass LP (Thorlabs, LP02785RU) filter are adopted to avoid excitation light while measuring the reference dye signal. An X-Y stage (Thorlabs CXY1) was used to precisely center the APD detector and thereby enabling accurate alignment. A data acquisition (DAC) device (National Instruments, USB-6216) along with a preamplifier (Femto – DLPVA) was used to acquire the signal from the APD. All parameters varied in the system (e.g. laser current, power meter settings, beam profile, spectrometer settings) and the measurement routine are controlled and automated using a user-specified Labview software.

2.2 Samples preparation

The samples used for this study were water-soluble $NaYF_4$:Tm core and core-shell UCNP samples (102-25-804) procured from Hangzhou Fluo Nanotech co. Ltd at a concentration of 10 mg/ml. The samples were diluted in distilled water at 5 mg/ml, 2.5 mg/ml for concentration repeatability measurements. These UCNPs were optimized during the synthesis for enhancement of the 800 nm emission transition. The reference dye used to calibrate the UCNPs signal was procured from Dyomics (Dy- 781). The dye has an emission wavelength centered similar to UCNP (800 nm) and a factory tabulated quantum yield of 11.9 % when dissolved in ethanol. The dye was diluted in ethanol solvent to have absorption values similar to 10 mg/ml UCNP samples used for this study. Two dedicated cuvettes with water and ethanol solvents were prepared as blank references to obtain absorption values of pure UCNPs and dye. 1 ml was the minimum quantity needed to perform the measurement. Therefore, 2 ml of each sample were placed in a quartz cuvette (Thorlabs, CV10Q3500FS) and the cap was sealed with a glue gun to avoid any evaporation of the ethanol and water solvents.

2.3 Measurement protocol and data analysis

A systematic procedure was adopted for both, the collection of data from the sample and analysis algorithm to extract compensated quantum yield values. The workflow for data collection and analysis is depicted in Figure 2.

Measurement protocol

At first, the UCNP and dye samples were prepared as mentioned in the sample preparation section and sonicated for 15 minutes. The broadband (350-1100 nm) emission spectrum of the UCNPs was acquired using arm 5. This was followed by broadband transmission measurements of samples in the following order: UCNPs, reference water, empty cuvette, dye sample, reference ethanol. Then the system was set up to create spot size S1 in both arms. The beam profile at S1 was captured using excitation arm1 with the beam profile camera, followed by luminescence signal measurements of UCNPs at various laser currents (976 nm, laser 20- 800 mA, step size 4 mA). The same process was thereafter directly repeated for the dye sample at various laser currents (785 nm, laser 20- 250 mA, step size 4 mA). The whole procedure of measuring the luminescence signal of UCNPs and dye at S1 was repeated with filter F1 & F1’ in the respective arms. Then, the whole sequence of measurements was repeated for beam profile S2. In total eight luminescence measurement series were conducted in the following order: UCNP-S1, dye-S1, UCNP-S1-F1, dye-S1-F1’, UCNP-S2, dye-S2, UCNP-S2-F2, dye-S2-F2’. This completes the measurement sequence of the multimodal system. This sequence was repeated for each sample to be characterized, in this study different concentrations of core and core-shell particles. The outputs of the measurement sequence are the emission spectrum of UCNP, in total five transmission data of UCNP and dye samples, two beam profiles of S1 and S2, and eight luminescence signal of UCNP and dye combined.

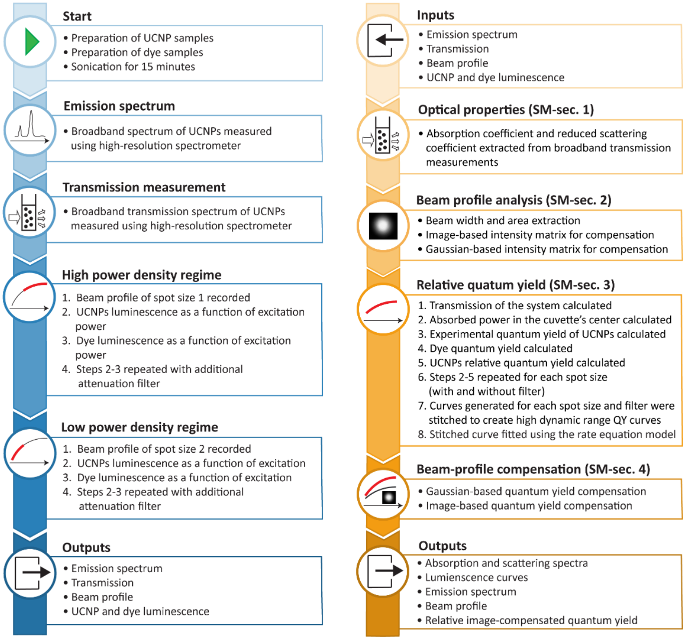

Fig. 2 Schematic flow chart depicting the measurement protocol and analysis algorithm.

Analysis methods

The analysis algorithm takes all the outputs of the measurements as inputs and calculates various optical parameters (absorption, scattering, emission spectra, beam profile) and subsequently uses the calculated data to compensate for possible distortions in the estimated high dynamic range quantum yield values of UCNP. The steps are briefly described in this section, more detailed equations and calculation steps could be found in the supplementary material (SM). The first step is to calculate the absorption and scattering spectra of UCNP and dye from the transmission measurement data. Beer Lamberts' and Mie scattering laws were used for the estimation of absorbance and scattering spectra of the samples as described in the SM-sec.1. The compensated absorption of UCNP at 976 nm was used as input to the quantum yield calculations. The acquired beam profiles of the 976 nm laser (S1 and S2) were employed to create i) image-based intensity matrix for compensation and ii) Gaussian-profile-based intensity matrix for compensation (SM-sec.2), utilized to calculate the image compensated quantum yield valued of UCNP. The experimental quantum yield (not compensated with dye quantum yield) is obtained by taking the ratio of luminescence signal of UCNP to the absorbed power per unit length in the middle of the cuvette (SM-sec.3). The relative quantum yield is estimated by calibrating the UCNP experimental quantum yield values with dye quantum yield values (SM-sec.3). The above process to find the relative quantum yield was repeated for all spot size (S1, S2) and filter (nil, F1) configurations which provides in total four quantum yield curves as shown in Figures 5(a-d). The relative quantum yield curves were stitched without any fitting parameters to provide a high dynamic range relative quantum yield curve as shown in Figure 5e. The relative quantum yield curves were compensated for the beam profile to avoid underestimating the QY values. This compensation was implemented by solving the quantum yield for each pixel in the beam profile using a 2-level rate equation for the 800 nm line. The balancing power density (ρ_b) and balancing quantum yield (ϕ_b) for all three high dynamic range relative quantum yield curves (uncompensated, compensated gaussian and image) were calculated. The various calculations of compensation methods were discussed in (SM-sec.4).

3. Results and Discussion

3.1 Beam profile and source characterization

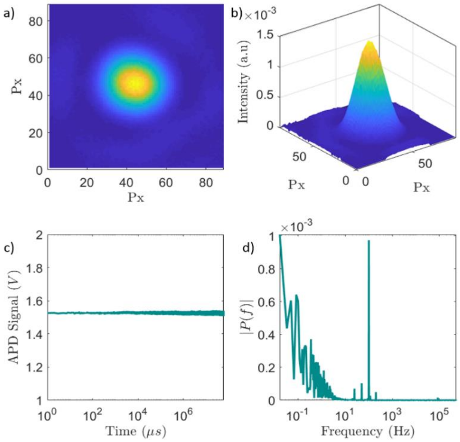

Fig. 3 Beam profile characterization a) Beam profile image b) Beam profile 3D plot c) Raw temporal signal from one pixel of the beam profile d) Fourier transform of the temporal signal

One of the key features of the system is the ability to obtain a speckle free uniform beam profile for a given spot size. This is achieved by using a single-mode fiber followed by an optical beam shaping lens set up to obtain spot size while preserving the speckle free beam profile. It is critical to have a uniform and stable power density (light intensity) across the beam profile as possible. Such a profile will lead to fewer compensations and thereby accurate estimations of relative quantum yield values. Figure 3(a-b) shows the beam profile acquired by the camera equidistant to the midpoint of the sample cuvette. The smooth speckle-free profile enables the algorithm to easily compensate for the beam-profile-based distortion to the evaluated quantum yield curves. However, it is also important to ensure the laser is temporally stable over the entire measurement period. To test this, the power meter at the distal end of the sample holder was temporarily replaced by a single-mode fiber (6 µm core diameter) with the other end of the fiber connected to an APD detector. The small fraction of light collected by the APD detector was acquired for 60 sec by using a DAQ card at a collection rate of 1 mega sample/sec. Figure 3c shows the raw data acquired by the APD detector. The variation in the amplitude of the laser during one minute is less than 0.5 %. To understand the key variation frequencies we performed a Fast Fourier transform (FFT) of the acquired signal (Figure 3d), a 1/f noise is evident from Figure 3d and signal at 50 Hz is observed which might be the signal corresponding to the power supply frequency (50 Hz).

3.2 Multi-modal measurements and compensation

The accuracy of the estimated quantum yield values of UCNPs depends on the accurate evaluation of various optical properties of UCNPs and optimal compensation for all contributing factors. It is ideal to measure all parameters of UCNPs simultaneously using a well-calibrated system to avoid possible changes in sample properties over time. The developed measurement protocol (section 2.3) allows for the efficient collection of data while minimizing delay, thereby maximizing accuracy when compensating for various contributing factors.

Absorption and Scattering Compensation

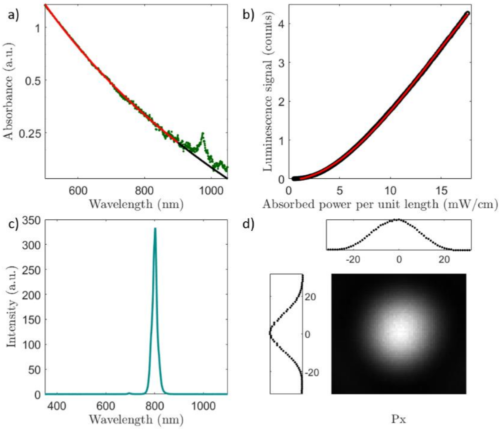

Fig. 4 Multimodal features of QY system a) Absorption and scattering spectra b) Luminescence signal of UCNP c) Emission spectrum of UCNP d) Beam profile of 976 nm laser.

The UCNP absorbance spectrum measured by the arm 5 contains both the absorption and scattering contribution. The measured transmission spectrum was fit to the wavelength dependence of Mie scattering. Figure 4a (black line) shows the Mie-scattering fit to the transmitted spectrum. The difference between the fitted scattering and the measured transmission spectra yields the actual absorption of the UCNP sample. For this particular sample, the absorption is estimated to be 66 % percent of the sample attenuation. In the absence of this compensation, the UCNP quantum yield would be underestimated by 34%.

Reference dye calibration and emission filter compensation

A calibration reference dye was used to convert the experimentally measured quantum yield values to corrected relative quantum yield values. For this to be accurate the spatial and spectral distribution of the luminescence emission needs to be the same for the samples. Both samples should emit isotropically, so the spatial assumption is believed to be fulfilled. In addition, the detection filters have to be compensated for, as the emission of the dye, in particular, is broader than the optical detection filter. For both samples, the percentage of the incident light was corrected by calculating the fraction of the emission profile being transmitted through the filters. It is also important to use a dye with a similar emission profile to the UCNPs as possible so that this correction factor can be minimized (yielding as small error as possible). This correction procedure is described in detail in SM-sec.4.

Beam profile compensation

The shape of the beam profile and characteristics of the laser affect the estimated quantum yield values. The absence of speckle and a smooth Gaussian beam profile is evident from Figure 4d. Importantly, any presence of speckles results in a random distribution of a light speckle pattern with different power density across the beam profile. This makes it difficult to accomplish accurate compensation for the beam profile. The system in this work is effectively free of both temporal and spatial speckles. The beam profile compensation algorithm (described in SM-sec.4) can thereby accurately compensate for the different power densities across the beam profile.

High dynamic range quantum yield curves

Figures 5 (a-d) show the relative quantum yield values estimated for different spot sizes and filter combinations. Unlike dyes, the quantum yield of UCNPs is a variable of the excitation power density. To be able to determine the quantum yield of UCNPs for a broad range of power densities is of great value. For example, Figure 5 (a-b) have valuable inputs for *in vivo* studies of deep tissue, as it needs quantum yield values for low power densities limited by light attenuation in tissue and safe human exposure levels whereas the microscope studies need to understand quantum yield values at high power density. Depending on the microscope objective and sample, Figure 5(c-d) provides insights into the emitted light from the sample. The system described in this paper has been designed to perform quantum yield measurements over a broad range of power densities (1:10^4). This is achieved by using two different spot sizes (S1, S2) in combination with/without the use of an ND filter. In total 4 measurement series were conducted for each sample to extract quantum yield values of UCNPs at a range of power densities and the results were stitched without any fitting parameter to obtain high dynamic range quantum yield curves. Figure 5e shows the quantum yield of a stitched curve along with image and Gaussian beam profile compensation. To the best of our knowledge, this is for the first time such high dynamic range curves were obtained, compensated for the influence of the beam profile.

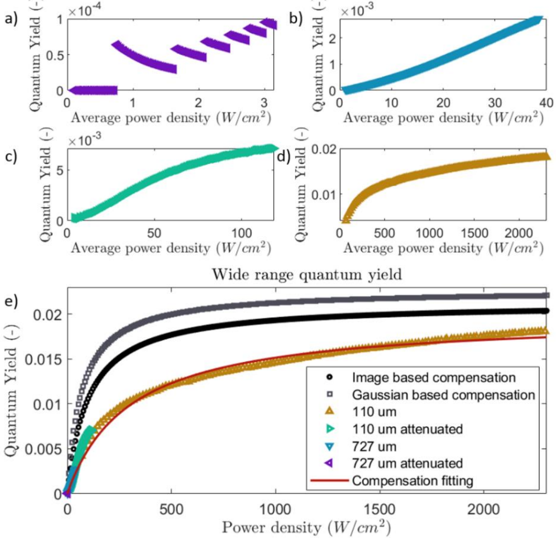

Fig. 5 Broadband high dynamic range quantum yield curve of UCNP a) Spot size S2 with filter F1, b) Spot size S2 without filter F1 c) Spot size S1 with filter F1 d) Spot size S1 without filter F1 e) Stitched experimental (yellow triangles), image compensated (black circles), Gaussian compensated (grey squares).

3.3 Stability and reproducibility

The QY system was tested under various experimental conditions to ensure the robustness of the system. The following four variables were considered a) sonication of the samples b) intra-day stability c) inter-day reproducibility d) different sample concentrations. The results of these measurements are summarized in Figure 6. The sonication time was tested to understand optimal sonication time for the samples and it's clear from Figure 6a that sonication time between 5-15 minutes does not influence to measured quantum yield of UCNPs much. Figure 6b elucidates that the intra-day variations were found to be within 4% variation at high quantum yield values. Inter-day reproducibility was found to have similar variations (Figure 6c). It is worth noting that in the absence of all measurements and compensations, we found the assessed quantum yield values to vary by up to 100%. The different sample concentrations were attributed to the changes in the turbidity of the UCNP sample. Correct compensation for turbidity from the transmission spectral measurements resulted in a remaining negligible variation in quantum yield values as illustrated in Figure 6d. In addition to the inter-sample variations, the absence of this compensation yielded on average a 60% underestimation in quantum yield values. These tests emphasize the need for multimodal measurement and compensation for the optimal characterization of UCNPs.

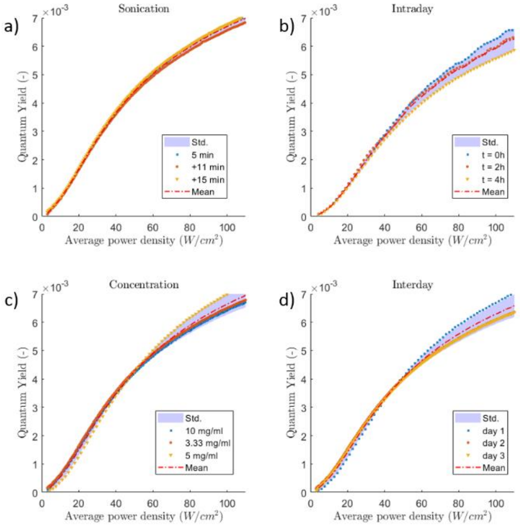

Fig. 6 Testing of QY system under different experimental conditions a) Sonication time, b) Intra-day (stability) c) Concentration d) Interday (reproducibility).

3.4 Commercial UCNP samples

The next step in this study was to employ the well-tested and validated multi-modal QY system to measure commercially available UCNP samples. We chose core and core-shell UCNPs from one supplier of NaYF4:Tm. The results for the core and core-shell UCNPs are shown in Figures 7 and 8, respectively. Comparing the results from Figures 7e and 8e, it is obvious that the core-shell particles have a higher quantum yield than the core nanoparticles. This is one of the main aims of having a surrounding shell to protect the core from exposure to external factors that could negatively affect the quantum yield of the particles. The absorption spectra for both particles are very similar, while a slight variation in scattering slope is observed between them. From Figures 7a and 8a, the core-shell particles studied here seem to be more turbid than the core particles. This again emphasizes the importance of scattering compensation in the assessment of the quantum yield. Figure 7c and 8c, both samples seem to have very similar spectral emission profiles, showing that the presence of a shell did not affect the emission profile of UCNPs. As expected, the luminescence intensity curve differs between the samples (Figure 7b and 8b) whereas the beam profiles across the measurements remain the same (Figure 7d and 8d).

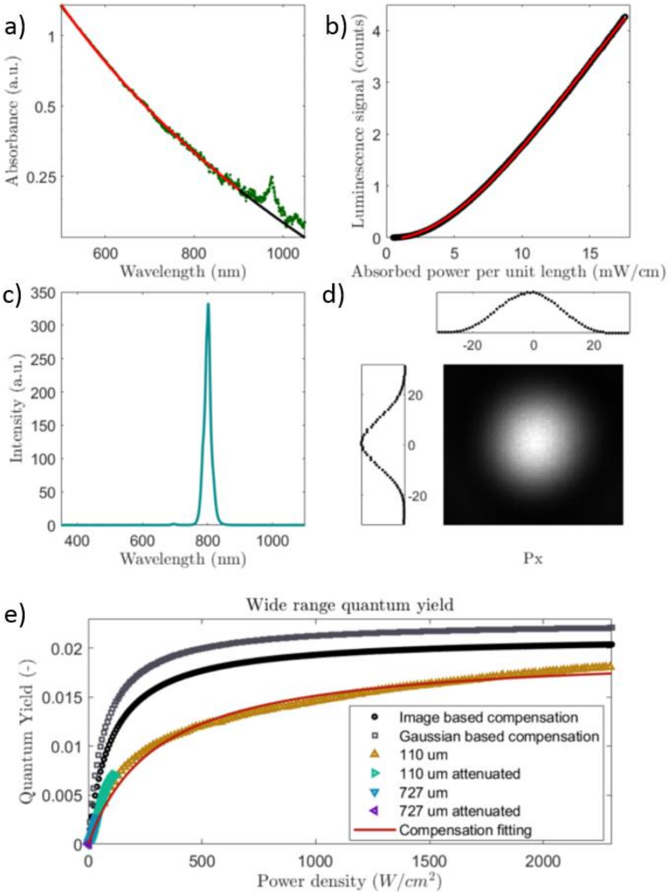

Fig 7. Multimodal measurement of core UCNPs a) Absorption and scattering spectra b) Luminescence signal of UCNP c) Emission spectrum of UCNP d) Beam profile of 976 nm laser e) Stitched experimental (yellow triangles), image compensated (black circles), Gaussian compensated (grey squares).

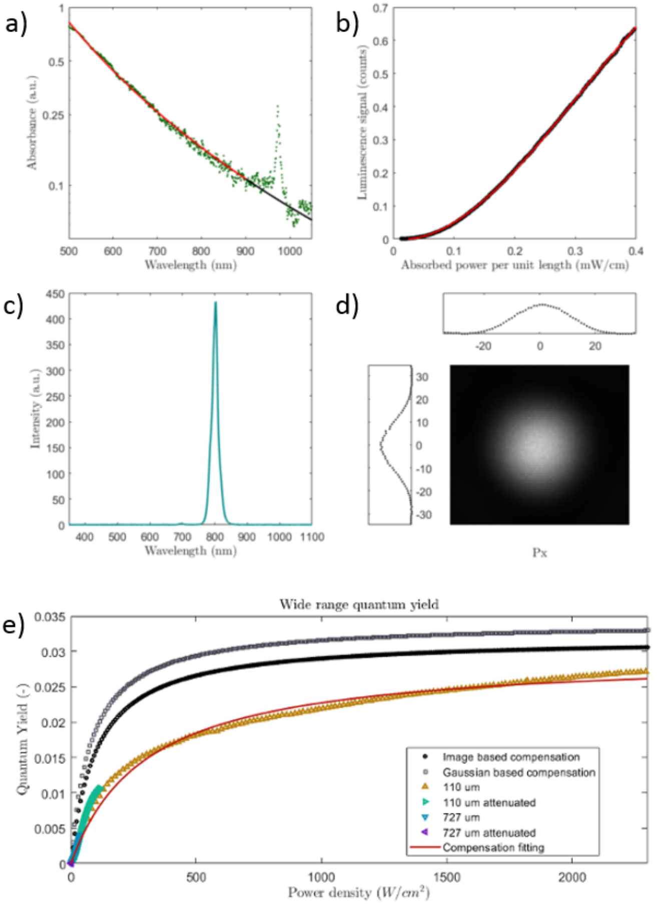

Fig 8. Multimodal measurement of core-shell UCNPs a) Absorption and scattering spectra b) Luminescence signal of UCNP c) Emission spectrum of UCNP d) Beam profile of 976 nm laser e) Stitched experimental (yellow triangles), image compensated (black circles), Gaussian compensated (grey squares).

3.5 Limitations of the work and future outlook

In this work, we consider only the 800 nm emission line of the $NaYF_4$:Tm UCNPs. An extension to other emission lines could be achieved easily, by changing emission filters in the system and by selecting a proper dye matching the emission wavelength of UCNPs. The UCNP laser remains the same, while the excitation laser of the reference dye needs to be chosen based on the measurement protocol used for the tabulated QY of the selected dye. Importantly, the rate equations (2 photon transition) developed for the 800 nm emission line may no longer be valid for other lines, as these lines might involve 3,4 or 5 photon transitions. Hence, the image or Gaussian based beam compensation algorithms will no longer be valid for those transitions. Therefore there is an obvious demand for rate equation models that take into account these other transitions. In the current configuration of the system, the sample and solvent are measured in sequence. Changes in the intensity of the light source may be present, leading to errors in the assessed optical properties and in the obtained quantum yield. This could be avoided by adding an extra arm with a cuvette holder for the blank sample containing solvent only. This would permit the transmittance spectral measurements to be performed simultaneously, thus avoiding possible errors. Also, a careful look into state-of-the-art detection technology might make it possible to further increase the dynamic range of the measured quantum yield curves. To thoroughly validate the system we were using two different arms for UCNP laser 976 nm and dye reference laser 785 nm. However, the purpose of the dye arm is to calibrate the quantum yield of UCNPs. This calibration factor will remain constant, provided, the system is robustly built and well tested under different experimental conditions. Therefore, the need for a reference arm could be eliminated once the calibration factor at each emission line is robustly estimated.

4. Conclusions

In this work, we have for the first time presented high dynamic range ($1{:}10^4$) quantum yield curves of UCNPs by carefully compensating for various effects (scattering, beam profile, inner filter effect, the limited bandwidth of filters) that influence the accuracy of estimated quantum yield values. The system has been well characterized and tested for stability and reproducibility with a variation of less than 4 % under different experimental conditions. The study revealed, obtained quantum yields of UCNPs could vary by 100% and have an offset of 60% in the absence of the multi-modal corrections included in this measurement protocol. The system was used to characterize commercially available core and core-shell UCNPs. As expected the core-shell particles were found to have a higher quantum yield than the core particles. The key results obtained in this work points to the importance of multi-modal measurement and compensation to achieve accurate and consistent quantum yield values for UCNPs. With increasing innovation rate in the field of UCNPs, we believe our work can act as a precursor for standardizing the measurements of quantum yield values.

Funding

Science Foundation Ireland targeted professorship award SFI/15/RP/2828.

Disclosures

The authors declare no conflicts of interest.

References

1. Zijlmans, H.J.M.A.A., et al., *Detection of Cell and Tissue Surface Antigens Using Up-Converting Phosphors: A New Reporter Technology.* Analytical Biochemistry, 1999. **267**(1): p. 30-36.
2. Chatterjee, D.K., A.J. Rufaihah, and Y. Zhang, *Upconversion fluorescence imaging of cells and small animals using lanthanide doped nanocrystals.* Biomaterials, 2008. **29**(7): p. 937-943.

3. Wang, M., et al., *Immunolabeling and NIR-Excited Fluorescent Imaging of HeLa Cells by Using NaYF4:Yb,Er Upconversion Nanoparticles.* ACS Nano, 2009. **3**(6): p. 1580-1586.
4. Kobayashi, H., et al., *In vivo multiple color lymphatic imaging using upconverting nanocrystals.* Journal of Materials Chemistry, 2009. **19**(36): p. 6481-6484.
5. Liu, K., et al., *Covalently Assembled NIR Nanoplatform for Simultaneous Fluorescence Imaging and Photodynamic Therapy of Cancer Cells.* ACS Nano, 2012. **6**(5): p. 4054-4062.
6. Zhang, P., et al., *Versatile Photosensitizers for Photodynamic Therapy at Infrared Excitation.* Journal of the American Chemical Society, 2007. **129**(15): p. 4526-4527.
7. Wang, C., et al., *Near-infrared light induced in vivo photodynamic therapy of cancer based on upconversion nanoparticles.* Biomaterials, 2011. **32**(26): p. 6145-6154.
8. Qiu, H., et al., *Recent Progress in Upconversion Photodynamic Therapy.* Nanomaterials (Basel, Switzerland), 2018. **8**(5): p. 344.
9. Wang, D., et al., *808 nm driven Nd3+-sensitized upconversion nanostructures for photodynamic therapy and simultaneous fluorescence imaging.* Nanoscale, 2015. **7**(1): p. 190-197.
10. Liu, Q., et al., *Sub-10 nm Hexagonal Lanthanide-Doped NaLuF4 Upconversion Nanocrystals for Sensitive Bioimaging in Vivo.* Journal of the American Chemical Society, 2011. **133**(43): p. 17122-17125.
11. Bloembergen, N., *Solid State Infrared Quantum Counters.* Physical Review Letters, 1959. **2**(3): p. 84-85.
12. Auzel, F., *Upconversion and Anti-Stokes Processes with f and d Ions in Solids.* Chemical Reviews, 2004. **104**(1): p. 139-174.
13. Auzel, F., *Multiphonon-assisted anti-Stokes and Stokes fluorescence of triply ionized rare-earth ions.* Physical Review B, 1976. **13**(7): p. 2809-2817.
14. Auzel, F.E., *Materials and devices using double-pumped-phosphors with energy transfer.* Proceedings of the IEEE, 1973. **61**(6): p. 758-786.
15. Haase, M. and H. Schäfer, *Upconverting Nanoparticles.* Angewandte Chemie International Edition, 2011. **50**(26): p. 5808-5829.
16. Wang, F., et al., *Upconversion nanoparticles in biological labeling, imaging, and therapy.* Analyst, 2010. **135**(8): p. 1839-1854.
17. Liu, T.-M., et al., *Smart NIR linear and nonlinear optical nanomaterials for cancer theranostics: Prospects in photomedicine.* Progress in Materials Science, 2017. **88**: p. 89-135.
18. Dong, H., L.-D. Sun, and C.-H. Yan, *Energy transfer in lanthanide upconversion studies for extended optical applications.* Chemical Society Reviews, 2015. **44**(6): p. 1608-1634.
19. Gnach, A. and A. Bednarkiewicz, *Lanthanide-doped up-converting nanoparticles: Merits and challenges.* Nano Today, 2012. **7**(6): p. 532-563.
20. Sedlmeier, A. and H.H. Gorris, *Surface modification and characterization of photon-upconverting nanoparticles for bioanalytical applications.* Chemical Society Reviews, 2015. **44**(6): p. 1526-1560.
21. Pollnau, M., et al., *Power dependence of upconversion luminescence in lanthanide and transition-metal-ion systems.* Physical Review B, 2000. **61**(5): p. 3337-3346.
22. Soukka, T., et al., *Photochemical Characterization of Up-Converting Inorganic Lanthanide Phosphors as Potential Labels.* Journal of Fluorescence, 2005. **15**(4): p. 513-528.
23. Krämer, K.W., et al., *Hexagonal Sodium Yttrium Fluoride Based Green and Blue Emitting Upconversion Phosphors.* Chemistry of Materials, 2004. **16**(7): p. 1244-1251.
24. Wang, F., J. Wang, and X. Liu, *Direct Evidence of a Surface Quenching Effect on Size-Dependent Luminescence of Upconversion Nanoparticles.* Angewandte Chemie International Edition, 2010. **49**(41): p. 7456-7460.
25. Zhao, J., et al., *Upconversion luminescence with tunable lifetime in NaYF4:Yb,Er nanocrystals: role of nanocrystal size.* Nanoscale, 2013. **5**(3): p. 944-952.
26. Niu, W., S. Wu, and S. Zhang, *A facile and general approach for the multicolor tuning of lanthanide-ion doped NaYF4 upconversion nanoparticles within a fixed composition.* Journal of Materials Chemistry, 2010. **20**(41): p. 9113-9117.
27. Bogdan, N., et al., *Synthesis of Ligand-Free Colloidally Stable Water Dispersible Brightly Luminescent Lanthanide-Doped Upconverting Nanoparticles.* Nano Letters, 2011. **11**(2): p. 835-840.
28. Wang, F., et al., *Simultaneous phase and size control of upconversion nanocrystals through lanthanide doping.* Nature, 2010. **463**: p. 1061.
29. Liu, H., et al., *Deep tissue optical imaging of upconverting nanoparticles enabled by exploiting higher intrinsic quantum yield through use of millisecond single pulse excitation with high peak power.* Nanoscale, 2013. **5**(20): p. 10034-10040.
30. Zhan, Q., et al., *Using 915 nm Laser Excited Tm3+/Er3+/Ho3+-Doped NaYbF4 Upconversion Nanoparticles for in Vitro and Deeper in Vivo Bioimaging without Overheating Irradiation.* ACS Nano, 2011. **5**(5): p. 3744-3757.
31. Yi, G.-S. and G.-M. Chow, *Water-Soluble NaYF4:Yb,Er(Tm)/NaYF4/Polymer Core/Shell/Shell Nanoparticles with Significant Enhancement of Upconversion Fluorescence.* Chemistry of Materials, 2007. **19**(3): p. 341-343.
32. Qian, H.-S. and Y. Zhang, *Synthesis of Hexagonal-Phase Core−Shell NaYF4 Nanocrystals with Tunable Upconversion Fluorescence.* Langmuir, 2008. **24**(21): p. 12123-12125.

33. Boyer, J.-C. and F.C.J.M. van Veggel, *Absolute quantum yield measurements of colloidal NaYF4: Er3+, Yb3+ upconverting nanoparticles.* Nanoscale, 2010. **2**(8): p. 1417-1419.
34. Mousavi, M., et al., *Beam-profile-compensated quantum yield measurements of upconverting nanoparticles.* Physical Chemistry Chemical Physics, 2017. **19**(33): p. 22016-22022.
35. Würth, C., et al., *Relative and absolute determination of fluorescence quantum yields of transparent samples.* Nature Protocols, 2013. **8**: p. 1535.
36. Würth, C., et al., *Integrating Sphere Setup for the Traceable Measurement of Absolute Photoluminescence Quantum Yields in the Near Infrared.* Analytical Chemistry, 2012. **84**(3): p. 1345-1352.
37. Thomasson, B., *High Accuracy Relative Luminescence Quantum Yield Measurements of Upconverting Nanoparticles*. 2016, Lund University.

38. Dyomics, "*Quantum yield of DY-781*", https://dyomics.com/en/products/nir-excitation/dy-781.html.